Poleward Expansion of the Hadley Circulation and Associated Dynamics

Thesis Submitted to

Cochin University of Science and Technology

In Partial Fulfilment of the Requirements
for the Award of

Doctor of Philosophy
in
Physics

Under the Faculty of Science

by

Sneha Susan Mathew

Space Physics Laboratory

Vikram Sarabhai Space Centre

Indian Space Research Organisation

Thiruvananthapuram – 695022

India

August 2018

Declaration

This is to declare that the work presented in this thesis was carried out at the Space Physics Laboratory (SPL), Vikram Sarabhai Space Centre (VSSC), Thiruvananthapuram for the award of the degree of Doctor of Philosophy in Physics from the Cochin University of Science and Technology, Cochin, Kerala State, India. This thesis is the outcome of the original work done by me and the work did not form part of any dissertation submitted for the award of any degree, diploma, associateship or any other title or recognition from any University/Institution.

August, 2018 **Sneha Susan Mathew**

Thiruvananthapuram (Author)

भारत सरकार
अंतरिक्ष विभाग
विक्रम साराभाई अंतरिक्ष केन्द्र
तिरुवनंतपुरम६९५०२२-
केरला, भारत
फोन२५६२५६३ ४७१ ००९१ :
फेक्स२७०६५३५ ४७१ ००९१ :

सत्यमेव जयते

Government of India
Department of Space
Vikram Sarabhai Space Centre
Thiruvananthapuram-695 022
Kerala, INDIA
Telephone: (0091-471) 2562563
Fax: (+91-471) 2706535
Email: k_kishorekumar@vssc.gov.in

अन्तरिक्ष भौतिकी प्रयोगशाला
SPACE PHYSICS LABORATORY

डॉके किशोर कुमार ./ Dr. K. Kishore Kumar
Scientist/Engineer-SF

August 2018

CERTIFICATE

Certified that the thesis entitled "**Poleward Expansion of the Hadley circulation and Associated Dynamics**" submitted by **Ms. Sneha Susan Mathew** (Ph.D. Reg.No.4961) to Cochin University of Science and Technology, Cochin, embodies the original results of the investigations carried out at the Space Physics Laboratory, Vikram Sarabhai Space Centre, Thiruvananthapuram, under my supervision. The work presented in this thesis has not been submitted for the award of any other degree, diploma or associateship to any other University or Institution.

Dr. K. Kishore Kumar
(Thesis Supervisor)

Countersigned

Dr. Radhika Ramachandran
Director, SPL

भारत सरकार
अंतरिक्ष विभाग
विक्रम साराभाई अंतरिक्ष केन्द्र
तिरुवनंतपुरम६९५०२२-
केरला, भारत
फोन२५६२५६३ ४७१ ००९१ :
फेक्स२७०६५३५ ४७१ ००९१ :

Government of India
Department of Space
Vikram Sarabhai Space Centre
Thiruvananthapuram-695 022
Kerala, INDIA
Telephone: (0091-471) 2562563
Fax: (+91-471) 2706535
Email: k_kishorekumar@vssc.gov.in

अन्तरिक्ष भौतिकी प्रयोगशाला
SPACE PHYSICS LABORATORY

डॉ के किशोर कुमार ./ Dr. K. Kishore Kumar
Scientist/Engineer-SF

August 2018

CERTIFICATE

This is to certify that all the relevant corrections and modifications suggested by the audience during the Pre-synopsis Seminar and recommended by the Doctoral Committee of **Ms. Sneha Susan Mathew** (Ph.D. Reg.No.4961) have been incorporated in the thesis.

Dr. K. Kishore Kumar
(Thesis Supervisor)

Dedicated to

My parents

who gave me wings to fly

and

My love

who toughened it up

ACKNOWLEDGEMENTS

I prayed the almighty for knowledge, wisdom and courage. So was I placed to do Ph.D at Space Physics Laboratory (SPL), VSSC which is equipped with state of the art facilities of the ISRO. I look back the five years of my research with great satisfaction and contentment. At this juncture, it is my bounden duty to acknowledge with thanks the generous support and encouragement received from all the benefactors who were closely associated with me in my research work from the very beginning till completion of this task.

First and foremost, I thankfully acknowledge the constant motivation and support of my supervisor Dr. K. Kishore Kumar. I would not have been able to complete this task successfully, but for his valuable guidance, constructive criticisms and humane approach. Kishore sir has been kind, patient, and was always ready to provide all the needed help and support during the course of my research work, which stood in good stead to complete my work successfully. I am grateful to Dr. Radhika Ramachandran, Director SPL, Dr. Anil Bhardwaj and Dr. K. Krishnamoorthy, former Directors of SPL, for providing me all the necessary facilities during the course of the present work. I gratefully acknowledge with thanks the constant motivation and guidance provided by Dr. Geetha Ramkumar, Head, ADB, towards the completion of this thesis. My special thanks are also due to my Doctoral Committee members, the SPL academic committee members as well as the Central Level Monitoring Committee members for their critical evaluation and timely guidance on the present work. I also express my sincere gratitude to my group members at SPL viz. Dr. K. V. Subrahmanyam, Dr. Siddardh Shankar Das, Dr. S.V. Sunil Kumar for their motivation and support for the fruitful completion of the thesis. I wish to place on record the generous support provided by Dr. K. V. Subrahmanyam in completing this project from the inception. A special word of thanks goes to Subbu sir for his genuine help in sorting out the academic as well as official matters at SPL and CUSAT. I also thank all the administrative staff at SPL, especially Ms. Sisira and Ms. Suseela for their immense help in dealing with the official matters. I appreciate the timely help received from VSSC library which provided me with internet facility as

well as remote access to scientific papers which has expedited the completion of my work.

I am thankful to SPL and its community for giving me the opportunity to grow myself academically and personally. I sincerely thank my beloved friends Vrinda and Kavitha for their relentless academic and emotional support. I also express my deep gratitude to my friends Suneeth, Aneesh, Jayachandran and Nithin. I owe much to my seniors Dr. Prijith, Dr. Madhav, Dr. Muhsin, Ms. Lakshmi, Mr. Ajesh, and Dr. Aryasree for their valuable guidance and advices on the academic matters at SPL; so also to Roshny, Govind, Koushik, Maria, Lavanya, Aswini, Aswathy, Edwin, and Nalini for all the good times they have given me at SPL. It is also worthwhile to mention here that I was greatly benefited during the formal and informal discussions I had with my friends at SPL.

The span of five years of research has provided me patience, perseverance and self-confidence necessary to complete this task successfully. I sincerely acknowledge the emotional support of my parents for raising me to be ambitious and hardworking. Had I not received the generous support and encouragement of my family and friends, it would not have been possible for me to complete this assignment successfully. I wish to express my heartfelt thanks to my younger sister Bhagya for all the love and care and the cheerful support rendered to me for completing this thesis. I also thank my in-laws for their generous support in accomplishing this task. Last, but not the least, I thank the most important person in my life, Lijo, my husband, for cheerfully encouraging me to beat the odds to complete this thesis in a successful manner.

CONTENTS

PREFACE

Differential heating of the Earth's surface by the Sun from equatorial to polar latitudes is one of the major factors that play a vital role in controlling the Earth's lower atmospheric dynamics. This differential heating induces large scale ascent of moist air at the equatorial latitudes, leading to formation of deep convective systems and release of large amount of latent heat. Subsequent meridional transport towards the poles near the tropopause level, descent of dry air over subtropics and a compensating low level transport towards the equator at low levels constitute the tropical Hadley Circulation (HC). This planetary scale circulation spans one-third of the globe from tropics to subtropics and controls the established climate patterns in these regions. By now it is well known that the HC is responsible for the wet and humid climate of the tropics and the dry and parched climate of the subtropics. The distinct biodiversity of the regions is adapted to these climatic and precipitation patterns.

Of late, the sinking latitudes of HC has gained importance because of the fluctuations they exhibit, mainly due to changes in meridional temperature gradient arising in response to the changing concentrations of greenhouse gases and other anthropogenic sources. Owing to its direct impact on subtropical climate, many researchers across the globe are focusing on quantifying the variability in the width and strength of the HC. In fact, recent observational studies have shown that the annually averaged HC has undergone a poleward expansion as well as strengthening over the past few decades. Although modelling simulations also project the HC expansion phenomena, a consensus is yet to emerge on the observed and modelled rates of expansion of the HC. Besides, studies are yet to reliably quantify the regional variations in HC expansion rate arising from the zonal undulations in topography. Several factors, natural as well as anthropogenic, have been proposed to be leading to the phenomena of tropical expansion. However their pathway of action is not clear yet and no conclusive evidence has been drawn on the ultimate driver of the HC expansion. Leading climate scientists have observed that the expansion of the HC

and the tropics will have serious consequences due to the associated shift in precipitation patterns, poleward movement of jet streams and storm tracks, changes in distribution of climatically important trace gases in the stratosphere as well as changes in the ocean circulation. The biodiversity of the tropics shall also be not spared from these consequences. The present thesis explores various facets of this phenomenon and the dynamics associated with it by means of reanalysis and observational datasets.

The thesis is entitled "***Poleward Expansion of the Hadley Circulation and Associated Dynamics***" and is organized in 7 Chapters. Chapter 1 provides a detailed discussion on the phenomena of poleward expansion of the HC, factors causing it, and future projection of expansion rates. Chapter 2 provides description on the four major reanalysis datasets (JRA-55, NCEP, ERA-I and MERRA) as well as ground-based and space-based observational datasets (IGRA, COSMIC GPS-RO, GPCP and TRMM-PR) used for analysis in the thesis. Chapter 3 characterizes the HC using meridional mass stream function (MSF) metric using reanalysis datasets and quantifies the annual cycle of the HC expansion rate. Prior to this, the reanalysis data is verified for their use in HC dynamical studies by comparing it with global network of radiosonde observations from IGRA. An expansion of $\sim 1.5^0$ latitude per decade during the month of July, significant at 95% confidence level, is brought out from this analysis. Chapter 4 is oriented towards delineating the regional features of the HC using the tropopause metric derived from high resolution GPSRO observations from COSMIC. The tropopause metric is utilized in three unique ways to zonally resolve the HC edges and determine the contribution of the each region to the zonal mean width of the HC during boreal summer and winter seasons. Chapter 5 is one step towards identifying the mechanism behind the HC expansion. In this chapter, the role of latent heat release in modulating the strength and width of the HC is investigated using space borne observations of precipitation latent heating from TRMM PR. The results are in support of the modeling simulations in this regard. Chapter 6 characterizes the long term changes in the parameters of hydrological cycle within the ascending and descending branches of the HC. The analysis brings out that the variations in relative humidity, cloud cover and rainfall within the ascending and descending branches of the HC, which are in conjunction with the

observed poleward expansion of the HC. Chapter 7 summarises the thesis as well as provides future scope for investigations into the phenomena of HC expansion. It is anticipated that the results presented in this thesis shall be of utmost interest to the scientific community as well as to rest of the readers.

Sneha Susan Mathew

LIST OF PUBLICATIONS

Thesis related publications:

1. **S.S. Mathew**, Kumar, K.K., K.V. Subrahmanyam, "Hadley Cell Dynamics in Japanese Reanalysis-55 dataset: Evaluation using other Reanalysis datasets and Global Radiosonde Network Observations", *Climate Dynamics*, 382, pp. 1-14, 2016, DOI: 10.1007/s00382-016-3051-5
2. **S.S. Mathew**, Kumar, K.K., "Zonally resolved width of the tropical belt using GPS-RO measurements", *IEEE Journal of Selected Topics in Applied Earth Observations and Remote Sensing,* 2018, DOI: 10.1109/JSTARS.2018.2828342
3. **S.S. Mathew**, Kumar, K.K., "On the role of precipitation latent heating in modulating the strength and width of the Hadley Circulation", *Theoretical and Applied Climatology*, 2018, DOI: 10.1007/s00704-018-2515-4
4. **S.S. Mathew**, Kumar, K.K., "Characterization of the long-term changes in moisture, clouds and precipitation in the ascending and descending branches of the Hadley circulation", *Journal of Hydrology (Submitted)*, 2018

Other Publications:

5. Kumar, K.K., **S.S. Mathew**, and K.V. Subrahmanyam, "Anomalous tropical planetary wave activity during 2015/2016 quasi biennial oscillation disruption", *Journal of Atmospheric and Solar-Terrestrial Physics*. DOI: 10.1016/j.jastp.2017.12.004, 2017
6. Kumar, K.K., K.V Subrahmanyam, **S.S Mathew**, N. Koushik, and G Ramkumar, Simultaneous observations of the quasi 2-day wave climatology over the low and equatorial latitudes in the mesosphere lower thermosphere", *Climate Dynamics*, pp. 1-13, DOI: 10.1007/s00382-017-3916-2, 2017

CONFERENCE PRESENTATIONS

1. **Sneha Susan Mathew**, Karanam Kishore Kumar, Kandula Venkata Subrahmanyam, Expansion of Hadley Cell in Climate Change Scenario: A Comparison between Reanalysis and Radiosonde Observations, *27th Kerala Science Congress (KSC 2015)* Alappuzha, India, 27-29 January, 2015.

2. **Sneha Susan Mathew**, Karanam Kishore Kumar, Kandula Venkata Subrahmanyam, Expansion of Hadley Cell in Climate Change Scenario: A Comparison between Reanalysis and Radiosonde Observations, *National Symposium on "WEATHER AND CLIMATE EXTREMES" (TROPMET 2015)*, Punjab University, Chandigarh, India, 15-18 February, 2015.

3. **Sneha Susan Mathew**, Karanam Kishore Kumar, Kandula Venkata Subrahmanyam, Expansion of Hadley Cell in Climate Change Scenario: A Study using Reanalysis and Radiosonde Observations, *AGU Chapman Conference on the Width of the Tropics: Climate Variations and Their Impacts*, Santa Fe, New Mexico, USA, 27-31 July, 2015

4. **Sneha Susan Mathew**, Karanam Kishore Kumar, Regional Features of the Hadley Circulation- A Tropopause Perspective, *19th National Space Science Symposium-2016 (NSSS-2016)*, Vikram Sarabhai Space Centre, Thiruvananthapuram, India, 9-12 February, 2016.

5. **Sneha Susan Mathew**, Karanam Kishore Kumar, New Insights into the Regional forcing of Tibetan Plateau Induced Dynamics on the Hadley Circulation, *19th National Space Science Symposium-2016 (NSSS-2016)*, Vikram Sarabhai Space Centre, Thiruvananthapuram, India, 9-12 February, 2016.

LIST OF FIGURES

Chapter 1

Chapter 2

Chapter 3

Chapter 5

Chapter 6

LIST OF TABLES

LIST OF ACRONYMS

1DVar	1Dimensional Variational data assimilation
20CR2	20th Century Reanalysis version2
3DVar	3Dimensional Variational data assimilation
4DVar	4Dimensional Variational data assimilation
AGCM	Atmospheric General Circulation Model
AIRS	Advanced Infrared Sounder
AM2.1	Atmospheric Model version 2.1
AMIP	Atmospheric Model Inter-comparison Project
AMSR-E	Advanced Microwave Scanning Radiometer for EOS
AMSU-A	Advanced Microwave Sounding Unit-A
AMSU-B	Advanced Microwave Sounding Unit-A
AMV	Atmospheric Motion Vectors
ATOVS	Advanced TIROS Operational Vertical Sounder
AVHRR	Advanced Very High Resolution Radiometer
BD	Brewer-Dobson circulation
BSS	Bulk Static Stability
BUFR	Binary Universal Format Representation
CAM-3	Community Atmosphere Model version 3
CAMS	Climate Assessment and Monitoring System
CDAAC	COSMIC Data Analysis and Archive Centre
CDAS	Climate Data Assimilation System
CERES	Clouds and Earth's Radiant Energy System
CF	Cloud Fraction
CFC	Chlorofluorocarbon
CFSR	Climate Forecast System Reanalysis
CHAMP	Challenging Mini-Satellite Payload
CIRA	COSPAR International Reference Atmosphere
CMIP3	Coupled Model Intercomparison Project- phase 3
CMIP5	Coupled Model Intercomparison Project- phase 5
COADS	Comprehensive Ocean Atmosphere Data Set

COSMIC	Constellation Observing System for Meteorology, Ionosphere and Climate
CPC	Climate Prediction Centre (NOAA)
CRM	Cloud Resolving Model
CRTM	Community Radiative Transfer model
DCAPE	Dynamic Convective Available Potential Energy
ECMWF	European Centre for Medium range Weather Prediction
ENSO	El-Nino Southern Oscillation
EOS	Earth Observing System
ERA-25,-40,-I	ECMWF Reanalysis -25,-40,-Interim
ERBE	Earth Radiation Budget Experiment
ERS-1,-2	European Remote Sensing Satellite
EUMETSAT	European Organisation for the Exploitation of Meteorological Satellites
FGGE	First GARP Global Experiment
FORMOSAT-3	Formosa Satellite Mission #3
GARP	Global Atmospheric Research Programme
GATE	GARP Atlantic Tropical Experiment
GCM	General Circulation Model
GEOS 5	Goddard Earth Observing System version 5
GEWEX	Global Energy and Water Cycle Experiment
GFDL	Geophysical Fluid Dynamics Laboratory
GHCN	Global Historical Climate Network
GHGs	Green House Gases
GISS	Goddard Institute for Space Studies (NASA)
GMAO	Global Model Assimilation Office
GMS	Geostationary Meteorological Satellite
GNSS-RO	Global Navigation Satellite Systems- Radio Occultation
GOCART	Goddard Chemistry Aerosol Radiation and Transport
GOES	Geostationary Operational Environmental Satellite
GPCC	Global Precipitation Climatology Centre
GPCP v2.1	Global Precipitation Climatology Project version 2.1
GPI	GOES Precipitation Index
GPM	Global Precipitation Mission

GPS RO	Global Positioning System Radio Occultation
GRACE	Gravity Recovery and Climate Experiment
GRAS	Global Navigation Satellite Systems Receiver for Atmospheric Sounding
GRIB	Gridded Binary
GSM	Global Spectral Model
GTS	Global Telecommunication System
HC	Hadley Circulation
HCFC	Hydrochlorofluorocarbons
HIRS	High-Resolution Infrared Sounder
IAU	Incremental Analysis Update
IFS	Integrated Forecast System
IGRA	Integrated Global Radiosonde Archive
IPCC	Intergovernmental Panel for Climate Change
IPCC AR4	Intergovernmental Panel for Climate Change fourth Assessment Report
IPCC AR5	Intergovernmental Panel for Climate Change fifth Assessment Report
IR	Infrared
ISCCP	International Satellite Cloud Climatology Project
ITCZ	Inter Tropical Convergence Zone
JAXA	Japan Aerospace Exploration Agency
JMA	Japan Meteorological Agency
JRA -25,-55	Japanese Re-Analysis -25,-55
LEO	Low Earth Orbiting satellite
LH	Latent Heating
LIS	Lighting Imaging Sensor
LRT	Lapse Rate Tropopause
LUT	Look Up Table
MERRA -1,-2	Modern Era Retrospective Analysis for Research and Application -1,-2
MeteoSat	Meteorological Satellite
MHS	Microwave Humidity Sounder
MLS	Microwave Limb Sounder

MODIS	Moderate Resolution Imaging Spectroradiometer
MSC	Meteorological Satellite Center (JMA)
MSF	Mass Stream Function
MSU	Microwave Sounding Unit
MTSAT	Multifunctional Transport Satellite
MW	Micro Wave radiation
NASA	National Aeronautics and Space Administration
NCAR	National Centre for Atmospheric Research
NCDC	National Climatic Data Centre
NCEP R1, R2	National Centre for Environmental Prediction Reanalysis 1,2
NH	Northern Hemisphere
NMC	National Meteorological Centre
NOAA	National Oceanic and Atmospheric Administration (USA)
NWP	Numerical Weather Prediction
OA	Optimal Averaging
OLR	Outgoing Longwave Radiation
OPI	OLR Precipitation Index
OSIRIS	Optical Spectrograph and Infra-Red Imaging System
PATMOS-x	Extended Pathfinder Atmospheres
PDO	Pacific Decadal Oscillation
P-E	Precipitation minus Evaporation
PR	Precipitation Radar
PTH	Precipitation Top Height
QC	Quality Control
QuickSCAT	Quick Scatterometer
RAOB	Radiosonde Observation
RAOBCORE	Radiosonde Observation Correction for Reanalysis
RATPAC	Radiosonde Atmospheric Temperature Products for Assessing Climate
RCP 8.5	Representative Concentration Pathway with the CO_2 induced radiative forcing maximising at $8.5Wm^{-2}$
RF	Rainfall
RH	Relative Humidity
RSS	Remote Sensing Systems

SAC-C	Satélite de Aplicaciones Cientificas-C
SH	Southern Hemisphere
SLH	Spectral Latent Heating
SO	Southern Oscillation
SSM/I	Special Sensing Microwave/Imager
SSMI/S	Special Sensing Microwave Imager/Sounder
SST	Sea Surface Temperature
SST	Sea Surface Temperature
SSU	Stratospheric Sounding Unit
STJ	Sub Tropical Jetstream
TCWV	Total Column Water Vapour
THF	Tropopause Height Frequency
TIROS	Television Infrared Observation Satellite
TIROS-N	TIROS-Next generation
TMI	TRMM Microwave Imager
TMPA	TRMM Multi-satellite Precipitation Analysis
TOA	Top of Atmosphere
TOGA-COARE	Tropical Ocean and Global Atmosphere- Coupled Ocean Atmosphere Response Experiment
TOVS	TIROS Operational Vertical Sounder
TpAO	Tropopause Annual Oscillation
TpGr	Tropopause Gradient
TRMM	Tropical Rainfall Measuring Mission
UCAR	University Corporation for Atmospheric Research (USA)
US	United States
UTC	Universal Time Coordinated
UV	Ultra Violet
VarBC	Variational Bias Correction
VIRS	Visible and Infrared Scanner
VTPR	Vertical Temperature Profile Radiometer
WC	Walker Circulation
WCRP	World Climate Research Programme
WMO	World meteorological Organization

CHAPTER 1
INTRODUCTION

1.1 Introduction to Earth's Atmosphere

1.1.1 Atmospheric Composition

The Earth's atmosphere is a deep blanket of gases surrounding the planet, and was formed as a result of continual outgassing from the primordial Earth. The atmosphere is believed to have reached its current composition in over billions of years, and as a result of the influence of the living organisms on the Earth. For instance, oxygen content in our early atmosphere was increased by the early plant life. The atmosphere in its present form is composed of *Nitrogen, Oxygen* and *Argon* which constitutes 78.08%, 20.98%, and 0.093% of the atmosphere, respectively, by volume (Wallace and Hobbs 2006). In addition, the atmosphere also comprises of variable gases in trace amounts, the most important of which are *Carbon dioxide* (0.035%) and *water vapour* (0 to 4%). These gases are responsible for maintaining the adequate near-surface temperature for the sustenance of life on the Earth. Yet another important gas which is present in trace amounts in the atmosphere is *Ozone* (0.002% in stratosphere) which protects the biota from the harmful Ultra Violet rays of the Sun. It is also responsible for the increasing temperature of the region enclosed between 16-50km altitude as opposed to the regions below and above it. Thus composition of the atmosphere determines the climate of the Earth. Changes in the constituent species as a result of the anthropogenic activities, especially in those which are of trace amounts, is thus bound to play a major role in the evolution of the current climate of the planet.

1.1.2 Thermal Stratification of Atmosphere

The weather and climate of the Earth is fuelled by energy from the Sun. The top of the atmosphere (TOA) receives solar radiation at wavelengths in the 200nm (Ultra Violet) to 4000nm (Infrared) spectral range, with intensity peaking at

500nm. The atmosphere, being transparent to a majority of these wavelengths, allows most of it to pass through to reach the surface of the Earth. The surface absorbs this energy and re-radiates it. The energy radiated by the Earth is at Infrared wavelengths, with peak emissions at 10-12μm, to which the atmosphere is not transparent. The atmosphere thus absorbs the radiation in this wavelength regime and warms up from a near-surface level. The amount of solar radiation absorbed at each level depends on the properties of the atmospheric constituents at the respective level. This results in a thermally stratified atmosphere in the vertical direction. The different layers in the Earth's atmosphere stratified in this manner are viz. the *troposphere,* the *stratosphere,* the *mesosphere* and the *thermosphere*. These four different layers of the atmosphere are shown in figure 1.1.

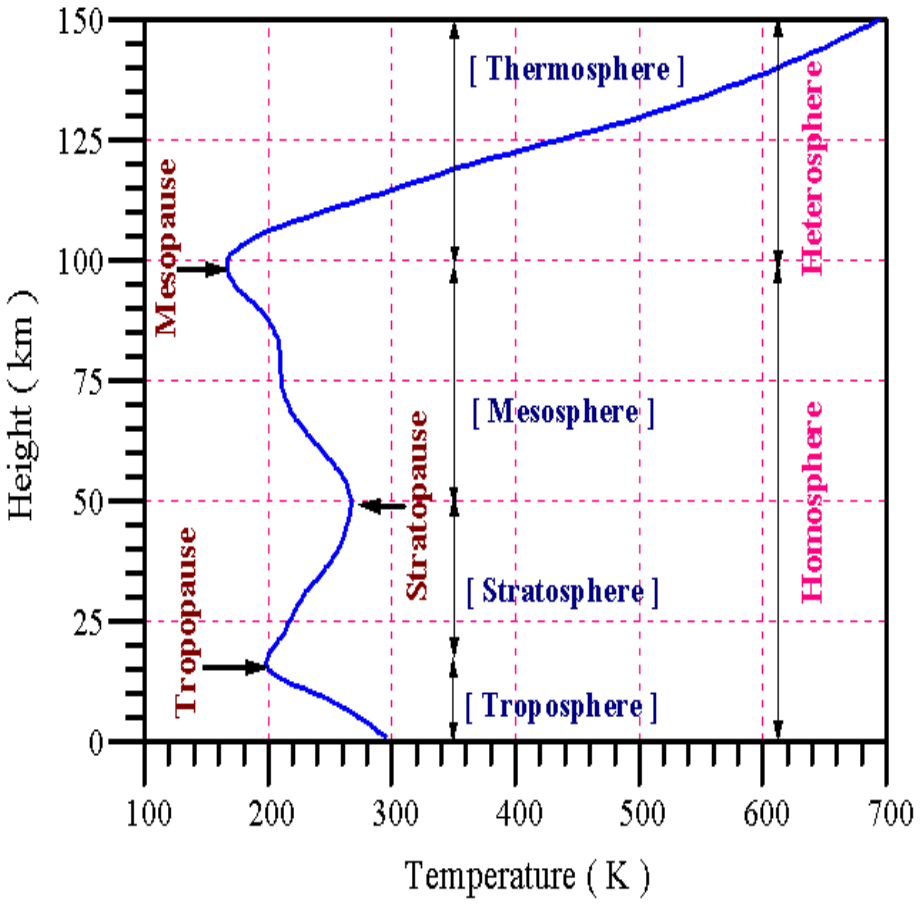

Figure 1.1: Structure of a thermally stratified atmosphere for the tropics obtained using the COSPAR International Reference Atmosphere (CIRA) model *(Figure taken from (Kumar 2004)).*

As mentioned before, the temperature of each layer is mainly determined by the composition and atmospheric density of that layer. The energy radiated out by the Earth's surface heats the atmospheric layers immediately above it. As the distance from the warm surface increase, the temperature decreases in the troposphere at the rate of 6.5^0C per kilometre (*lapse rate*) (Liou 2002). This steady fall in temperature is conducive for most of the weather phenomena in the atmosphere. The temperature decrease is stalled at the *tropopause*, which records a typical minimum temperature of ~190K in the tropical regions (Fueglistaler et al. 2009). Note that the tropopause height decreases from the tropics (*~16-18km*) to mid-latitudes (*~11-13km*) and further to the poles (*~6-8km*) as a result of the changes in convective activities at the respective latitudes. Beyond the tropopause, the temperature increases with height as a result of absorption of Ultra Violet radiation from the Sun by a layer of ozone molecules with peak abundance near 25km (Mohankumar 2008). This region of temperature inversion is called the stratosphere, the upper limit of which is the *stratopause* occurring at 50km in the atmosphere. Beyond the stratosphere, there are only fewer molecules left in the upper layers of the atmosphere to absorb the solar radiation. Above stratosphere lies the mesosphere, where temperature decreases with height. This decrease is due to the radiative cooling by the Carbon dioxide molecules present in these levels. The mesosphere is, in fact, the coolest region in the atmosphere, with the *mesopause* (~90km) recording the minimum atmospheric temperature (~175K). The mesopause altitude and temperature, however, show significant seasonal and latitudinal variations. The mesopause of the high latitudes is in fact found to be higher and warmer during winter (100km, 200K) than during summer (85km, 150K) (John and Kumar, 2011 and references therein); whereas that over the equatorial latitudes is found to be consistently at 100km with a mean temperature of 170K (Ratnam et al. 2010). Above the mesospheric layer lay the thermosphere, the region of atmosphere where temperature increases with height due to absorption of extremely short wave radiation from the Sun by the Oxygen molecules existing in this layer. Since there are only very few molecules at these altitudes, even a slight absorption of solar energy at these levels can lead to temperatures as high as 1700^0C. The thermosphere extends up to 500km, after which the mean free path of the

molecules become so large that the molecules can escape the Earth. This level then marks the upper limit of the atmosphere.

The most dynamic region of a thermally stratified atmosphere is the troposphere. The physical processes happening in the troposphere are the ones which are of utmost importance in weather and climate research activities, owing to their direct impact on the life of mankind. Fifty per cent of the atmosphere is confined within the first 5.5km from the surface (Leroux 2014), making troposphere the densest part of the atmosphere. The processes of turbulent and convective mixing hence dominate in the tropospheric layer, making it the most active region in terms of weather. Troposphere houses most of the water vapour and other greenhouse gases, which plays a dominant role in keeping the mean temperature of the Earth. This lowest layer of atmosphere is also influenced by the nature of the underlying surface. For instance, a land surface emits more than the oceans. Again, deserts emit more than a vegetated or forest land. Geography of the surface thus determines the amount of short wave radiation that is absorbed at the surface and the quantity of long wave radiation that is emitted to space. The radiative imbalance produced due to such geographical undulations lead to the formation of most of the zonal atmospheric circulation systems.

1.1.3 Radiation budget of the Earth-Atmosphere System

The state of balance between the incoming shortwave solar flux and the emitted long wave terrestrial flux is called *radiative equilibrium*. All processes in the atmosphere are so oriented that the radiative equilibrium condition is satisfied. The redistribution of solar energy received at TOA in the earth- atmosphere system to emit an equal amount of long wave radiation at the same level is called the *radiation budget* of the Earth. An illustration of the same is shown in figure 1.2. The earth-atmosphere system receives energy from the Sun in the form of shortwave radiation. Of the 100% of insolation that reaches the TOA, 29% is reflected back to space by clouds, atmospheric particles, as well as by the surface (ice/snow). Out of the rest 71%, 23% is absorbed by the atmospheric gases and 48% by the surface. Since every surface above absolute zero temperature radiates energy depending on its temperature, the atmosphere and surface should also radiate the energy they have absorbed. Then only the temperature of the planet will remain stable. Out of the 71% of the long wave radiation that is

emitted by the earth-atmosphere system as a whole, the satellite measurements showed that the contribution of the atmosphere is 59% (in place of the 23% it has absorbed) and that of the surface is only 12% (whereas it has absorbed 48%). But neither the surface temperature rise in response to the heat it retains, nor does the temperature of the atmosphere fall so low in response to the heat it loses. This behaviour can be understood if only the energy budget of the surface and the atmosphere are considered separately.

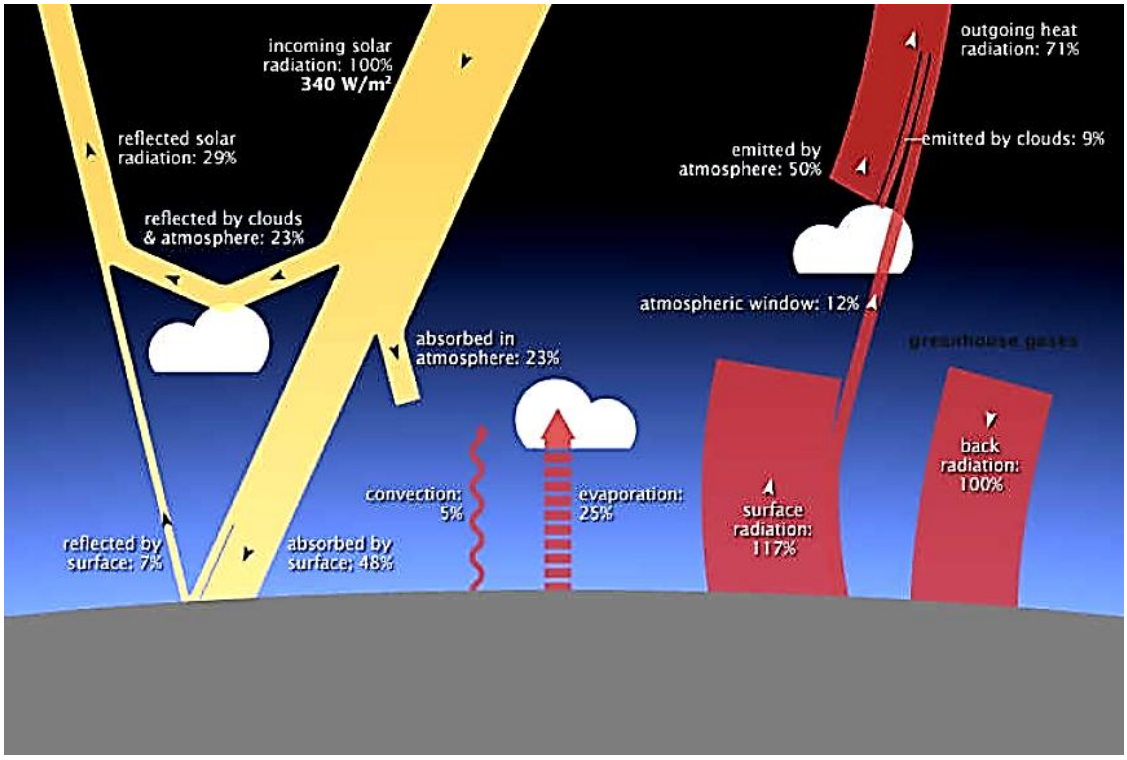

Figure 1.2: Earth's energy budget *(Figure adapted from https://earthobservatory.nasa.gov/Features/EnergyBalance).*

Of the 48% of energy absorbed by the surface, 25% is lost by way of convection, 5% is used for evaporation and 18% is emitted as thermal infrared (IR) radiation. The surface thus gave up what it has absorbed. 12% of the long waves emitted by the surface are directly radiated to space, while the rest is absorbed in the atmosphere (25% from convection+ 5% from evaporation+ ~6% from IR). This is in addition to the 23% of the incoming short wave radiation it has already absorbed. Thus the atmosphere absorbs 36% of energy from the surface too, along with the directly absorbed 23%, leading to a total of 59% absorption of radiation. The atmosphere has been observed to emit 59% and surface 12% of radiation, all of what it has absorbed. This leads to a total of 71% long wave

emission at the TOA by the earth-atmosphere system, which is same as the amount of short wave radiation input to the system at the TOA. Thus, a radiative equilibrium is established on Earth.

The earth-atmosphere system receives a total of 340 W/m^2 of energy at the TOA from the Sun; however, after accounting for the albedo of earth, about 240 W/m^2 of energy reaches the surface. Various meteorological processes reshuffle the 240 units of energy within the system before radiating out the same amount of energy to space, so as to maintain the radiative equilibrium. It is to be noted that this equilibrium does not hold true for any specific region on the Earth, or for short time spans.

1.1.4 Latitudinal variation of insolation

The Earth and the atmosphere together do not maintain the radiative balance at all latitudes (Ahrens 2009). Since the amount of terrestrial flux remain more or less uniform along all latitudes, it is quite understandable that the above difference is mainly due to the latitudinal variation of insolation.

The difference in insolation with respect to latitude is mainly caused by the tilt of the spherical Earth about its rotational axis, and a seasonal variation to it is caused by the orbital motion of the Earth around the Sun. The spherical shape of the earth causes the angle of incidence of the solar radiation over surface to vary from 90^0 over the tropics to 0^0 over the Polar Regions. Greater the angle of incidence, lesser is the area to be illuminated, and hence higher the intensity of insolation over these regions. This means that the Polar Regions will be completely devoid of any radiation. However, the tilt of the rotation axis of Earth ensures that the Polar Regions also receive energy during the respective hemisphere's summer. Because of the same tilt, the angle of incidence in the tropics varies only between 90^0 and $43^0$06' (Leroux 2014); hence tropical regions receive the maximum amount of insolation as compared to Polar Regions. Again, the length of daylight hours is extended during the summer solstice, which implies that the summer hemisphere is exposed to energy from the Sun for a lengthier time. The ellipticity of the orbit is responsible for seasonal variation in the amount of radiation reaching the surface. During NH winter solstice, the sun is at perihelion, which reduces the mean Sun-Earth distance, thus leading to an

increase in the amount of solar radiation reaching the surface during this time of the year.

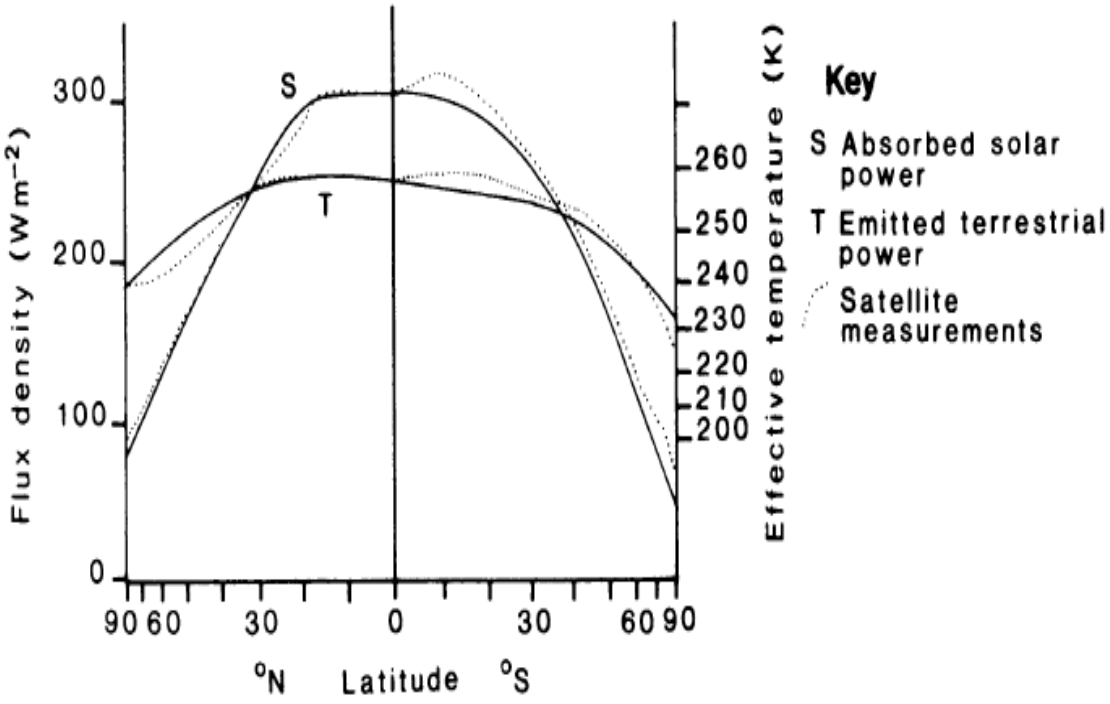

Figure 1.3: Latitudinal distribution of absorbed shortwave and terrestrial long wave radiation *(Figure taken from McIlveen, (1992)).*

Thus, the amount of insolation reaching the Earth's surface is influenced by the shape, rotational and revolutionary motions of the earth. And, under the assumption of uniform features on earth, the absorbed short wave radiation exhibits a strong maximum within the tropics. However, the terrestrial flux is more or less uniform along all latitudes. Figure 1.3 is an illustration of the same. The tropics absorb ~300W/m^2 of shortwave energy as compared to the ~80W/m^2 absorbed by the Polar Regions. Of this, only ~240W/m^2 is radiated out, leading to a surplus of ~60W/m^2 in the tropical regions. On the other hand, the high latitudes emit ~240W/m^2 of terrestrial radiation which is thrice larger than the amount of shortwave radiation absorbed there. Thus there is a clear excess of energy absorbed by the surface over the tropical latitudes and a deficit over the Polar latitudes. This latitudinal gradient in energy forms the basis of all meridional circulation patterns. The excess energy is transported from the tropics to the polar regions in the form of sensible heat, latent heat, and potential energy (Lockwood 1979; Trenberth and Stepaniak 2004) by way of atmospheric

Hadley Circulation and deep oceanic circulation. On the other hand, differences in topography lead to longitudinally undulating patterns of heating and cooling. For instance land locked regions undergo intense warming during day and cooling during night time, whereas the temperature changes are only moderate in oceanic or coastal regions. Zonal circulation patterns evolve under such longitudinally varying geography of the Earth.

1.2 Large Scale Circulations in the Earth's Atmosphere

The general pattern of atmospheric response to unequal heating of Earth's surface are well represented when the circulations of scale >1000km are considered. Such circulations have pattern of winds and pressure that either recur seasonally, or is present throughout the year. These large scale circulations can be either zonal or meridional. While the tri-cellular model explains the idealized large-scale meridional circulation pattern within the troposphere, the Brewer-Dobson circulation gives an account of that within the stratosphere. The large scale circulation confined to a zonal plane within the troposphere is called the Walker circulation.

1.2.1 Global Tropospheric Wind Climatology

In order to explain the climatology of winds in the troposphere, one needs to consider two factors:

1. Differential heating of the Earth and its atmosphere by the Sun
2. Angular momentum of the earth-atmosphere system due to rotation of the Earth.

While the atmospheric motions are initiated by factor 1, the latter determines the direction and speed of these motions. Under the assumption of a zonally uniform topography, there are three major prevailing surface wind belts in each hemisphere on a rotating Earth:

1. Tropical easterlies/Trade winds
2. Subtropical Westerlies
3. Polar easterlies

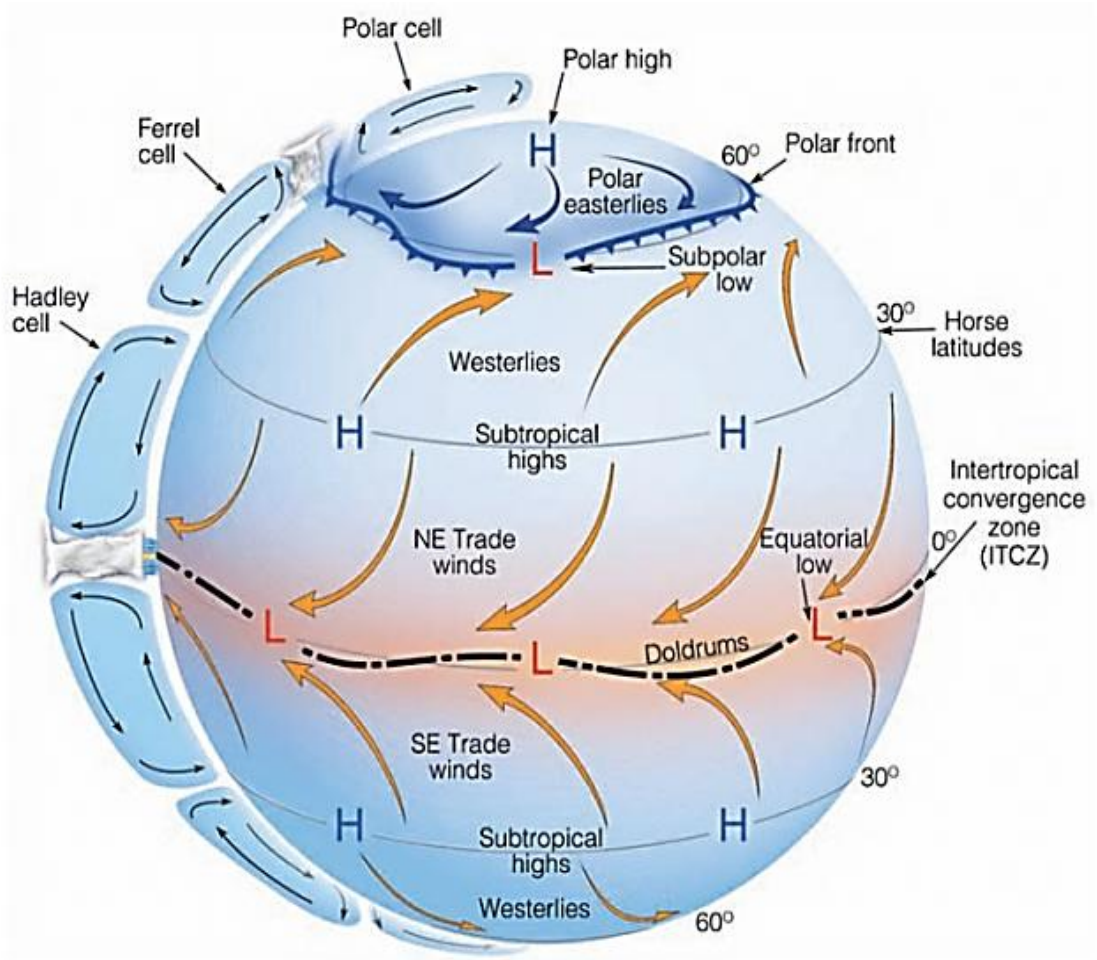

Figure 1.4: An idealized pattern of the general circulation of the atmosphere *(Figure taken from (Ahrens 2009)).*

Tropical easterlies cover the latitudes from 0^0-30^0N/S; *Polar easterlies* are enclosed between the polar and the 60^0N/S latitudes; and embedded within the 30^0-60^0N/S latitudinal belt are the *Subtropical westerlies*. These prevailing winds are the surface counterparts of the *tri-cellular model* of the atmospheric general circulation, which is shown in figure 1.4. This simple model of general circulation was developed by C. G. Rossby in 1947 and improvised by others in the later years. According to this model, there are three dominant meridional circulation cells in the troposphere, viz. *Hadley cell, Ferrel cell, and Polar cell*. The easterly/westerly component of the prevailing winds is due to the presence of *Coriolis force* arising out of the angular momentum conservation on a differentially rotating earth. There occur considerable changes in the strength and extent of the prevailing winds if the longitudinal differences in surface pressure due to topography are also taken into consideration.

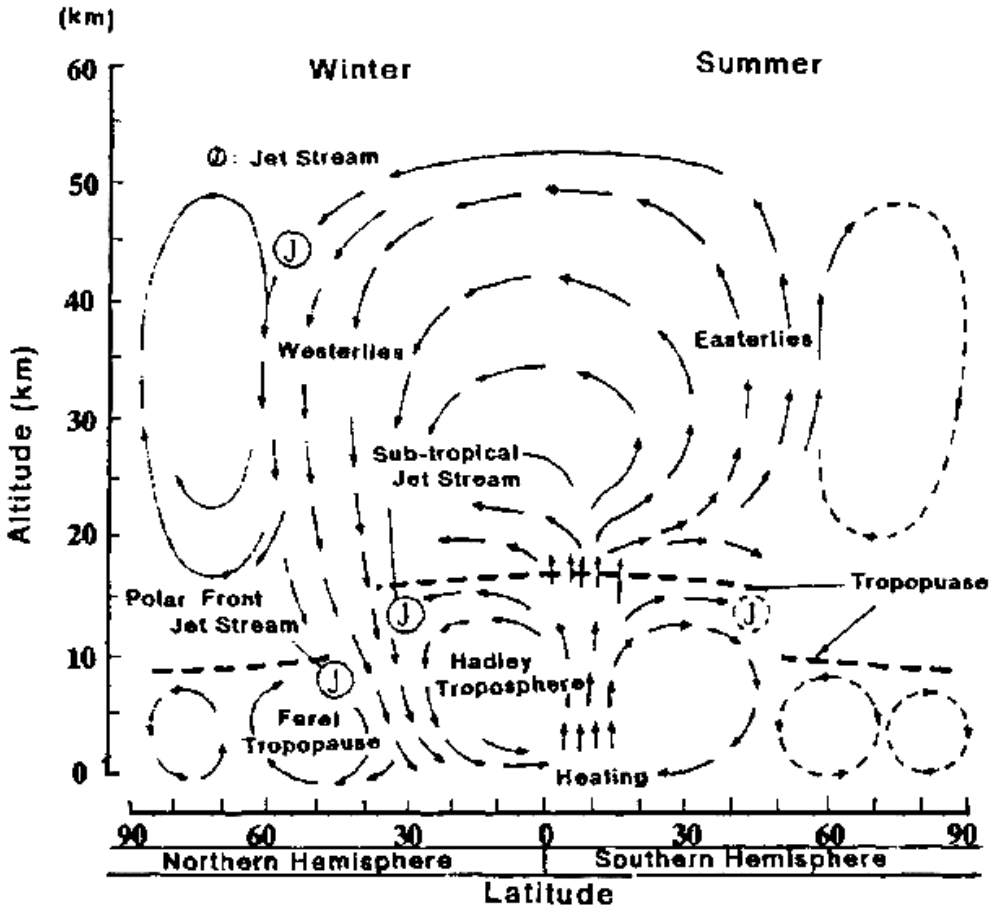

Figure 1.5: Schematic of the tropospheric and stratospheric circulations *(Figure taken from Murakami, (1995)).*

Figure 1.5 shows a schematic of the vertical cross-section of the meridional circulations within the troposphere and the stratosphere. This figure clearly indicates the prevailing wind directions at different altitudes in the atmosphere. According to the tri-cellular model of the atmosphere, at higher levels in the troposphere, the wind systems are poleward over the tropics and equatorward over the subtropics. These upper-tropospheric winds develop a westerly component following the principle of angular momentum conservation. Such high speed zonal westerly winds are called *Jet Streams*. On similar lines of thought, the upper-level equatorward flow of air over the mid-latitudes should acquire an easterly component. However observations show that the mid-latitude wind system aloft is westerly. This observation could be explained only by incorporating the fact that longitudinal variation in surface pressure as well as friction breaks down the principle of angular momentum conservation over these latitudes. The westerly component of the poleward flowing upper-tropospheric

winds over the mid-latitudes was thus found to be achieved by the transport of eddy momentum flux from the upper-level winds of low and high latitudes.

1.2.2 Hadley Circulation

Hadley circulation (HC) is the tropical branch of the general circulation which is characterized by rising motions in the equatorial region and sinking motion in the sub-tropical regions. As mentioned in section 1.1, the tropical atmosphere is heated in excess than the poles which causes a low pressure to develop in these regions making the air parcels buoyant. The rising parcels in the warm tropics cools adiabatically, condensing the water vapour present within it. During the process latent heat is released, triggering further convection. Air parcels rising in such organized convections near the equator reaches up to the tropopause, from where further vertical motion is restricted by the stable stratosphere. The parcels then start spreading out towards the poles. During this process, air cools radiatively and gets denser; in addition, a piling up of air also happens since the radius of the Earth decrease poleward. By the time it reaches $\sim 30^0$N/S latitude, the parcel becomes dense enough, and sinks. A part of the sinking air flow back towards the tropics, completing the so called HC. This circulation is responsible for the copious amount of rainfall received at the tropics and at the same time, for the dry climate of the subtropics. A schematic of the idealized HC[1], is shown in figure 1.6. The HC thus typically has a two cell structure with ascending limb located close to the equator. Near-surface wind flow in the equatorward branch of the HC is known as *trade wind*. Convergence of the trade winds in both hemispheres feeds the ascending branch of the circulation with the sufficient amount of moisture. The mid-tropospheric latent heat release in the ascending branch of the HC maintains the temperature gradient required to sustain the HC at higher levels in the atmosphere (Webster 1994). The poleward wind flow in the upper troposphere ends in high speed westerlies, known as the Sub-Tropical Jetstream (STJ).

The HC is responsible for the poleward transport of energy and momentum from the tropics to the extra-tropics, and for the equatorward transport of the moisture content from the subtropical to the tropical regime. Clear skies of the

[1] HC has been originally proposed under the assumption of zonally uniform topography for the Earth. The structure and intensity of the actual HC exhibits deviations from the schematic HC of figure 1.6.

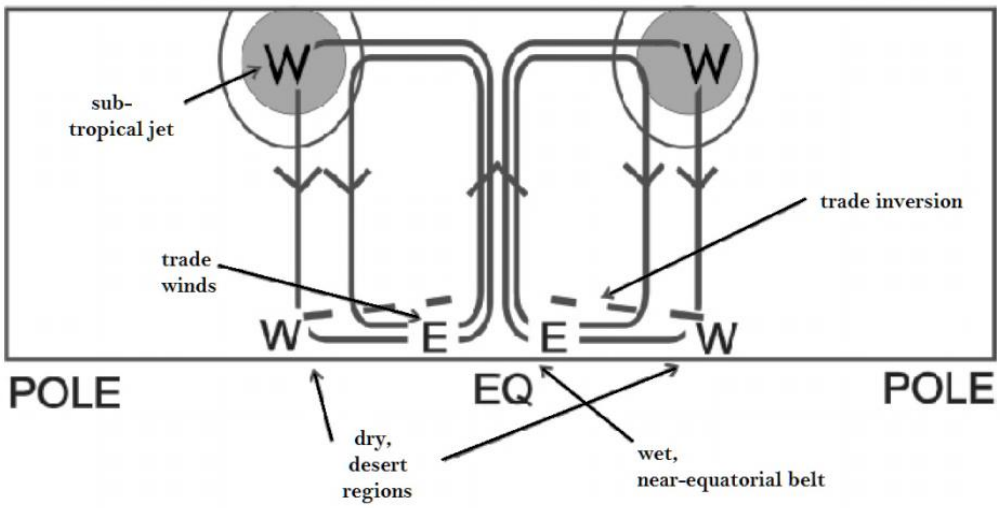

Figure 1.6: Schematic of an idealized Hadley Circulation *(Figure taken from Marshall and Plumb, (2008)).*

subtropics, occurring as a result of the descending limb of the HC, allows more solar radiation to reach the surface. This causes evaporation from the subtropical ocean surface, increasing the moisture content over these regions. Equatorward branch of the HC at the near surface level transports this moisture content into the tropics, where it converges into the ascent region and feeds the rising branch of the HC. The ascending limb of the HC thus carry energy obtained as a result of the sensible heating (from insolation) and latent heating (from transport) components from the near-surface to aloft, and from there towards the mid-latitudes. Besides poleward transport of energy, HC also take part in the angular momentum transport within the tropical-subtropical regime. The presence of easterly trade winds in the tropics (the surface part of the HC) helps the atmosphere to gain angular momentum over the tropics. Eddies in the upper level wind flow transport this angular momentum to the mid-latitude westerlies, where it continually loses angular momentum due to friction with the underlying surface. HC is thus closely associated with the energy, momentum and moisture budgets in the atmosphere (Rind and Rossow 1984).

The HC exhibits significant seasonal variability with respect to its total width, intensity, as well as location of the ascending limb. The ascending limb is primarily located in the summer hemisphere during solstices, causing the hemispheric cells of the HC to shift their location seasonally (Bates 1972; James

2003). Again, the winter hemispheric cell has been found to be wider and more intense than the summer hemispheric cell (Bates 1972; Lindzen and Hou 1988; James 2003). Such variations are attributed to the presence of continents and oceans on the Earth, as proposed by various modelling studies. For instance, the GCM simulations by Cook, (2003) showed that the presence of continents doubles the intensity of the winter hemispheric HC and halves the intensity of the summer hemispheric HC. Another study using climate model simulations by Clement, (2006) brought out that the inclusion of ocean heat transport resulted in significant weakening of both summer and winter hemispheric HC, and also caused the HC ascending limb to shift deeper into the summer hemisphere (by 10° to 15°). Thus the land-sea contrasts were found to have a significant influence on the seasonality of the HC. HC also exhibits significant interannual variability in its width and strength, the studies on which has motivated the current thesis.

1.2.3 Walker Circulation

Walker circulation (WC) is a series of zonal circulation cells which arise as a result of the longitudinal variation in atmospheric heating due to gradients in sea surface temperature as well as topographical asymmetries on the surface of the Earth. Figure 1.7 shows a schematic of the WC. Typically, the region between 5^0S and 5^0N is used to define and characterize the zonal WC. The rising motion of the WC cells happens over the warmer continents as well as in the regions of higher sea surface temperatures. Descending motion of each cell occurs in the adjacent oceans which are cooler.

The largest of the WC cells is the one over the Pacific, characterized by rising motion over the West Pacific and descending motion over the East Pacific. The ascent and descent motions are connected by easterly winds at the surface and westerlies aloft. Lower level easterly winds lead to a piling up of the warm waters in the West Pacific, increasing the temperature in the regions. This is compensated by an increased upwelling of cold, nutrient rich, subsurface water in the East Pacific, thus further reducing the temperature in this region. An increase in the easterly wind speed strengthens the WC, resulting in the so called *La-Nina*

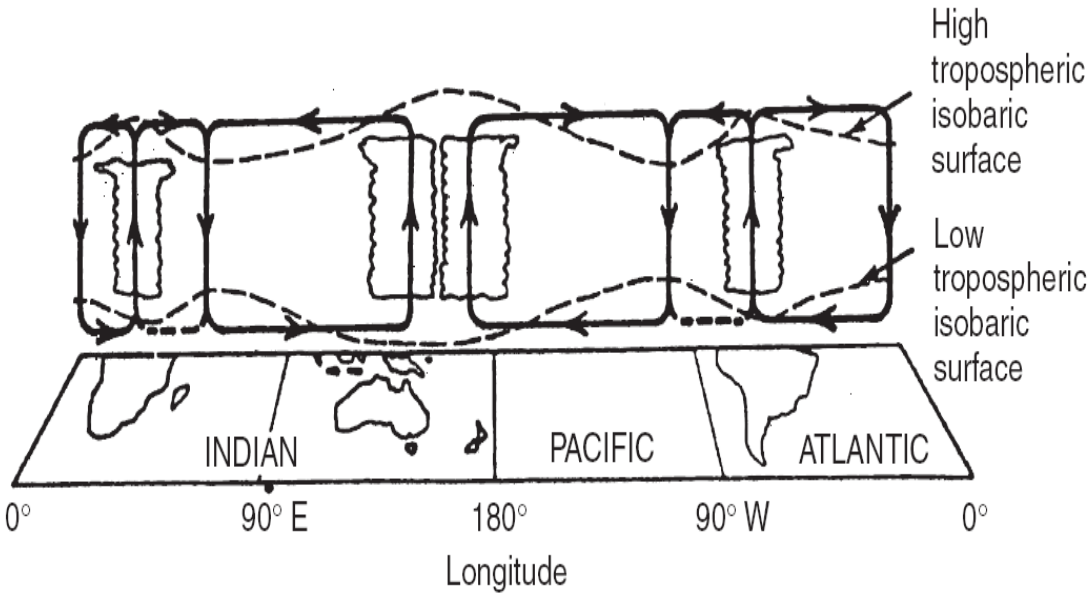

Figure 1.7: Schematic of a Walker Circulation *(Figure taken from Lau and Yang, (2002)).*

condition. Increased temperature in the West Pacific also increases the convection and cloud formation in these regions, thus inhibiting the amount of solar radiation reaching the surface. Consequent surface cooling weakens the convection activity and hence, the WC. This leads to slower surface easterlies which sometimes change direction too. A shift in the direction of the surface easterlies is associated with the *El-Nino condition,* during which the WC is reversed. Thus the tropical atmosphere and oceans act in a coupled manner to change the intensity of the WC every two to five years. This periodic oscillation in the strength of the WC is coincident with the atmospheric pressure variations in the equatorial Pacific Ocean, known as the *Southern Oscillation* (SO). SO is characterized by a low mean sea level pressure near the West Pacific (in Darwin, Australia) and high pressure near the East Pacific (in Tahiti), which very much coincides with the atmospheric condition for a WC to exist; conditions are similar to that of El-Nino when the pressure difference between the two stations decrease. Hence the El-Nino and La-Nina are considered to be the warm and cold phases of a single phenomenon- the *El-Nino Southern Oscillation (ENSO)*. The Indian Ocean cell and the Atlantic Ocean cell form the other two main circulation cells within the WC. All the WC cells, together, play an important role in determining the weather condition in the tropics. For instance, regions such as

Indonesia and North East Brazil suffer from droughts (floods) during El-Nino (La-Nina), whereas those such as Peru and Ecuador suffer from floods (droughts) when similar conditions prevail.

The rising branch of the zonally averaged HC exists within the 10^0S-10^0N latitudinal belt. Hence it is presumed that the HC and WC are well connected. Also, it has been identified that the width and strength of the HC is affected by the ENSO phenomena, which is essentially a modification in strength of the WC. Oort and Yienger, (1996) found that the HC strengthens during the warm phase of ENSO (El-Nino conditions), while the strength of the WC reduces. Further studies have shown that the HC is narrow and intense during warm phase of ENSO, and wider and weaker during the cold phase of ENSO (La-Nina conditions) (Lu et al. 2007; Stachnik and Schumacher 2011; Loeb et al. 2014; Lucas et al. 2014). Gastineau *et al.*, (2009) reported that the weakening of the WC during ENSO episodes are correlated with the strengthening of the NH cell of the HC and weakening of the SH cell of the HC. Changes in the strength of the WC during the time of El-Nino or La-Nina are compensated by changes in the strength of the ascending motions within the HC, leading to a stronger and narrower HC (Lu *et al.*, 2007 and references therein). However, climate model simulations have shown that the impact of global warming is felt more in the strength of the WC than in the HC (Gastineau *et al.*, 2009 and references therein).

1.2.4 Brewer Dobson Circulation

The zonally averaged large scale circulation existing within the stratosphere is called the *Brewer Dobson* (BD) circulation, and can be thought of as an extension of the ascending limb of the tropospheric HC into the stratosphere (Telegadas 1971). The circulation essentially consists of the entrance of tropospheric air into the stratosphere at the tropics, poleward movement of this air, and its descending motion in the mid-latitudes as well as poles. The air sinking over the subtropics re-enter the stratosphere and move back towards the tropics, whereas that which sink in the polar latitudes accumulate there at the polar stratosphere itself. This extremely slow circulation (~20m/day) was able to explain the abundance of

ozone in the polar stratosphere, which is quite away from the tropical stratosphere where it is produced in plenty.

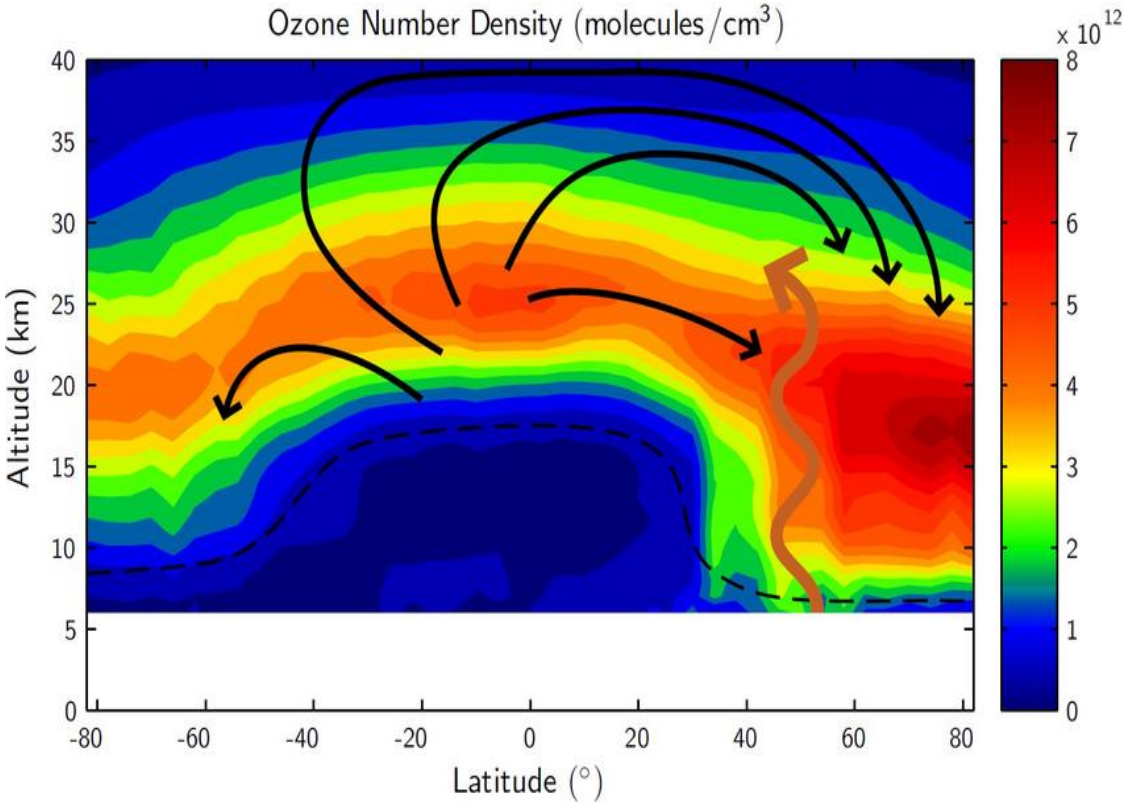

Figure 1.8: A schematic of the Brewer Dobson circulation (solid black lines) and the distribution of stratospheric ozone associated with it for March 2004 *(Figure taken from Remsberg, (2015)*).

Figure 1.8 shows the latitudinal distribution of stratospheric ozone obtained for March 2004 from the ozone number density measurement of Optical Spectrograph and Infra-Red Imaging System (OSIRIS) instrument on board the Odin Satellite. The solid black lines in the figure represent the BD circulation and the dashed black lines represent the tropopause. The figure shows the piling up of ozone molecules in the NH extra-tropical regions, in response to the stratospheric circulation. In addition to ozone, the BD circulation has also been found to be responsible for the observed latitudinal distribution of water vapour, nitrous oxide, methane and other trace species in the stratosphere. The BD circulation is primarily confined to the stratosphere and during winter time when the wave activities are dominant. The circulation is driven by the breaking of planetary waves in the extra-tropical stratosphere during winter (-illustrated by

using orange squiggly lines in figure 1.8). The deposition of energy by the wave breaking produces a westward force on the parcels there. Because of the "quasi-gyroscopic" (Holton et al. 1995) effect due to rotation of the Earth, these westward moving parcels start drifting poleward. Hence a void is created in the middle latitudes. Air is pulled towards this void from the equatorial stratosphere. In this process air rises over the tropics and adiabatically cools to a temperature lower than its radiative equilibrium value. Accumulation over the polar latitudes leads to sinking of parcels, which in turn causes adiabatic warming of parcels to a temperature which is above the radiative equilibrium value. This mechanism was called by the name '*extra-tropical wave driven pump*' (Holton et al. 1995). The circulation could effectively explain the observed deviation of temperature from their radiative equilibrium values. Besides, it is via the tropical uplifting branch of the BD circulation that water vapour as well as tropospheric trace constituents enters the stratosphere, where it is destructed. Hence the circulation also forms an essential factor in determining the lifetime of the tropospheric trace species.

Changes in the BD circulation also have been projected by models in a warming climate, wherein the tropospheric warming due to GHGs accelerates the wave generation activity that drives the circulation (Garcia and Randel, 2008 and references therein). Such changes in the strength of the BD circulation can affect the meridional distribution of the trace species in the stratosphere, which in turn influences the atmospheric radiative balance. These changes have been found to be coherent with the intensification of the tropospheric HC (Salby and Callaghan 2005).

1.3 Hadley Cell Dynamics: Literature Review

1.3.1 Metrics for HC characterization

As mentioned in the previous section, the HC is a meridional circulation that spans the tropical latitudes and the one that is responsible for the climatic patterns of the tropical-subtropical regime. Researchers are zealous to characterize this circulation since subtle changes to the HC width or strength can influence the span of the arid regions as well as the frequency and severity of the extreme precipitation events associated with it. Several atmospheric features have been used to characterize the HC, counting on the distinct nature of the each

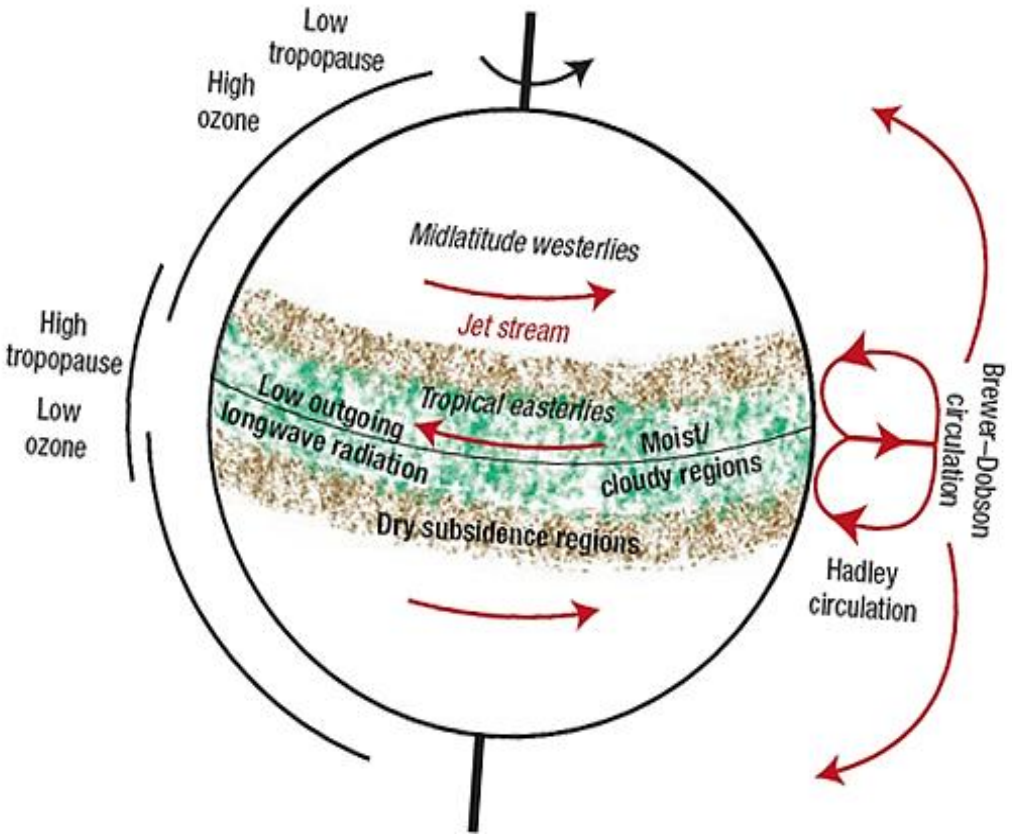

Figure 1.9: Metrics for HC characterization *(Figure taken from Seidel et al., (2008)).*

of these features in the tropics and the extra-tropics. For example, the amount of precipitation minus evaporation (P-E) is positive in the moist tropics whereas negative in the dry subtropics, the amount of Outgoing Long-wave Radiation (OLR) is low in the cloud covered tropics whereas high in the dry subtropics, tropopause is at higher heights in the tropical convective regions and at lower heights in the mid-latitudes, surface winds are easterly in the tropics whereas westerly in the mid-latitudes, and so on. Such atmospheric features used to describe the HC are known as the *HC indicators* or the *HC metrics.* Of these, the observable parameters which exhibit sharp gradients at the edges of the HC, such as the atmospheric ozone concentration, amount of Outgoing Long-wave Radiation (OLR), height of the thermally defined tropopause (LRT), etc. are termed as *physical indicators* of the HC. Characterization of the HC in terms of dynamical features such as the location of the Subtropical Jetstream (STJ), meridional Mass Stream Function (MSF), direction of prevailing surface winds, etc. is called the characterization by means of *dynamical indicators* of the HC.

Figure 1.9 illustrates some of the common HC indicators used to characterize the HC.

General features of the HC deduced by using these metrics, either independently or in a combination, are used to characterize the HC in terms of its structure, intensity, as well as the circulation energetics. It has been derived from these metrics that the hypothesized two-cell structure of the HC (Held and Hou 1980; James 2003), which consists of individual cells of opposite directionality on either side of the equator, is valid only during the equinoctial seasons (Barry and Chorley 2003; Nguyen et al. 2013). During the solstices, the summer cell is so weak that the HC seem to consist of only a single cell, which is in the winter hemisphere (Bates 1972; Oort and Yienger 1996; Waliser et al. 1999). The increased intensity of the winter hemispheric cell is attributed to the greater pole-to-equator temperature gradient in the winter hemisphere (Goody and Walker 1972; James 2003). The rising branch of the HC always exists in the summer hemisphere, except during equinoxes. Winter cells are hence cross-equatorial cells and exhibits larger width. Poleward boundary of each cell occurs within the subtropical regions. The location of the descending branch of the HC is broad, rather than being confined only to a single latitude (Lucas et al. 2014). The circulation also shows considerable seasonal shift in its location, thus making the determination of the poleward boundary of the HC never a simple task.

1.3.2 Expansion of HC and the tropical belt

The HC characterization studies using the above mentioned metrics revealed a major fact: the location of the descending limb of the HC is shifting poleward! One of the earliest efforts to identify the poleward movement of the HC was the studies of Fu *et al.*, (2006). Their studies, using satellite derived atmospheric temperature data, identified an enhancement in the tropospheric warming and stratospheric cooling over the 15^0-45^0 latitudinal belt. Changes in the tropospheric and/or stratospheric temperature are bound to increase the height of the radiative-convective equilibrium level, which is nothing but the tropopause. Theories have shown that the height of the tropopause scales with the width of the HC, according to the equation:

$$\phi_H = \left(\frac{gH_t}{\Omega^2 a^2}\,\frac{\Delta_H}{\theta_0}\right)^{\frac{1}{2}} \quad \text{---------- (1)}$$

where H_t is the height of the tropical tropopause, Δ_H is the equator-to-pole surface potential temperature difference in radiative equilibrium, θ_0 is the global mean temperature, a is the radius of the Earth, Ω its angular velocity and g is the acceleration due to gravity (Lu *et al.*, 2007, and references therein). The study thus suggested an increase in the width of the HC associated with tropospheric warming and stratospheric cooling in a warming climate. A deeper analysis of this observation by the authors revealed that the tropical circulation has widened by $\sim 0.7^0$ latitude per decade. Satellite-derived total ozone measurements of Hudson *et al.*, (2006) also revealed a poleward shift of the NH HC by $\sim 1.1^0 \pm 0.1^0$ latitude per decade. These studies were followed by the tropopause-height based studies of Seidel and Randel, (2007) who brought out that the tropics have widened by $\sim 1.8^0$-3^0 latitude per decade by making use of the observed seasonal changes in tropopause height over the subtropical locations. A widening of the HC, $\sim 1.8^0$ latitude per decade, was also revealed from the OLR based studies of Hu and Fu, (2007). Expansion of the HC was brought out in the studies using the dynamical indicators too, especially from the MSF metric (Hu and Fu 2007; Johanson and Fu 2009; Stachnik and Schumacher 2011; Nguyen et al. 2013). The MSF metric has been the most widely employed dynamical indicator in the HC expansion studies because it closely follows the movement of mass within the tropical circulation. Together, these studies brought out an average expansion rate of $\sim 1^0$ latitude per decade for the HC. Several other studies also have addressed the phenomena of increasing width of the HC, each unique in its own way. This is possible since the HC is defined in different ways by the HC metrics, the definitions being either subjective or objective in nature. A coarse summary of such studies on HC expansion using different metrics and their variant definitions is given in Lucas et al. (2014). Mean state variability in the expansion trend of the HC among different reanalysis datasets was found to be minimal (Stachnik and Schumacher 2011), thus proving the robustness of this phenomena.

The expansion of the HC was identified by not just observational studies, such as the ones mentioned above, but by modelling simulations too. These studies were carried out under a warming climate scenario, primarily by means of increasing greenhouse gases (GHGs). However, the trends derived from these studies were found to be lower than that estimated by the observational studies (Johanson and Fu, 2009;Seidel *et al.*, 2008). Allen *et al.*, (2014) suggested in their study that this discrepancy could be due to the short span of observational records, model deficiencies, or even due to the natural variabilities in some metrics. The reasons behind this disparity are still being explored, for which a complete understanding of the drivers and processes behind the HC expansion phenomena is necessary.

Changes in the strength of the circulation were also reported by the researchers, in association with the poleward expansion of the HC. For instance, Quan *et al.*, (2004) have used reanalysis and model simulations to conclude that the intensity of the winter cell has been on the rise since 1950; and that this intensification is partly in response to the warming of the tropical oceans and intensification of interannual variability of El-Nino events. The authors have also used GPCP dataset, a combination of surface and satellite observations of precipitation, in the above study to associate the winter HC intensification to the intensification of the hydrologic cycle, which is characterized by increase in equatorial oceanic rainfall and drying up of the subtropical land regions. Liu *et al.*, (2012) probed into the multi-decadal variability in the strength and width of the HC using the 20th Century Reanalysis (20CR2) dataset. They reported that the NH and the SH HC strength have increased by ~26.9% and 12%, respectively, since 1871. This was observed to be in accordance with the global mean surface temperature increase since 1871. Positive trend in NH and SH HC strength was observed in all seasons, except for the SH HC during summer. The vertical structure of trend in NH and SH strength was also explored in this study, which revealed that the intensification is present at all levels, from the surface to the upper troposphere. An intercomparison of HC strength and width represented in eight reanalysis datasets by Stachnik and Schumacher, (2011) showed that the HC strength has significant variability among the chosen reanalysis datasets. Mean trend in the strength of the HC was identified to be ~0.4 x 10^{10}kg/s in the NH and by ~0.07 x 10^{10}kg/s in the SH. An ensemble mean trend of ~1.1^0 latitude per decade for the

HC width was also identified in this study, with minimal variability among the eight reanalysis datasets.

All of the above studies made use of the MSF metric to determine the strength of the HC. A unique study regarding the changes in the HC strength was by Chen *et al.*, (2002) who used observational quantities such as total cloud amount from ISCCP, upper tropospheric relative humidity from HIRS, surface air temperature from GISS, and TOA shortwave and long wave flux from ERBE and CERES, along with 500hPa pressure vertical velocity from NCEP data. The long term changes in these quantities were analysed for the equatorial, tropical and subtropical regimes separately. The analysis showed that the downwelling over the subtropics have increased by 7.6×10^{-4} Pas^{-1}, leading to a decrease in upper tropospheric relative humidity by ~1.5%, decrease in cloud amount by ~1.7%, and hence increase in TOA long wave flux by $2.8 Wm^{-2}$. The upwelling regions within the equatorial zone showed exactly opposite character, from which it was concluded that the rising limb of the HC has intensified. Considering the long term behaviour of the atmospheric properties in both the regions, the study concluded that the HC has strengthened in the recent decade. However, these authors could not derive the trend in HC strength since the influence of Walker Circulation on the ascending limb of the HC could not be separated out. Trend in the HC strength values can also be derived using observational data on wind speed and direction; but is limited by the lack of sufficient data (Chen *et al.*, 2002).

While the observational studies state evidently that the HC has intensified, the modelling simulations predict a weakening of the circulation. For instance, Lu *et al.*, (2007) predicted that the HC weakens in a warming climate, along with a poleward expansion of the circulation. This study was carried out, again, under the scenario of increasing GHGs from the IPCC AR4 project. Increased static stability of the subtropics in a warming climate was attributed to be the reason behind this circulation weakening, because the static stability inhibits the vertical development of convective motions. Climate model simulations of Vecchi and Soden, (2006) for the IPCC AR4 project, and that of Kjellsson, (2015) for the IPCC AR5 project also suggested a weakening of the tropical circulation in a warming climate. However, their study showed that the simulated weakening of the

tropical circulation scenario is noticeable within the zonally asymmetric component of the tropical circulation (i.e., WC), rather than in the HC. Gastineau *et al.*, (2009) also noticed that the weakening of the WC is stronger than that of HC in a global warming scenario. A standalone study was by Mitas and Clement, (2005), which compared the strength of the boreal winter cell of the HC represented in the reanalysis and in the atmospheric GCMs. In contrast to other modelling simulations on the strength of the HC, the ensemble mean of GCM simulations in their study yielded a significant strengthening of the NH winter cell. However, the magnitude of the trend derived by the GCMs was lower than that obtained from the reanalysis datasets. Mitas and Clement, (2006) investigated the source of this discrepancy by exploring the thermodynamic structure of the tropical troposphere in a warming climate. Tropical mid-troposphere is warmer in models, and thus has larger static stability. Since the static stability and HC strength is inversely related, the HC strength represented by models is lesser. Reanalysis data, on the other hand, are constrained by radiosonde observations which show a cooling in the upper tropical troposphere. The intensification of HC is the response of the circulation to this cooling aloft, so that the desired amount of poleward heat transport is attained. Thus the authors concluded that the different ways in which the tropical thermodynamics is represented in models and in reanalysis leads to the observed discrepancy in the HC strength between the models and reanalysis.

It is clear from the above discussion that there is considerable ambiguity in the long term trends in the width and strength of the HC. The type of metric used, the definition of the chosen metric, type of data in use, as well as time span of the dataset- all these factors result in an inaccurate determination of the trends in HC features. Lack of sufficient observational data record, uncertainty in the available observations, biases and errors in models, and the method of data assimilation in reanalysis limits the characterization of the long term behaviour of the HC (Mitas and Clement 2006). In addition, the diverse number of HC metrics, their different definitions, as well as the data span (pre/post-satellite era) contribute to the ambiguous nature of the trends (Lucas et al. 2014).

An increase in the upper level boundary of the HC- the tropopause, has also been reported by the researchers in addition to the poleward expansion of its

meridional boundary. For instance, Seidel *et al.*, (2001) detected an increasing trend in the tropopause height ~20m per decade over the deep tropics by analysing the radiosonde data from selected stations during the period 1978-1997. Globally, the height of tropopause was estimated to show positive trends ~64±21m per decade by Seidel and Randel, (2006) using radiosonde data from 1980-2004. These studies are suggestive of an increase in the width of the HC as given by Equation (1); however it is to be noted that there are limitations in determining the trend using radiosonde data. A positive trend in the global mean tropopause height ~47m per decade was also shown in study by Wilcox *et al.*, (2012) using ECMWF-Interim reanalysis for the period 1989-2007. The trends were found to vary with respect to latitude in this study, with the largest positive trends being shown by the subtropical latitudes. This implies that the regions showing high tropopause heights (i.e., the tropics) are expanding into the subtropics, which is in conjunction with the expansion of the HC.

Thus the HC expansion phenomena and the tropopause height increase, together, has led to an increase in the volume of the tropical atmosphere by 5% (Seidel et al. 2008). And the *tropical belt*, defined as the region confined between the NH and SH boundary of the HC, was concluded to have increased its area over the past few decades.

Studies having stated unanimously that there is a poleward expansion of the HC, the focus have now shifted to the regional variability in the rate of expansion. This is important because the zonal mean HC is capable of being influenced by the presence of regional variations in topography. Karnauskas and Ummenhofer, (2014) investigated the dynamics of the subtropical drying observed in the 15°-40°S latitudinal band during austral winter, using Coupled Model Intercomparison Project- Phase 5 (CMIP5) simulations under an RCP8.5 forcing scenario. They found that the drying is not zonally uniform, but localized near the eastern coastline of the subtropical oceans. Further analysis by the authors using NCEP reanalysis data revealed that the equatorward surface flow is mainly concentrated along the eastern coastline of the subtropical oceans (i.e., the western coastline of the subtropical land masses). This was attributed to the zonal pressure gradients arising from the heating up of the continents and the air-sea interaction associated with it. Contribution of different regions to the

zonal mean expansion has been brought out by Lucas and Nguyen, (2015), and Mathew and Kumar, (2018a), whereas the regional variation in expansion rates have been brought out by Chen *et al.*, (2014) and Grise *et al.*, (2018). It is expected that more of such studies can provide conclusive evidence on the factors behind the tropical expansion phenomena.

1.3.3 Consequences of the HC expansion

The expansion of the HC has serious consequences as a result of the associated changes in the precipitation patterns, poleward movement of jet streams and storm tracks, changes in distribution of climatically important trace gases (such as water vapour) in the stratosphere, changes in biodiversity, as well as changes in the ocean circulation (Seidel et al. 2008). The first and foremost consequence of the expansion of the HC is the changes in the climatic zones within the tropical belt, especially in the location of the arid and semi-arid zones near the edges of the tropical belt. Water resources in these areas of marginal rainfall are further constrained due to the shift in the precipitation patterns associated with the HC widening. Studies have already reported changes in the dry zones associated with the expansion of the HC. For instance, Cai *et al.*, (2012) investigated the rainfall reduction in the SH subtropics using rain gauge precipitation datasets for the period 1951-2010. These authors observed that out of the three major semi-arid regions in the SH, the South East Australian region shows a rainfall reduction in line with the poleward movement of the HC edge during April-May season. Changes in precipitation pattern within the tropics has also been reported in association with the intensification of the HC (Zhou et al. 2011). Chen *et al.*, (2002) has already identified an increase in the ascending motions using satellite observations. Zhou *et al.*, (2011) identified an increase in precipitation in the regions under the ascending limb of the HC and a decrease in the regions under the descending limb of the HC. This was carried out using ISCCP and GPCP datasets. The observations and modelling simulations point towards a delayed water cycle (Wang and Lau, 2006 and references therein), which follows the HC intensification. This increases the range between the wet and dry season precipitation and also increases the severity of droughts and floods (Chou *et al.*, 2013 and references therein). Climate models from IPCC 2007 has predicted droughts for regions which had earlier enjoyed a temperate Mediterranean type

climate, such as for the Southern Australia (Issac and Turton 2014). Studies of Shin *et al.*, (2012) also drew evidence on the expansion of the regions with steppe and desert climate as a consequence of the intensification of the HC.

The effects of such changes in precipitation have far reaching consequences, and are not mild enough to be ignored. Changes in water availability affect as much as 90% of the population of the tropics which thrive upon agriculture. Extreme weather events caused by the HC intensification can pose a threat to the food security. Other arenas which are affected by the changes in water availability include urban settlements, farming, hydropower, forestry, and biodiversity. An example of the influence of subtropical dry zone expansion on biodiversity is the poleward expansion of the warm adapted North-East American butterfly community, which has tracked the poleward expansion of the tropical warm climate (Breed et al. 2013). The risk here, however, is that species which find it difficult to track the expansion, and are put under the verge of extinction. Current lag of the species in tracking the tropical expansion has been observed to be as large as 100km (Issac and Turton 2014). HC changes also influence the trace species transport into the stratosphere, such as water vapour, that affects the mean temperature of this layer of the atmosphere. This becomes a positive feedback to the HC expansion phenomena.

The changes in the climate of the Earth due to the observed expansion and intensification of the HC are not just confined to the tropical belt, but to the extra-tropics as well. This is evident from the poleward shift in the location of the mid-latitude storm tracks and the associated cloudiness (Bender et al. 2012; Tselioudis et al. 2016), causing calamities in the regions that lie under these storm tracks. The HC expansion thus can affect the whole ecosystem of the Earth, thus emphasizing the need for better management of resources for agricultural, industrial and human development.

1.3.4 Drivers of the HC expansion

Rind and Rossow, (1984) listed out a number of processes that can bring about changes in the HC. This includes changes in insolation, Sea Surface Temperature (SST) pattern, as well as changes in convection and latent heat release. According

to these authors, changes in topography over geological time periods as well as changes in surface friction can also bring about changes in the HC. Taking into consideration the role of mid-latitude eddies in transporting the angular momentum poleward, these authors also proposed that changes in baroclinicity and the eddy characteristics can also influence changes in the HC. The changes in insolation have been found to affect only 5% of the HC changes (Leroux 2014). Some of the studies, such as that by Hu et al., (2013), state that the HC expansion is driven by an increase in the global mean temperature by means of GHG. Hu *et al.*, (2013), by means of CMIP5 historical simulations, identified that the rate of poleward expansion under GHG forcing is $0.15^0 \pm 0.06^0$ latitude per decade. It was further reported that GHG is expected to continue its role in the poleward HC expansion phenomena during the 21st century as well. However, the exact mechanism by which GHG leads to an expansion of the HC is still unclear.

Staten et al. (2012) investigated the role of SST warming, GHG concentration, as well as that of stratospheric ozone depletion in the expansion of the HC using GFDL AM2.1 model, and concluded that SST warming is the main driver of tropical expansion. Modelling simulations of Kang *et al.*, (2013) also found that SST changes influence the trends in HC width. Observational studies have also gathered evidence on the HC changes being driven by variations in the SST changes, such as that from the studies on the influence of warm and cold phases of the ENSO on HC strength and width (refer to section 1.2.3). Researchers have also explored the relation between tropical expansion and the Pacific Decadal Oscillation (PDO), which is a major mode of long term SST variability in the North Pacific Ocean. A major effort in this regard was by Allen *et al.*, (2014). Using historical simulations of CMPI5, these authors brought out that PDO plays a significant role in the expansion of the NH cell of the HC. The rate of expansion simulated in this manner was found to be closer to that of observations, thus reducing the observed discrepancy between the observed and modelled trends in the HC width for the NH. On the other hand, stratospheric ozone depletion has been found to be the driver of the HC expansion in the SH. This has been brought out in the studies of Polvani *et al.*, (2011) and Son *et al.*, (2009, 2010). However, a recent study by Waugh *et al.*, (2015) state that the stratospheric ozone depletion

was the major cause of the HC expansion in the SH only between 1979 and the 1990s; and after that SST was found to play a major role in the same.

The role of tropospheric warming agents, such as the trace species and aerosols, is also an important factor in modulating the strength and width of the HC. CAM-3 simulations that incorporate aerosol physics has been used by Allen *et al.*,(2012) to probe into the role of aerosols in driving the poleward expansion of the HC during the period 1979-2009. This study brought out that the heterogeneity of warming agents such as Black Carbon and tropospheric ozone induces an expansion of $\sim 0.07^0$ to 0.12^0 per decade for the NH cell of the HC. These authors also projected that anthropogenic aerosols are an important factor in determining the rate of expansion of the HC. This argument was however ruled out in the study by Tao *et al.*, (2015). Instead they projected, by means of CMIP5 simulations, that GHG increase and stratospheric ozone depletion are the main drivers of the poleward expansion of the HC during the 1970-2005 period.

Adam *et al.*, (2014) stated, by way of AMIP simulations driven by prehistoric SST and CMIP5 simulations driven by GHG, that an increase in global mean temperature can widen the HC, and so does a weakening of the meridional temperature gradients. Theoretically, as given by Equation (1), pole-to-equator temperature gradient is also a major factor in determining the HC width. The study by Adam *et al.*, (2014) infer that HC widening during 1979-1997 was driven by global warming; while that during 1997-2012 was identified to be due to the reduced meridional temperature gradients as a result of elevated mid-latitude SSTs. This inference was possible since global mean temperatures had remained somewhat stable during the period 1997-2012.

Although the exact mode of action of the drivers of expansion of the HC is unknown, it is definite that these drivers modulate the convective activity in the atmosphere. Typically, in an atmosphere that warms as a result of the increasing CO_2 concentrations, the circulation is expected to weaken because the moisture-holding capacity of the air increases (Schneider et al. 2010), delaying the process of saturation and condensation. Also, increased moisture content alters the static stability of the atmosphere by modulating the amount of mid-tropospheric latent heating due to convective activities. Studies by Feldel and Bordoni, (2016), which use CMIP5 simulations forced by quadrupling of CO_2 concentrations, showed that

the HC weaken up to about 2.6% per Kelvin at quasi-equilibrium. CMIP5 projections by Seo *et al.*, (2014) also project a weakening of the winter hemispheric circulation under the RCP8.5 scenario. According to these authors, the strength of the HC in a warming climate is influenced by the changes in meridional potential temperature gradients. Studies by Frierson *et al.*, (2007) also shows that an increase in surface temperature, moisture content and hence static stability in the subtropics pushes the latitude of baroclinic instability onset poleward, leading to widening of the HC. This is in conjunction with the study of Rind and Rossow, (1984).

In the present scenario, although many factors have been suggested as the drivers of HC expansion, the real cause of the expansion of the HC is still unclear. Some even speculate that the HC widening observed in the recent decades could be a part of natural long period oscillations in the atmosphere that have not yet completed a full cycle (Liu et al. 2012). It is required not only to gain knowledge on the agents that cause HC expansion, but also on the pathways of their action in order to gain a complete understanding on the HC and its widening.

1.3.5 Projection of the HC expansion in CMIP5

A prediction into the future is important in order to formulate the right kind of adaptation strategy. Climate models take the dual responsibility of identifying the future rate of expansion of the HC as well as the reasons behind such an expansion in a plausible manner. Although most climate models predict the tropical expansion phenomena, the rate of expansion given by these models are lower than that given by the observations and reanalysis datasets (Seidel *et al.*, 2008, and references therein). The reason for this discrepancy is still a topic of investigation. With this caveat, the modelling simulations have been extensively used to make projections for the 21st century changes to the HC. These projections are being made for different external forcing conditions, also called forcing scenario. The Coupled Model Intercomparison Project (CMIP) is a global climate modelling initiative that brings together several historical simulations and projections under a variety of forcing scenarios, all under one roof, with the provision for inter-comparison among the models (Hurrell et al. 2011; Taylor et al. 2012). The future projections in CMIP5 are made with four major

Representative Concentration Pathways (RCPs) that lead to radiative forcing levels of 2.6, 4.5, 6 and 8.5 W/m^2 by the end of the period 1850-2100. Each RCP has associated emission and concentration for each GHG (Hurrell et al. 2011). Studies on 21st century projections from CMIP5 model under RCP8.5 scenario by Hu *et al.*, (2013) has shown that GHGs will cause a continuous poleward expansion of the HC. Tao *et al.*, (2015) also project a tropical expansion for the 21st century under the same forcing scenario, but only for the tropical NH cell. The projected expansion of the NH cell $\sim 0.26^0$ latitude per decade was found to be significant only during boreal autumn season. These authors have also predicted a weakening of the HC in both hemispheres under the RCP8.5 scenario for the period 2006-2100. On the other hand, Seo *et al.*, (2014) explored future changes in the winter HC intensity for the period 2081-2100 and projected a weakening of the same under the RCP8.5 scenario of the CMIP5 simulations.

As mentioned before, the rate of tropical expansion given by CMIP projections are lower than that given by observations and reanalysis (Seidel et al. 2008). A realistic prediction of the HC expansion rate by the climate models under the action of an external forcing mechanism, which is consistent with the observations, is expected to also point towards the ultimate driver of the HC expansion. Allen *et al.*, (2014) attributed the observed discrepancy between CMIP5 model projections and observations to the inadequate of representation of radiative forcing due to aerosols in these models. This inference was based on the improved co-variability of model derived expansion trends to observed trends in historical simulations of CMIP5 forced by SST. They also considered the previous work by Allen *et al.*, (2012), which had used a model that has an improved representation of aerosols, and derived that the inter-hemispheric asymmetry of aerosols can influence the rate of expansion of the HC. A very active research in the realms of CMIP5 projections of HC expansion is underway to explore the current trends and future projections of HC edges and strength.

1.4 Motivation for the present study

As is evident from the previous sections, the HC plays a major role in the atmospheric energy, momentum and moisture budgets. In the present climate, the factors which influence the atmospheric energy, momentum and moisture

budgets in the atmosphere are undergoing perturbations. Hence it is expected that changes will occur in the HC as well. On the contrary, changes to the width and intensity of the HC in a changing climate affects the energy, momentum and moisture budgets of the atmosphere, which in turn drives further changes in the HC. The interplay between the individual budgets also makes it a complex task to determine the variability of the HC in an accurate manner. Still, the researchers have brought out by means of observational analysis and modelling simulations that the width and strength of the zonal mean HC is on the rise. However there are discrepancies between the observational and modelling studies in projecting the changes in the strength and width of the HC. Simulated rate of expansion of the HC is lower than that derived from observations; and the model simulations on the strength of the HC show opposite result to that from observational studies. An intensification of the HC has been brought out by means of observational datasets, whereas modelling simulations show a weakening of the circulation. Such differences between modelled and observed changes in the strength and width of the HC are still topics of research.

Detection of a true persistent tropical expansion, at least in a statistical sense, is hindered by the scarcity of observational records as well as by considerable uncertainty in the estimates of the magnitude of expansion (Mathew et al. 2016). The lack of globally complete observational records has been partly addressed by reanalyses, which combine model fields with sparsely distributed observations to form a spatially complete gridded meteorological dataset. Thus it has become the need of the hour that reanalysis datasets are validated using observations for global circulation studies. It is also important to evaluate the newer reanalysis datasets for investigating the HC dynamics.

It is also necessary to determine the rate of expansion of the HC at different longitudes, since the zonal variations in topography can influence the HC. The rate of tropical expansion has been identified not to be uniform at all longitudes. However, a longitudinal delineation of the HC features, and trend if any, has been carried out only by a limited number of studies. A clear understanding on the drivers of the HC and their mode of action is essential to determine the long term changes to the width and strength of the HC, with greater accuracy. Studies have brought out a list of factors that can affect the HC, including global warming due

to GHGs, stratospheric ozone depletion and SST changes. However their pathway(s) of action in bringing about changes to the HC are unclear. Due to the very same reason, the true factor behind the expansion phenomena is yet to be precisely identified.

Whichever be the factor behind the HC expansion, it is capable of modulating the thermal structure of the troposphere and hence the convection activity in the atmosphere. This is a major intermediate step in the phenomena of HC expansion, since it decides the amount of latent heat release into the mid-troposphere that sustains the HC. This aspect reinforces the fact that quantification of the relationship between latent heat distribution and the HC dynamics is essential to understand the pathways through which various factors influence the HC expansion. Many modelling studies have looked into the role of atmospheric convection processes in altering the strength and width of the HC. However, there are only very less number of observational evidence on the same.

The first reflection of the changes in HC is in the parameters of the hydrological cycle, which includes atmospheric humidity, clouds and surface precipitation. Proper mitigation strategies can be formulated if only the pattern of changes in the hydrological cycle associated with the expansion and intensification of the HC in the present warming climate is correctly identified. Strengthening of the hydrological cycle in a warming scenario has been brought out by climate model simulations as well as by observations. A “rich-getting-richer” mechanism has been proposed by these studies, according to which the regions that are already wet experience a further wetting trend and the regions that are already dry experience a further drying up trend. These regions happen to be none other than the regions falling under the ascending and descending regions of the HC. Thus the intensification of the HC is expected to intensify the wet and dry conditions in the regions falling within the ascending and descending branches of the HC, respectively. Most of the research efforts in establishing the role of HC dynamics in modulating the components of hydrological cycle relied on climate model simulations. However, a clear signature of the HC changes in moisture, cloud and precipitation is far from understating in the present day climate.

All these factors have motivated to take up the present study on the “*poleward expansion of the Hadley Circulation and associated dynamics*”. The present thesis

thus explores the poleward expansion of the HC and associated dynamics using observational and reanalysis datasets, with prime focus upon some of the major gap areas in this realm of climate research.

1.5 Objectives

In the wake of the above discussion, the central objectives of the current thesis have been charted out as follows:

1. To characterize the HC using meridional mass stream function metric and to quantify its poleward expansion rate in reanalysis datasets

2. To estimate the zonally resolved HC edges and to delineate the regional features of the HC

3. To investigate the role of latent heat release in modulating the strength and width of the HC

4. To divulge the changes in parameters associated with hydrological cycle within the ascending and descending branches of the HC

1.6 Organization of the Thesis

The thesis is organized in 7 chapters. **Chapter 1** provides a brief introduction to the Earth's atmosphere including its composition, thermal structure and radiation budget. The various large scale circulations such as Hadley Circulation, Walker Circulation and Brewer-Dobson Circulation embedded in it are also introduced in this chapter. Special emphasis is given to the ways and means of characterizing the HC and its dynamics. A detailed discussion on the phenomena of poleward expansion and intensification of the HC is provided in this chapter. It also includes a discussion on the factors behind the HC expansion as well as future projection of the expansion rates in a warming climate. This chapter also provides the motivation for the present study and states the central objectives of the thesis.

Chapter 2 provides description on the datasets used in the analysis of the HC dynamics in the current thesis. Datasets of three major types are used for the studies in this thesis- *reanalysis data* [European Centre for Medium Range

Weather Forecast Reanalysis-Interim (ERA-I), National Centre for Environmental Prediction (NCEP), Japanese Reanalysis-55 (JRA55), and Modern Era Retrospective Analysis for Research Applications (MERRA)], *space-based observations* [Constellation Observing System for Meteorology, Ionosphere and Climate (COSMIC)- Global Positioning System Radio Occultation (GPS-RO), Tropical Rainfall Measuring Mission (TRMM) Precipitation Radar (PR)], and *ground-based observations* [Integrated Global Radiosonde Archive (IGRA)]. The study also uses Global Precipitation Climatology Project (GPCP) dataset, which is a merged product of both ground and space based observations. The reanalysis datasets are employed in determining the centre, edges, total width, as well as strength of the HC. The meridional mass stream function (MSF) metric derived from meridional wind is used for the same. Comprehensive radiosonde data from IGRA is used to validate the MSF metric derived from reanalysis datasets. Temperature measurements of the COSMIC GPS-RO are used to derive the tropopause altitude. The latitudinal and inter-annual variability observed in these measurements are used to derive the regional features of the tropical belt. Latent heating data product of the TRMM PR is employed to quantitatively describe the influence of latent heat release on the HC centre, width and strength obtained from reanalysis data. Precipitation data from GPCP is used to bring out the long-term changes in precipitation within the ascending and descending branches of the HC. In addition to the above datasets, total cloud fraction and relative humidity data products of ERA-I are also used in the current thesis.

Chapter 3 provides the results on characterization of HC using MSF metrics obtained from relatively new JRA55 reanalysis dataset and three widely used reanalysis datasets, *viz.*, NCEP, MERRA and ECMWF. The four reanalysis datasets have been compared with radiosonde observations from IGRA, for the first time, using the subsampling technique. The verification of the MSF metric for general circulation studies by means of radiosonde observations from IGRA, the use of relatively new JRA55 dataset, as well as the estimation of annual cycle of HC expansion rates are the highlights of this chapter.

Chapter 4 brings out the zonally resolved width of the tropical belt from three objectively defined tropopause-based metrics for the first time, using seven years

of COSMIC GPS-RO observations. It is envisaged that the present results will have potential applications in investigating the zonally resolved trends in the tropical expansion.

Chapter 5 quantifies the influence of latent heat (LH) release on the spatial extent and intensity of the HC using the vertical profiles of LH derived from 16 years of space-based observations of TRMM PR and MSF derived from the ERA-I reanalysis data. This study is unique since it provides for the first time an observational evidence for the modelled influence of LH release on the strength and width of the HC.

Chapter 6 characterizes the spatial distribution of trends in moisture, cloud fraction and precipitation within the HC ascending and descending branches by means of ERA-I reanalysis and GPCP observations so as to bring out the changes in hydrological cycle associated with the observed changes in the HC. The boundaries of the HC are identified in the present study using the MSF metric. Unlike earlier studies which have reported the trends in precipitation within the ascending/descending regions of HC as a whole (assuming that the trends are uniform in these regions), the present study localize the trends within the ascending and descending regions of HC. The current chapter is envisaged to contribute to the present understanding on the relation between the HC changes and the intensification of the hydrological cycle in a warmer climate.

Chapter 7 provides a summary of the current thesis as well as scope for future investigations into the poleward expansion of the HC.

CHAPTER 2
DATA AND METHODS

2.1 Introduction

To investigate the dynamics of the Hadley Circulation (HC), which is a global scale phenomenon predominant in the meridional direction, geophysical parameters such as meridional winds on global scale are essential. The thesis focuses on characterizing the HC and associated dynamics using a combination of observations and reanalysis datasets. In order to achieve the objectives projected in Chapter 1, the present thesis utilizes data from:

a. Reanalysis
b. Ground-based measurement systems
c. Space-based measurement systems

Meridional wind (v-wind) from reanalysis dataset is mainly used to determine the long term trends in the poleward expansion of the HC. Ground-based measurements of v-wind from the *Integrated Global Radiosonde Archive* (IGRA) are used to validate the reanalysis datasets for their use in trend analysis. Space-based measurements of temperature from the *Constellation Observing System for Meteorology, Ionosphere and Climate* (COSMIC) are employed to determine the longitudinal features of the HC, and that of latent heating from the *Tropical Rainfall Measuring Mission* (TRMM) satellite is utilized to explore the association between tropical convection and the HC strength/width. In addition to these datasets, a combination of several ground- and space-based measurements of precipitation archived as the *Global Precipitation Climatology Project* (GPCP) is also used in the thesis. This data is used for the analysis of precipitation trends within the HC ascending/descending regions. The trends in relative humidity as well as cloud fraction are also explored in conjunction with precipitation changes within the HC regime, and reanalysis data is once again used for the same. The current chapter gives a brief discussion on each of the above datasets. The chapter also provides a description on the primary tool used to characterize the HC- the meridional Mass Stream Function (MSF). The MSF metric locates the HC

centre/ edges, determines the HC intensity, and also the latitudinal span of the HC ascending and descending regions from the reanalysis data.

2.2 Reanalysis Data

Long term data that is continuous in space and time is quintessential for any climate study. The studies related to long term trends cannot rely on observational data alone, since the observational sources are sparsely distributed and evolves continually with the advancement of technology. Global model simulations can prove helpful in this regard, since they provide information about the long term evolution of atmospheric parameters that is homogenous in space and time. However such simulations are prone to errors from differences in the physical representation of a variable within the model. Such forecasts will be realistic if constrained by observations in a process known as *data assimilation* (Kalnay 2002). For instance, a model shall generate an estimate of the air temperature at any grid for a later time t_1 when initialized with the values at time t_0, and combines it with the actual temperature measurement at the time t_1 by means of data assimilation. The analysis finally provides a constrained value of air temperature at t_1 which is closer to the observed value of the variable. Thus, a simple *atmospheric analysis* generates a model estimate of a variable that is constrained by actual observation of this variable, with the help of data assimilation methods.

However an atmospheric analysis is less useful in long term trend analysis. This is because (a) the underlying global model that is used to make the forecast, (b) the data assimilation methods used in it, as well as (c) the NWP models used to derive the 'a-priori' estimates for the global model, each one of these evolves over time (Kalnay 2002; Bengtsson et al. 2007). A suggested possible solution to this dilemma is to "regenerate" the synoptic analysis using a fixed data assimilation system as well as a fixed NWP model that generates 'a-priori' estimates, in combination with state-of-the-art global forecast models. The process is called *reanalysis*. The observational input to reanalysis comes from the weather station, balloon, radiosonde, aircraft, and satellite data archived by different meteorological institutions across the world. The reanalysis generates data even in the regions where observations are not easily or routinely available (such as

over oceans), to give output that is continuous in space and time (Bengtsson et al. 2007; Randall 2008). Although this is an advantage of reanalysis data, there are concerns regarding the accuracy of the reanalysed variable in the data-sparse regions because of the limited number of observations available to constrain the model forecasts.

As we know, the accuracy of data generated by any reanalysis is determined by the quality and availability of observations which are used to constrain the model fields (Dee et al. 2011). Data from several observational sources are subjected to rigorous quality control and bias correction before using them to constrain the model forecasts. In addition, the observations are also weighted against nearby observations as well as against model forecasts, before accepting or rejecting it in the process of data assimilation (Kalnay et al. 1996). The accuracy of the reanalysed outputs improved post 1979, when the satellite data became available in large numbers for assimilation (Randall 2008). Further with the advancement of computational power, it was also possible to use forecast models with higher resolutions that can assimilate observations in a better way. This too has led to an improvement in the accuracy of the reanalysis fields. A comparison of the various reanalysis outputs with different types of observations and climatologies brings out the usefulness of the dataset for atmospheric research, and this is a never ending process.

There exist several reanalysis by the world's major meteorological institutions. The list includes *National Centre for Environmental Prediction- Reanalysis 1,2* (NCEP- R1,-R2) by the National Meteorological Centre (NMC) Climate Data Assimilation System (CDAS), *ECMWF Reanalysis -25,-40,-Interim* (ERA-25,-40,-I) by the European Centre for Medium range Weather Forecast (ECMWF), *Modern Era Retrospective Analysis for Research and Application -1,-2* (MERRA-1, -2) by the NASA's Global Model Assimilation Office (GMAO), and *Japanese Re-Analysis -25, -55* (JRA-25,-55) by the Japanese Meteorological Agency (JMA). The newer versions of reanalysis are motivated especially by the growing needs of the scientific community. Though reanalysis use state-of-the-art NWP models and assimilation schemes, scientific community still find it challenging to deal with

the uncertainties in reanalysis due to the changing biases in models and observations. Irrespective of the uncertainties, reanalysis data has gained popularity due to its data homogeneity, long term data availability, as well as general consistency with the actual observational data.

The current thesis uses ECMWF Reanalysis-Interim (*ERA-I*), Japanese Reanalysis 55 (*JRA55*), National Centre for Environmental Prediction Reanalysis2 (*NCEP-R2*), and Modern Era Retrospective analysis for Research and Application- 1 (*MERRA*). The investigations in the present thesis make extensive use of the meridional wind data product of these reanalysis datasets. The datasets were the newest version of their respective organizations during the period of study. The ERA-I and the MERRA data is available since 1979, JRA55 data is available since 1958, and NCEP since 1948. These reanalyses differ among each other depending on the parameterization of sub-grid scale processes within the underlying forecast model, scheme of data assimilation, and the time-steps and resolution of the output data. ERA-I and JRA55 uses the 4DVar data assimilation scheme, which is advanced as compared to the 3DVar data assimilation scheme used by NCEP and MERRA datasets. Further information is provided in the forthcoming sections, wherein the features of these reanalysis datasets are discussed briefly.

2.2.1NCEP Reanalysis

National Centre for Environmental Prediction (NCEP)/National Centre for Atmospheric Research (NCAR) Reanalysis is a project under the initiative of the National Meteorological Centre (NMC) Climate Data Assimilation System (CDAS). The project came into operation in 1994, using the state-of-the-art model for forecast (T62/28-level NCEP Global Spectral Model) and a 3DVar technique (Spectral Statistical Interpolation scheme) for data assimilation. The reanalysed output is available since 1948 in a gridded format at 4times-daily, daily, and monthly temporal resolutions. Details on the NCEP reanalysis is extensively provided by Kalnay *et al.*, (1996) and Kanamitsu *et al.*, (2002); a few of them are discussed here.

NCEP assimilates data from all available observational sources, since 1957. This includes global rawinsonde data from NCEP Global Telecommunication System

(GTS) as well as from the Radiosonde Observation (RAOB) archives of various nations such as Canada, Argentina, Brazil, UK, France and US. Upper air data from Chinese State Meteorological Administration for the period 1954-62 and from USSR stations for the period 1961-78 are also inputs to the reanalysis. In addition to the data from NCEP GTS (since 1962), aircraft data from field experiments such as GATE (1974) and FGGE (1979) is also used in the assimilation scheme. In the regions/period where GTS lacks observation, collaboration with other national agencies provides the data. For instance, JMA provides data that is not available in GTS; and ECMWF provides complementary data for the 1989-1991 period when GTS had less number of data over US and China. 3-hourly surface land synoptic data from United States air force or NCEP since 1967 is also used in assimilation. Data from ships, buoys, near surface data from ocean reports etc., archived in the Comprehensive Ocean-Atmosphere Data Set (COADS), provides the surface marine data that is to be assimilated in the NCEP global forecast model. Radiances from TOVS satellite sounders (HIRS, MSU, and SSU) were also incorporated in the assimilation process as soon as they were made available in November 1978. VTPR IR sounder data and HIRS data available before 1979 for the SH is also assimilated; however the problems due to the assimilation of the above data have not been quantified. In addition to these data, NCEP also assimilates the satellite cloud drift wind data from NMC as well as from JMA for the period 1978-91. NCEP however does not assimilate surface wind speeds from Special Sensing Microwave/Imager (SSM/I) to avoid significant slowdown of the reanalysis due to high volume of this data.

The observational data from all the above sources for 00UTC, 06UTC, 12UTC, and 18UTC are collected and converted into a uniform format – Binary Universal Format Representation (BUFR). The data is then subjected to stringent quality control so as to remove the erroneous data, before being assimilated into the model. It is worth noting here that NCEP assimilates data only since 1957, although the period of the NCEP reanalysis is from 1948-present. During 1948-1956 period, the synoptic observations were made at 03UTC, 09UTC, 15UTC and 21UTC, as against the synoptic observations made at 00UTC, 06UTC, 12UTC, and 18UTC in the later period. The results for 00UTC, 06UTC, 12UTC, and 18UTC

during 1948-1956 were obtained by means of a forecast, and these values were used in the calculation of daily and monthly mean of different atmospheric variables in the NCEP reanalysis data.

The forecast model used for the generation of the NCEP/NCAR reanalysis, which is fixed in time, is the *T62/28-level NCEP Global Spectral Model*. The boundary layer and the stratosphere are well resolved in this model by the inclusion of five levels within the boundary layer and three levels above 100hPa. Top-of-Atmosphere (TOA) is fixed to be at 3hPa. The parameterization of all major physical processes is done in the model. This includes convection, shallow convection, large scale precipitation, gravity wave drag, diurnal cycle of radiation and its interaction with the clouds, boundary layer physics, and the vertical and horizontal diffusion processes. The original model, however, has been improvised by the inclusion of Arakawa-Schubert convective parameterization scheme, a better diagnostic cloud scheme, and a new soil model. Such changes in the forecast model were found to influence the upper level divergent flow, precipitation, and stratospheric winds produced by the reanalysis. The Arakawa-Schubert parameterization scheme for convection was found to have resulted in better prediction of precipitation. Model generated OLR values agreed with the observations in a better manner by the inclusion of the newer diagnostic cloud scheme. Studies also showed that the incorporation of the new soil model resulted in realistic predictions for surface temperature and summer precipitation in North America.

In addition to the computation of grid-point values, NCEP also provides data that is averaged over space and time in certain specified areas, using the method of Optimal Averaging (OA). This increases the ability of the reanalysis to detect 'climate' change since the small-scale variability is removed in the averaging process. In the NCEP/NCAR reanalysis, OA is carried out for temperature, specific humidity, u and v components of winds, and wind speed at seven pressure levels (1000, 850, 700, 500, 300, 200, and 100hPa) and along nine 20^0 latitudinal bands from the South Pole to the North Pole. The regions chosen by the Intergovernmental Panel for Climate Change (IPCC) for climate monitoring are also subjected to the process of OA in the NCEP/NCAR reanalysis.

The output variables of the NCEP/NCAR reanalysis are provided in a gridded format. Variables are grouped into four classes, based on the extent to which they are influenced by the observational data and/or model. *Class A* output variables are heavily constrained by the observations, making them the most reliable of all reanalysis fields. Examples are upper air temperature and wind data. The *Class B* variables, such as humidity and surface temperature, are strongly influenced by both observational data and model characteristics. If there are no observations that directly affect the output variable and the value of this variable is solely derived from the model field, they are grouped into *Class C* (e.g. clouds and precipitation). On the other hand, *Class D* variables are fields such as plant resistance, land-sea mask etc., that are fixed from the climatological values and have no dependence on the model. Thus all output fields of reanalysis are not uniformly reliable. However, data homogeneity is ensured in reanalysis by transporting information from the data rich to the data poor regions.

2.2.2 ERA-I Reanalysis

European Centre for Medium Range Weather Prediction (ECMWF) Reanalysis-Interim (ERA-I) is the atmospheric reanalysis initiative of ECMWF for the period 1979-present. The ERA-I dataset uses a frozen-in forecast model which has been in operation at ECMWF during 2006-2007 and a 4DVar scheme for assimilation of observational data. ERA-I succeeds ERA-25 and ERA-40 reanalysis datasets, the first and second generation reanalysis initiatives of the ECMWF. Dee *et al.*, (2011) carried out a wide discussion on the system configuration and performance of ERA-I reanalysis, some of which are briefly described in the following paragraphs. ERA-I assimilates as much as 10^7 observations per day, which is inclusive of both conventional as well as satellite observations. Conventional observations include upper air temperature, wind and specific humidity data from sources such as radiosondes, pilot balloons, aircrafts, and wind profilers. The conventional observations also include inputs on surface pressure, 2m temperature, 2m relative humidity, and near surface (10m) winds from sources such as ships, drifting buoys etc. The major inputs from satellites are clear sky radiance measurements, atmospheric motion vectors, total precipitable water vapour estimates, and atmospheric refraction measurements. Following paragraph gives

a brief description of the satellites and instruments providing these measurements.

Clear sky radiance measurements are obtained from (a) MSU, SSU, HIRS instruments onboard TOVS and AMSU-A, AMSU-B, HIRS onboard ATOVS (*polar orbiting sounders*) (b) SSM/I, SSM/S, AMSR-E (*passive microwave imagers*) (c) GOES (8-13), MetoSat (5,7,8,9), and MTSAT (1R) (*geostationary satellites*) and (d) AIRS onboard EOS-AQUA satellite *(sun synchronous satellites*).

All satellite derived radiance data are subjected to variational bias correction, except for the SSM/I data. Direct assimilation of clear sky radiance data from SSM/I was introduced in 2002. The data is, however, assimilated only over the oceans and not over land due to difficulties in modelling the land surface emissivity. The highest peaking channels of SSU and AMSU-A, which measure the stratospheric radiances, is also assimilated in ERA-I without any bias correction. This is because biases in stratospheric radiance measurements are typically less than the model background errors at these levels. ERA-I also assimilates satellite radiance data that was not used in the operational forecast model of the ECMWF. An example is clear sky radiances from AIRS, which is assimilated since April 2003. Only the AIRS footprint with warmest field of view is assimilated in the ERA-I system so as to maximize the chances of observing a clear scene. *Atmospheric refraction measurements* obtained from the GPS RO measurements were assimilated into the operational forecast model since 2001. CHAMP (since June 2001) and COSMIC (since December 2006) satellites and GRAS instrument onboard Metop-A satellite provides the necessary data for the same. These data are used without bias correction because of their very high accuracy. Studies have revealed that assimilation of GPS-RO data has led to a systematic warming in the tropopause and lower stratosphere since December 2006. Nevertheless, the GPS-RO data is the standard reference to constrain the variational bias adjustments in satellite radiance observations. Satellites also provide observations of upper air wind field, which is known as *Atmospheric Motion Vectors (AMVs)*. These data complements the conventional atmospheric wind data from radiosondes, pilot balloons, aircraft, and wind profilers. Geostationary satellites such as MeteoSat, GOES, GMS and MTSAT provide AMV data within 55°N - 55°S to the forecast

model for assimilation. At high latitudes, AMVs are obtained from the cloud and water vapour features identified by MODIS instruments onboard EOS-TERRA and EOS-AQUA satellites.

The forecast model for the ERA-I reanalysis is *Integrated Forecast System (IFS) Cy31r2 model*, which has been in operation at ECMWF from 2006-2007. The model has a resolution of T255/60layers (equalling to 79km on a reduced Gaussian Grid). TOA is fixed to be at 0.1hPa. The model has fully coupled components for the atmosphere, land surface and the ocean waves. As compared to the forecast models used in the previous versions of the reanalyses produced by ECMWF, the IFS Cy31r2 model use revised schemes for cloud and convective parameterization. Introduction of a moist boundary layer scheme is also a primary change in this model. Also implemented in the model is a parameterization scheme for supersaturation with respect to ice in a grid box that is cloud free at temperatures <250K. The impact of these changes to the forecast model on the total and low cloud cover has been analysed by means of observational data from ISCCP. The analysis revealed an increase in marine stratocumulus cloud cover (15-25%), increase in total cloud cover over tropical land regions (20-30%), increase in the mid-latitude low and medium cloud cover (5%), and a decrease in total cloud cover over the tropical oceans (5-15%). Hence it was shown that there are considerable improvements in the reanalysed output using IFS Cy31r2 model as compared to that produced by the previous versions of reanalyses from ECMWF.

In addition to the improvised 'frozen-in' forecast model, the ERA-I reanalysis uses an advanced version for data assimilation (4DVar method with a 12 hour assimilation window) as compared to the ERA-25 and ERA-40 reanalysis datasets. The highlight of the assimilation scheme used in ERA-I is a variational bias correction for the satellite data input. The bias parameters for satellite radiances are obtained as a part of the assimilation scheme itself, hence automating the bias correction process of the satellite data. The bias parameters of radiance data from newly added satellites are also closely followed in this assimilation scheme. This process thus enables inter-calibration of data from

different satellites, sensors, and channels against the conventional observations. Whenever the number of observations is scarce, radiance data is assimilated without any bias correction so as to avoid the influence of model background errors. Any discontinuity that may be produced in the reanalysis due to changes in observational systems is taken care of by means of the sequential data assimilation scheme that advances in time. For instance, onboard calibration errors in MSU radiance due to orbital drift was recorded as large bias variations in the assimilation system and subjected to corrections. This improves the temporal consistency of the dataset, thus enabling us to bring out the climate change signals in a reliable manner.

Yet another improvement in the assimilation part of ERA-I reanalysis is the use of a combination of the 1DVar and 4DVar schemes to assimilate Total Column Water Vapour (TCWV). The 1DVar assimilation scheme uses the rain-affected radiance data to determine the TCWV over the cloud and precipitation areas; TCWV then becomes the input to the 4DVar assimilation scheme. ERA-I also use a revised assimilation scheme developed by Holm (2003) for humidity analysis, so as to improve the representation of the hydrological cycle. The impact of this change on the precipitation estimates of ERA-I was analyzed by comparing it with the observed estimates from GPCP for the year 1990. The study revealed that the precipitation estimates of ERA-I are closer to GPCP than ERA-40 over the tropical oceans and at higher latitudes. It was also revealed that TCWV from ERA-I is closer to that observed by the Remote Sensing Systems (RSS). The continental precipitation from ERA-I was also found to be very close to the GPCC v2.1 data. Monthly variability of rainfall from ERA-I dataset for four different locations in British Isles were also found to be in agreement with the GPCC estimates over these regions. The improved forecasts in ERA-I can be attributed to the smaller background departure of the specific humidity field in ERA-I, which was obtained by comparison against the radiosonde observations of specific humidity at 700hPa.

Thus an analysis of the system performance showed improvements in the representation of hydrological cycle and stratospheric circulation, as well as improvement in temporal consistency as compared to the previous versions of

reanalyses from ECMWF. Studies reveal that monthly variability and trends in global mean surface, lower troposphere and lower stratosphere temperatures from ERA-I compares well with observations, whereas upper troposphere temperature is overestimated as a result of assimilation of the warm-biased aircraft data. Variability and trends in precipitation estimates from ERA-I were found to be accurate over land, but unreliable over oceans due to biases in the model. Such statements bring out the advancements in the ERA-I reanalysis as compared to its previous versions. This has, in fact, been the goal of the ERA-I reanalysis initiative. The ERA-I dataset is available to the scientific community as synoptic, daily mean, monthly average of daily means or synoptic monthly mean of the variable in a spatially gridded format at varying resolutions (presently as fine as 0.75° latitude x 0.75° longitude).

The present thesis uses the monthly mean v-wind data product of ERA-I from 1979-2012, as well as the cloud and relative humidity data from 1979-2016. The total cloud fraction, as well as low-, middle- and high cloud fractions from ERA-I are used in the thesis to determine the changes in these parameters within the ascending and descending branches of the HC.

2.2.3 JRA55 reanalysis

The JRA55 is the second reanalysis initiative of Japanese Meteorological Agency (JMA) covering 55 years since 1958 and the first one to apply 4DVar data assimilation scheme for the last half of the 20th century. This section gives a short description of the JRA55 reanalysis which has been discussed in detail in Kobayashi *et al.*, (2014).

The JRA55 reanalysis uses a *Global Spectral Model (GSM)* for forecast, which has been in operation at JMA in December 2009. The model has a horizontal resolution of TL319 (~55km on a reduced Gaussian grid system) and 60 layers extending up to 0.1hPa, in addition to a surface layer. The cumulus convection scheme is parameterized in the model by means of Arakawa-Schubert scheme as in JRA-25. The scheme, however, has been modified with a new triggering mechanism called the “Dynamic CAPE” (DCAPE) generation rate to deal with the

problem of overactive daytime convection in the model during summer over the land regions. Other improvements in the operational forecast model for JRA55 are the revised radiation schemes as well as inclusion of greenhouse gases along with the effect of their time-varying compositions. Previous version consisted of radiative forcing due to carbon dioxide only, whose concentration was also held fixed (at 375ppmv); JRA55 now takes into account the radiative forcing due to six species, viz. carbon dioxide, methane, nitrous oxide, CFC-11, CFC-12, and HCFC-22, as well as the changes in their composition with time.

As mentioned before, JRA55 reanalysis uses a 4DVar scheme for data assimilation. The resolution of models used to produce the first-guess fields and the analysis increments are not the same. JRA55 uses a lower resolution model to produce the analysis increments (T106) as compared to that used to produce the first-guess fields (TL319) so as to reduce the computational cost. The bias correction parameters for satellite radiance data is also produced as a part of the data assimilation step. This scheme adjusts the satellite data biases automatically, and is termed as the Variational Bias Correction (VarBC).

The observations that go into the JRA55 reanalysis are obtained mainly from the ECMWF (ERA-40) and JMA archives. This includes conventional data, satellite radiances, AMVs, scatterometer ocean surface winds, and GNSS-RO refractivities. In addition, upper air observations from NCEP were obtained for the year 1979 to fill in the gap in ERA40 data during this time. For the period before August 2002, JRA55 uses conventional data from JMA's archive over Japan alone, whereas JRA25 have used all the available data in the archive. The observational data are subjected to Quality Control (QC) so as to avoid the possible errors and biases that can creep into the reanalysis output. JRA55 uses a Dynamic QC scheme for conventional data assimilation in which a threshold value is defined as a linear function of local horizontal gradient and the first guess fields. In the regions where more than one data source is available for the same variable, data duplication is avoided by preferring the consolidated ERA-40 dataset over the others. The discontinuities in the radiosonde temperature observations due to technological advancements and the resulting biases in the observations are corrected before the assimilation process in JRA55 by means of Radiosonde

Observation Correction for Reanalysis (RAOBCORE) versions 1.4 and 1.5 that employs ERA-40 and ERA-I temperature departure statistics.

A significant amount of aircraft and satellite data became available for assimilation in JRA55 since 1990s. JRA55 incorporates satellite radiances from IR sounders (VTPR, HIRS/2), MW sounders (MSU, AMSU-A, AMSU-B, MHS), MW imagers, and the water vapour channels of the geostationary satellite imagers. However, the radiance observations contaminated by clouds are removed before assimilation into the model since JRA55 does not simulate the effect of clouds on satellite radiances. The radiance data is also subjected to VarBC before using them to constrain the forecast in the assimilation step. An exception is GNSS-RO refractivities. Because of their high accuracy, GNSS-RO observations are assimilated into the JRA55 reanalysis without any bias correction. JRA assimilates as much as 500 GNSS-RO refractivity profiles in a single analysis cycle, beginning since July 2006. Together, GNSS-RO and radiosonde observations play an important role in constraining the model biases as well as strengthening the VarBC scheme. Also directly assimilated are the radiance data from MW imagers over sea from the vertically polarized channels of 19, 22, 37 and 90GHz frequency bands, provided the cloud contaminated data has been removed. Satellite data from historical periods are reprocessed with latest and improvised retrieval algorithms before using them in the reanalysis. For instance, AMVs and clear sky radiances from the past Geostationary Meteorological Satellite (GMS) and Multifunctional Transport Satellite (MTSAT) have been reprocessed with the retrieval algorithms of 2009. AMVs were first obtained over all longitudes in 1979 during FGGE. AMVs from geostationary satellites were assimilated into the JRA55 since January 1979, and those from polar orbiting satellites, since June 2004. For assimilation, AMVs too undergo a QC procedure similar to that applied for conventional data. Reprocessed AMV data is used whenever it is available, such as from EUMETSAT (1979, 1987-2009) and from JMA/MSC (1982-2000). Also used in JRA55 reanalysis are the reprocessed refractivities from CHAMP, COSMIC and GRACE satellites archived in the CDAAC from 2006-2012.

A first cut analysis of the performance of the data assimilation system on temperature and specific humidity brought out vertically varying biases in each of these parameters. The temperature at levels near 500hPa obtained from JRA55 showed better consistency with the radiosonde observed temperatures. A cold bias is observed in the lower tropospheric (~850hPa) temperature, and a warm bias in the upper tropospheric (~250hPa) temperatures. However the warm bias in the upper troposphere decreased after 2006 as a result of the inclusion of the GNSS-RO observations in data assimilation. Cold bias observed in the lower stratospheric (~30hPa) temperature in the JRA25 data has been reduced in JRA55. "Analysis increments" of the global mean monthly specific humidity shows moistening(drying) above(below) 850hPa, which point towards a dry(moist) bias in the lower(middle and upper) troposphere in the forecast model. Besides, JRA55 has also been found to have improved its temporal consistency.

The accuracy of representation of hydrological cycle parameters in the JRA55 reanalysis was also analysed by comparing the precipitation estimates from the reanalysis with precipitation rates derived from GPCP version2.2, as well as from other reanalysis datasets. The analysis showed that the representation of precipitation in middle and high latitudes, which is underestimated in other reanalysis datasets, has improved in JRA55 reanalysis. It was also revealed in this analysis that JRA55 overestimates precipitation in the tropics. This was attributed to the dry bias of the forecast model in the regions of deep convection. Harada *et al.*, (2016), however, reports that spatial correlation between JR55 precipitation estimate in the tropics and the TRMM Multi-satellite Precipitation Analysis (TMPA) precipitation estimate is high as compared to that obtained for JRA25 and ERA-I. Time series of the global monthly mean precipitation anomalies from JRA55 is fairly consistent with that from GPCP as against the time series from ERA-40 and MERRA datasets which show strong trends. Also, the spatial anomaly correlation of JRA55 against GPCP revealed that the correlations have improved after 1980s by the introduction of SSM/I observations of humidity. This again brings out that the satellite observations play a major role in reproducing the precipitation in JRA55 reanalysis, as compared to other reanalysis datasets.

The JRA55 reanalysis products are available in a GRIB format at resolution of 1.25° latitude x 1.25° longitude for 37 levels at daily and monthly mean time resolutions. The daily data is available every 6 hours, i.e. at 00UTC, 06UTC, 12UTC and 18UTC. Although JRA55 data production spans the years 1958-2012, it is still being continued on a real-time basis and is called as JRA55 itself.

2.2.4 MERRA Reanalysis

Modern Era Retrospective Analysis for Research and Application (MERRA) is the first generation of the reanalysis initiative of NASA's Global Model Assimilation Office (GMAO), and is described in detail in Rienecker *et al.*, (2011). The current section gives a brief description of the same. MERRA spans the period 1979-2015, and is aimed to use the NASA's EOS satellites for climate analysis. MERRA is also targeted at improving the representation of hydrological cycle as compared to other reanalysis datasets. The forecast model used in MERRA is the *Goddard Earth Observing System (GEOS)-5 Atmospheric General Circulation Model (AGCM)*, and was frozen in 2008. Spatial resolution of the model is fixed at $\frac{1}{2}^{o}$ latitude x $\frac{2}{3}^{o}$ longitude. There are 72 vertical levels in the model and the TOA is fixed at 0.01hPa. The model incorporates moist physics with prognostic clouds as well as a modified version of the Arakawa-Schubert scheme for convective parameterization.

MERRA uses a 3DVar scheme based on the Gridpoint Statistical Interpolation technique for data assimilation. Model equivalent radiance, required as a background to estimate the satellite bias correction parameters, are calculated by means of Community Radiative Transfer Model (CRTM). The analysis correction to the model forecast is implemented gradually, in every 6hours, by means of an incremental analysis update (IAU) procedure. Climatological aerosol distribution generated by the GOCART model, and the analyzed ozone generated by the data assimilation system of MERRA AGCM are the ancillary data to the model. The boundary values for SST and sea-ice concentration are derived from the time-interpolated SST product of Reynolds *et al.*, (2002).

MERRA assimilates a variety of observational data, and has been benefited by the data archives of NCEP, CFSR and ECMWF. Conventional observations of standard atmospheric variables were provided by weather stations, balloons, aircraft, ships and buoys. Quality controlled radiosonde observations were taken from the NCEP database and subjected to further processing and corrections at GMAO. Assimilation of satellite observations are an inevitable part of the MERRA data assimilation module. Satellite infrared radiances are obtained from HIRS and SSU (1979-2006) whereas microwave radiances are obtained from MSU (1979-2007) and AMSU-A (1998 onwards). AMVs are obtained for assimilation from geostationary satellites and MODIS (2002 onwards). Moisture-sensitive radiances from SSM/I (1987-2009), AMSU-B (1998 onwards), GOES sounders and AIRS are also assimilated into MERRA. Ocean surface wind data is provided by SSM/I, ERS-1,-2 (1991-2001) and QuickScat (1999-2009). Rain rate from TRMM is also an input to the MERRA satellite data assimilation module. The satellite radiance data is subjected to variational bias correction in which the bias parameters are continuously updated during each analysis cycle of the data assimilation module. This is characteristic of the 3DVar scheme. The radiance data from certain satellites are subjected to cross-calibration before using it in the data assimilation process. This reduces the difference in bias estimate for the same instrument onboard different satellites. For instance, bias estimates of the radiance observations from MSU instrument onboard TIROS-N and the NOAA series of satellites differ by >1K; however recalibrated data onboard these satellites has been found to exhibit uniform biases. MERRA uses the recalibrated radiances for MSU (channel 2-4) onboard NOAA -10,11,12, and 14. It is worth noting here that MERRA does not assimilate the high accuracy GPS-RO measurements which can constrain the model forecasts and satellite biases in an effective manner. GMAO has thus currently moved to the second generation reanalysis, MERRA2, with advanced data assimilation system that is able to assimilate the observations from all modern satellites, including the GPS-RO observations. Also assimilated in MERRA2 are the space-based observations of aerosols and their interaction with other physical processes affecting the Earth's climate and is the first long term global reanalysis to do the same (Ref: https://gmao.gsfc.nasa.gov/reanalysis/MERRA-2/).

Initial evaluation of the MERRA with respect to deviation of observations from model forecast, and from analysis output revealed that the reanalysis has a cold bias in the planetary boundary layer and a warm bias in the upper troposphere. This is consistent with the biases obtained for the MLS observations that are not assimilated into MERRA. The above evaluation also brought out that the inclusion of aircraft data in the upper tropospheric levels can have a significant impact on the reanalysis output. Similar changes in the observing systems have also been found to affect the global precipitation estimates in MERRA. An example is its sensitivity to the assimilation of SSM/I as well as the AMSU-A data (channels1,2,3, and 15). While inclusion of AMSU data has been found to increase the global mean precipitation in MERRA, the inclusion of SSM/I data has been observed to dry up the atmosphere. The biases in total column water vapour in MERRA is estimated with respect to the SSM/I data, and compared to that in ERA-I and was found to be nearly the same. Precipitation estimate from MERRA was also found to compare well with the observational precipitation data from GPCP at climatological time scales. However several biases and deficiencies in water cycle have been observed on shorter time scales. For instance, the diurnal precipitation intensity in MERRA is considerably less as compared to observations. Also, the precipitation peaks during night in observations whereas it is during noon in MERRA. Despite these deficiencies, it can be stated that on longer time scales MERRA has achieved its goal of improving the representation of hydrological cycle.

The MERRA data is produced and distributed in three streams:

a) MERRA100 stream - January 1, 1979 to December 31, 1992
b) MERRA200 stream - January 1, 1993 to December 31, 2000
c) MERRA300 stream - January 1, 2001 to February 29, 2016

The reanalysis' data products are available on a native horizontal grid at resolution $\frac{1}{2}^{o}$ latitude x $\frac{2}{3}^{o}$ longitude X 42 vertical levels. The present thesis uses the analyzed v-wind data from MERRA on a monthly basis for the period 1979-2012.

2.3 Satellite Observations

2.3.1 Global Positioning System-Radio Occultation

(a)

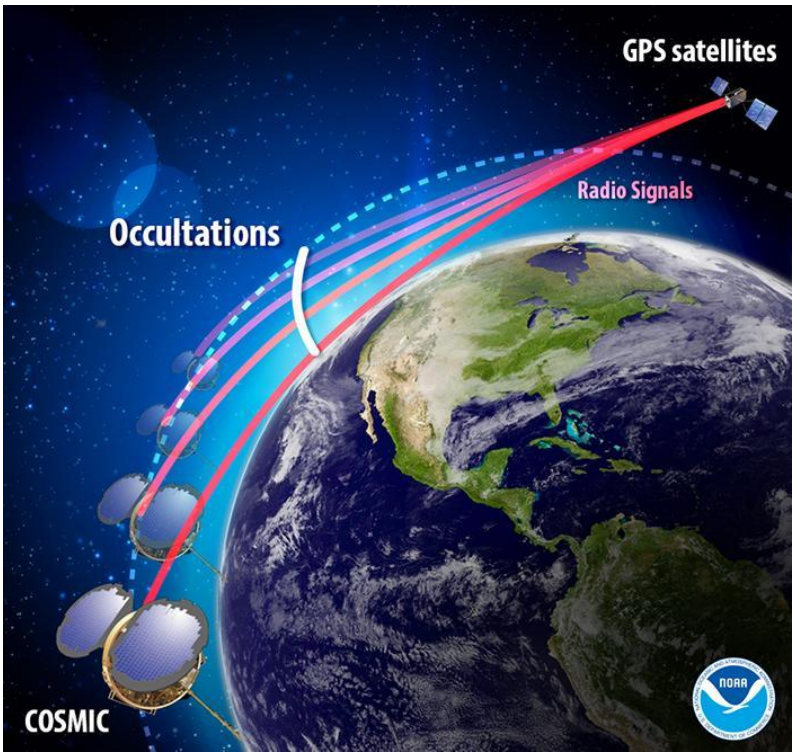

(b)

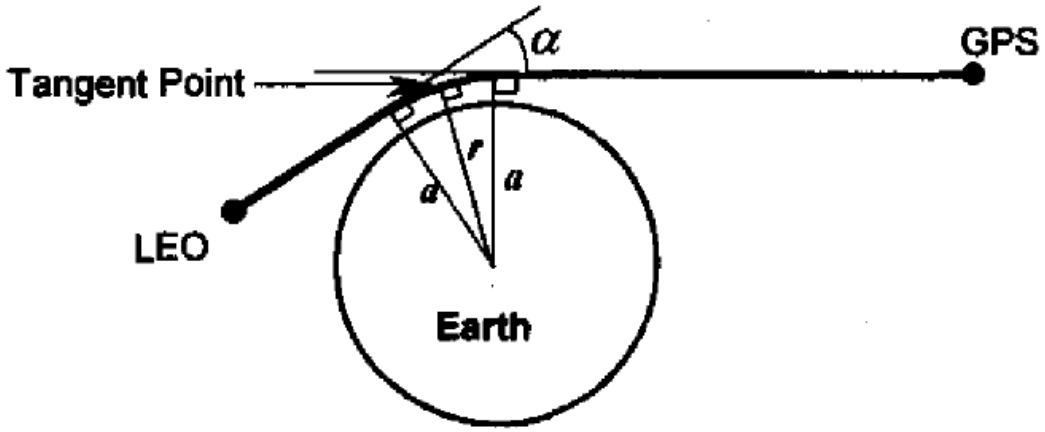

Figure 2.1: (a) A schematic demonstrating the GPS- RO technique. *(Figure taken from the site: https://www.nesdis.noaa.gov/content/small-satellites-doing-big-work-measuring-earth%E2%80%99s-atmosphere-using-gps).* (b) Instantaneous occultation geometry for GPS and LEO satellites; '*α*' is the bending angle and '*a*' is the impact parameter (*Figure taken from Kuo et al., (2000)*).

The technique of Global Positioning System-Radio Occultation (GPS-RO) makes use of a combination of the constellation of GPS satellites as well as Low Earth Orbiting (LEO) satellites in order to measure the atmospheric properties. The GPS occultation receiver on board the LEOs receives the radio signal transmitted by GPS satellites at higher orbits as they rise or set behind the Earth. Figure 2.1 is an illustration of the occultation phenomena and the occultation geometry that is used to bring out the atmospheric properties using the GPS-RO technique. The GPS is a constellation of 24 satellites distributed in six orbital planes around the Earth at a height of ~20,200km. Each GPS satellite transmits at two frequencies- L1 (1.575GHz) and L2 (1.227GHz). The LEO satellites at ~800km altitudes are set to receive the amplitude, phase as well as the pseudo-range (time delay between the transmitted and received signals) of these signals. The highlight of the GPS-RO technique is the limb-viewing geometry, where the atmosphere lies between the GPS transmitter and the LEO receiver. As a GPS transmitted signal passes through the atmosphere, the ray undergoes refraction due to density gradients in the atmosphere. The transmitted signal is thus deflected from its actual path, leading to a phase and time delay in the signal received at the LEO satellite. The Doppler shift in the transmission frequency measured at the LEO receiver is then combined with the information on the position and velocity of GPS and LEO satellites to calculate the *bending angle* $\boldsymbol{\alpha}$ at the ray tangent point represented in figure 2.1. Under the assumption of spherical symmetry for the local refractive index field, the bending angle can be expressed as a function of the *impact parameter* $\boldsymbol{a}$. The bending angle profiles are then converted into that of refractive index (n) using suitable inversion methods, such as the *Abel's transform*. Refractive index is expressed as a function of bending angle using the relation:

$$n(r) = exp\left[\frac{1}{\pi}\int_{a_1}^{\infty}\frac{\alpha}{\sqrt{a^2 - a_1^2}}\mathrm{d}a\right]$$

where $a_1 = nr$ is the impact parameter of the ray whose tangent radius is r (Kurisinski et al. 1997). Since refractive index of the atmosphere is close to 1, refractivity $N = (n-1) \times 10^6$ becomes the basic quantity to be retrieved from the GPS-RO measurements.

Various atmospheric geophysical parameters are thereafter derived from the refractivity profiles by considering the contributions of dry neutral atmosphere, water vapour, free electrons in the ionosphere, and particulates (such as liquid water) to atmospheric refractivity. At microwave wavelengths, the refractivity is related to each of the above factors as given by the relation:

$$N = (n-1) \times 10^6 = 77.6\frac{P}{T} + 3.73 \times 10^5 \frac{P_w}{T^2} + 4.03 \times 10^7 \frac{n_e}{f^2} + 1.4W$$

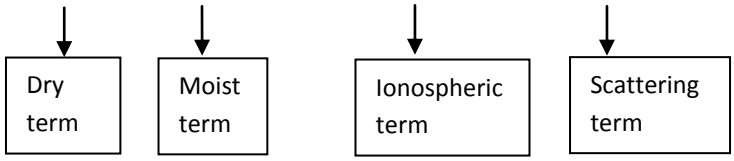

where N=refractivity; P=atmospheric pressure (in mb); T=atmospheric temperature (in K); P_w=water vapour partial pressure (in mb); n_e= electron number density per cubic meter; f = transmitter frequency (in Hz); W=liquid water content (in g/m^3).

For realistic suspensions of water and ice, the scattering term ($1.4W$) is negligible when compared with other terms, and hence can be neglected. Contribution of the ionosphere to refractivity profiling of the neutral atmosphere is also separated and removed by using the L1 and L2 frequencies in tandem, as described in Kurisinski *et al.*, (1997). Of the remaining dry and moist terms in the equation for refractivity, the moist term is neglected in the regions of the atmosphere where the atmosphere is drier than a volume mixing ratio of 10^{-4} (Kurisinski et al. 1997).

Thus the equation for refractivity reduces to $N = 77.6\frac{P}{T}$ in the regions where water vapour is negligible. According to the ideal gas law, $P = \rho\left(\frac{R}{m}\right)T$, where ρ is the density and m is the molecular mass of dry air (Holton 2004). Thus $N = 77.6\,\rho\left(\frac{R}{m}\right)$ in the regions where the presence of water vapour is negligible.

Since our aim is to retrieve the atmospheric parameters from the GPS-RO measurements of refractivity N, the above relation can be alternatively stated as:

$\rho = \frac{Nm}{77.6\,R}$,

where the dry atmospheric density is represented as a function of refractivity. Thereafter, the atmospheric pressure is obtained by assuming hydrostatic equilibrium and then integrating from top to bottom, and the atmospheric temperature is obtained using the gas law.

In the lower tropospheric regions, where the water vapour concentration is large enough, contribution of the dry term to refractivity can be separated using the relation:

$$\rho = \frac{m}{77.6\,R}\left(N - \frac{3.73\times10^5 P_w}{T^2}\right),$$

if an estimate of P_w is available from independent measurements. GPS-RO technique can also retrieve the profiles of water vapour partial pressure or specific humidity from refractivity measurements using the equation: $P_w = \frac{NT^2 - 77.6\,PT}{3.73\times10^5}$, provided the temperature and pressure information is available a priori from climatology or observations.

The GPS-RO measurements of atmospheric parameters are characterized mainly by their fine vertical resolution, global coverage, all-weather capability as well as very high accuracy. The insensitivity of the GPS wavelengths to scattering by clouds, aerosols and precipitation allows for the all-weather capability of the GPS-RO measurements; while the atomic clocks onboard the GPS and LEO satellites provides highly accurate measurement of the various geophysical parameters. The technique is thus the best alternative to radiosondes for measuring atmospheric parameters (Rieckh et al. 2014). Long term GPS-RO measurements, once available, can be expected to provide reliable information on the climatic trends in the atmosphere.

2.3.2 COSMIC GPS-RO Measurements

The GPS-RO observations were first introduced for sounding of the Earth's atmosphere by the GPS-MET programme during the period 1995-1997. This was followed by CHAMP (September 2001-September 2008), SAC-C (March 2006-August 2011) and GRACE (March 2007-December 2013), COSMIC (April 2006-December 2013), and MetOp (2006 onwards) missions. Each of these missions

provides copious information on the atmospheric parameters for the analysis of weather and climate of Earth. The present thesis utilizes the data derived from the COSMIC GPS-RO mission. COSMIC mission was introduced in April 2006 as collaborative mission between the Taiwan and the US and was in operation until December 2013.

The Formosa Satellite Mission#3 (FORMOSAT3)/ Constellation Observing System for Meteorology, Ionosphere and Climate (COSMIC) mission is a system of 6 Low Earth Orbiting (LEO) satellites orbiting the Earth at an altitude of 800km and at an inclination of 72^0 with zero eccentricity. The data is available since 2007 at a high vertical resolution (100m), with the measurements starting near the surface and extending up to as high as 40km in the atmosphere. The COSMIC provides a snapshot of the earth's atmosphere every 100 minutes and covers the four diurnal cycles. A nearly uniform global coverage is obtained with more than 2000 soundings recorded per day. Figure 2.2 draws a comparison of the coverage of the COSMIC GPS-RO soundings for a 24-hour period against the coverage provided by the radiosonde locations.

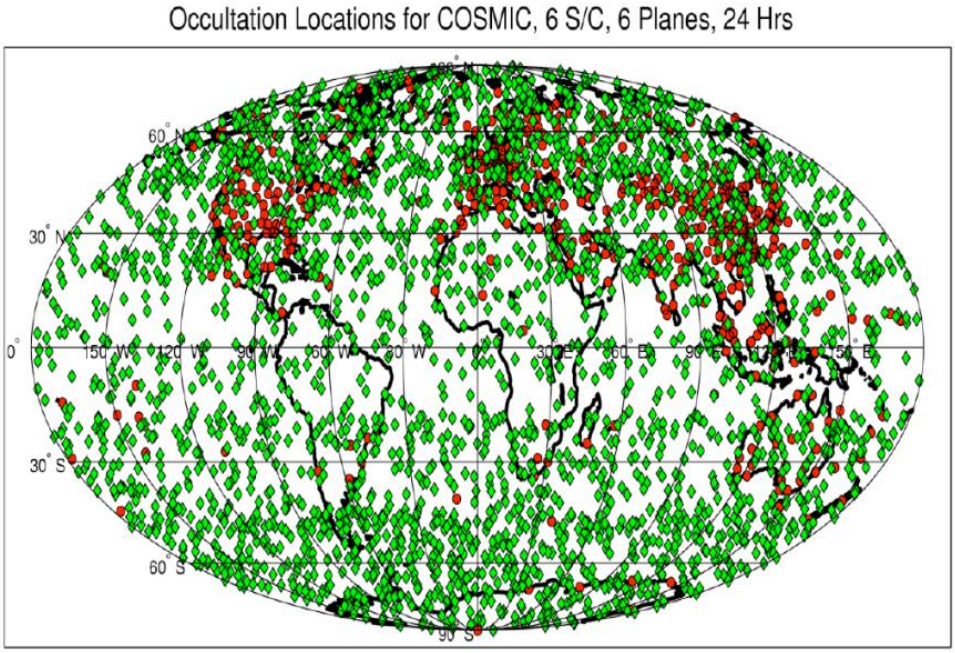

Figure 2.2: Typical 24-hour distribution of the COSMIC GPS-RO soundings, shown by green dots. Operational radiosonde stations are shown by red dots *(Figure taken from Ho et al. (2009)).*

Atmospheric refractivity measurements from COSMIC GPS-RO are free of biases as a result of the highly accurate measurements of the signal time delay and the insensitivity to surface emissivity. Hence, unlike other satellites, the COSMIC data is assimilated into atmospheric reanalysis without any bias correction, thus making it the standard reference for satellite bias correction. The data from COSMIC is presently being used in all recent reanalysis projects such as ERA-I, JRA55, and MERRA2 reanalyses.

The COSMIC observations are processed and archived for distribution at the Cosmic Data Analysis and Archive Centre (CDAAC) at UCAR. The present thesis uses temperature profiles derived from the COSMIC GPS-RO measurements from 2007 to 2013, archived under the head *wetPrfdata*. The temperature profiles derived from COSMIC have an accuracy better than 0.5 K (Kursinski et al. 1997). These temperature profiles are then used to derive the lapse rate tropopause (LRT) height, which is then used to derive the regional features of the tropical belt. The exact methodology shall be discussed in the forthcoming chapters.

2.3.3 Tropical Rainfall Measuring Mission

The Tropical Rainfall Measuring Mission (TRMM) is a joint mission between the NASA and the JAXA to monitor the four dimensional distribution of the tropical and subtropical precipitation and the latent heating associated with it. Continuous space-based monitoring of precipitation by the TRMM is achieved by following an inclined (35^0) and non-sun synchronous Low Earth Orbit for the component satellites. The initial orbital altitude was 350km and was boosted to 403km in August 2001, with the aim to extend the lifetime of the mission. The orbit is also set to be precessing so that the diurnal variation of tropical rainfall over a given location is captured efficiently. TRMM data is available for the period November 1997 - June 2015 over a latitudinal range of 35^0S to 35^0N.

There are five instruments on board the TRMM- TRMM Microwave Imager (TMI), Precipitation Radar (PR), Visible and Infrared Scanner (VIRS), Lightning Imaging Sensor (LIS) and Clouds and the Earth's Radiant Energy System (CERES) (shown in figure 2.3). TMI, PR and VIRS are rain measuring instruments, whereas LIS and CERES instruments measure the total upwelling radiant energy (Kummerow et al.

2000). TMI and VIRS are passive radiometers operating in the microwave and visible/infrared frequencies, respectively. On the other hand, PR is an active gain radar operating in the 13.8GHz frequency range. The instruments, together, yield important information on

a) the rainfall structure and variability in the tropics at various time scales;
b) the latent heat released during the process of precipitation, its four dimensional structure, and its role in tropical and extratropical circulations;
c) the precipitation type (convective/stratiform) and its variability within the tropics
d) improving the current understanding on the global energy and hydrological cycles.

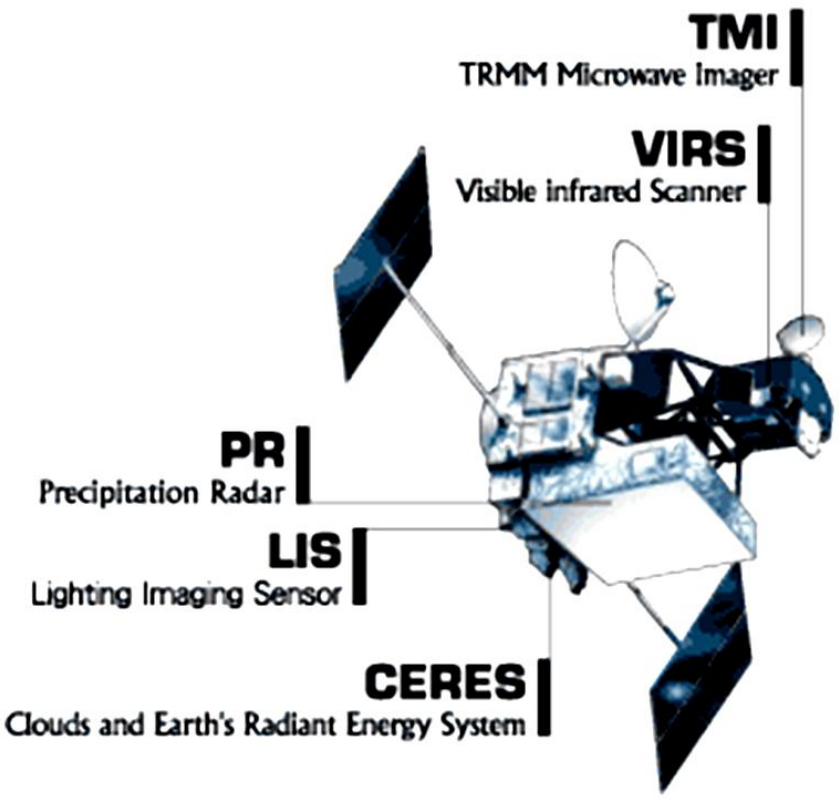

Figure 2.3: Configuration of the various instruments onboard the TRMM (*Figure taken from https://pmm.nasa.gov/trmm/trmm-instruments*).

In addition, TRMM also evaluates the scope of space-based precipitation measurements. Liu et al., (2012) provides a summary of the available TRMM data products. More details on TRMM and the mission objectives can be found in

Kummerow *et al.*, (2000) and Simpson *et al.*, (1988). A more advanced Global Precipitation Mission (GPM) with dual frequency radar and other precipitation monitoring instruments succeed the TRMM mission.

2.3.4 Precipitation Radar onboard TRMM

The Precipitation Radar (PR) on board TRMM is the first space-borne precipitation radar that measures the time delay of the precipitation-backscattered return power (reflectivity). The instrument has a swath width of 247km at surface, with 5km horizontal footprint at nadir. PR operates in the Ku-band (2.17cm or 13.8GHz), and has a sensitivity of 18dBz (post orbit boost). Vertical resolution of the reflectivity measurements is 250m. The specifications of TRMM's PR instrument, along with that for other instruments onboard TRMM, are summarized in figure 2.4.

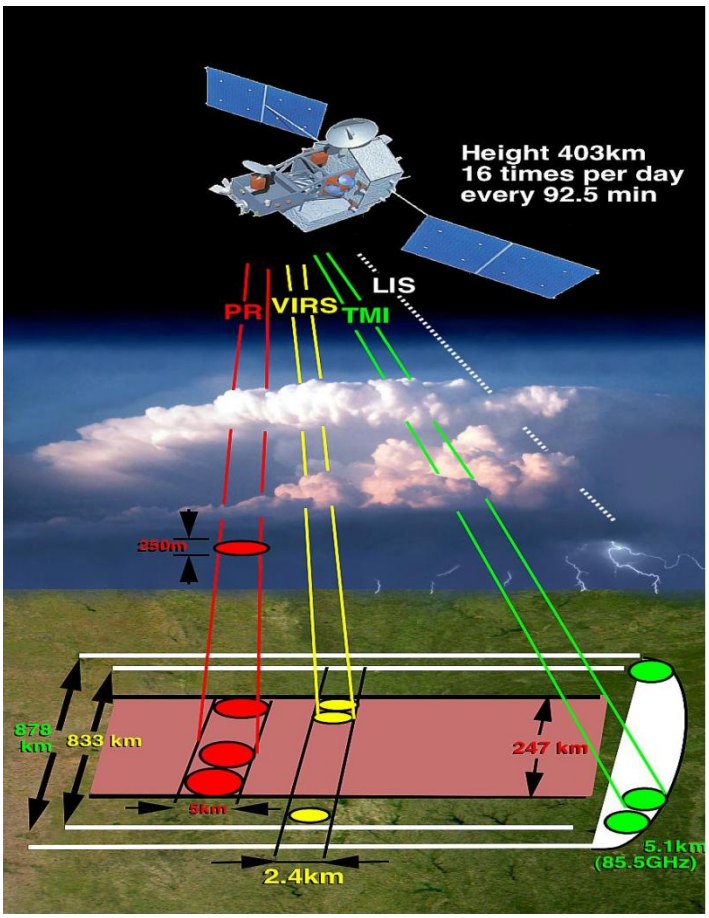

Figure 2.4: An illustration of the instrument specifications of the PR (shaded in red), along with that for other instruments onboard TRMM *(Figure taken from https://trmm.gsfc.nasa.gov/overview_dir/background.html).*

The time delay in receiving the signal backscattered from precipitating sources by the TRMM PR provides height information, which is in turn used to retrieve the precipitation profiles. The vertical profiles of rain rate obtained using TRMM PR are classified into three groups- convective rain, shallow stratiform rain, or anvil rain (deep stratiform rain with a melting level). The profiles of latent heat release by each of these rain types vary substantially; hence the accuracy of this segregation determines the accuracy of the latent heating profiles estimated from the PR.

2.3.5 Spectral Latent Heating

In the atmosphere, there occurs energy changes associated with the change in phase of water. The energy released/absorbed in the process is called *latent heat*. Tropical circulations are maintained by the latent heat release from precipitating cloud systems. As mentioned before, the latent heating profiles vary among the different rain types. While convective rains produce heating profiles that is positive throughout the troposphere, heating profiles associated with stratiform rain are negative below the *melting level* and positive above it (Houze 1997). Hence to evaluate the latent heating due to precipitating cloud systems, an accurate classification of the rain type is necessary.

TRMM make use of a Cloud Resolving Model (CRM) to obtain the profile of latent heat release at a given location due to the different rain types. CRMs use sophisticated microphysical schemes to simulate the precipitation from clouds and the associated latent heat release (Tao et al. 2006). Such heating profiles are indexed in the form of a look up table (LUT) for the precipitation type- whether it is convective, shallow stratiform or anvil rain. This type of an indexing process saves computation time and computation cost. CRM simulation of the tropical cloud systems in the Tropical Ocean and Global Atmosphere Coupled Ocean-Atmosphere Response Experiment (TOGA COARE) were used to produce the LUT for the various rainfall types from TRMM (Shige et al. 2004; Shige et al. 2007).

In the Spectral Latent Heating (SLH) algorithm, LUTs make use of rainfall profiles spectrally arranged according their precipitation top height (PTH) and the rain type. For anvil rains, precipitation rate at the lowest observable level and at the

melting level is used for indexing instead of PTH (Shige et al. 2007). This becomes necessary because of the insensitivity of the PR to small ice-phased hydrometeors.

When TRMM PR rainfall profiles give information on the convective/stratiform fraction, PTH, and the precipitation rate at the lowest observable and melting levels, the CRM simulated precipitation profile matching these criteria is chosen first. Thereafter, the heating profile corresponding to this information is adopted from the LUT. In the SLH algorithm, the vertical profiles of precipitation obtained from TRMM are carefully compared against the CRM simulated precipitation profiles to give the most accurate latent heating profile.

The current study uses the gridded (0.5^0x0.5^0) monthly spectral latent heating product of TRMM (3H25) version 7 for the period 1998- 2013. The zonally averaged distribution of latent heating in the tropical troposphere obtained from PR is critically analysed to determine the influence of latent heating from precipitating cloud systems on the HC centre, edges and intensity.

2.4 Ground-based Observations: Integrated Global Radiosonde Archive

Integrated Global Radiosonde Archive (IGRA) is a comprehensive set of radiosonde data from more than 1500 world-wide radiosonde stations, which is compiled and processed by the National Climatic Data Centre (NCDC). Durre et al. (2006) gives a detailed description of this dataset. IGRA compiles data from 11 different sources, which are classified into 3 groups- core, other large scale, and country specific datasets. 82% of the total soundings in IGRA come from the core group, which contains the data from NCDC historical GTS, NCAR/NCEP GTS, NCEP GTS and NCDC real-time GTS. Data from the Russian GTS, United States air force, and the Australian GTS constitute the other large scale group, and contribute as much as 6% to the total soundings in IGRA. In addition to these two groups of data, country-specific data from US, Australia, Argentina and South Korea make up the rest 12% of the total soundings in IGRA. The stations have a global coverage in all core group datasets, and in Russian GTS and in United States air force data. Australian GTS covers the whole SH, whereas the country specific

datasets have coverage in their respective regions. Data merging is carried out in an appropriate manner with the core GTS as the base data and rest of the data groups acting as supplementary to the core group data. The merged data is then subjected to a sequence of algorithms (described in Durre *et al.*, (2006)) to ensure reduction of gross errors and hence, the quality of the data in the IGRA archive. The soundings archived in IGRA provide information on pressure, temperature, geopotential height, wind speed, wind direction, and dew-point depression. Of these variables, atmospheric temperature, pressure, and geopotential height are of the highest quality in IGRA, since they are the most scrutinized data. The IGRA observations are provided at standard, surface, tropopause and significant levels. The overall period of IGRA is from 1938-present. The data is freely accessible online as both individual soundings and monthly means for 00UTC as well as 12UTC for all years after 1958, and at 03UTC and 15UTC before 1958. Of all the stations, as much as 800 stations presently give data on 80% of the days in a year, as compared to the 300-400 stations which had been giving information during the 1960s for 80% days in a year. The resolution of the dataset has also improved over time. The data has been provided only at the mandatory pressure levels in the 1960s; presently the data is also provided at 35 levels in addition to the mandatory levels. The vertical extent of the soundings has also improved from 100hPa in 1960s to 10hPa at present (since as much as 35% of the soundings reach the 10hPa level during the present time). Thus, the vertical resolution of IGRA data is sound and the spatio-temporal coverage of this dataset is by and large complete over US, Western Europe, Russia and Australia. The data can be used for inter-comparison with other measurement systems, and also for verifying model outputs. The archive can also be a tool for boundary layer studies. Such studies are required to proceed under the caveat that the IGRA data account for inhomogeneities neither from the changes in instrumentation nor from the changes in observation practices. IGRA derived products such as the Radiosonde Atmospheric Temperature Products for Assessing Climate (RATPAC) which account for these inhomogeneties also can be used instead.

In the current thesis, the IGRA data is used for the comparison of the reanalysis datasets for HC dynamical studies by means of the MSF metric.

2.5 Global Precipitation Climatology Project Dataset

Global Precipitation Climatology Project (GPCP) is the initiative of the World Climate Research Programme (WCRP) and its component Global Energy and Water Cycle Experiment (GEWEX), dedicated to produce the community analysis of global precipitation to improve the current understanding of the hydrological cycle. Details of the project is given in Huffman et al. (1997) as well as in Adler et al. (2003), and are being summarized in this section. GPCP combines the satellite as well as ground based observation of precipitation to produce a comprehensive dataset that is globally complete. The data is available since 1979 on monthly basis at resolutions 2.5° latitude x 2.5° longitude. GPCP also provides pentad global analysis as well as daily 1° latitude x 1° longitude analysis. The GPCP precipitation data is archived and distributed by the World Data Centre- A at NOAA National Climatic Data Centre (NCDC). The surface-based observations are obtained from the GPCC rain gauge analysis and the GHCN-CAMS Guage Analysis. GPCC operated by the German weather service provides data since 1986. During the period not covered by the GPCC, i.e. from 1979-1985, a combination of the GHCN and CAMS rain gauge data produced by the NOAA CPC group is used in the GPCP precipitation analysis.

In addition to the surface measurements, rain rate derived from MW data provided by the low orbiting satellites and IR data provided by geosynchronous satellites are also merged in the GPCP analysis of precipitation. Data from 19GHz and 22GHz channels of the SSM/I instrument measures the MW emission estimates over the ocean and that from the 85GHz channel measures the MW scattering estimates over the land. On applying adequate algorithms, data from these channels provide rain rate, which is merged in the GPCP precipitation analysis. The minimum sensitivity of the 85GHz channel is 1mm/hr. Geosynchronous IR-based estimates of rainfall are also an input to the GPCP analysis. IR-based estimates of global rainfall obtained from geostationary satellites (GOES, GMS, MeteoSat) are merged together using the GOES Precipitation Index (GPI) technique. The technique derives rain rate from cold cloud top area, and has been in use in GPCP since 1986. Data gap areas in the geostationary measurements are filled in by means of that from AVHRR onboard

the NOAA polar orbiting satellites. Another polar orbiting satellite data that is extensively used in GPCP is the data from TOVS instruments onboard NOAA satellites. TOVS estimates precipitation from a regression relationship between rain gauge measurements and the TOVS parameters for cloud volume. TOVS precipitation estimates, since July 1987, complements the SSM/I precipitation estimates. In the 40°N to 40°S zone, where there is an SSM/I data void, TOVS data is used after bias adjustment against the zonally averaged SSM/I data. In the Polar Regions, SSM/I data is replaced by the TOVS data, after carrying out a bias adjustment using the rain guage data in these regions. SSM/I and TOVS precipitation estimates are given equal weightage in the rest of the regions. Yet another input to GPCP is OLR Precipitation index (OPI), which makes use of the OLR measurements from LEO satellites. As already known, a reduced OLR amount corresponds to higher precipitation rate. OPI data is used in lieu of the satellite precipitation estimates during the pre-SSM/I period (i.e., from 1979-1987). Each of the satellite-based estimates of precipitation is bias adjusted against guage measurements. Bias errors are removed in this analysis procedure, leaving out only random errors to be estimated separately. The weight for each dataset is produced in the process of error estimation. Once this is done, "the multi-satellite data and the guage data are combined with inverse error variance weighting to produce the final merged analysis" that is spatially uniform. The GPCP precipitation estimate and its climatology have been found to reproduce the mean precipitation pattern on earth. The average precipitation rate from the dataset has been recorded as 2.6mm/day, with the oceans (2.8mm/day) recording more precipitation than over land (2.1mm/day). However, the values of mean precipitation over oceans are debatable because of the less number of guage observation over oceanic regions. So is the case with the precipitation over the polar latitudes. Stations providing long term observations over Polar Regions are less in number and the GPCP precipitation over these regions are entirely derived from the TOVS or OLR data products. It has also been noted that GPCP underestimates precipitation over some mountainous regions since neither there are many rain gauges in mountainous terrain nor does the satellite capture shallow orographic precipitation. Users are also cautioned to consider the inhomogeneity of the input datasets, especially during the pre-SSM/I period while analysing the global and regional trends in precipitation. Irrespective of the

limitations, the GPCP data is of immense utility to the scientific community because it provides a globally complete account of precipitation in a comprehensive manner. The monthly mean precipitation rates obtained from GPCP version 2.3 for the period 1979-2014 are used in the present study.

2.6 Meridional Mass Stream Function (MSF)

Meridional Mass Stream Function (MSF) is the most physically plausible metric that can closely track the atmospheric flow; and is hence used in the present thesis to characterize the HC. Mathematically, stream function is defined as a fluid flow that satisfies Laplace's equation and hence, irrotational in nature. MSF is thus the flow of atmospheric mass in the meridional direction, and is derived by solving the zonally averaged mass continuity equation for a zonally averaged meridional wind (Oort and Yienger 1996). The equation is given as:

$$\psi = \frac{2\pi a \cos\phi}{g} \int_0^p [\bar{v}] dp$$

where 'ψ' is the MSF expressed in kg/s, 'a' is the radius of the Earth, 'g' is the acceleration due to gravity, 'ϕ' is the latitude, $[\bar{v}]$ is the time averaged (denoted by over bar) and zonally averaged (denoted by []) meridional wind, and p is the pressure level. To ascertain mass balance in the vertical direction, the mass weighted vertical mean value is subtracted from $[\bar{v}]$. Ψ is assumed to be zero at the TOA, which is fixed to be at 10hPa for reanalysis data and at 5hPa for radiosonde data (Waliser et al. 1999). A positive value for ψ denotes a northward flow, whereas a negative value for ψ denotes a southward flow. MSF defines HC edges as the first latitude poleward of the cell centre where MSF at 500hPa becomes zero (Stachnik and Schumacher 2011). The distance between the HC edge in the NH and that in the SH gives the total width of the HC. On the other hand, magnitude of maximum(minimum) MSF in the NH(SH) gives the HC strength (Stachnik and Schumacher 2011).

Meridional wind data product of the reanalyses as well as the IGRA data is used to determine the MSF. Figure 2.5(a) is a pressure-latitude section of the MSF (ψ) charted out from the ERA-I reanalysis v-wind data product for the period 1979-2012. The figure has been obtained for the March-April-May season, and clearly

shows the two cell structure of the HC during the equinox, with the cell centre occurring at the equator. Figure 2.5(b) depicts the MSF at 500hPa as a function of latitude. The location of the HC centre as well as edges is clearly illustrated in this figure as the latitude where MSF changes direction; these latitudes are identified using a linear interpolation scheme. For this equinoctial season, the HC centre is seen to be fixed at the equator, the edges fall at $\sim 30^0$N/S latitudes, and the NH and SH cells are seen to be equally intense ($\sim 1.5 \times 10^{11}$ kg/s). The intensity of the hemispheric HC, however, varies during the solstice seasons. This shall be discussed further in the forthcoming chapters.

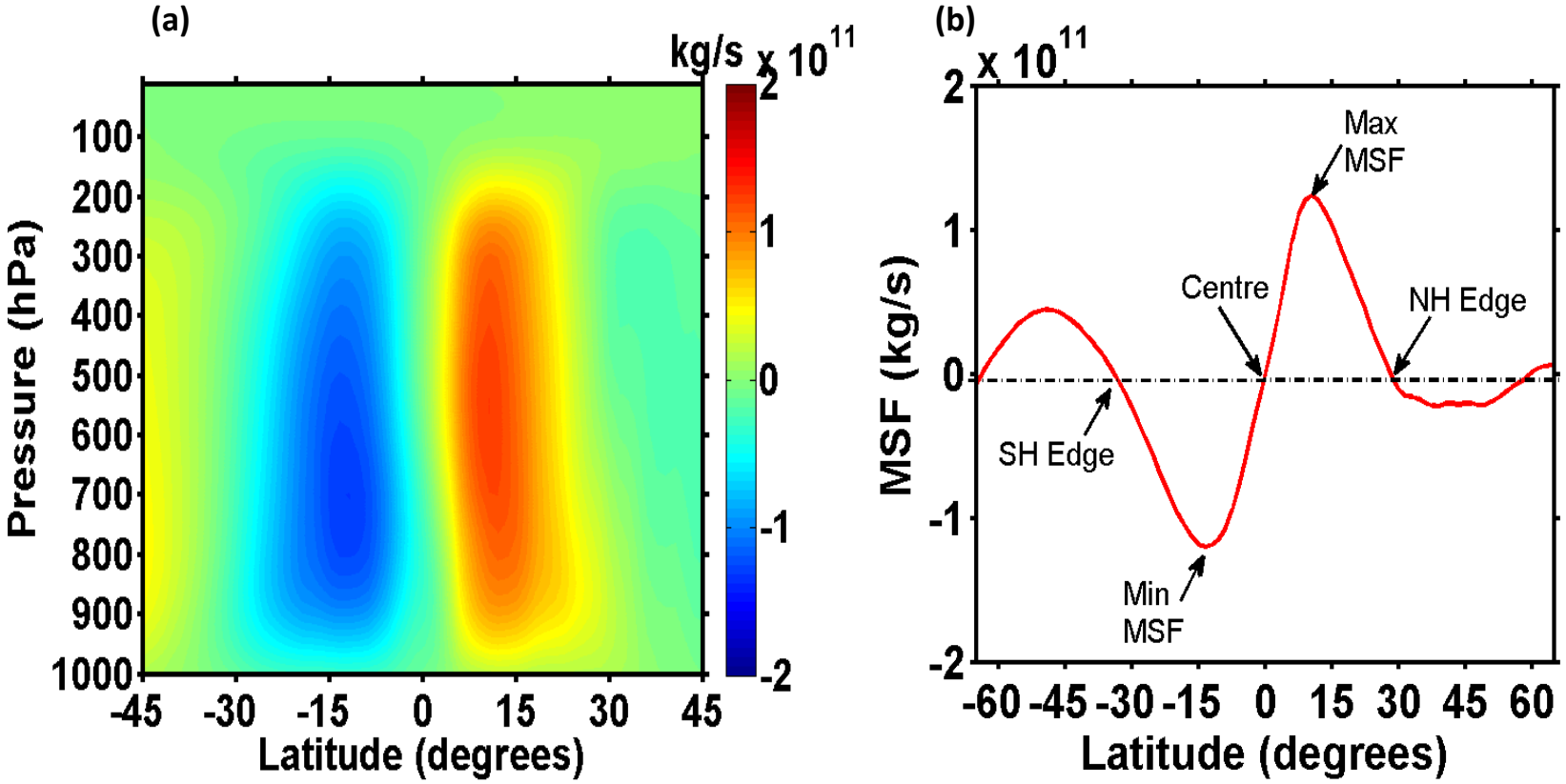

Figure 2.5: (a) Pressure-latitude section of the zonally averaged MSF for the March-April-May season from 1979-2012 *(Data source: ERA-I reanalysis)*. (b) Latitudinal distribution of MSF at 500hPa illustrating the characteristic HC parameters.

CHAPTER 3

CHARACTERIZATION OF THE ZONAL MEAN HADLEY CIRCULATION AND QUANTIFICATION OF ITS POLEWARD EXPANSION

3.1 Introduction

As discussed in Chapter 1, differential heating of the Earth's surface by the Sun from equatorial to polar latitudes is one of the major factors that play a vital role in controlling the Earth's atmospheric dynamics. The large scale ascent of the moist air at the equatorial latitudes due to this differential heating and latent heat release, subsequent meridional transport towards the poles, and descent of dry air over subtropics constitute the general circulation of atmosphere and thereby control the climate zones of the earth. One such planetary scale circulation spanning one-third of the globe from tropics to subtropics is the Hadley Circulation (HC), whose variability will have explicit impact on the established temperature and precipitation patterns of the planet earth (Held and Hou 1980; Diaz and Bradley 2004; Johanson and Fu 2009). By now it is well known that the HC is responsible for the wet, humid climate of the tropics and the dry, parched climate of the subtropics. The distinct biodiversity of these regions is also adapted to the established climate and precipitation patterns.

Of late, sinking latitudes of HC has gained importance because of the fluctuations they exhibit, mainly due to the changes in meridional temperature gradient arising in response to the changing concentrations of greenhouse gases and other anthropogenic sources (Lucas *et al.*, 2014 and references therein; Seidel *et al.*, 2008). Owing to its direct impact on subtropical climate, many researchers across the globe are focusing on quantifying the variability in HC dynamics and its consequences. Many indicators are used in such a comprehensive study on HC. Among these parameters, the meridional mass stream function (MSF), velocity potential (Nguyen et al. 2013), tropopause height, total ozone, outgoing long-

wave radiation (OLR), position of subtropical jet, cloud amount and precipitation are widely used to investigate the HC dynamics. A summary of all the studies till 2014 making use of a majority of the indicators mentioned above is provided by Lucas et al. (2014), and has also been discussed in Chapter 1.

Oort and Yienger, (1996), using 26 years (1964-1989) of radiosonde upper air wind observations over several parts of the globe, reported the inter-annual variability in the intensity of HC and found significant correlation with El-Nino Southern Oscillation (ENSO). These authors also reported significant seasonal variations in the HC strength, latitude and height of maximum MSF. Waliser *et al.*, (1999), using global radiosonde network observations and NCEP reanalysis data, introduced an innovative method to verify the adequacy of the radiosonde sampling over the globe to study the HC dynamics. This study also evaluated the extent of NCEP reanalysis data in reproducing the major features of HC. These authors sampled the NCEP reanalysis data over the radiosonde stations and computed the MSF. The comparison between in-situ and subsampled reanalysis data suggested stronger HC in both hemispheres as compared to in-situ observations, which is attributed to biases in the reanalysis. In a seminal study, Chen *et al.*, (2002) reported strengthening of the tropical circulation using satellite observations of outgoing long wave radiation and reflected short wave radiation. These authors also verified their assertion independently using upper tropospheric humidity, cloud amount, surface air temperature, and vertical velocity, which confirmed the strengthening of both Hadley and Walker circulation. Using global circulation model simulations, Cook, (2003) reported the land surface forcing on the HC. These simulations showed that the presence of land surface double the intensity of winter cell and halve the intensity of summer cell. Subsequently, Clement, (2006) evaluated the role of ocean dynamics in setting the structure and strength of the seasonal HC. Recently, many studies on HC dynamics has shown changes in the horizontal scale and strength of the circulation, in fact a poleward expansion, over the past few decades (Hu and Fu 2007; Johanson and Fu 2009; Liu et al. 2012; Nguyen et al. 2013). Hu and Fu, (2007), using three reanalysis datasets (uses MSF metric) and OLR datasets, showed that the HC has a noticeable expansion of $\sim 1.5^0$ and $\sim 1^0$ latitude per decade, respectively. These authors reported that the poleward expansion of HC

is prominent during summer and fall. It has also been observed that the rate of expansion of HC is sensitive to the indicator metrics Ao and Hajj, (2013). For instance, tropopause height was used as an indicator to find an expansion of $\sim 0.4^0$-0.7^0 latitude per decade by Reichler and Held (2005) (c.f. Reichler 2009). Hudson et al. (2006) used total ozone and estimated an expansion of $\sim 1^0$ latitude per decade (for NH alone). Using eight sets of reanalysis, Nguyen et al. (2013) investigated the HC dynamics. These authors reported HC expansion in both hemispheres, most pronounced and statistically significant during summer and autumn, at an average rate of expansion of 0.55^0 latitude per decade in each hemisphere. However, significant differences were found in the strengths and tendencies of the analysed features among the eight reanalysis datasets. Davis and Rosenlof, (2012), using a suit of tropical edge latitude diagnostics such as tropopause height, precipitation minus evaporation (P-E) and OLR derived from satellite observations and reanalysis datasets, suggested that the wide range of trends in tropical belt expansion is due to the use of different datasets and edge definitions. These authors also found statistically significant HC expansion based on MSF in the range 1^0-1.5^0 latitude per decade. Very recently, Chen et al. (2014), using six reanalysis datasets, investigated the intensification and poleward expansion of HC at regional scales. These authors chose African, Indian Ocean, western Pacific, eastern Pacific, South America and Atlantic regions to study the regional features of HC. The results showed significant and uniform trends in poleward expansion of the boreal HC over all the regions except western Pacific. In southern hemisphere (SH), only South American region showed a significant trend in the poleward expansion of HC. Several other studies in the recent past has also focused on intensification and poleward expansion of the HC using reanalyses as well as long-term observational datasets to find a widening $\sim 1^0$ latitude per decade, excluding the outliers and taking into consideration both observational uncertainties as well as the differences in methodologies (Reichler, 2009).

Observed expansion of HC is also reproduced by climate models, but to a lesser extent than observations (Seidel et al. 2008). Johanson and Fu, (2009) compared the observed widening of the HC with GCM simulations. There were noticeable differences in observed and GCM simulated widening of HC. These results

insisted on the need for investigating the reasons behind the significant discrepancies between GCM simulated and observed widening of HC. The GCMs simulating the influence of increased greenhouse gases produce weakening of the tropical overturning circulation, which affects the Walker Circulation more strongly than the HC. Apart from GCM, there were studies using Coupled Model Intercomparison Project (CMIP) simulations. For example, GCMs in the WCRP CMIP3 project which make use of the increase in greenhouse gases as a forcing, shows a poleward expansion of the HC of approximately $\sim 1^0$-2^0 latitude accompanied by a decrease in intensity of the HC (Lucas *et al.*, 2014). Lu *et al.*, (2007) using simulations of 21st century climate taken from A2 scenario of the IPCC AR4 project reported that in response to increased global warming, a significant weakening and poleward expansion of HC is observed. The authors attributed the expansion of the HC to an increase in the subtropical static stability, which extends the baroclinic instability zones towards poles and hence the edge of the HC. The observed trends of expansion of HC in reanalysis datasets were also found to be more than that obtained using CMIP simulations. Hu et al. (2013), using CMIP5 historical simulations with greenhouse gas forcing, reported a total widening of $\sim 0.15^0 \pm 0.06^0$ per decade for the period 1979–2005. These trends were reported by the authors to be approximately six times weaker than the trends from reanalyses. Quan *et al.*, (2014) diagnosed the climate model simulations to understand the rate of expansion of tropical belt. These authors reported that the rapid expansion of tropical belt observed in the various reanalysis datasets during 1979-2009 is implausible. Thus there exists a discrepancy between the observed and climate model simulations on HC expansion. Irrespective of the discrepancies, the climate model simulations are significant since they are driven by a variety of forcings (including anthropogenic) derived from the climate of the past and indicative of the reasons behind the expansion of the HC (Reichler et al. 2009; Lucas et al. 2014).

Above discussion on the phenomena of HC and its poleward expansion has brought out that the width and intensity of the HC has significant inter-annual variability and a net poleward moving trend in the recent decades. This discussion also brought out that a consensus is yet to be reached among different studies on the actual rate of expansion of the HC for it has been found to differ

with respect to the season under consideration, data used, time span of the study, and the metric used for the analysis. Long term observational data, if available, would have enabled the scientific community to determine the true rate of expansion. However there are inherent limitations in producing spatially homogenous, globally complete and long term observational data.

The lack of globally complete observational records have been partly addressed by reanalysis, which combine model fields with sparsely distributed observations to form a spatially complete gridded meteorological dataset (Rienecker et al. 2011); however, their use for estimation of climate trends is still a subject of debate (Stachnik and Schumacher 2011). Sturaro, (2003) noted that the trends in HC expansion obtained using reanalysis datasets may be biased due to the quality as well as quantity of the data being assimilated. As discussed in Chapter 2, such kinds of biases arise out of the spatial inhomogeneity of observational network and continuous evolution of the observational platform that incorporate the radical technology. The bias can also arise from the difference in data assimilation methods of various reanalyses as well as from the difference in representation of the various physical processes within the underlying model in these datasets (Waliser et al. 1999; Lucas et al. 2012). The effects of these biases are reflected in the output of the reanalysis, posing a challenge to the evaluation of a long term climatic trend.

Thus it has become the need of the hour that reanalysis datasets are evaluated using observations for global circulation studies and for HC in particular. Although there have been studies which compared the available reanalysis datasets among each other with regard to the HC expansion (Stachnik and Schumacher 2011; Nguyen et al. 2013), only a few of them have compared reanalysis datasets with observations. An example is the study by Waliser et al., (1999) who, using global network of radiosonde observations and NCEP reanalysis data, introduced an innovative method to verify the adequacy of the radiosonde sampling over the globe to study the HC dynamics. These authors sampled the NCEP reanalysis data over the radiosonde station locations and computed the MSF, and evaluated the ability of NCEP reanalysis data in reproducing the major features of HC. The comparison between in-situ and

subsampled reanalysis data in their work suggested that the HC from the subsampled reanalysis data, in both hemispheres, is stronger than that from in-situ observations. The authors attributed this discrepancy in HC strength to biases in the reanalysis which arises due to obvious reasons discussed beforehand. Hence such comparisons between reanalysis data and actual observational data is bound to convey useful information on the utility of reanalysis datasets for studying the large scale circulations in the atmosphere, and for HC studies in particular. Besides, it is also necessary that newer generations of reanalysis projects are evaluated for their use in HC dynamical studies. In this regard, the present chapter focusses on the analysis of long term changes in the HC by means of the relatively new Japanese Re-Analysis (JRA55) data and its comparison with three other widely used reanalysis datasets, viz. National Centre for Environmental Prediction (NCEP), ECMWF Re-Analysis – Interim (ERA-I), and Modern Era Retrospective-analysis for Research and Applications (MERRA) datasets for a period of 34 years (1979-2012), as well as on the validation of these datasets against monthly mean global upper air observations obtained from the Integrated Global Radiosonde Archive (IGRA). In addition to substantiating the use of these reanalysis datasets for climate studies by means of in-situ data, the current chapter also discusses on the long-term trends in the monthly mean width of the zonally averaged HC in these reanalysis datasets. The newer aspects of the present study as compared to earlier ones are (1) the evaluation of relatively newer JRA55 for studies on HC dynamics, and (2) comparison of JRA55, NCEP, ERA-I and MERRA reanalyses with IGRA data using the '*subsampling*' technique. Section 3.2 provides data and methodology, results are discussed in section 3.3 and section 3.4 provides a summary of the results.

3.2 Data and Methodology

The present work utilizes the meridional winds from four reanalysis datasets (resolution specified in brackets): JRA55 (1.25^0 x 1.25^0 x 37 levels), NCEP (2.5^0 x 2.5^0 x 17 levels), ERA-I (1.5^0 x 1.5^0 x 37 levels), and MERRA ($1/2^0$ x $2/3^0$ x 42 levels). In order to establish the reliability of these reanalysis datasets for HC studies, global upper air observations obtained from the Integrated Global Radiosonde Archive (IGRA) are used. A description on each of these datasets has

been provided in Chapter 2. As the year 1979 marks the beginning of inclusion of satellite observations into the reanalysis datasets which made them more reliable, the period of present study is from 1979 to 2012 for all the datasets.

The MSF metric is used in this study to closely track the atmospheric motions and hence, the HC edges and centre. The procedure to calculate the MSF metric from zonally averaged meridional wind data has been discussed in Chapter 2. The v-wind product from the reanalyses/IGRA is zonally averaged to calculate the MSF by means of the procedure outlined in Chapter 2. The reanalysis datasets are evaluated for their use in HC studies in the current study by means of observational data from IGRA using the method *'subsampling'* introduced by Waliser et al., (1999). In this technique, the reanalysis data is subsampled over the location of IGRA stations for the same period. Those data points in reanalysis data are selected where in-situ observations are available and MSF is calculated. The MSF from subsampled datasets are then compared with the MSF calculated from IGRA data in order to establish the reliability of reanalysis datasets for HC studies using the MSF metric. The MSF metric evaluated in this manner is thereafter used to determine the HC edge latitudes and centre. Following Stachnik and Schumacher (2011), HC edges are defined as the first latitude poleward of the cell centre where MSF at 500hPa becomes zero. These latitudes are determined for each hemisphere using a linear interpolation scheme, and annual cycle of the edges as well as centre is estimated, along with their monthly variability. The study also looks into the interannual variability in the zonal mean HC width to explore the trend in the poleward expansion of the HC.

3.3 Results and Discussion

3.3.1 Mass Stream Function and the HC edges

The MSF is estimated using all four reanalysis datasets by employing the procedure outlined in chapter 2. A qualitative comparison is carried out for winter (DJF) and summer solstices (JJA), and the vernal (MAM) and autumnal equinoxes (SON) with respect to the NH. Since the features are more pronounced during solstices than equinoxes due to the varied amount of insolation reaching

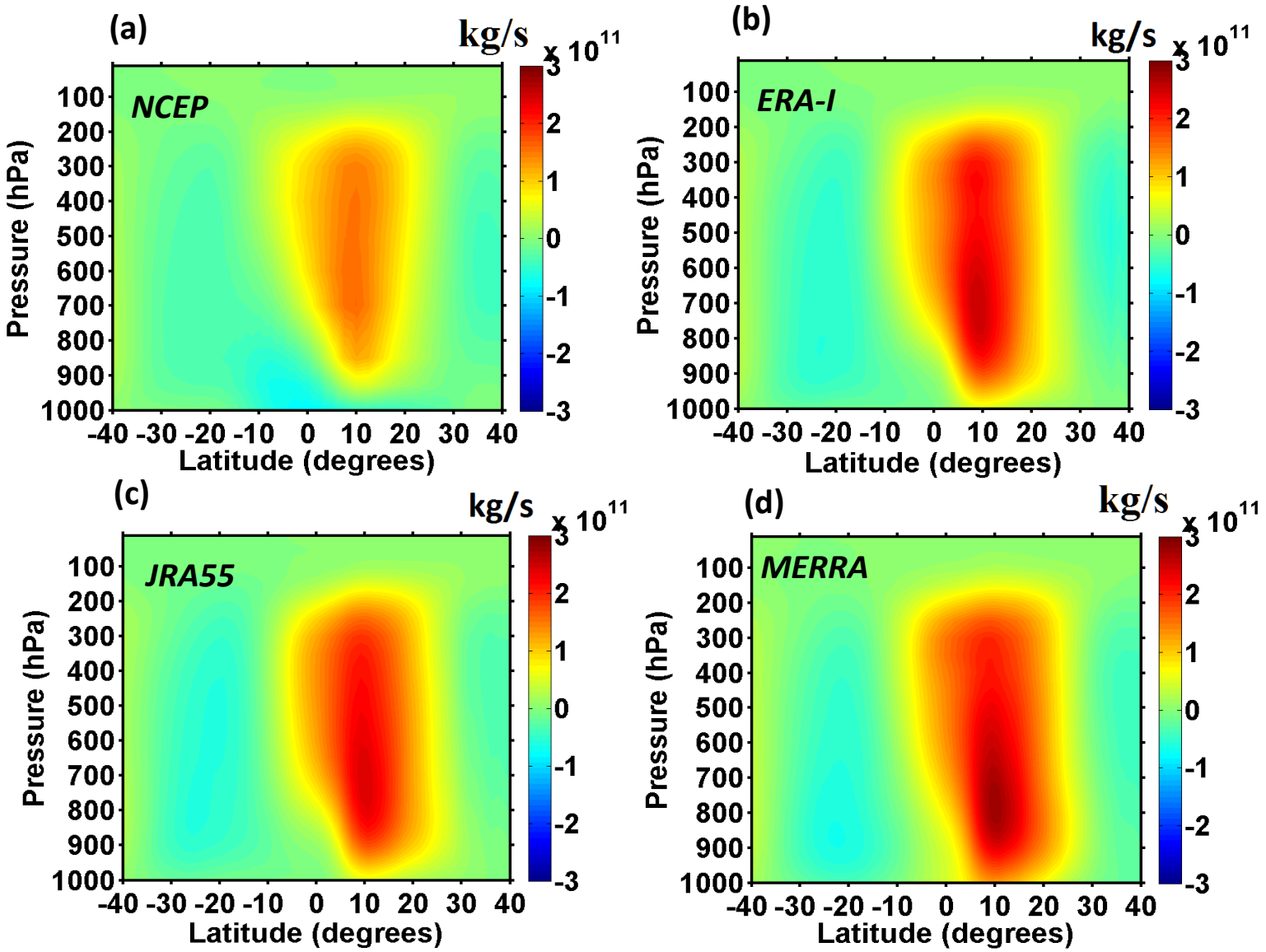

Figure 3.1: Mean meridional Mass Stream Function (MSF) for boreal winter estimated from (a) NCEP, (b) ERA-I, (c) JRA55 and (d) MERRA reanalysis datasets during the period 1979 to 2012.

each hemisphere during this period, the present study compares the MSF for solstices alone. However, MSF were computed for every month. Figure 3.1(a-d) shows the pressure- latitude section of MSF (in kg/s) for winter solstice using NCEP, ERA-I, JRA55 and MERRA reanalysis datasets respectively for the period 1979 to 2012. Figure 3.2(a-d) represents the same for summer solstice. From these two figures, it is evident that all the four reanalysis datasets reproduce the known gross features of HC. For instance, the rising limb is in SH ($\sim 9^0$S) during boreal winter and in NH ($\sim 17^0$N) during boreal summer in all the four datasets. In either hemisphere, it is clear that winter cell is stronger than their summer counterparts. This is because of the increased meridional temperature gradient during winter season (Goody and Walker 1972). The predominance of land regions in NH can also strengthen the winter cell due to increased surface friction and hence, increased angular momentum flux which is in turn balanced by an increase in the meridional velocity (Cook 2003). Summer cells are weakened by monsoon circulation in NH and by convergence zones in the SH (Karnauskas and Ummenhofer 2014). These are well known features of HC delineated using the MSF metric, and are in agreement among all the reanalysis datasets. However, there are a few discrepancies in the observed broad features among the reanalysis datasets. The summer cell extends well into the winter hemisphere at lower levels in NCEP data, which is not observed in other datasets. This can be an artefact of low vertical resolution of this dataset as this is removed upon interpolation of the number of levels.

As discussed in the Chapter 2, the MSF at 500hPa level is used for identifying the SH edge, centre, NH edge and total width of the HC. These quantities are segregated by month to construct their annual variations using 34 years of data. Figure 3.3(a-d) shows annual cycle of SH edge, centre, NH edge and total width of the HC respectively. The vertical bars indicate the standard deviation, which represents the inter-annual variability. The annual cycle of the observed quantities are found to be consistent with the current understanding of the HC dynamics, which validates the present algorithm for estimating MSF and identifying the HC edges.

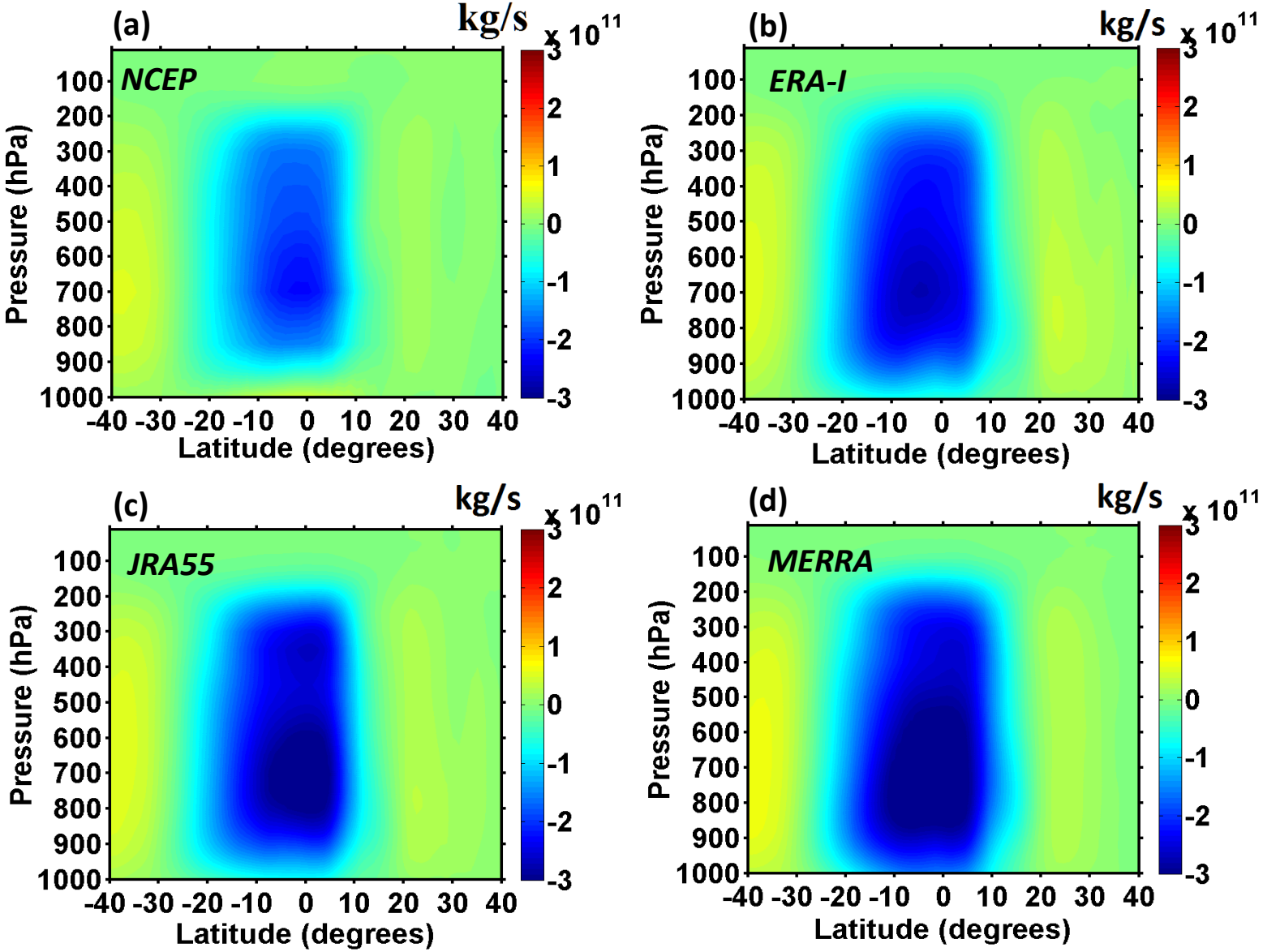

Figure 3.2: Same as figure 3.1 but for boreal summer.

Figures 3.3(a) and 3.3(b) draw a comparison between the poleward extent of HC in the northern and southern hemispheres, respectively. From figure 3.3(a) it is evident that the SH edge of HC is consistent among all the datasets with marginal discrepancies during the austral summer solstice and autumnal equinox. The annual cycle of NH edges also shows consistency among the four datasets with noticeable differences during the months April through June. Although the extent toward poles is expected to reach a maximum during the summer months of the respective hemisphere and a minimum during the respective winter months (Nguyen et al. 2013), deviations are seen to be present and is noticeable in the NH. Deviancy is that the minimum of poleward extent of NH edge does not occur during winter, but during the vernal equinox. It is evident from figure 3.3(b) that the interannual variability is large during the months of June and July, which is consistent among all four datasets. The maximum poleward extent of HC in NH ($\sim 40^0$ to 43^0 latitude) is reached during August and decreases thereafter; this is consistent across all datasets. SH shows a more or less steady and consistent pattern of the annual cycle of poleward extent, with maxima in February ($\sim 36^0$ to 38^0) and minima during June (July for JRA55 dataset). It is also clear from figures 3.3(a) and 3.3(b) that the maximum of poleward extent in NH is further poleward than the maximum of extent in SH. Apart from these minor discrepancies, the annual cycle of both northern and southern hemispheric HC edges shows consistent pattern among all the four datasets. The interannual variability, represented by vertical bars in the figures, is also in good agreement among the datasets.

Figure 3.3(c) shows the annual cycle of the centre of the HC, which is in fact the location of the ascending branch of the HC. Annual cycle of HC centre is in accordance with the seasonal shift in the latitude of average annual maximum of heating. The centre is far south ($\sim 14^0$S), during January-February, crosses the equator during April, and reaches far north ($\sim 20^0$N) during July-August months. Thereafter the retreat of the HC centre towards the south begins and the equator is crossed once again during November. Such kind of a motion is consistent among all the reanalyses, and is very much similar to the present understanding of the HC. Very low inter-annual variability of the HC centre is suggestive of consistency of the location of the rising limb of the HC, year after year. The annual

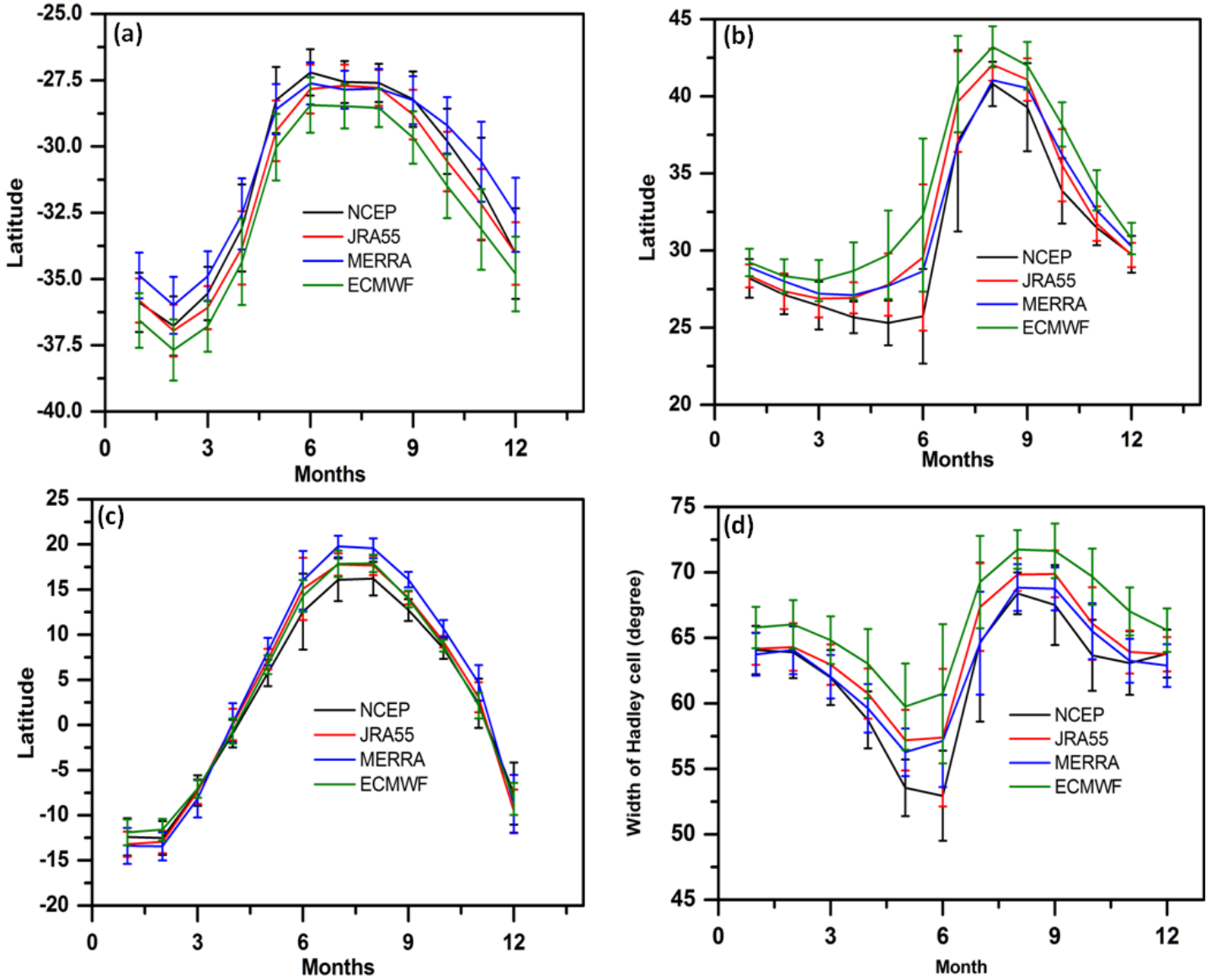

Figure 3.3: Annual cycle of (a) SH edge, (b) NH edge, (c) Centre and (d) Total width of the HC derived from four reanalysis datasets. Vertical bars indicate the standard deviation depicting the interannual variability.

cycle of the HC centre and its inter-annual variability is also consistent among the four datasets. Figure 3.3(d) shows the total width of the HC, which is obtained by adding the SH and NH edges of the HC shown in figures 3.3(a) and 3.3(b) respectively. From this figure, it is noted that the total width is maximum ($\sim 70^0$) during August-September and minimum ($\sim 55^0$) during May-June. As the location of NH summer HC edge is more poleward than that of SH summer cell, the total width during NH summer is more as compared to the SH summer. A similar pattern has been suggested by Davis and Birner, (2013) also, using the ERA-I dataset. Thus the MSF-based HC characteristics derived using the four reanalysis datasets show consistent annual cycles in SH edge, NH edge, centre, and total width of the HC, with their interannual variations also comparable.

3.3.2 Comparison between Reanalyses and Radiosonde observations

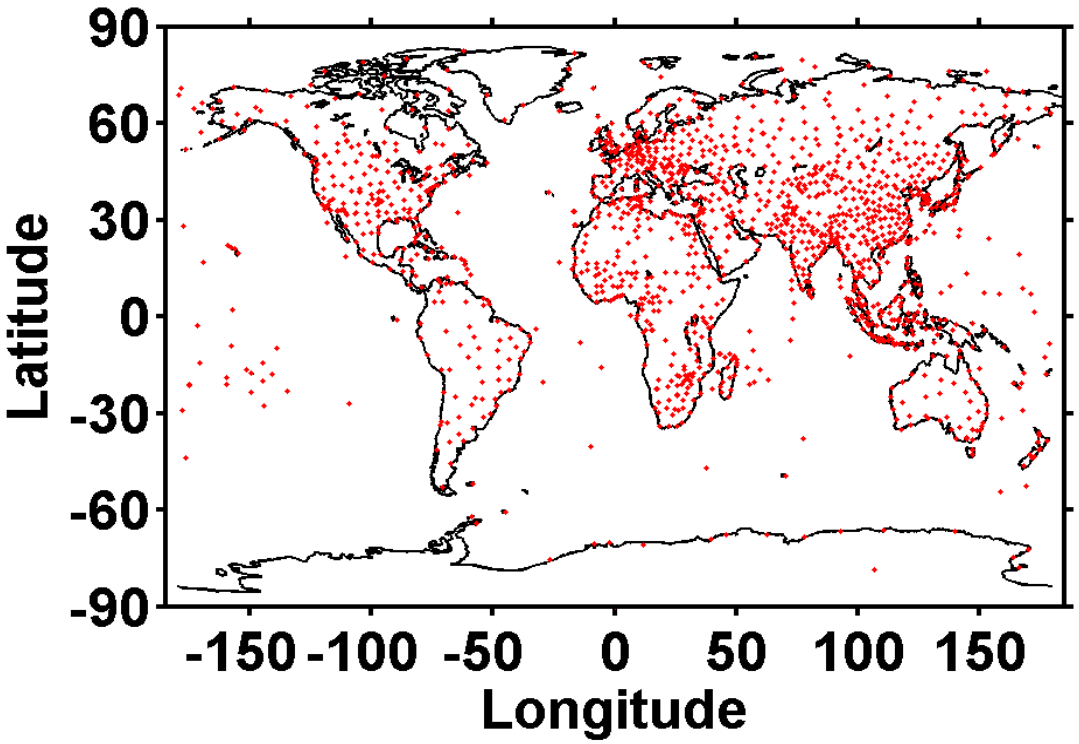

Figure 3.4: Geographical distribution of radiosonde stations included in IGRA.

Even though the reanalysis datasets are used extensively to study the climatological features of the many atmospheric processes, there is a need to evaluate these datasets from time to time using observations (Mathew et al. 2016). It is also essential to examine whether reanalysis datasets are suitable for studying particular atmospheric phenomenon for example, the HC. As mentioned

in the section 3.1, Waliser *et al.*, (1999) compared the NCEP datasets with operational radiosonde network observations. In the present study, we compare the four reanalysis datasets mentioned in section 3.2 with IGRA observations qualitatively. Figure 3.4 shows the geographical locations of IGRA stations. From this figure, it is evident that NH has more coverage as compared to SH. Only those stations are selected whose data record spans the period from 1979 to 2012.

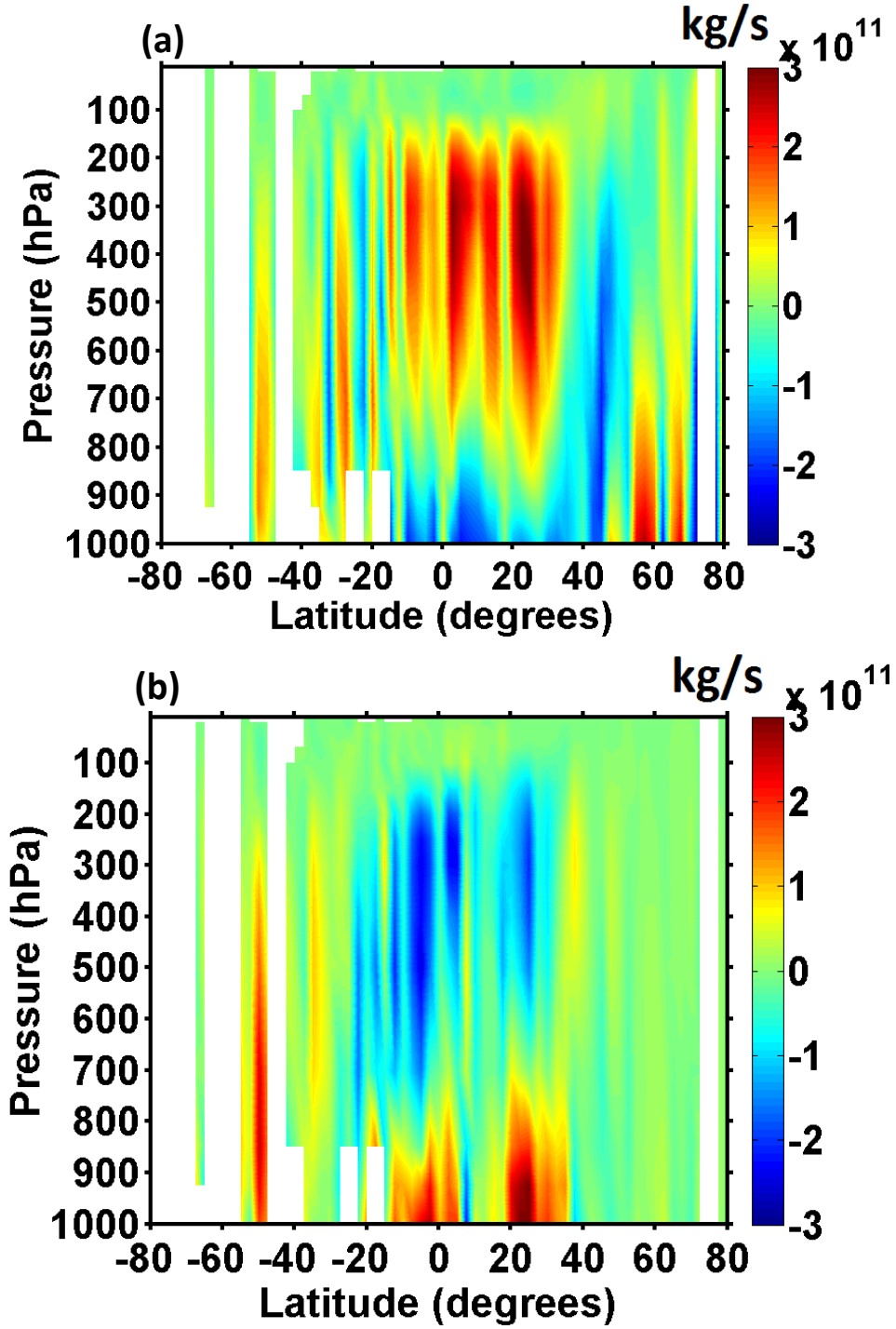

Figure 3.5: Mean merdional Mass Stream Function (MSF) obtained from IGRA during the period 1979 to 2013 for (a) boreal winter and (b) boreal summer.

MSF is calculated from the monthly meridional wind data obtained from IGRA over the above time span for boreal winter (DJF) and boreal summer (JJA). The pressure-latitude sections of MSF for each of these seasons are shown in figures 3.5(a) and 3.5(b), respectively. The data gaps in the SH occur as a result of scarcity of observations over oceans. Abrupt transitions in these two figures, in contrast to the smooth transitions in reanalyses datasets, arise as a result of the spatial inhomogeneity of the radiosonde dataset. The winter and summer cells cannot be distinctly identified in these figures as a result of the sharp transitions and data gaps; however the features above ~800hPa in these figures show signatures of the HC. For instance, a clockwise circulation is predominant above ~800hPa during DJF (figure 3.5(a)), while an anticlockwise circulation is predominant at the same level during JJA (figure 3.5(b)). The HC centre cannot be clearly made out in these figures for the reasons mentioned earlier.

After estimating the MSF using radiosonde observations using the subsampling procedure detailed in section 3.2, the MSF were estimated from reanalysis datasets and is shown in figures 3.6(a-d) and 3.7(a-d) for boreal winter and summer, respectively. The figures 3.5, 3.6 and 3.7 together draw a comparison of MSF obtained from the subsampling of the four reanalysis datasets - MERRA, JRA55, NCEP and ERA-I with the IGRA data for DJF and JJA, respectively. From these figures, it is evident that the large-scale features in the subsampled reanalyses datasets are very much similar to that in the radiosonde dataset except for the sharp transitions in the observations. However, there are discrepancies in the magnitude of MSF derived from IGRA and reanalyses datasets. The circulation features in a subsampled dataset are, in fact, found to be weaker than that in IGRA for boreal winter. For boreal summer, the reverse is true. The features in the MSF obtained from subsampled datasets are also comparable among each other; and variations, if at all present, occur in terms of the magnitude. High resemblance of the subsampled reanalyses datasets with global radiosonde dataset, thus, substantiates the fact that reanalysis datasets employed in the present study can be a worthy tool for characterising the HC dynamics. As mentioned earlier, the use of reanalysis datasets for a given study should be substantiated by evaluating them with observations. For the first time,

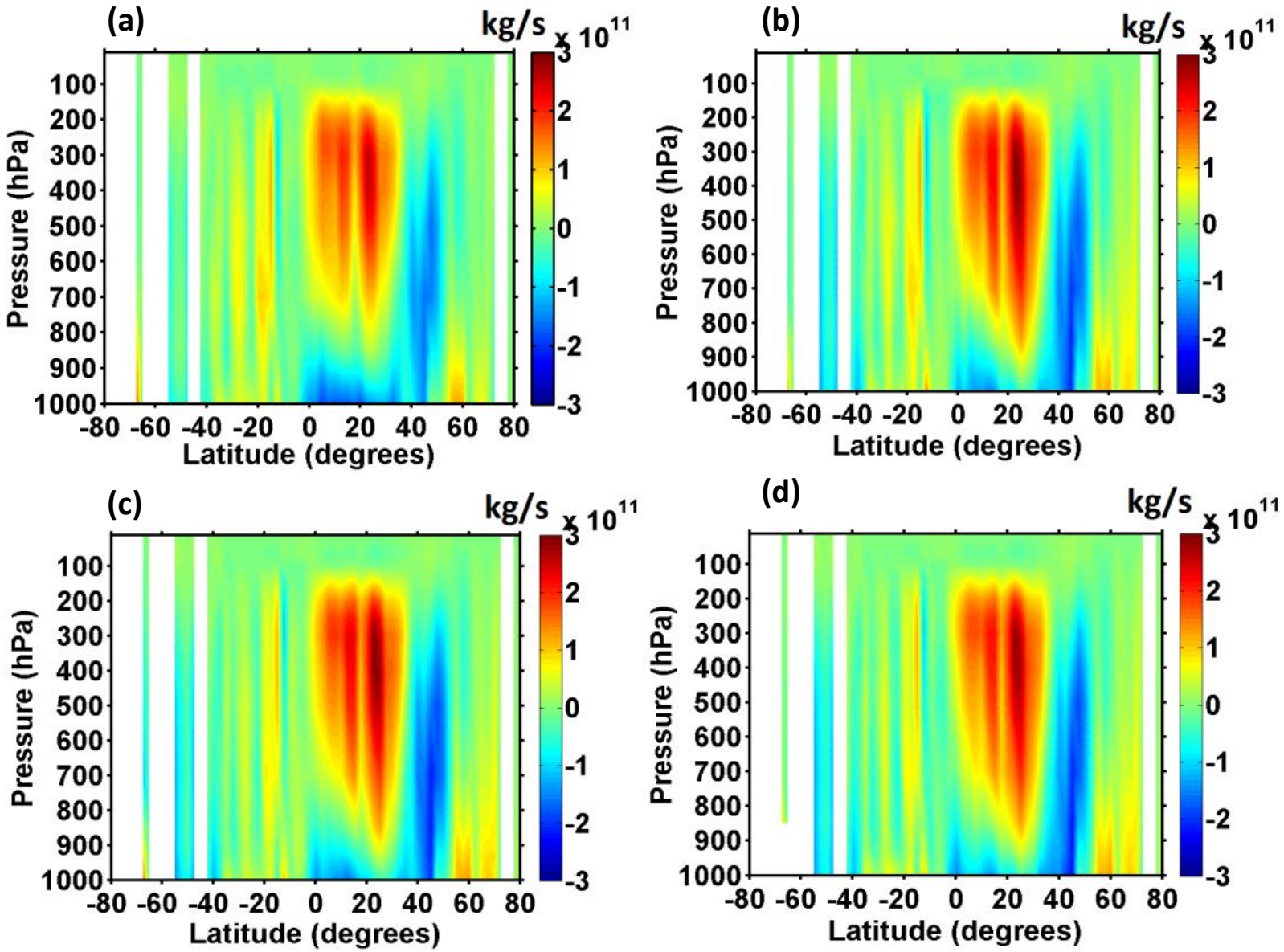

Figure 3.6: MSF obtained from subsampled reanalysis datasets of (a) NCEP, (b) ERA-I, (c) JRA55 and (d) MERRA for boreal winter.

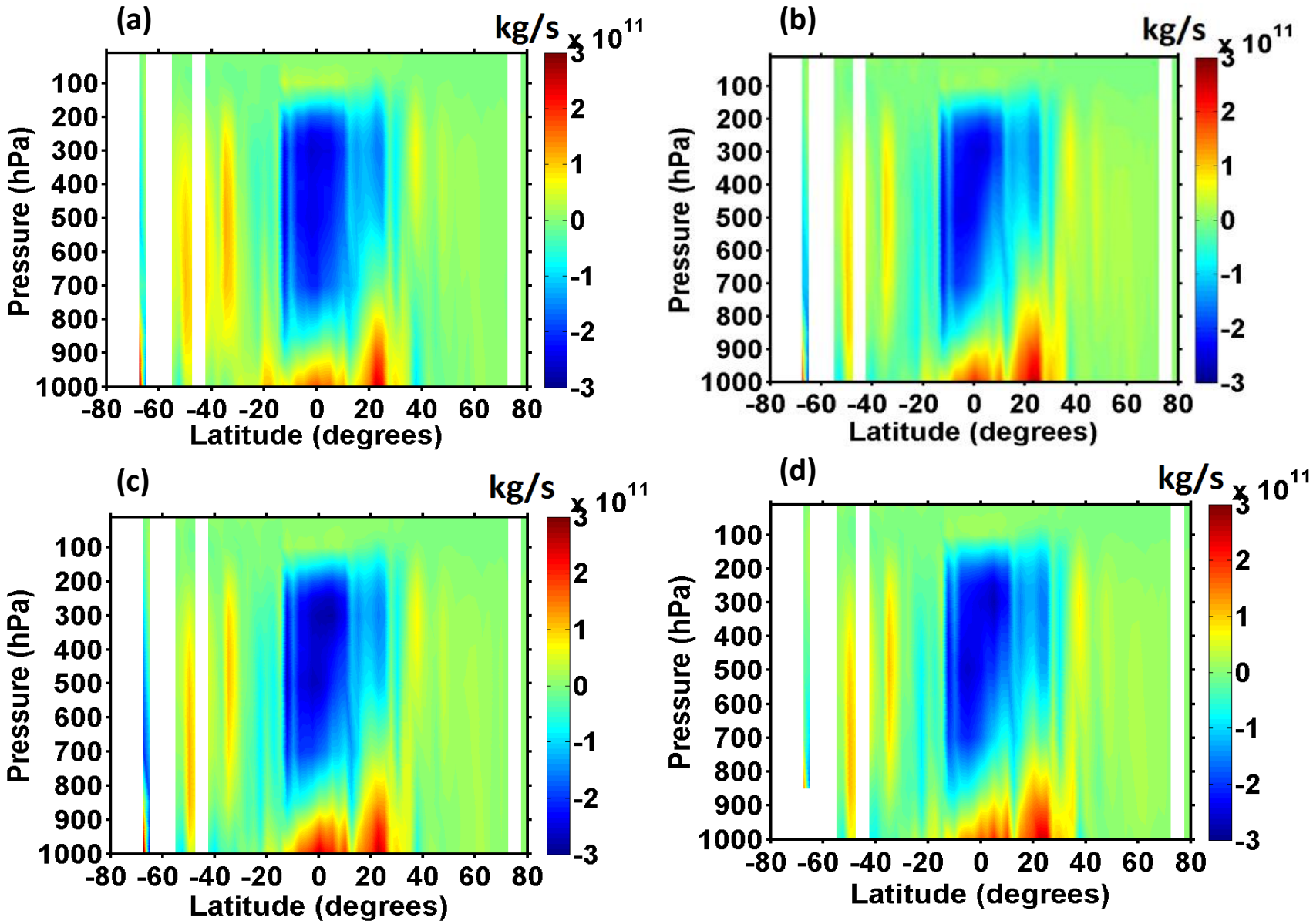

Figure 3.7: Same as figure 3.6, but for boreal summer.

the MSF estimated using MERRA, JRA55, NCEP and ERA-I are verified with observations for general circulation studies using the subsampling procedure outlined by Waliser *et al.*, (1999).

3.3.3 Interannual Variability and Trends in HC width

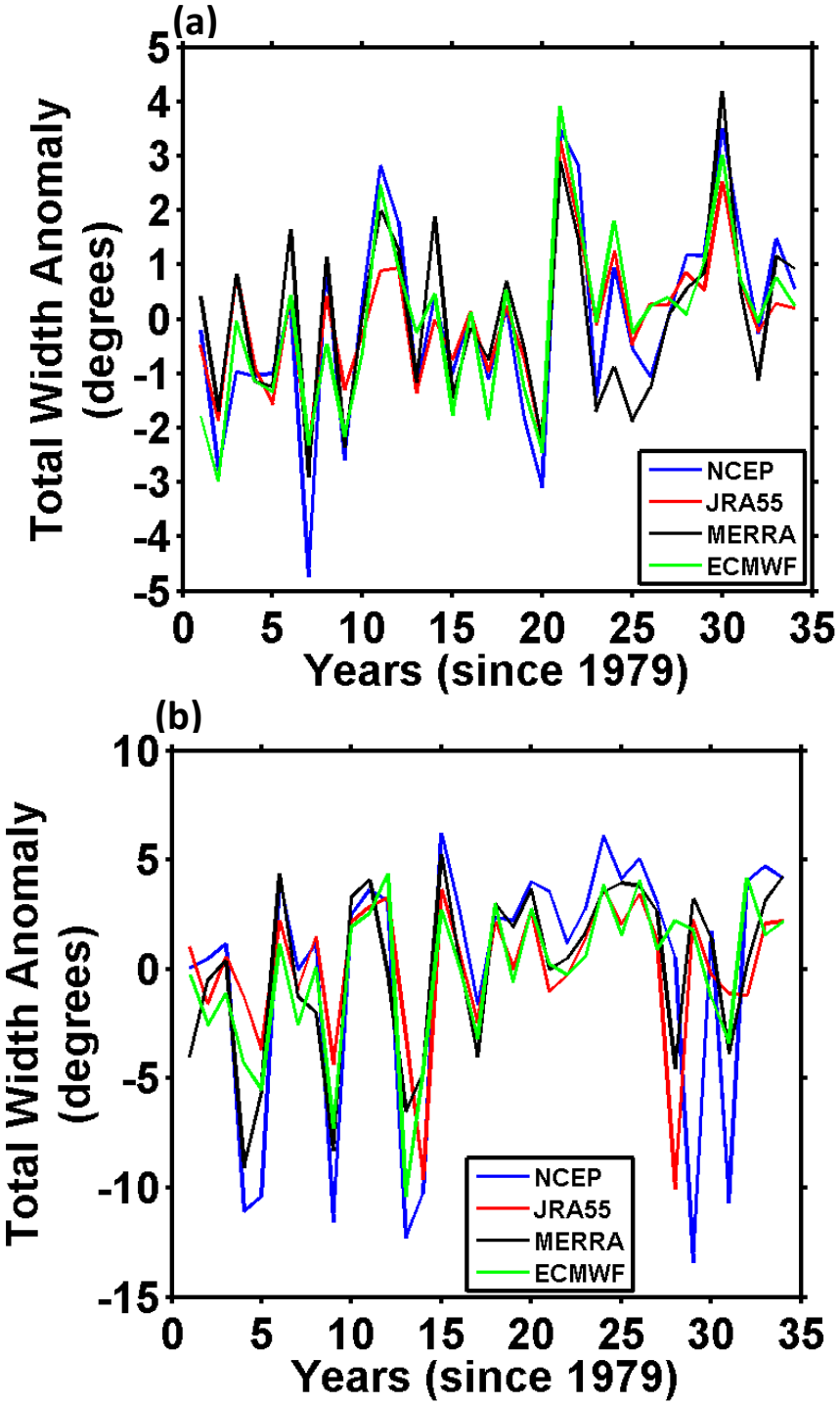

Figure 3.8: Time series of anomaly in the total width of HC for the month of (a) January and (b) July obtained using four reanalysis datasets during 1979-2012.

As discussed in Chapter 1, there were many studies on estimation of trends in HC width using observations, reanalysis datasets and climate models. However, most of them have focused on trends in annual and seasonal mean HC width. The present study attempts to estimate the monthly trends in total width of HC using the procedure outlined by Santer et al. (2000). In order to identify this trend, interannual variability in the total width of the HC for 34 years and their anomaly is first calculated. Year to year variability in the total width of the HC sheds light upon the long term changes that have occurred to the meridional extent of HC over a 34 year period. Figure 3.8 shows an inter-comparison of the anomalies in the total width of HC for the months of January and July among four reanalysis datasets for a period spanning the years 1979 to 2012. Positive value for the anomaly shows expansion of the HC, and a negative value shows contraction with respect to mean width of the HC.

It is clear from the figures 3.8(a) and 3.8(b) that the expansion in a given year is followed by a tendency towards contraction in the next year, and a further expansion in the succeeding year. This process repeats across all datasets although the magnitudes differ. Generally a tendency towards expansion has occurred in 34 years since 1979. The figures depict that the yearly transitions are smooth as well as consistent among the datasets during the month of January. However in July, the case is different. Interannual variability of the total width anomaly becomes larger, and the consistency amongst the datasets is reduced during the month of July. The deviations are pronounced in the case of NCEP data, wherein the width anomalies are showing large negative values. Still there is a net tendency towards expansion in NCEP data as well as in the rest of the datasets noticeable during the months of January and July. One more interesting aspect revealed by the interannual variation of total width anomaly shown in figure 3.8 is their periodic oscillations. A varying periodicity can be noticed during both January and July. To quantitatively know the periodicities in the observed oscillations, the time series of total width anomalies for each month derived from all the four datasets are subjected to Fourier analysis. It is noticed that the prominent periodicities varied from one season to other, and also varied among the datasets. However, most of the datasets showed a prominent periodicity with significant amplitude in the 4-8 year band during the boreal

summer and 2-3 years during boreal winter (figure not shown). The source mechanisms for the observed periodicity are not well known, except that the 2-3 year band is close to quasi biennial oscillation which is prominently observed in the equatorial stratosphere.

The time series of anomaly in the total width of the HC has been constructed for the each month and the linear trends are estimated using least-square fitting procedure. The trend (per decade) in the variability of total width of the HC for each month is quantitatively represented in figure 3.9. The vertical bars in the figure indicate the 95% confidence intervals estimated using the method of Santer, (2000).

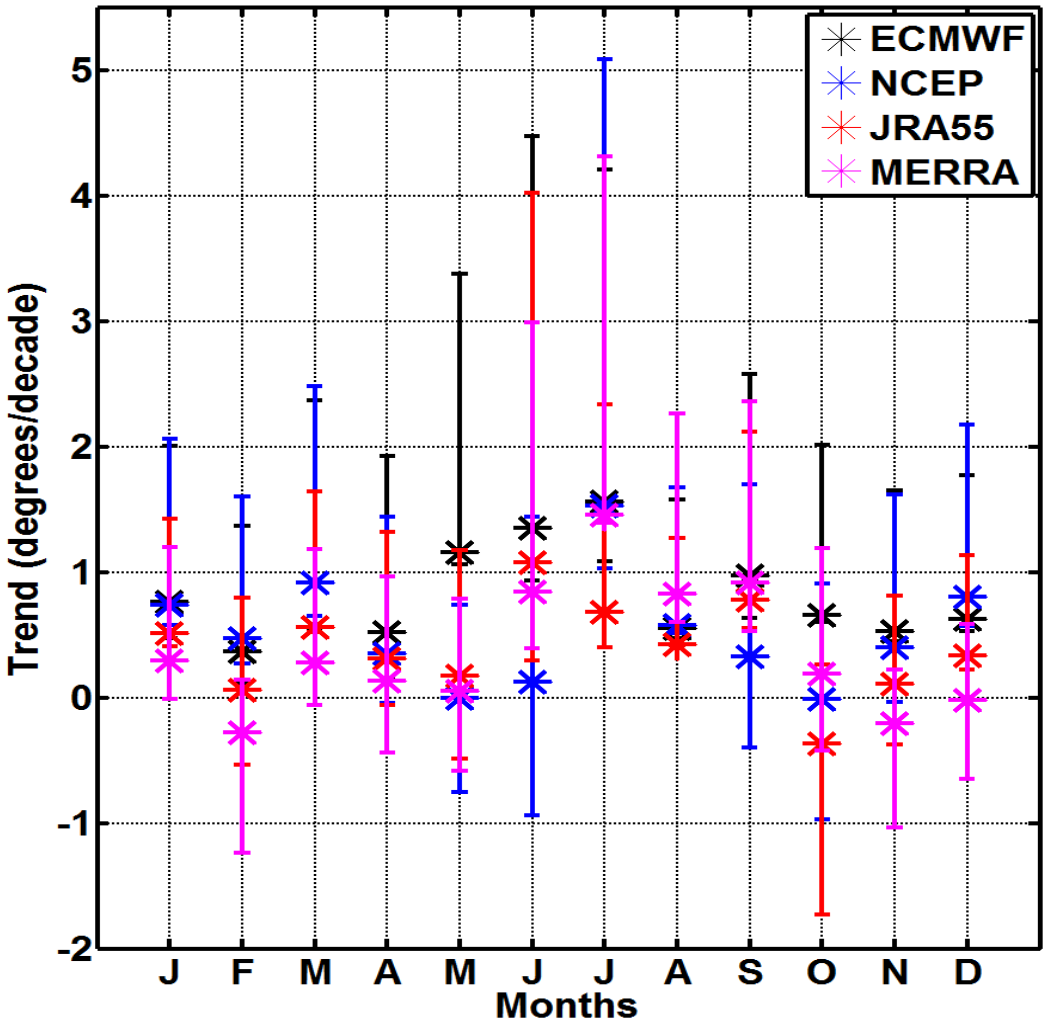

Figure 3.9: Monthly trend (in degrees per decade) in the total width of the HC calculated for NCEP, JRA55, MERRA and ERA-I datasets. Vertical bars represent the 95% confidence intervals of the estimated trend.

The trends estimated using four reanalysis datasets show consistent annual pattern with trends being positive during most of the months. Exceptions include the MERRA dataset, which shows negative trends during the months of February and November, and the JRA55 dataset, which shows negative trend during the month of October; all the other datasets show positive trend in the total width of the HC. The trend towards expansion is on the rise during the months of June and July for all the datasets. During the month of June, all datasets other than NCEP show an expansion close to 1^0 latitude per decade. The NCEP dataset shows maximum expansion during the month of July, which is $\sim 1.5^0$ latitude per decade. This expansion rate is also consistent with all other datasets, except for JRA55. Thus from figure 3.9, it can be noted that maximum expansion of the HC is observed in the month of July, which is consistent in three reanalysis datasets (NCEP, MERRA and ERA-I). According to this trend pattern for the month of July, the HC has expanded $\sim 5.1°$ in the past 34 years. The confidence intervals of trend obtained for few datasets include the zero, which indicates that null hypothesis cannot be neglected in these cases. However in the month of July, where maximum expansion of the HC is observed in three out of four datasets, the 95% confidence interval derived from all four reanalysis datasets show significant trend. The present study thus provides unambiguous climate change indicators in terms of the HC expansion, which is envisaged to have profound climate implication especially over subtropics.

3.4 Summary

The present study characterized the HC in terms of its centre, NH and SH edges using relatively new JRA55 reanalysis dataset and three widely used reanalysis datasets (NCEP, MERRA and ERA-I) by employing MSF metric. Using subsampling technique, the MSF metric estimated using reanalysis datasets are evaluated with radiosonde observations as reference. The poleward expansion of the HC has been brought out by means of trend analysis. The following are the concluding remarks brought out from the present study:

1. A qualitative comparison of MSF among all the reanalysis datasets for winter and summer solstices reproduces the well-known features of the HC. Annual cycle of the NH and SH edges, centre and total width of the HC

has been analyzed, and considerable consistency with present knowledge on the same has been found. This serves to validate the algorithm that has been developed to estimate the MSF as well as edges of the HC.

2. It has been found that the annual cycle of HC edges in both hemispheres, its centre, as well as its total width are consistent among the datasets, with interannual variability also being comparable. These results brought out the consistency among reanalysis datasets in characterizing the HC.
3. The maximum poleward extent of HC in NH ($\sim 40^0$ to 43^0 latitude) is found during August and in SH it is found during February ($\sim 36^0$ to 38^0 latitude). The annual cycle of HC centre is found to be in accordance with the seasonal shift in the latitude of average annual maximum of heating. The results showed that the total width of HC is maximum ($\sim 70^0$) during August-September and minimum ($\sim 55^0$) during May-June.
4. The four reanalysis datasets has been compared with radiosonde observations from IGRA, for the first time, using the subsampling technique outlined by Waliser *et al.*, (1999). Large scale features in the subsampled datasets show high resemblance with the IGRA dataset, reinforcing the fact that reanalysis datasets can be used for studies on the global circulation, and the HC in particular.
5. Interannual variability in the total width of the HC has been charted out for each month in order to bring out the monthly trend towards expansion of the HC. It has been found that during the month of July, the trends obtained at the 95% confidence interval derived from all the four reanalysis datasets are significant, and that the observed expansion trend (1.5^0 latitude per decade) is consistent for three among the four reanalysis datasets used, the exception being JRA55.

Thus, the current study has brought out the poleward expansion indications in HC using JRA55, NCEP, MERRA and ERA-I datasets. It is envisaged that the present results will bring more credibility for the reanalysis datasets in evaluating the HC dynamics.

CHAPTER 4

REGIONAL FEATURES OF THE HADLEY CIRCULATION: A TROPOPAUSE PERSPECTIVE

4.1 Introduction

As described in Chapter 1, the geophysical parameters used for determining the tropical/Hadley cell expansion includes a wide range of atmospheric phenomena such as changes in precipitation patterns, shift in subtropical jet streams (STJ), shifts in the Hadley cell edges inferred from meridional mass stream function (MSF), changes in total column ozone, differences in the outgoing long-wave radiation (OLR), and tropopause height changes (Reichler 2009). Many of the above mentioned metrics have given evidence on tropical widening from a zonally averaged point of view. However in reality, the difference in land-sea distribution and topography can modulate diabatic heating, potentially causing the expansion rates to vary from region to region. For instance, Chen et al. (2014) have reported the HC expansion rates over six locations *viz.,* Africa, Indian Ocean, Atlantic, Eastern Pacific, Western Pacific, South American regions, using OLR, vertical and horizontal velocities and precipitation. The aim was to identify the regions which make the maximum contribution to the zonal mean HC expansion in both hemispheres. In the study, the authors identified that expansion of the SH zonal mean HC is mainly driven by the expansion of the South American regional HC. These kind of regional variations, largely arising due to the inherent topography differences and land-sea contrast along a longitudinal belt, are masked when one uses the zonal-mean metrics for identifying the HC expansion. The need of the hour is, thus, a zonally resolved metric that can be used globally to identify the longitudinal variability of the HC edges (Mathew and Kumar 2018a). Again, the wind-based metrics such as STJ, MSF and velocity potential suffer from uncertainties inherent to reanalysis as there are no space-based

global wind measurements available for the tropical lower atmosphere. Although metrics such as OLR and precipitation are globally measurable, these have subjectivities in defining the HC edges in terms of the thresholds. A longitudinally averaged metric is therefore not adequate to derive reliable regional expansion trends of the tropics. There have been some attempts in the past to focus on a measurable metric that can be employed to investigate the regional features of the tropical belt (Baines 2006; Seidel and Randel 2007; Chen et al. 2014) which is still a poorly explored area of the HC dynamics. The present study is focused on inferring the regional features of width of the tropical belt using space-based observations of a measurable objective metric.

In this context, the tropopause height seems to be one of the promising 'measurable' metrics, with a global character and better accuracy, in order to study the width of the tropical belt and its expansion. However before it can be used to identify the edges of the HC, it needs to be justified whether the HC edges identified by means of the tropopause metric and that identified by the wind-based MSF metric are one and the same. Earlier studies have used the edge of the tropics and that of the HC synonymously as both are theoretically related. For example, as the poleward branch of HC flowing from the tropical upper troposphere approaches the subtropical region, a subtropical jet stream develops at the flanks of the HC so as to conserve the angular momentum. The subtropical jet stream, on the other hand, is also related to the region of high baroclinicity where the tropopause break is observed. This aspect has been discussed in Davis and Birner (2016). Hence the edges of tropics and the HC are theoretically related. As of now, there are many studies which have used tropopause as a metric for inferring the width of the tropical belt (Seidel and Randel 2007; Birner 2010; Wilcox et al. 2012; Davis and Birner 2013). However some studies have been skeptical on the co-variability of the tropopause-based and wind-based metrics to identify the HC edges (Solomon et al. 2016; Davis and Birner 2017). It will be shown later in this chapter that they co-vary and represent the same (see section 4.3.5). The current chapter, hence, use the words 'tropical belt' and 'Hadley Cell' interchangeably.

Among the various definitions of tropopause, the Lapse Rate Tropopause (LRT) can be calculated from atmospheric temperature profiles and can be applied globally. Hence, it turns out to be a well suited parameter for tropical expansion studies. LRT is defined as the lowest point at which the lapse rate decrease to 2K per km or less, and the average lapse rate within the next higher 2km does not exceed 2K per km (WMO definition, 1957). Studies in the past have used the LRT in several ways to identify the tropical expansion. A simple LRT metric for tropical expansion studies makes use of the fact that the tropopause is bimodal in the subtropics, i.e., >15km in the subtropical locations closer to the equator and <13km in the subtropical locations closer to the mid-latitudes (Seidel and Randel 2007). According to the tropopause height frequency (THF) methodology, if the frequency of occurrence of LRT height >15km for any subtropical latitude exceeds '*x* ' days per year (*x*=200, typically), the given latitude is regarded as tropical (Seidel and Randel 2007). However, this method has a few shortcomings. Firstly, the method is sensitive to the choice of arbitrary thresholds (Birner 2010). Secondly, these studies were based on radiosonde measurements of vertical profiles of temperature from various geographical locations. The sparsity of radiosonde observations for long term upper air measurements, especially over the oceans, limits the determination of a reliable expansion trend using the tropopause metrics. While the former shortcoming can be addressed by means of an objective approach to define the edge latitudes (Davis and Rosenlof 2012), the use of space-based observations such as Global Positioning System Radio Occultation (GPS-RO) soundings can help in case of the latter (Ao and Hajj 2013). In the past decade, GPS-RO soundings has become the best remote sensing measure of thermal structure of the tropopause region with its high vertical resolution (<1km), greater accuracy, long term stability, all weather capability, and above all, a good global coverage (Ao and Hajj 2013; Rieckh et al. 2014). The characteristics of various tropopause parameters using GPS-RO has been explored in detail by Rieckh et al. (2014), and the seasonal variations in LRT has been examined by Liu et al. (2014).

In addition to providing a global coverage, high vertical resolution of the GPS-RO measurements also resolves the tropopause parameters in a better way. There are limitations in identifying the HC edges using tropopause metrics with

arbitrary thresholds (Birner 2010; Davis and Rosenlof 2012). These shortcomings were successfully addressed by Davis and Rosenlof (2012), Davis and Birner (2013) and Ao and Hajj (2013) in their studies. One of the objective approaches proposed by Davis and Rosenlof (2012) was an 'extrema' method using reanalysis data, wherein the latitude of maximum meridional gradient of LRT height is identified as the edge of the tropics. This metric will be referred as the *'tropopause gradient (TpGr)'* in the present study. Davis and Birner (2013) introduced yet another objective tropopause-based metric known as the tropospheric *dry bulk static stability (BSS)* using GPS-RO measurements, which maximize near the subtropical tropopause breaks. The present study uses the *TpGr* metric as well as the *BSS* metric for delineating the zonally resolved features of the width of the tropical belt for the first time.

The above discussion emphasizes the fact that space-based temperature profile observations in the lower atmosphere inferred by the GPS-RO technique is one of the most promising methods to investigate tropical belt characteristics using the tropopause metric. It has also emerged from the earlier discussion that there is a need for zonally resolving the width of the tropical belt in order to investigate its regional variations. The present study examines both these ideas by means of the tropopause-based metrics. Until this point of time, longitudinal variability of the HC edges have been reported using the OLR and precipitation metrics (Baines 2006; Chen et al. 2014). The current study attempts to look into the zonal variations of the meridional HC from the perspective of tropopause height variations. Two of the existing metrics are used in this effort. These are (1) the latitude of maximum meridional gradient in tropopause height, called the *'tropopause gradient (TpGr)'* in the present study, and (2) '*tropospheric bulk static stability (BSS)*' metric, which is the latitude of maximum tropospheric dry bulk static stability. As discussed before, these metrics have been already proven helpful in determining the long term changes to the zonal mean HC width. The present study attempts to point out the suitability of these metrics as indicators of regional HC width. In addition to *TpGr* and *BSS* metrics, the current study also proposes a new tropopause-based metric that can be a proxy to identify the longitudinal variations of the width of the tropical belt. The newly proposed metric is called the *'tropopause annual oscillation (TpAO)',* which is the latitude of

maximum annual oscillation/variability in tropopause height. The motivation behind using three tropopause-based metrics is to verify their robustness in delineating the zonal structure of tropical belt edges. All the three metrics are evaluated by means of a comparison with the meridional mass stream function (MSF) metric, estimated from a reanalysis dataset. The central objective of the present study is thus to evaluate tropopause-based approach for studying the regional features of the width of the tropical belt/HC using radio occultation measurements. The data used and the method followed in the present study is provided in section 4.2, section 4.3 discusses the results, and section 4.4 summarize the results.

4.2 Data and Methodology

The present study uses the GPS-RO data from the Formosa Satellite Mission#3 (FORMOSAT3)/ Constellation Observing System for Meteorology, Ionosphere and Climate (COSMIC) mission. Details on the COSMIC mission and the GPS-RO technique for retrieval of atmospheric parameters have been given in Chapter 2. Basically, the GPS-RO technique involves measurement of time delay in receiving a signal transmitted by GPS satellite by a LEO satellite. The measured time delay is used to infer the bending angle of the signal by making use of orbital geometry. From the bending angle, atmospheric refractivity can be derived. Subsequently, geophysical parameters such as pressure, temperature and humidity are retrieved. However humidity is not an independent measurement of GPS-RO, but is constructed via a 1D-VAR scheme. As mentioned in Chapter 2, vertical resolution of the GPS-RO data is 100m, extending up to 40km in the atmosphere. The temperature profiles derived from COSMIC have an accuracy better than 0.5K (Kurisinski et al. 1997). Seven years of COSMIC derived temperature profiles (wetPrfdata) from 2007 to 2013 are used in the present study. In addition to the COSMIC data, ECMWF Reanalysis-Interim (ERA-I) data (resolution 1.5^0 x 1.5^0 x 37 levels) from 2007 to 2013 are used for evaluating the proposed metrics.

Based on the WMO definition (WMO 1957), the LRT height is derived from each of the COSMIC measured temperature profiles and grouped in 2.5° latitude X 10° longitude grids for each month and for a span of 7 years (2007-2013). It is observed that in a given month on 2.5° latitude X 10° longitude grids there are, on

an average, 30-40 temperature profiles in deep tropics (10^0S-10^0N), 60-90 profiles in 20^0N(S)-70^0N(S) latitudes and 10-20 profiles in polar latitudes. These statistics have been obtained after removing some odd profiles, which show very large deviations from the mean profile. Latitudinal gradient of LRT heights are computed to derive the *TpGr* metric. The *BSS* metric is arrived at by taking the difference between the potential temperatures at the tropopause and the surface. The surface potential temperature is calculated by taking the temperature and pressure measurements of the lowest altitude for each profile, following Davis and Birner (2013). The newly proposed *TpAO* metric is identified based on the observed amplitude of the monthly LRT perturbation with respect to its annual mean. In order to derive this metric, the perturbations of monthly mean LRT height from its annual mean are determined for each 2.5^0x10^0 grid. The locations of maximum perturbation are then identified as the edge of the tropical belt. The zonally resolved width of the tropics is determined from all three tropopause-based metrics. Further, the zonally averaged width of the tropical belt identified by means of these metrics are compared against the total width obtained from the zonal mean MSF metric using the ERA-I reanalysis dataset (Dee et al. 2011). The monthly meridional wind data from the ERA-I reanalysis is chosen for the period 2007-2013 and the zonally averaged MSF is calculated using the method described in Chapter 2. The first latitude poleward of the cell centre where MSF at 500hPa becomes zero is taken to be the edge of the tropics (Hu and Fu 2007; Stachnik and Schumacher 2011), and are identified for each hemisphere by means of a linear interpolation scheme.

4.3 Results and Discussion

4.3.1 Global Tropopause Characteristics and its Seasonal Variability

Seven years (2007-2013) of COSMIC measurements of temperature profiles over the entire globe are used to construct the mean climatology of LRT heights. Figure 4.1(a-d) shows the global variation of LRT height for four seasons, viz. boreal winter (DJF), vernal equinox (MAM), boreal summer (JJA) and autumnal equinox (SON) respectively. The well-known meridional gradient of tropopause height is discernible in these figures, with exceptions occurring based on geography and the season under perusal (Schmidt et al. 2005; Son et al. 2011). As expected, the LRT height >15km is mostly limited to the 20°S-20°N latitudinal

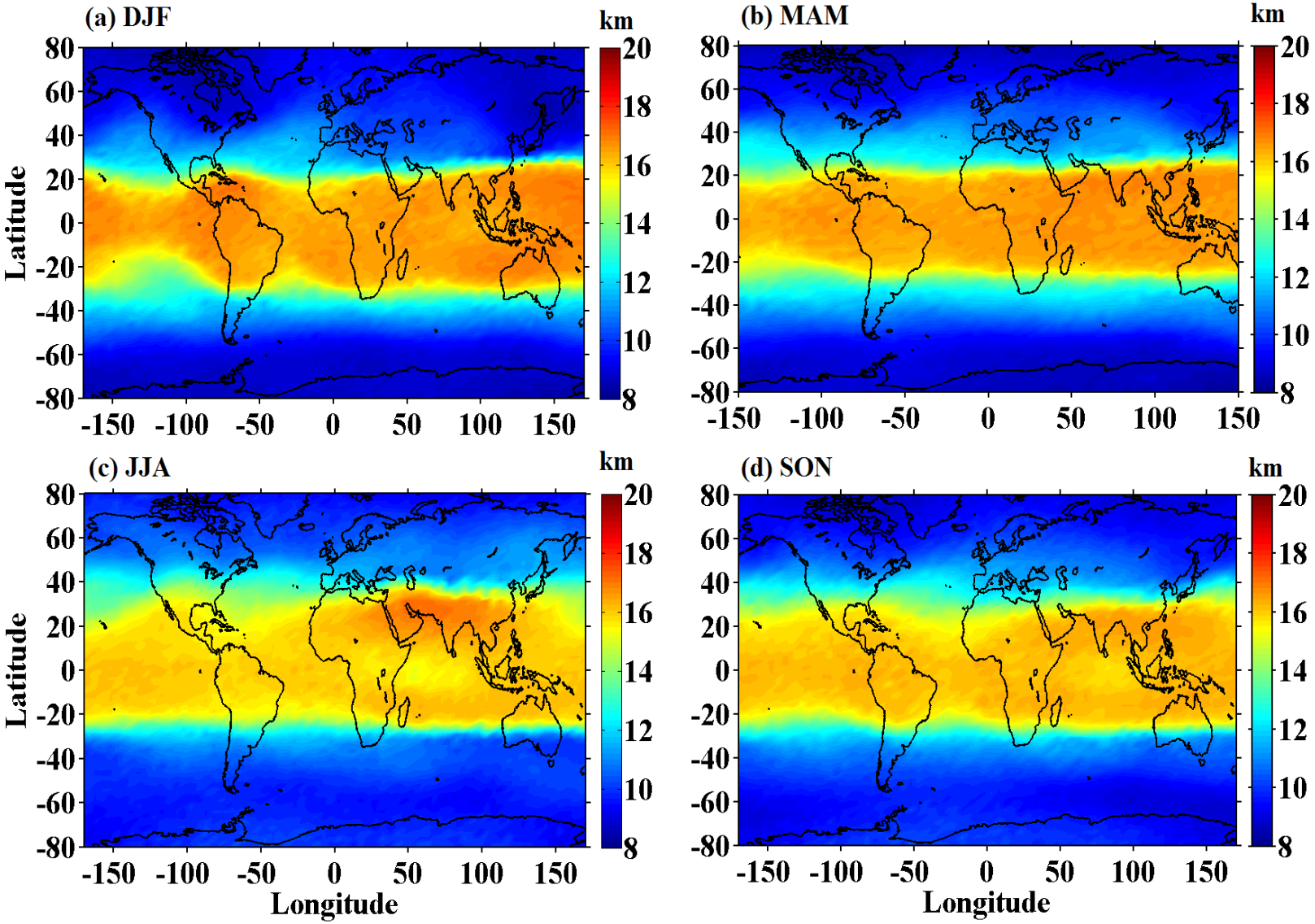

Figure 4.1: Global distribution of seven year mean LRT height (in km) for four seasons, viz. (a) DJF, (b) MAM, (c) JJA and (d) SON.

belt. The average LRT height during NH summer over the tropics is ~16km, whereas it is relatively high (~18km) over the region of Indian Summer Monsoon. These observations are consistent with earlier reports on LRT features using space-based observations. LRT heights are relatively less during summer than winter in the tropical latitude belt because of the decreased planetary wave activity over mid and high latitudes which results in a weak Brewer-Dobson circulation (Rieckh et al. 2014). However, LRT heights remain high over the Indian Summer Monsoon regime as a result of the high heating over the Tibetan Plateau and the resulting circulations and deep convection activities. One more interesting feature that can be noted in the LRT height variation during boreal winter depicted in figure 4.1(a) is that the latitudinal span of tropical LRT height >15km in the 100°W-130°W longitudinal belt is relatively very narrow as compared to other longitudinal belts. This feature is observed clearly in boreal winter and to some extent during vernal equinox, but not observed during the other two seasons. The reason behind this narrowing of LRT>15km region during boreal winter has not been explicitly reported earlier; further investigations are needed to address this issue. Beyond 50° latitude, in both hemispheres, the LRT heights are <10km. Confined between these latitudes and the tropics is the sub-tropical zone, where LRT heights are usually between 12km and 14 km.

To characterize the LRT variation as a function of latitude, seven years of LRT measurements are zonally averaged and is shown in figure 4.2. Vertical bars show the longitudinal as well as interannual variability for LRT height at any given latitude. In general, LRT heights are maximum in the tropics and relatively less over the mid-latitudes and poles, which is a well-known aspect of the tropopause. However slight variations to this pattern occur with respect to seasons. During boreal summer, the LRT is at lower heights (~15.9km) over the tropics as compared to boreal winter (~16.7km). Such kind of a pattern has also been observed by Reid and Gage, (1996) and several others for various tropical stations wherein the LRT is highest in winter, decreases thereafter and falls to a minimum in summer. Total variability over these latitudes has been observed to be ~1.5km. Similar to the tropics, a wintertime increase in LRT height can also be noticed in the SH polar latitudes (i.e., beyond 60°S), wherein the LRT height is ~1.5km higher during austral winter as compared to that during austral summer;

LRT height of NH polar regions, on the other hand, follows the annual march of the Sun. This exclusive behaviour of the SH polar latitudes as compared to NH polar regions can be again attributed to the difference between the land and ocean distribution and the intensity of polar vortex in these regions. Because the SH polar latitudes is land dominated, variation of the LRT height during solstices will be more prominent in these regions as compared to their NH counterparts (Liu et al. 2014).

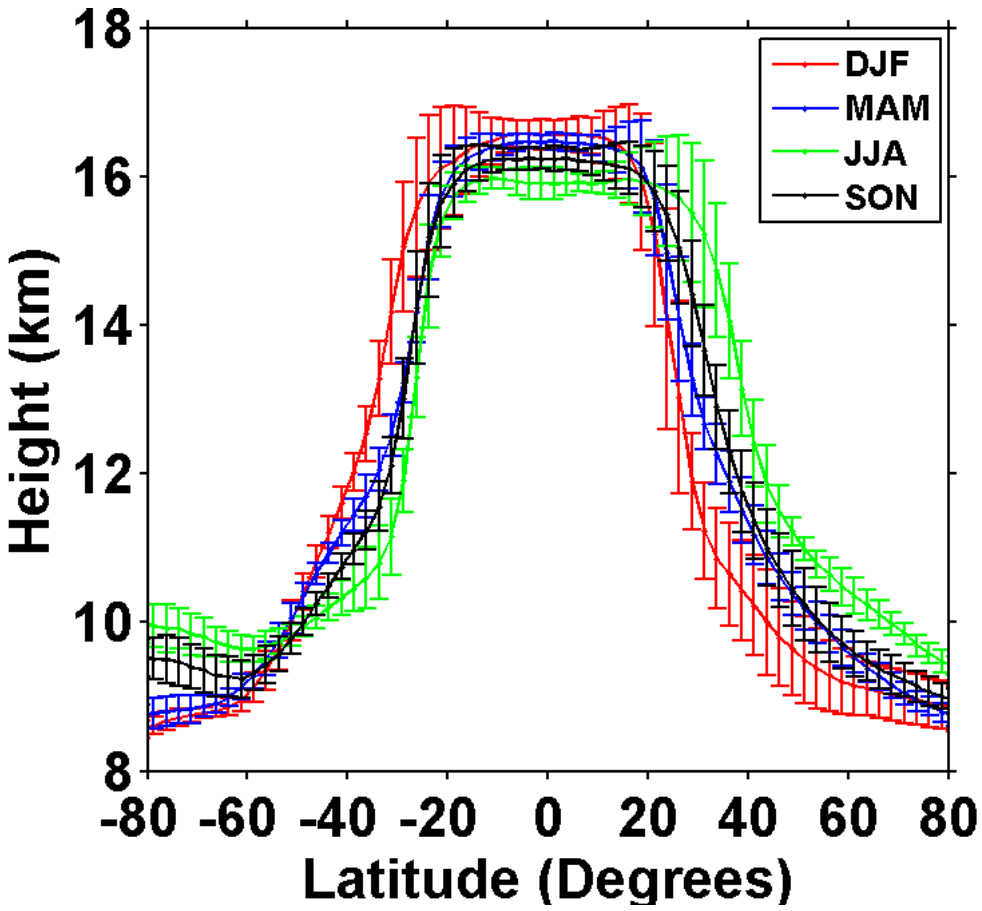

Figure 4.2: Latitudinal variation of LRT height for four seasons averaged over the observational period (2007-2013). Vertical bars represent the longitudinal variability.

The latitudes of prime importance in the present analysis turn out to be those locations where the height variations in LRT shift drastically from the characteristic ~16km of the tropics to the characteristic ~12km of the mid-

latitudes, especially during the winter and summer seasons. As figure 4.2 shows, LRT height between 20°N and 40°N changes drastically from ~16km to a minimum of ~10.3km (in boreal winter) and maximum of ~12.8km (in boreal summer), which is typical of the subtropical locations. In the SH, similar variation in LRT height lies between ~11.5km (in austral winter) and ~14.5km (in austral summer) at 30°S. This shows that within the subtropics, LRT is higher during summer than winter in accordance with the annual variation of insolation. The summertime LRT of SH subtropics are at lower heights than that of the NH subtropics as it follows from the previous discussion. Subtropical LRT height during the equinoctial seasons also varies with hemisphere. While in the SH, LRT occur at the same height for both equinoctial seasons, in the NH (at 30°N), autumnal equinox LRTs are at higher heights than vernal equinox LRTs (by ~1km). One of the striking features shown in figure 4.2 is the largest latitudinal variability of tropopause height at the region of transition from tropics to subtropics. This aspect of the latitudinal distribution of tropopause is employed in the present study to infer the width of the tropical belt by estimating the meridional gradient of LRT height (labeled as *TpGr* metric).

4.3.2 Annual Cycle of Tropopause height as a function of latitude

To further understand the LRT height variability over subtropics, the annual cycle of LRT height in the Northern Hemisphere (NH) and Southern Hemisphere (SH) is constructed at every 10° latitude and is shown in figures 4.3(a) and 4.3(b), respectively. It is noticeable from these figures that the annual cycle of LRT height in both hemispheres follows a pattern that is similar to the annual cycle of incoming solar radiation. However, exceptions occur in the latitudinal bands of 10°N-20°N in the NH and 50°S-60°S in the SH, wherein an increase in LRT height during respective hemisphere's winter is observed. In the 10°N-20°N bands, such an increase is probably due to the increased equatorial upwelling as a result of the strengthened Brewer-Dobson circulation during NH winter (Rieckh et al. 2014). In the SH high latitudes (50°S-60°S), the increase in LRT during austral winter can be attributed to more intense polar vortex during that season. However, the mechanism by which LRT is shifted to higher heights during austral winter over the SH polar region are yet to be understood in detail. From figure

4.3 it is clear that the LRT heights over 30°-40° latitude in both hemispheres exhibit pronounced annual variation as compared to other latitudinal belts shown in the figure. The subtropical regions show extra-tropical LRT character

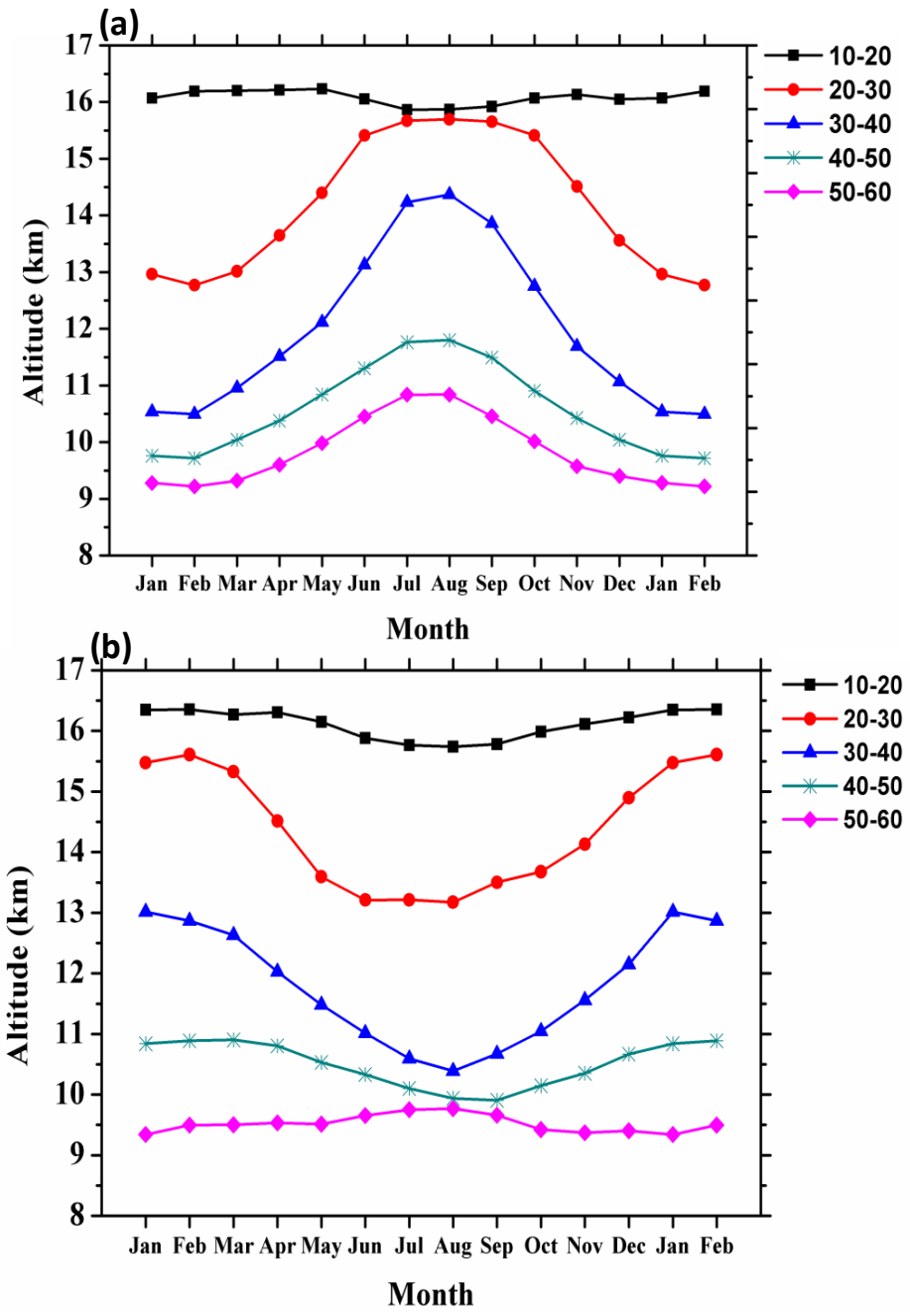

Figure 4.3: Annual cycle of zonal mean LRT height for different latitudinal bands (each of width 10°) in (a) NH and (b) SH.

during winter and tropical character during summer, thus exhibiting bimodal characteristics. The LRT height variability over this latitudinal belt ranges from

3km to 4km with respect to the annual mean, and therefore can be regarded as the transition region, as discussed earlier. This variability of the LRT height with respect to its annual mean is utilized in identifying the HC edge latitude using the *TpAO* metric (The methodology to derive *TpAO* metric has been described in section 4.2).

4.3.3 Meridional Structure of Bulk Static Stability

Tropospheric dry bulk static stability is defined as the difference in potential temperatures between the tropopause and the surface, and is a measure of the stability within a layer irrespective of its thickness (Davis and Birner 2013).

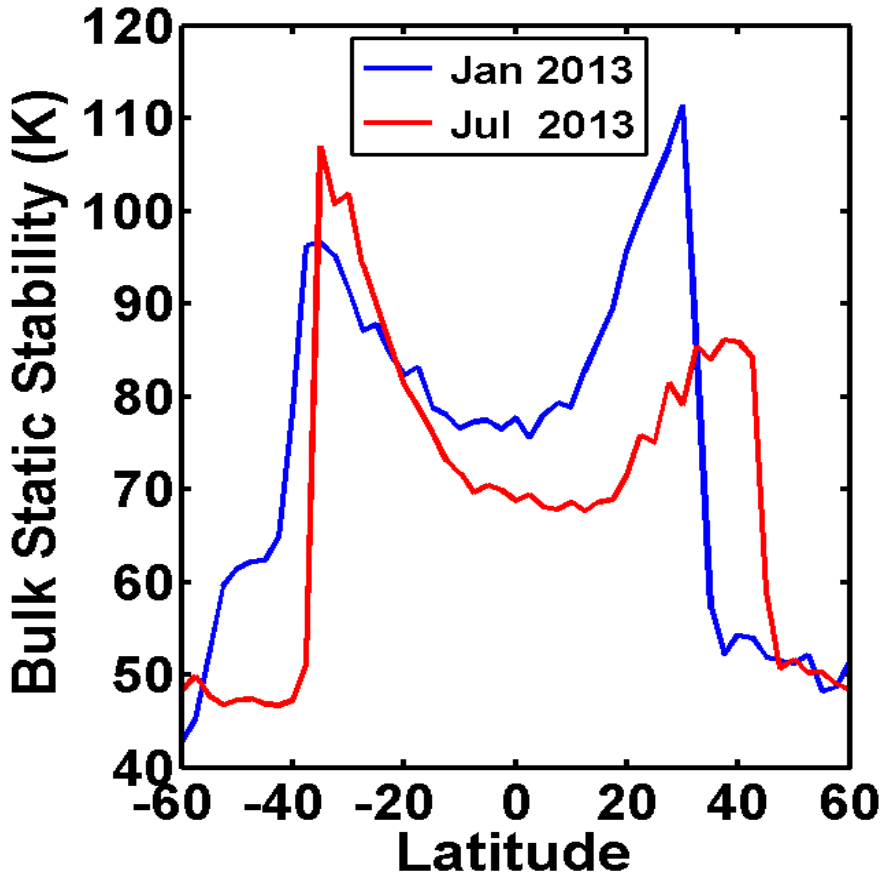

Figure 4.4: Latitudinal variation of zonal mean tropospheric dry bulk static stability for January and July, 2013.

Being a function of temperature, the *BSS* parameter is expected to have a distinct meridional gradient, which is evident in figure 4.4. The latitudinal variation of the zonal mean tropospheric *BSS* for January and July months of the year 2013 is shown in figure 4.4, which shows that the *BSS* values exhibit a sharp peak over the subtropical locations in both January and July. The *BSS* magnitudes are observed to be higher in the winter hemisphere as compared to their summer counterparts. For instance, during July 2013, the peak *BSS* value is ~110K in the SH and ~85K in NH; whereas in January 2013, the peak *BSS* value is ~110K in NH and ~95K in SH. This is consistent with the reduced surface radiative heating and convective activity in the winter hemisphere. The hemispheric difference in the observed *BSS* is relatively more during boreal summer (~25K) as compared to austral summer (~15K). Though the peak values of *BSS* vary in magnitude, their positioning in the 30^0-40^0 latitudinal belt is extremely clear and represents the relatively stable sub-tropical locations. As mentioned earlier, Davis and Birner, (2013) has extensively validated this metric for identifying the zonal mean width of the tropical belt.

4.3.4 Latitudinal Cross-Section of the Tropopause-based Metrics

Figure 4.5(a-c) depicts the latitude-month projection of the zonal mean *TpGr, TpAO* and *BSS* metrics, respectively, for the year 2013 derived as detailed in section 4.2. The figures illustrate the maximum magnitude of each metric over the subtropical locations, thus identifying the transition region from tropics to subtropics. LRT height changes abruptly from the characteristic ~16km of the tropics to ~12km of the extra-tropics, leading to the maximum LRT gradient, i.e. maximum *TpGr* value, in the subtropical regions. This is depicted in figure 4.5(a). A pronounced annual cycle of the *TpGr* metric can be noticed in the NH as compared to the SH, which is probably due to the dominance of land areas in the NH. High heating of the land areas in the NH during summer causes the LRT heights to remain higher in the tropics and allows the latitude of the maximum tropopause gradient to move poleward during this season. Elevated intra-annual variations in the NH can be further noted in all the three metrics, clearly indicating the response of the tropopause height to the land- sea contrast between the two hemispheres. Figure 4.5(b) shows the latitude-month projection

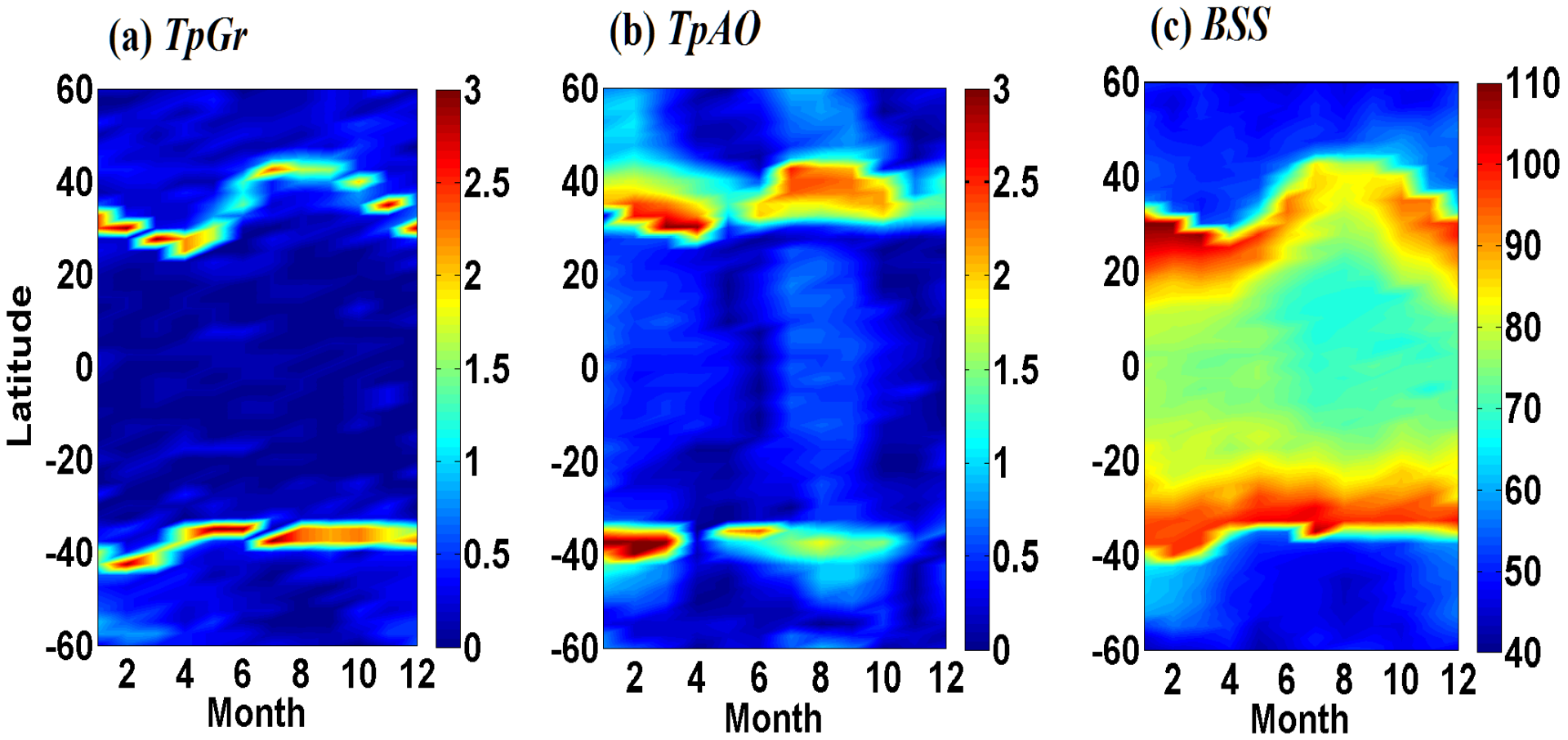

Figure 4.5: Latitude-month section of the zonal mean (a) meridional gradient in LRT height *(TpGr)*, (b) amplitude of annual oscillation in LRT height *(TpAO)*, and (c) tropospheric bulk static stability *(BSS)*, for the year 2013.

of perturbation of the monthly LRT height with respect to its annual mean for the year 2013. This perturbation is called the annual oscillation of the tropopause, or the *TpAO* in short. The magnitude of *TpAO* is the largest over the subtropical regions, especially during the solstice months (~3km). This is again indicative of the bimodal character of the sub-tropical tropopause. Figure 4.5(c) brings out the meridional as well as annual variation in *BSS* values for the year 2013. It can be seen from this figure that *BSS* is ~70-80K in the tropical regions and ~40-60K in the extra-tropical regions. However, the *BSS* magnitudes are ~90-110K in the subtropical latitudes, which is higher than the other regions. Thus all the three metrics show distinct characteristics over the transition region from the tropics to the subtropics.

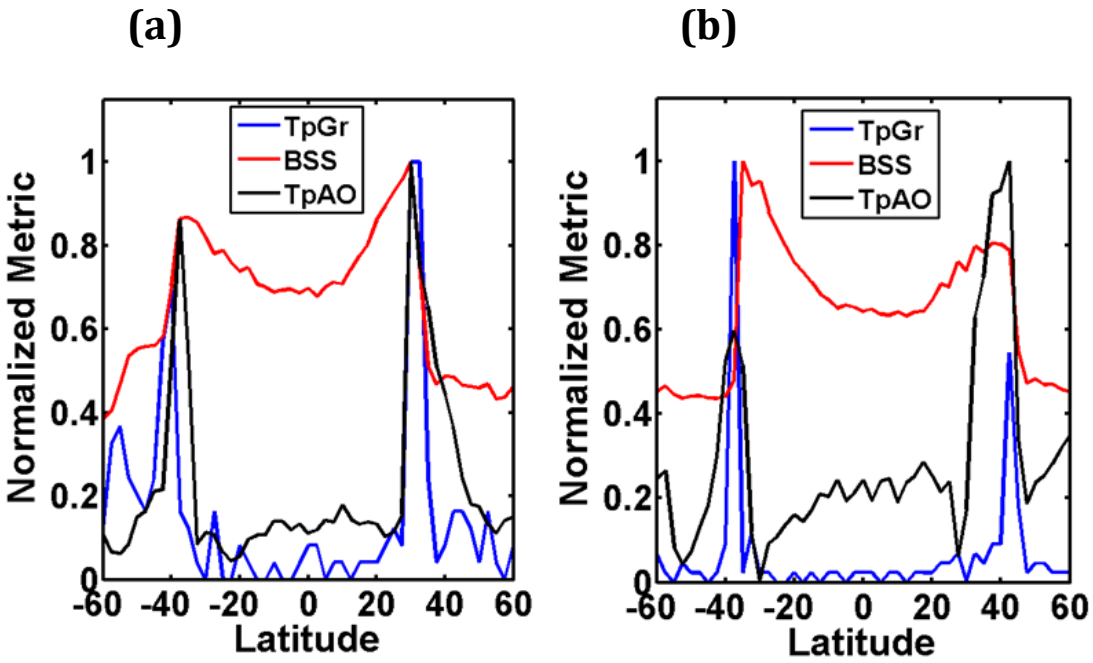

Figure 4.6: Latitudinal variation of the normalized (to peak) value of the *TpGr*, *BSS* and *TpAO* metrics for the year 2013 (a) DJF and (b) JJA.

Figure 4.6(a-b) shows the zonal mean latitudinal variation of the *TpGr, BSS* and *TpAO* metrics normalized to their peak values, for January and July of the year 2013, respectively. The figures indicate strong meridional variations, with sharp peaks over the subtropics for the *TpGr* and *TpAO* metrics and gradually increasing *BSS* metric. The peak values for the *TpGr* metric follows a pattern

similar to that of the *BSS* metric, which shows larger magnitude in the winter hemisphere as compared to the summer hemisphere. However, the *TpAO* metric show peaks of larger magnitude always in the NH. Although differences occur among the metrics in terms of magnitude, it is encouraging to note that all the three metrics seem to locate the HC edges in a consistent manner. The observed consistency among the three tropopause-based metrics owes to the fact that the tropopause altitude is common to all the metrics.

4.3.5 Validation of the Tropopause-based Metrics

The annual cycle of the zonal mean width of the tropical belt located by each of these metrics is estimated and compared with the total width obtained from the MSF metric (derived from ERA-I dataset), as shown in figure 4.7. For all metrics

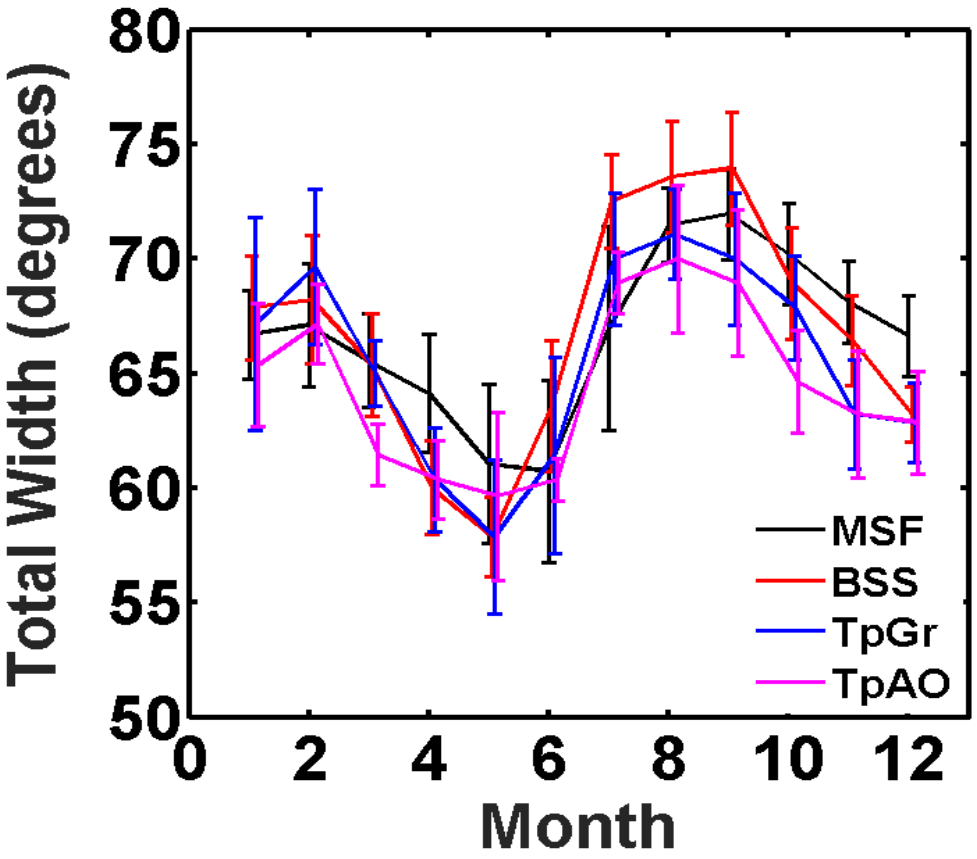

Figure 4.7: Inter-comparison of the annual cycle of the width of the tropical belt estimated from the *TpGr*, *BSS* and *TpAO* metrics (obtained from COSMIC) with those derived from the MSF metric (obtained from the ERA-I reanalysis dataset). The x-axis is shifted by 0.05 for each metric for clarity.

the total width peaks during the two solstices; the peak value falls within 65^0-70^0 during February and within 70^0-75^0 during July-August-September. The MSF metric shows amplitudes closer to that of the *TpAO* metric. The amplitude of annual cycle of tropical width is minimum for the *TpAO* metric ($\sim 10^0$) and maximum for the *BSS* metric ($\sim 16^0$). Thus the annual cycle of the width of the tropical belt calculated from the tropopause-based metrics has been found to reproduce quite a majority of the features of those calculated from the MSF metric. However, it is not possible to substantiate from the present analysis which is the best tropopause-based metric for estimating the width of the tropical belt.

To explore the co-variability of these metrics on inter-annual time scales, we compare the deseasonalized time series of the monthly mean tropical belt width obtained from the *BSS* and MSF metrics, as shown in figure 4.8(a). The deseasonalization removes the influence of the Sun. A 12-point running mean is applied to each so as to reflect the annual mean. We deseasonalize to remove the influence of the annual cycle, as done in Solomon et al. (2016) and Davis and Birner (2017). It is evident from this figure that the tropical belt width as measured by the *BSS* and MSF metrics co-vary during most of the observational period. We perform a regression analysis to further quantify this co-variability (figure 4.8(b)), finding that their correlation coefficient is 0.61, which is statistically significant at the 95% level. This correlation only decreases to 0.45 when 3-month smoothing is applied.

Solomon et al. (2016) and Davis and Birner (2017) report that both month-to-month and interannual correlations between the tropical belt as measured by the tropopause break latitude and the Hadley cell edge derived from MSF are not statistically significant. It is to be noted that these studies have used reanalyses and climate models in which the tropopause heights are poorly resolved. The present study uses high vertical resolution COSMIC observations, which likely better resolves the tropopause height. Further, the present analysis performs 3 and 12 month smoothing on the data, while both Solomon et al. (2016) and Davis and Birner (2017) examined the correlations on raw monthly data. Thus, it may also be possible that this connection between the tropical belt width measured by

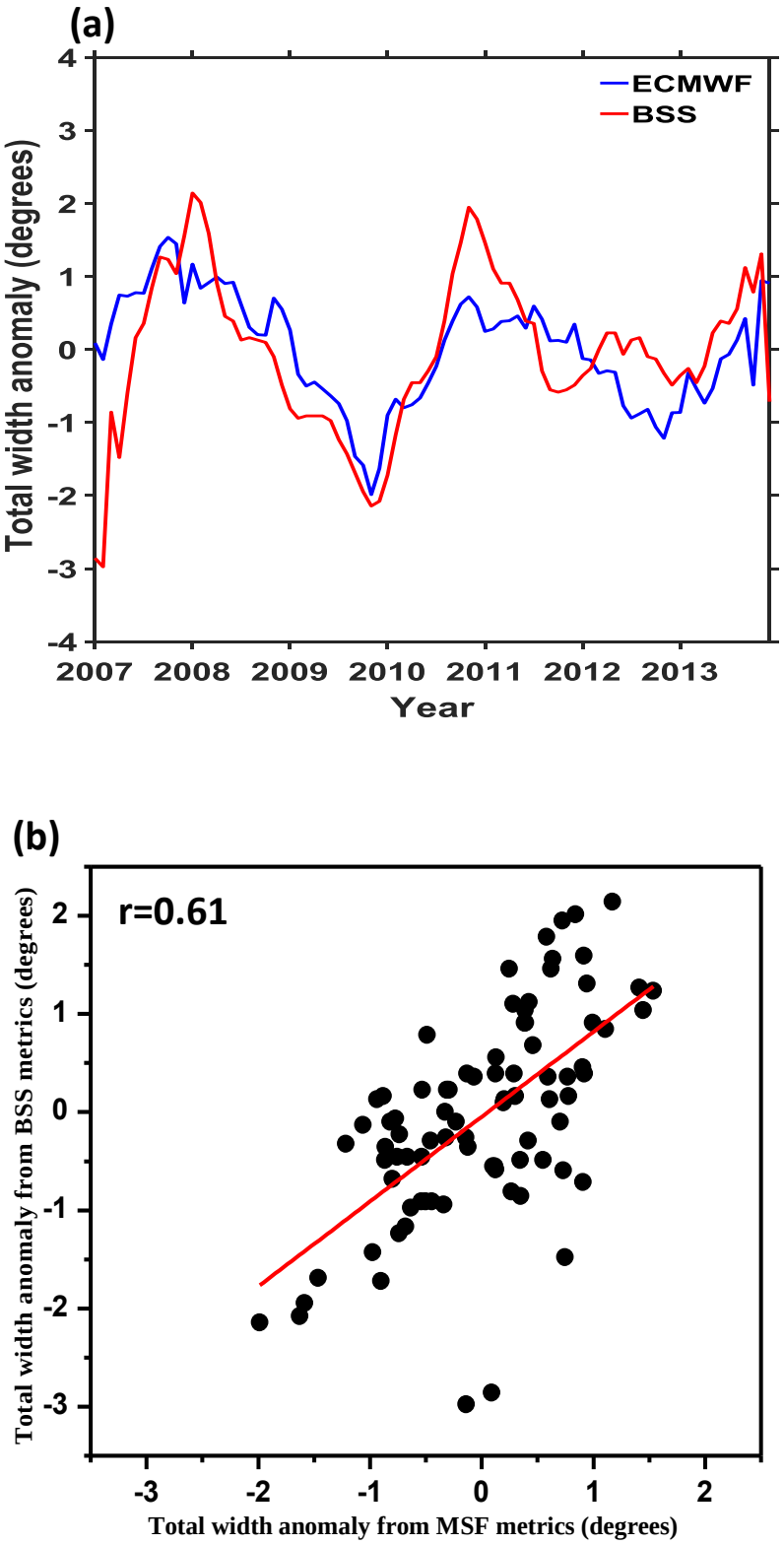

Figure 4.8: (a) Time series of deseasonalized monthly mean tropical width anomaly estimated from the *BSS* and MSF metrics (12-point running mean is applied on both the time series) and (b) scatter plot of time series depicted in figure 4.8(a). The red line represents the linear-fit.

the tropopause and the Hadley cell edge only manifests on longer timescales. A detailed analysis with more high resolution tropopause observations may be required to further substantiate the co-variability of the *BSS* and MSF metrics, which is currently being pursued. Nevertheless, the present results show a very good degree of co-variability between the two metrics. A similar analysis has also been carried out using the *TpGr* and *TpAO* metrics, and it is found that the *BSS* metric exhibit the best co-variability with the MSF metrics. However regional features of the tropical belt are inferred using all the three metrics, and are discussed in the following section.

4.3.6 Regional Features of the Width of the Tropical Belt

Figure 4.9 shows the edges of the tropical belt identified for every 10^0 longitude using the three tropopause-based metrics for January (left panel) and July (right panel), respectively, for a representative year (2009). The figures represent a striking similarity in the regional tropical belt edges identified by all three metrics. The poleward displacement of the edges over land areas for the respective hemisphere's summer is clearly evident in all three metrics. The minimum tropical width is seen in the East Pacific region (150^0W-110^0W) during boreal winter. There are large variations in the longitudinal pattern of edges for the *TpAO* and *BSS* metrics as compared to the *TpGr* metric, especially in the winter hemisphere. Thus all the three metrics captures the longitudinal structure of tropical belt prominently. However, there seems to be some difficulty in defining the tropical boundaries over few sectors such as the Atlantic and the East Pacific. It can also be noted from figure 4.9 that the SH edges are much more consistently defined among the metrics.

Seasonal mean of the edges of the tropical belt in both hemispheres is estimated for every 10° longitude, and is shown in figure 4.10(a-b), for boreal winter and summer, respectively. Seven years of COSMIC observations (2007-2013) are used to obtain the seasonal mean. The vertical bars represent the inter-annual variability of the edges of tropical belt. All the three metrics seems to be consistent in capturing the similar regional features of the width of the tropical belt. However, there are minor differences in the estimated edge latitudes over a few longitudinal sectors, as mentioned above. Also, edge latitudes identified from

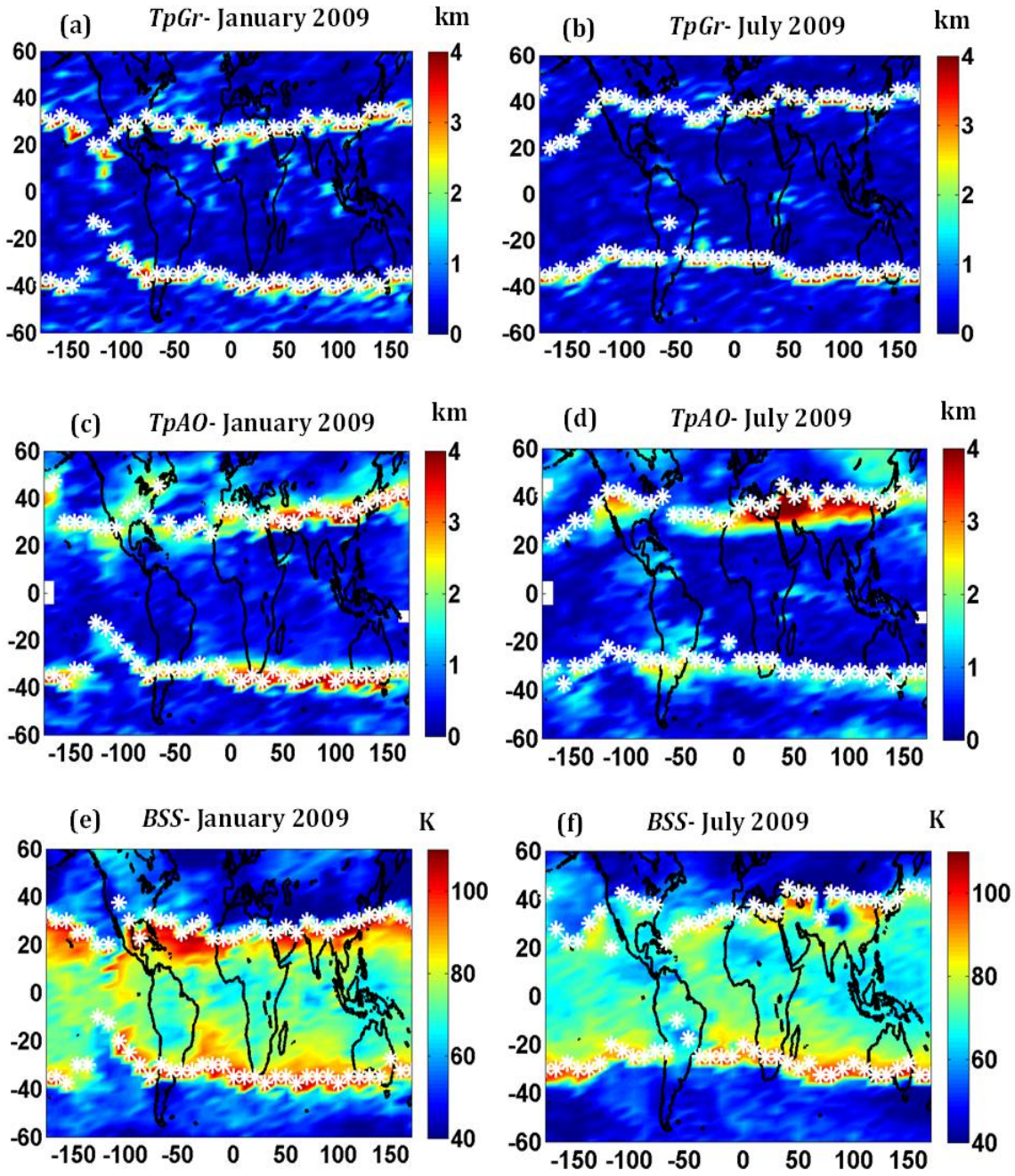

Figure 4.9: (a) The meridional gradient in tropopause height identified at each latitude-longitude grid for January 2009. The latitude of peak *TpGr* value for each longitudinal grid is marked with white stars. (b) Same as (a), but for July 2009. (c) The monthly LRT height perturbations from the annual mean at each latitude-longitude grid for January 2009. The latitude where the absolute magnitude of LRT perturbation peaks in each longitudinal grid is marked with white stars. (d) Same as (c), but for July 2009. (e) The tropospheric dry bulk static stability identified at each latitude-longitude grid for January 2009. The latitude of peak *BSS* value for each longitudinal grid is marked with white stars. (f) Same as (e), but for July 2009.

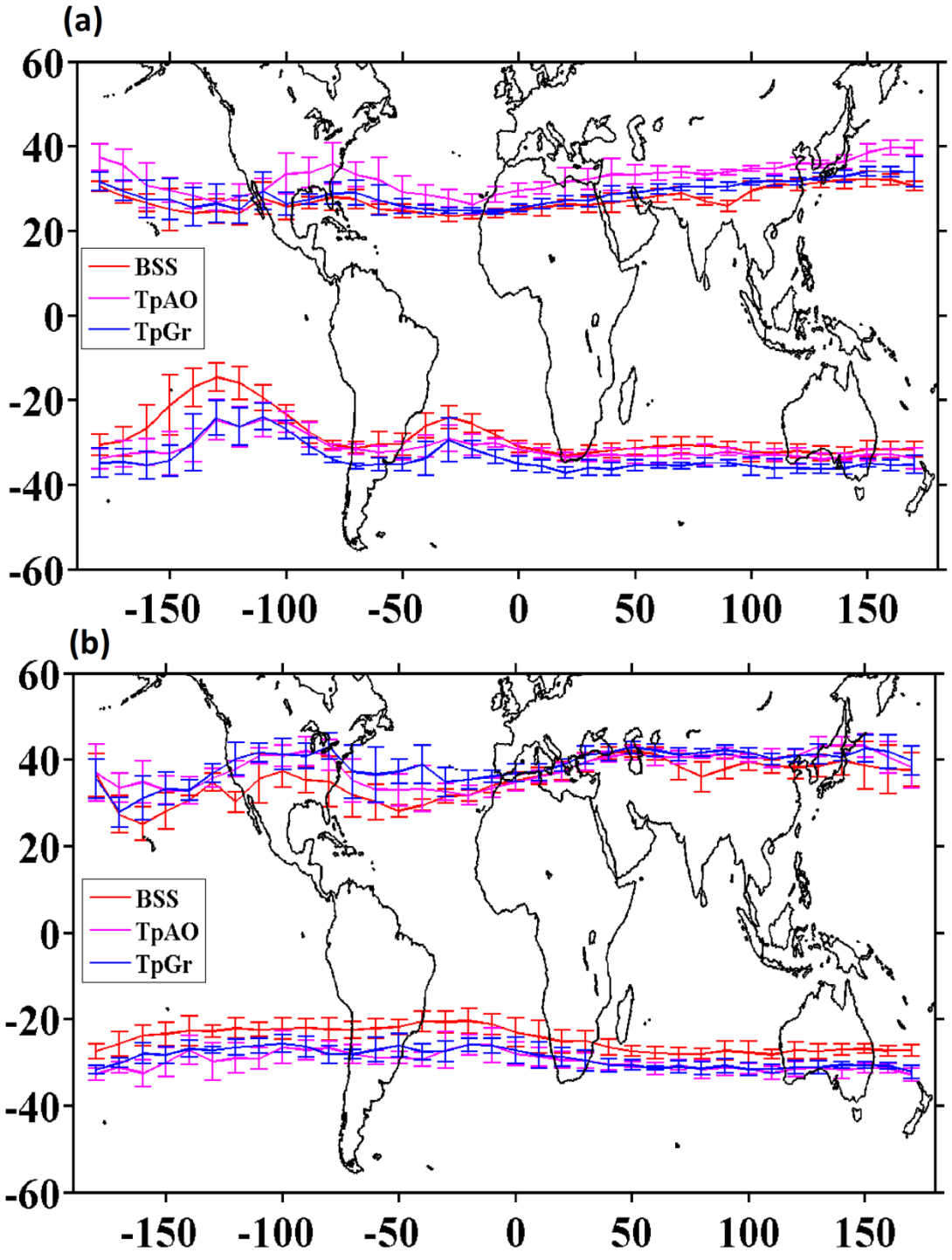

Figure 4.10: Longitudinal variability of the tropical belt edges in the NH and SH for two seasons, (a) DJF and (b) JJA, estimated using the LRT-based *TpGr*, *BSS* and *TpAO* metrics. Vertical bars are representative of their inter-annual variability over a period of 7 years (2007-2013).

the metrics are seen to be consistent during both boreal winter and summer. In the NH, edges of the tropical belt identified for boreal summer is further north as compared to boreal winter. As Inter-Tropical Convergence Zone (ITCZ), which is considered as the centre of the HC, migrates towards NH low latitude during boreal summer, the tropical belt edge also moves further north. This observation again confirms the suitability of the tropopause-based metrics to delineate the longitudinal structure of the edges of the tropical belt. The desert regions, which form due to the descending branch of the Hadley cell, also can be identified in figure 4.10. There is a clear poleward excursion of the tropical belt edge latitude in these regions, indicative of a region of relatively high pressure and hence subsidence which is conducive to the maintenance of desert climates.

It can be observed in figure 4.10(a) that in the SH during austral summer, longitudinal variations are more in the East Pacific (150^0W-100^0W) and the Central Pacific (150^0E-150^0W); the *BSS* metric show larger variations than rest of the two metrics over this region. Comparatively low inter-annual variability is observed for the edge locations identified from all the three metrics over the Australian region during Austral winter and over the subtropical locations of the South American and African continents during Austral summer. In the NH, over the Middle East and the South Asian regions, inter-annual variability of the tropical edges is relatively low during JJA. Recently, regional characteristics of the tropical expansion were reported by Lucas and Nguyen (2015) using global radiosonde observations. The study has used LRT metric to calculate the rate of tropical expansion over six continental-centred regions. The analysis revealed highest expansion rate over the Asian region in the NH and the Australia-New Zealand region in the SH. As discussed earlier, Chen et al. (2014) also reported tropical expansion rates over six locations using reanalysis datasets. In the study, the authors identified that expansion of the SH zonal mean HC is mainly driven by the expansion within the South American region.

Figure 4.10 thus suggest that there seem to be certain specific sectors which contribute more to the zonal mean width of the tropical belt during both the solstices. To further elucidate this aspect, the contribution of each 10^0 degree longitudinal sector to zonal mean width of the tropical belt estimated using the

BSS metric is shown in figure 4.11. Negative (positive) values imply that the tropical belt width at the given longitude sector is narrower (wider) than the zonal mean tropical width. The figure brings out that the contribution to total

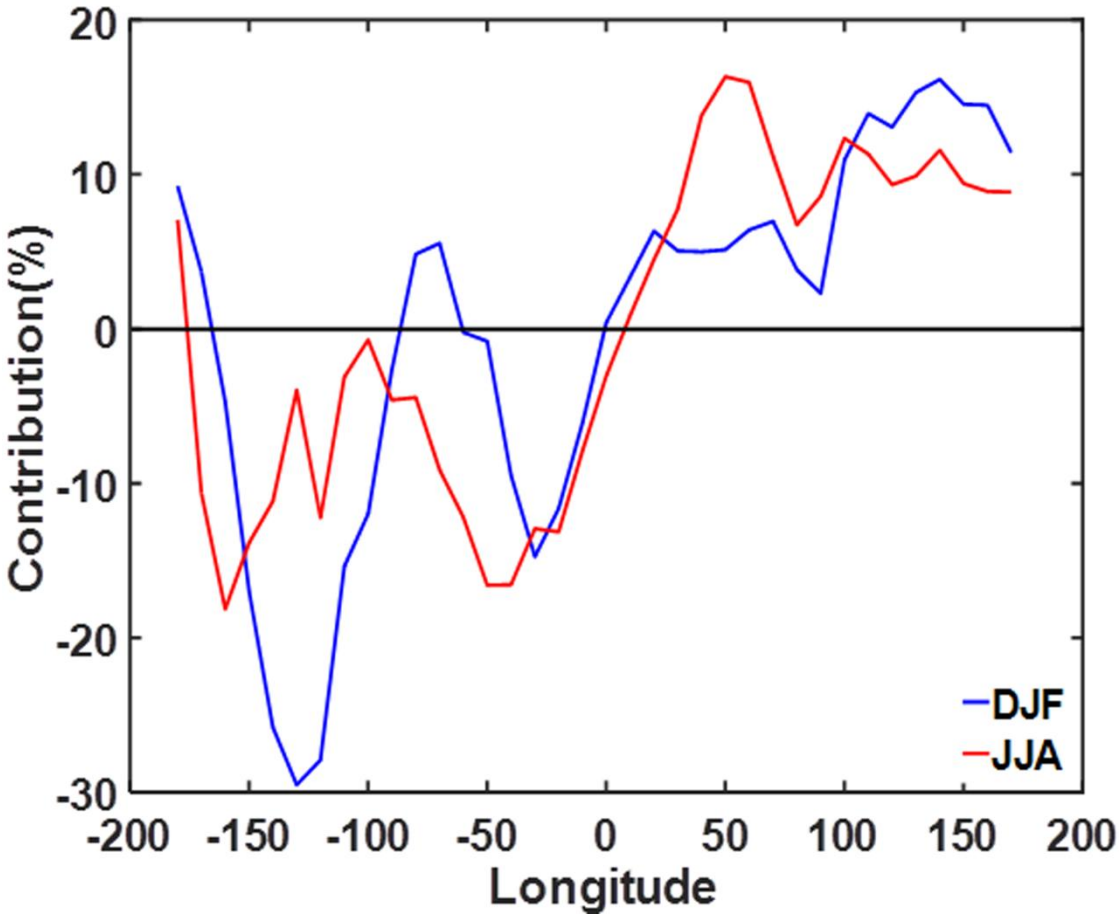

Figure 4.11: Zonally resolved contribution to the zonal mean tropical width during boreal winter and summer estimated using the *BSS* metrics.

width is largely positive in the Eastern hemisphere and negative in the Western hemisphere. An exception is the South American region (50^0W-80^0W) which has positive contribution to zonal mean tropical belt width during boreal winter, but only ~5%. During boreal winter, the tropical widths are significantly below the zonal mean over East Pacific (110^0W-150^0W) by ~30% and Atlantic (10^0W-40^0W) by ~15% and above the zonal mean over West Pacific (100^0E-150^0E) by ~15% and South American sector (50°W-80°W) by ~5%. During this season,

over Africa and the Indian Ocean the tropical width is wider than the zonal mean. During boreal summer, the tropical width is narrower than its zonal mean over East Pacific by ~15% and Atlantic by ~15%, and above the zonal mean over the West Pacific by ~12%. The Indian Ocean sector (40^0E-100^0E) also has a significant positive contribution of ~15% during boreal summer, indicative of the possible impact of the Indian Summer Monsoon circulations on the regional width of the tropical belt at this sector. Thus during boreal summer, zonal mean tropical belt width increases as a result of the contribution from the Indian sector and the West Pacific sector; and it decreases due to negative contribution from the East Pacific and the Atlantic sectors. Also, West Pacific sector contribute relatively more during DJF as compared to JJA to the zonal mean of the tropical belt. The figure thus yields important information on the regional contribution to the zonal mean width of the tropical belt. This result has important implications when compared with the zonal mean tropical widths estimated by using the radiosonde observations (which biases towards land). There could be an overestimation of the tropical width obtained from radiosonde data by not including the observations over the oceanic regions, especially from the East Pacific and the Atlantic regions which negatively contribute to the tropical belt width as shown in figure 4.11. However, this overestimation may be compensated by not including the observations over the Indian Ocean and Western Pacific, which positively contribute to the zonal mean tropical width.

The observed longitudinal structure of width of the tropical belt and its seasonal variability can be associated with changes in the north-south movement of the ITCZ since the ITCZ forms the rising limb of the Hadley cell. We have used COSMIC observations of specific humidity profiles to estimate the location of the ITCZ following the method proposed by Laderach and Raible (2013). On average, it is observed that the tropical belt is wider when the ITCZ is displaced further from the equator. However, a one-to-one correspondence between the ITCZ latitude and tropical belt width is not observed in the present analysis; this aspect will be a topic for future investigations. The present study thus brought out the regional features of the width of the tropical belt using a globally measurable parameter for the first time using tropopause-based metrics. The expansion rates of the tropical belt for different regions can be quantified in a

reliable form using tropopause-based metric, once long-term GPS-RO measurements are available.

4.4 Summary

The present study delineated the regional features of the tropical belt using three globally measurable metrics, *viz. TpGr*, *BSS* and *TpAO,* based on the tropopause height derived from the high vertical resolution COSMIC GPS-RO temperature profiles. The sharp meridional gradient in tropopause height as well as the peak in tropospheric bulk static stability over the subtropics is employed in deriving the *TpGr* and the *BSS* metrics, respectively. In addition, pronounced amplitude of the annual cycle of tropopause height exhibited by the subtropics is utilized to identify the edge latitudes of the tropics using the *TpAO* metric. Since this newly proposed metric does not rely on a gradient or threshold calculation, it may be useful for the analysis in climate models with a poor tropopause structure.

The annual cycle of the width of the tropical belt derived from the *TpGr, BSS,* and *TpAO* metrics were found to agree very well with that derived from the MSF metric. Further, to verify the co-variability between the tropopause-based and the MSF metrics at interannual time scales, the deseasonalized time series of the monthly mean tropical width derived from the *BSS* and MSF metrics were analyzed. The result showed that the *BSS* metric is correlated with the MSF metric at inter-annual time scales with a correlation coefficient of 0.61. This result assumes its importance as some of the recent studies using reanalysis and climate models stated that there is very less co-variability between the tropopause-based metrics and the MSF metric. The significant co-variability observed in the present results can be attributed to the improved vertical resolution of the COSMIC data around the tropopause as compared to reanalysis and climate models.

The current study also derived regional features of the width of the tropical belt from the *TpGr*, *BSS* and *TpAO* metrics. All the three metrics were found to capture the longitudinal structure of the tropical belt edges in a consistent manner. Interannual variability in the seasonal mean of the regional tropical belt edges from these metrics were found to be lower in the Middle East and South Asian

regions during boreal summer, in the Australian region during austral winter, as well as in the South American and African continents during austral summer. These regions, where there is a consistent pattern of the width of the tropical belt, may be favourable for identifying the expansion rate of the tropics. On the other hand regions such as the East Pacific and the Atlantic regions, where there is considerable interannual variability, it may be difficult to identify the expansion rates. The study also discussed the zonally resolved contribution to the zonal mean width of the tropical belt in a quantitative manner. This analysis brought out that the Indian and West Pacific sectors increases the zonal mean tropical belt width during boreal summer, whereas the West Pacific and South American sectors increases zonal mean tropical belt width during boreal winter. On the other hand, Atlantic and East Pacific sectors decrease the zonal mean tropical belt width during boreal summer as well as winter seasons. The zonal structure of tropical belt shows some similarity with the seasonal changes in the movement of ITCZ, which need to be substantiated by means of further investigations in the near future. Thus the present study brings out the capability of the three tropopause-based metrics derived from the high vertical resolution GPS-RO technique to capture the zonally resolved width of the tropical belt as well as its variability in an effective manner. The study is envisaged to have potential application in investigating the longitudinal differences in the rate of expansion of the HC.

CHAPTER 5

ROLE OF LATENT HEATING IN MODULATING THE STRENGTH AND WIDTH OF THE HADLEY CIRCULATION

5.1 Introduction

As discussed in Chapter 1, the differential heating of the Earth's surface by the solar radiation from equatorial to polar latitudes is the principal component in driving the Hadley Circulation (HC). However, Riehl and Malkus (1958) proposed that the latent heating in the deep convective clouds over the tropics maintains the HC. The latent heat released during the process of adiabatic ascent of moist air parcels within the towering cumulonimbus clouds over the tropics plays a vital role in heating of the tropical troposphere. The latent heat released in the tropical troposphere maintains the meridional pressure gradient force necessary to sustain the vertical extent of the HC. A number of modelling studies have been carried out in the past to investigate the response of tropical atmosphere to the latent heat release associated with the moist convection. Many convective parameterization schemes have also been developed to explain the large scale flows due to latent heating and their role in transporting heat, momentum and moisture to the deficient regions (Bates 1972). These studies revealed that the altitudinal profile of heating associated with the latent heat release plays a major role in setting up the vertical extent of the HC (Webster 1994). In the middle troposphere, the latent heat release compensate significantly for the cooling effect arising from the enhanced vertical motion (Danard 1966). Release of latent heat reduces the tendency for vertical circulations to destroy the existing horizontal temperature contrasts. This process maintains the meridional temperature and pressure gradient throughout the troposphere, fuelling the HC to move to higher altitudes. As the vertical extent of the HC increase, its width and strength are also expected to vary accordingly. Thus the latent heating in the tropics influences the structure and dynamics of the HC.

As discussed in Chapter 1, studies have shown that HC has undergone an expansion of ~1-3^0 latitude per decade (Seidel et al. 2008; Stachnik and Schumacher 2011; Nguyen et al. 2013; Lucas et al. 2014; Mathew et al. 2016), implying a dramatic shift in the locations of the arid and semi-arid zones on the earth (Shin et al. 2012). The possible causes and consequences of the HC expansion phenomena have been detailed in Chapter 1. It was brought out in this chapter that the contributors to the HC expansion includes the tropospheric warming due to greenhouse gas forcing (Hu et al. 2013), stratospheric cooling due to ozone depletion (Polvani et al. 2011; Waugh et al. 2015), SST variability within the tropics (Staten et al. 2012; Allen et al. 2014), as well as the inter-hemispheric asymmetry of absorbing aerosols such as black carbon (Allen and Sherwood 2011; Allen et al. 2012). Though the HC expansion and the factors contributing to it is well reported, atmospheric processes through which these factors influence the HC is not very clear. However, all the factors listed above can influence the thermal structure of the troposphere, which in turn can affect the cloud formation and latent heating distribution (Mathew and Kumar 2018b). This aspect reinforces the fact that quantification of the relationship between latent heat distribution and the HC dynamics is essential to understand the pathways through which various factors influence the HC expansion. The current chapter is thus oriented in this direction.

A significant number of modelling studies were performed in the past to quantify the role of latent heat in controlling the strength and width of the HC. Using a simplified model for nonlinear axially symmetric circulation, Held and Hou (1980) investigated on parameters that controls the strength and width of the HC. This model based study clearly demonstrated the importance of latent heating and its distribution in controlling the structure of the HC. These authors proposed that moist convection can modulate the height of the momentum conserving flow through the modulations in tropical tropopause altitude, thus affecting the width of the HC. A study by Lindzen and Hou, (1988) proposed that the intensity of winter cell increases remarkably for off-equatorial heating centred at 6^0 from equator. Hack *et al.*, (1989) using a numerical model investigated the sensitivity of the HC strength to the location and width of diabatic forcing. These authors reported that when the diabatic heating source is

centred on 12^0 off the equator, the strength of the winter HC is twice that of the summer cell. These simulations also showed that the half-width of the heating plays a vital role in shaping the meridional circulation. Hou and Lindzen, (1992) showed that a highly concentrated heating, such as in ITCZ, was found to strengthen the HC to values higher than that of observations. Their study showed that when the thermal forcing is displaced from the equator and is redistributed over the entire HC domain, rather than being concentrated in the narrow ITCZ, the mean meridional circulation was found to strengthen to values which were consistent with observations. These studies emphatically showed that even a small change in tropical heating distribution can profoundly alter the intensity of the HC.

In addition to maintaining the horizontal temperature gradients at higher levels, the latent heat release in the mid-tropospheric levels can also slow down the HC by increasing the static stability of the tropical troposphere. While most of the modelling simulations predict this kind of a weakening of the circulation, studies using reanalysis datasets show a strengthening of the HC (Liu *et al.*, 2012 and references therein). Mitas and Clement, (2006) attributed this difference to the ways in which tropical dynamics and thermodynamics are handled in modelling studies. These authors showed that the HC strength and diabatic heating in the ascending limb of the HC have a high degree of co-variability. Recently, Loeb *et al.*, (2014) reported the interannual variations of atmospheric heat budget terms within the ascending and descending branches of the HC using satellite and reanalysis data in order to investigate the variability in the strength of the HC. These authors used the column-integrated divergence of dry static energy and kinetic energy derived from satellite observations of radiation, precipitation latent heating and sensible heat fluxes from reanalysis datasets. However, this study was more focused on the variability of various heating terms within the ascending and descending branches of HC rather than on their intensity and the width.

It is evident from the above discussion that the earlier studies on HC have acknowledged the role of latent heating in modulating the vertical heating structure of the tropics, as well as in influencing the general characteristics of the

large-scale tropical circulations. Simulations have been carried out extensively to understand the extent to which latent heating can modulate the width and strength of the HC; however observations have been seldom used for the same. The observational evidences and quantification of relation among various HC and LH distribution parameters using observational data are the missing elements in understanding the influence of tropical latent heating on the HC dynamics. With the availability of the vertical profiles of precipitation latent heating derived from Precipitation Radar (PR) measurements on board the Tropical Rainfall Measuring Mission (TRMM), it is now possible to investigate the role of latent heat in controlling the strength and width of the HC using observational data. Parenthetically, it is also one of the goals of the TRMM -"What is the role of LH released in the tropics in both tropical and extra-tropical circulations?" (Simpson *et al.*,1988). In this context, the present study aims at investigating the extent to which the distribution of latent heat can modify the spatial extent and strength of the HC, by using TRMM measurements and reanalysis data from the European Centre for Medium Range Weather Forecast (ECMWF). The current study is the first attempt to investigate the HC strength and width variability with respect to tropical latent heating using precipitation latent heating measurements derived from TRMM observations. The data used and the methods employed are described in section 5.2, results are discussed in section 5.3 and conclusions are provided in section 5.4.

5.2 Data and methods

The present study uses precipitation LH profiles retrieved from the Tropical Rainfall Measuring Mission (TRMM) observations using the Spectral Latent Heating (SLH) algorithm, originally introduced by Shige et al., (2004) as well as the meridional wind data of the European Centre for Medium Range Weather Forecast (ECMWF) Reanalysis- Interim (ERA-I) dataset (Dee et al. 2011). TRMM is a joint US-Japan mission launched in 1997 to monitor the tropical and subtropical precipitation and to estimate the associated latent heating. Precipitation Radar (PR) on board TRMM is the first space-borne precipitation radar operating in the Ku-band frequency (13.8GHz or 2.17cm) and with sensitivity of 18dBZ. The vertical resolution of the TRMM PR is 250m, and the

spatial resolution is ~4.3km. PR measures the time delay of the precipitation backscattered return power, and hence can directly obtain the vertical precipitation profile over the tropical regions. The latent heating profiles are derived from the observed precipitation profiles by means of definite sets of retrieval algorithms (Tao et al. 2006), of which the Spectral Latent Heating (SLH) retrieval algorithm (Shige et al. 2004; Shige et al. 2007) is one. The details of TRMM PR and the SLH algorithm have been discussed in detail in Chapter 2. The present study uses the gridded (0.5^0x0.5^0) monthly mean spectral latent heating product of TRMM - version 7 (3H25 v7) with 1 km vertical resolution for the period 1998- 2013. It is to be remembered that the TRMM's PR provides the precipitation latent heating alone and will not include the LH due to freezing and deposition as well as condensational heating in the non-precipitating clouds to which PR is not sensitive. However, it has been shown in the past that the TRMM's SLH product reproduce majority of known features of the tropical diabatic heating. In the present study therefore we use the term LH synonymous with precipitation LH.

In addition to the TRMM measurements, the study also uses the monthly mean meridional winds from the European Centre for Medium Range Weather Forecast (ECMWF) Reanalysis- Interim (ERA-I) dataset (Dee et al. 2011) whose spatial resolution is 1.25^0 X 1.25^0 X 37 levels, as described in Chapter 2. The dynamic indicator -meridional Mass Stream Function (MSF) is chosen to determine the HC parameters, viz. HC centre, edges, and strength, from the monthly mean meridional winds. The MSF at a given pressure level is calculated using the method described in Chapter 2. As done in the previous chapters, the HC edges are defined as the first latitude poleward of the cell centre where MSF at 500hPa becomes zero. HC strength is defined as the maximum (minimum) value of the MSF in NH (SH) at 500hPa. HC total width is the total distance between the HC edges in either hemisphere. The region between the latitudes of maximum MSF in the NH and minimum MSF in the SH are the latitudes where large scale ascending motions prevail, and are of particular interest in this study.

The zonal mean latent heating is averaged in the 4-17km height domain to focus on mid to upper tropospheric region, which has significant influence on the HC

dynamics. A Gaussian fit centred on maximum heating is applied to the latitudinal distribution of latent heating, and the *latitude of peak LH* is identified for different seasons. The *width of LH* is identified as the full-width-at-half-maxima of the Gaussian fit to the latitudinal distribution of LH. The *total LH released in the ascending limb of HC* is estimated by identifying the ascending region of HC from the latitudinal cross section of MSF and summing up the heating rates within this region. The correlation analysis of each of these LH parameters with the HC centre, total width and strength is carried out to quantify the extent of their co-variability. The correlation analyses have been carried with and without deseasonalization.

5.3 Results and Discussion

5.3.1 Distribution of LH over the tropics and the meridional mass stream function

The precipitation latent heating over the tropics is estimated for the period 1998-2013 using TRMM measurements and its mean latitude-longitude section is shown in figures 5.1(a-b) for boreal winter and summer, respectively. The figures represent the average LH release within the tropical atmospheric column, enclosed within 4-17km. As the HC dynamics is more sensitive to mid-tropospheric latent heating, the present study focuses on this altitude region (Diaz and Bradley 2004). It is clear from these figures that the LH release is primarily over the continental regions of the summer hemisphere, which can be attributed to the large convective activity over land during summer. LH release in SH during December-January-February (DJF) is largely over South America, Central and Southern parts of Africa, Australia and the warm equatorial Indian and south Pacific Oceans. On the other hand, during June-July-August (JJA), large LH release happens over Central and North America, Northern parts of Africa, Indian subcontinent and surrounding Oceanic regions and Western pacific region. Figure 5.1 thus clearly brings out the zonal asymmetries in the distribution of LH within the tropical atmosphere. The pattern of LH shown in figure 5.1 is consistent with present understanding of the movement of ITCZ and thus reassures the credibility of the TRMM's LH measurements (Schumacher et al. 2004).

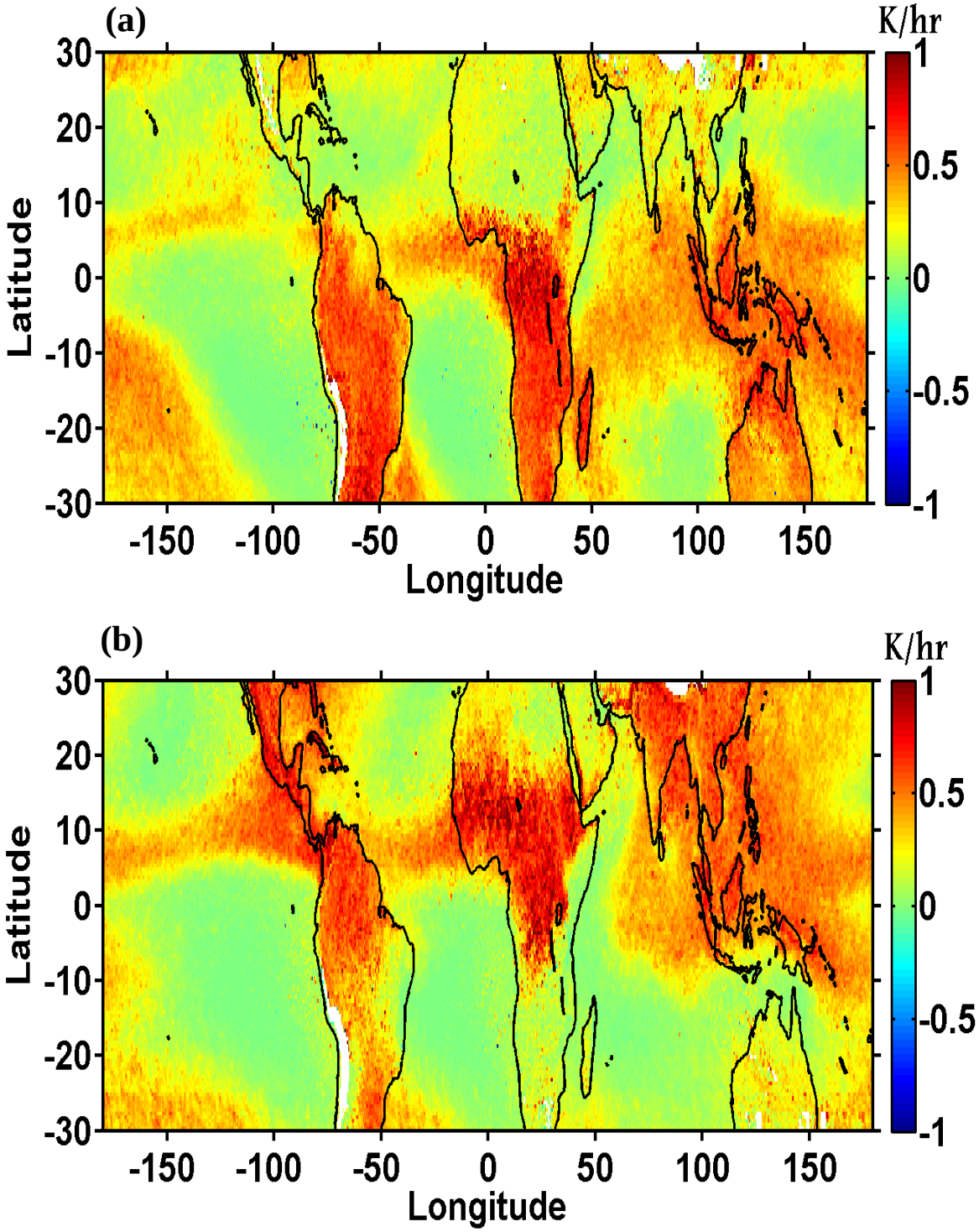

Figure 5.1: The latitude-longitude section of the average LH within 4-17km altitude estimated from the TRMM PR measurements during the period 1998-2013 for (a) DJF and (b) JJA.

As mentioned in section 5.1, the altitudinal extent of the HC depends on the profile of LH release in the atmosphere. Hence it is important to know the vertical profile of the atmospheric latent heating. Also, as evident in figure 5.1, the sources of LH release and the amount of heating due to LH release vary from region to region. To bring out the comprehensive relation between HC and LH distribution, zonal mean LH distribution and MSF are employed.

Figure 5.2(a) and 5.2(c) shows the height- latitude section of the zonally averaged mean latent heating within the atmosphere over the tropics. These figures bring out the thermodynamics associated with the physical mechanisms of cloud formation as well as precipitation. As the air parcels rise through the atmosphere, they cool adiabatically, leading to saturation of water vapour and cloud formation. The condensation of water vapour as well as freezing of liquid water and deposition processes release LH into the atmosphere, which further fuels the atmospheric convection. Most of the LH released in the tropics within 1-3km as shown in figure 5.2(a) and 5.2(c) is due to the formation of marine stratocumulus clouds within this layer (Schumacher et al. 2004). The stratocumulus clouds are frequently formed under the descending branches of the HC. The figure also brings out the LH changes associated with the adiabatic ascent/descent within the rising/falling limb of the HC. In fact, the signature of the mean meridional circulation is clearly visible in the LH magnitudes above ~4km. The signature of winter hemispheric HC is completely discernable, and the summer hemispheric cell partly in these figures. Large amount of LH release, extending up to 10-12km, can be seen in the 10^0S-10^0N latitude band and corresponds to the mean location of the ascending limb of the HC during both DJF and JJA. The low amount of LH in the 20^0N-30^0N latitudinal belts during DJF and 20^0S -30^0S during JJA correspond to descending branches of HC. The peak heating due to deep convective clouds occurs within the 6-8km altitudinal range of the summer hemisphere. One more striking feature of latitudinal distribution of zonal mean LH is that the LH release is relatively intense and narrow in the NH during boreal summer, whereas it is broadly distributed in the SH during austral summer. Thus figure 5.2(a) and 5.2(c) brings out the salient features in the zonal mean latitude-height distribution of LH during DJF and JJA constructed using 16 years of TRMM observations.

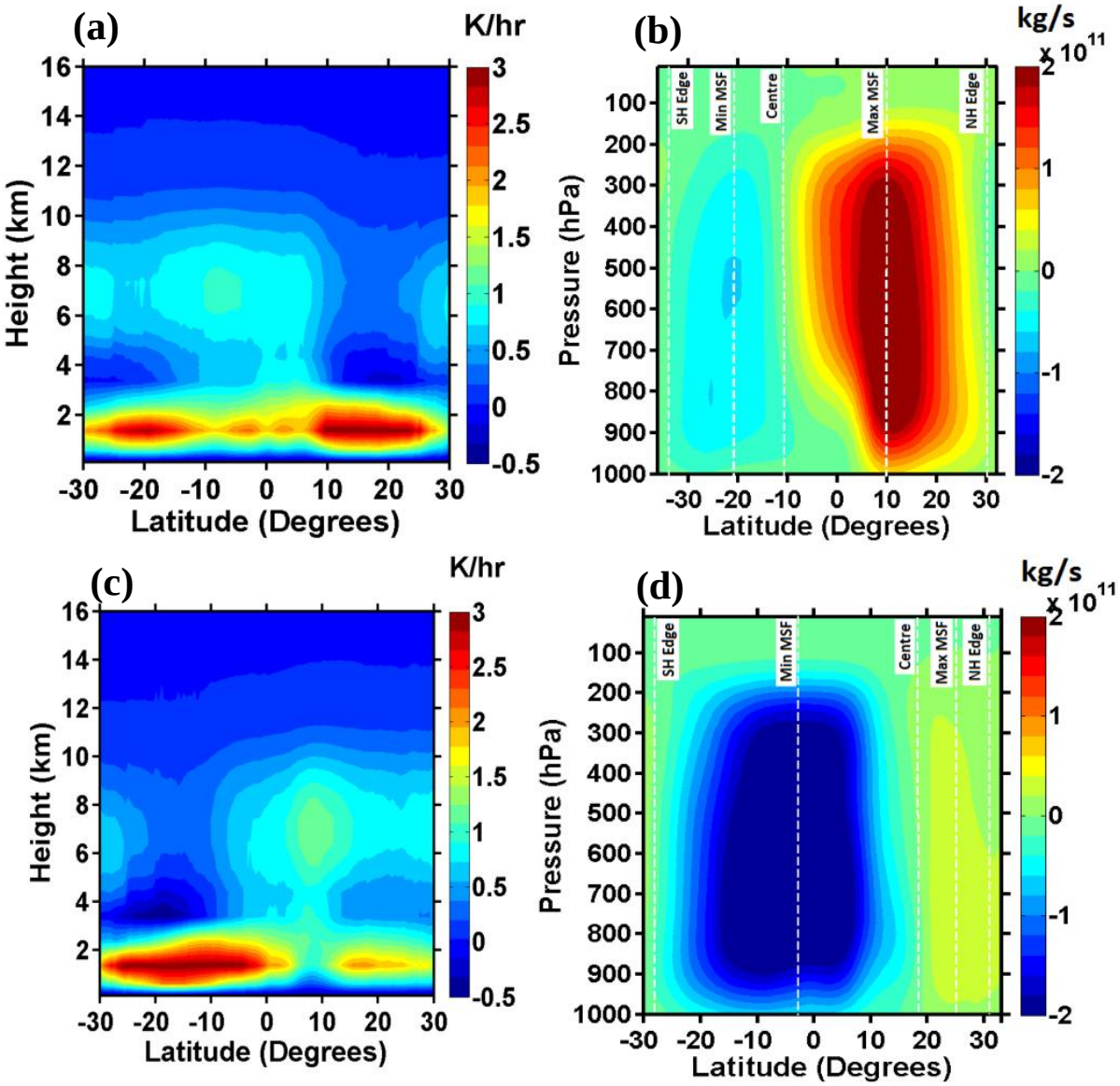

Figure 5.2: The latitude-height section of zonal mean LH over the tropics estimated from the TRMM PR measurements during the period 1998-2013 for (a) DJF (c) JJA. Also, vertical cross-section of MSF estimated from ERA-I reanalysis data during the period 1998-2013 for (b) DJF (d) JJA. The HC boundaries are marked by dashed lines in (b) and (d).

The vertical cross-section of the meridional mass stream function (MSF) in terms of height-latitude section, which is estimated using ERA-I reanalysis data for the observational period, i.e., 1998-2013, is depicted in figures 5.2(b) and 5.2(d) for DJF and JJA respectively. As mentioned in section 5.2, the MSF metric is used to

characterise the HC in the present study. The HC centre, edges and strength are extracted from these figures as outlined in the previous section. It can be noticed from these figures that the rising limb occur at ~10^0S during DJF and at ~17^0N during JJA. During DJF, the latitude of maximum positive intensity happens to be at ~10^0N, and that of maximum negative intensity occur at ~20^0S. The HC edges, where the MSF at 500hPa pressure level becomes zero, are also estimated from these figures. The edges occur near 30^0N/S in both hemispheres during DJF as well as JJA. The figures also show a dominant winter hemispheric cell with intensity exceeding 2x10^{11}kg/s during both solstices, which is consistent with the present understanding. Ascending motions prevail within the latitudes of maximum positive and negative intensities, i.e., between 20^0S to 10^0N for DJF; and between 10^0S and 25^0N for JJA. An inter-comparison of latitude cross sections of LH and MSF depicted in figure 5.2 shows that the LH release above ~5km is positive within those regions of the HC where ascending motions prevail and negative in the regions where descending motions occur. For instance during DJF, ascending motions prevail within 25^0S to 10^0N latitudes (refer to figure 5.2(b)) and relatively large LH is found in the 4-16km over this region (figure 5.2(a)). Within 10^0N to 25^0N, where descending motion occurs in the winter cell (figure 5.2(b)), LH value is relatively low (figure 5.2(a)). Similarly, ascending motions prevail within 7^0S and 20^0N during JJA, where relatively large LH is found and descending motions of winter cell within 7^0S and 25^0N, wherein relatively low LH is found (figure 5.2(a, c). Hence it can be inferred that the vertical structure of LH derived from TRMM measurements exhibits the HC features, which are consistent with those inferred from the vertical cross-section of the MSF depicted in figure 5.2.

5.3.2 Characterisation of zonal mean distribution of the LH and HC parameters

Figure 5.3 represents the latitudinal structure of zonally averaged LH for boreal winter and summer seasons at a representative level of mid-troposphere, i.e., at ~8km. This altitude is chosen as maximum latent heat is released at this altitude region (~6-8km) in the middle troposphere. This mean picture is obtained by averaging the TRMM observations during 1998-2013. During JJA, the peak LH

release occurs at ~9^{0}N and is ~1.1K/hr. This relatively large value of LH is confined to a narrow latitudinal belt as compared to that of DJF, wherein the LH pattern is broadly distributed within the 15^{0}S-5^{0}N latitude belt. The peak heating rate at ~8km during DJF is ~0.85K/hr, which is 23% lower than that of JJA.

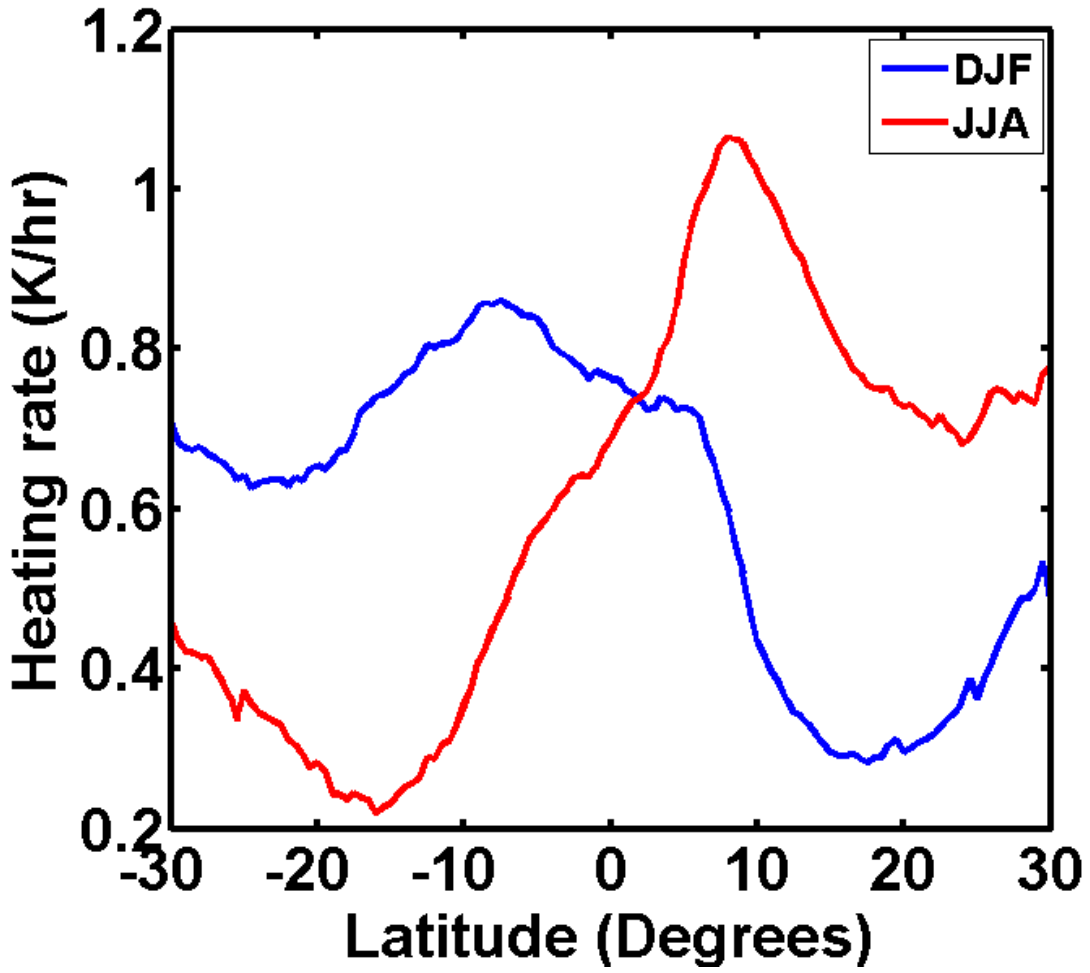

Figure 5.3: Latitudinal distribution of zonally averaged LH at 8km height during the solstices; TRMM observations are averaged for the period 1998-2013.

The locations of the peak LH magnitudes are in corroboration with the location of the annual march of the ITCZ. The unique features to be noted in this figure are that the LH release is limited to a narrow region during boreal summer, whereas it is spread over broad latitudinal band during austral summer. This is evidently due to the influence of land-ocean contrast in the NH and SH and the direction of the cross- equatorial flow. The cross-equatorial flow is from ocean-dominated SH to land-dominated NH during JJA, which brings in more moisture to the ascent

latitudes, and thereby leading to larger amount of LH release during this season. In addition, strong convection over land concentrates the ascent to a smaller area. On the other hand, the cross equatorial flow is from land-dominated NH during austral summer, thus bringing in air that is devoid of much moisture to the ascent latitudes in SH. Convection over the ocean dominated SH is also relatively weak,

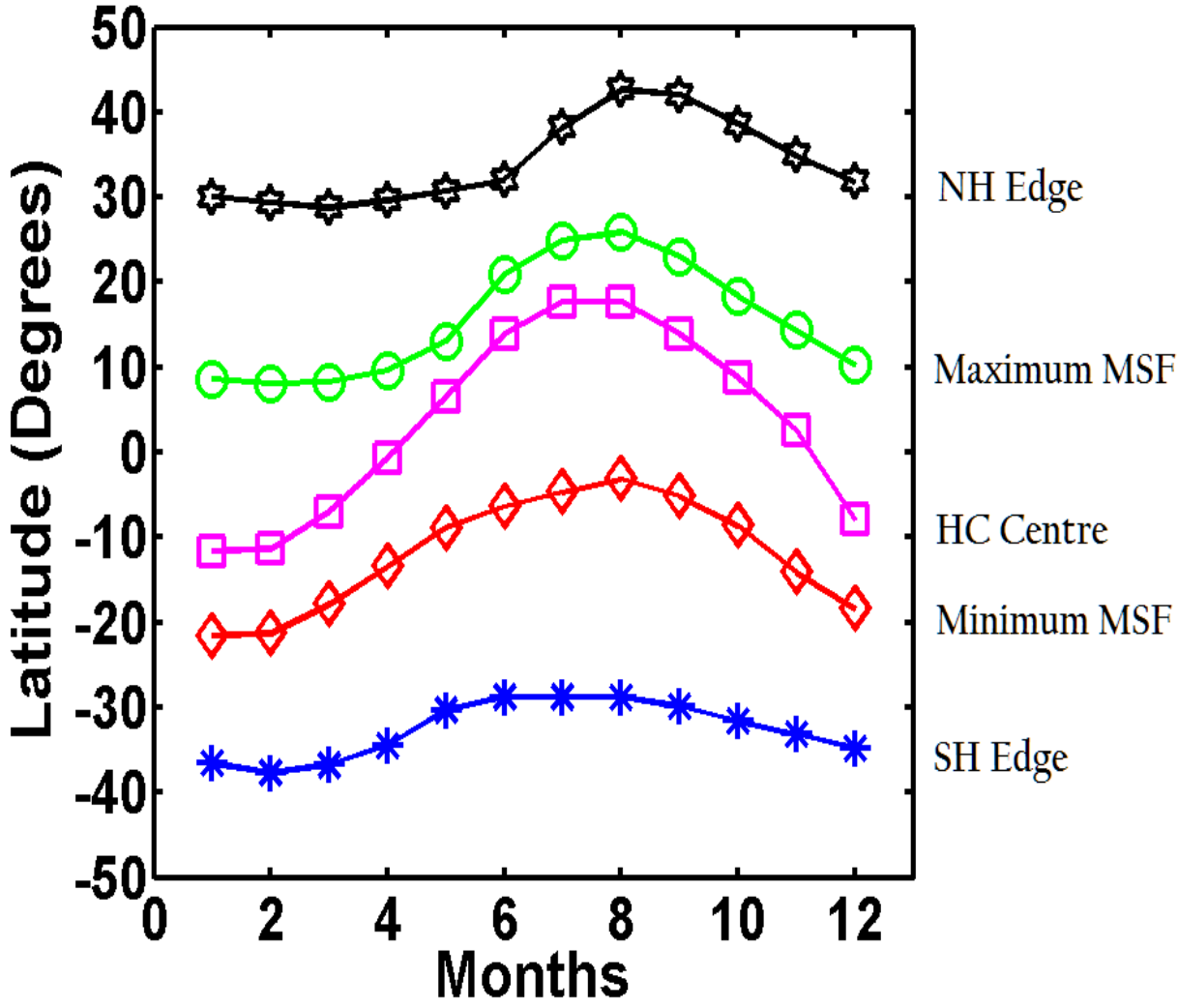

Figure 5.4: Annual cycle of the HC centre, NH/SH edges of the HC, and the latitude of max/min intensities, obtained using MSF metric from the ERA-I reanalysis data for the period 1998-2013.

leading to a broad pattern in LH release. Thus, the latitude of peak LH is in the NH during boreal summer and in the SH during austral summer in the mid troposphere; the width of peak heating is less in boreal summer and is more in austral summer; and finally, the magnitude of LH is more during boreal summer than in austral summer. This forms a general pattern of the LH release in the

tropical latitudes. As mentioned in section 5.2, a Gaussian fit is applied to the zonal mean latitudinal distribution of latent heating averaged in 4-17km height domain for each month and the latitude of peak LH as well as full-width at half-maximum of LH distribution are estimated.

In order to discuss the variability of the LH distribution and its influence on the HC, the annual cycle of the HC centre, edges and the latitudes of maximum positive and negative intensities, which represents the boundaries of ascending limb of HC, are estimated from the zonal mean MSF averaged during 1998-2013 and are shown in figure 5.4. The annual cycle of these parameters is in corroboration with the annual march of the Sun across the tropical latitudes. As expected, the maximum poleward movement of all the HC parameters is during the respective hemisphere's summer season. The location of the HC centre translates from $\sim 10^0$S during DJF to $\sim 15^0$N during JJA. Again, it is consistent with the movement of ITCZ. The latitudes of maximum intensities also move by $\sim 15^0$ from one solstice to another. The NH edge reaches its maximum poleward location during the month of August and SH edge, during the month of February. Figure 5.4 thus brings out the annual cycle in HC parameters. Over all, there seems to be a good degree of co-variability among various LH and HC parameters at a seasonal time scale. A detailed discussion on this co-variability will be made in the forthcoming sections.

5.3.3 Co-variability of the LH and HC parameters

The preceding discussion brings out that three main parameters of LH can play an important role in determining the spatial structure and strength of the HC:

1. *Latitude of peak LH*, which is the latitudinal position of peak latent heating
2. *Width of the LH distribution*, which is the full-width at half maximum of the latitudinal distribution of LH
3. *Total LH within the ascending limb of the HC*

These three parameters are estimated for every month over the period 1998-2013 and correlated with the HC parameters, viz. centre, intensity, and total width. The results are quantified in term of correlation coefficients along with their 95% confidence intervals.

5.3.3.1 HC centre and the LH parameters

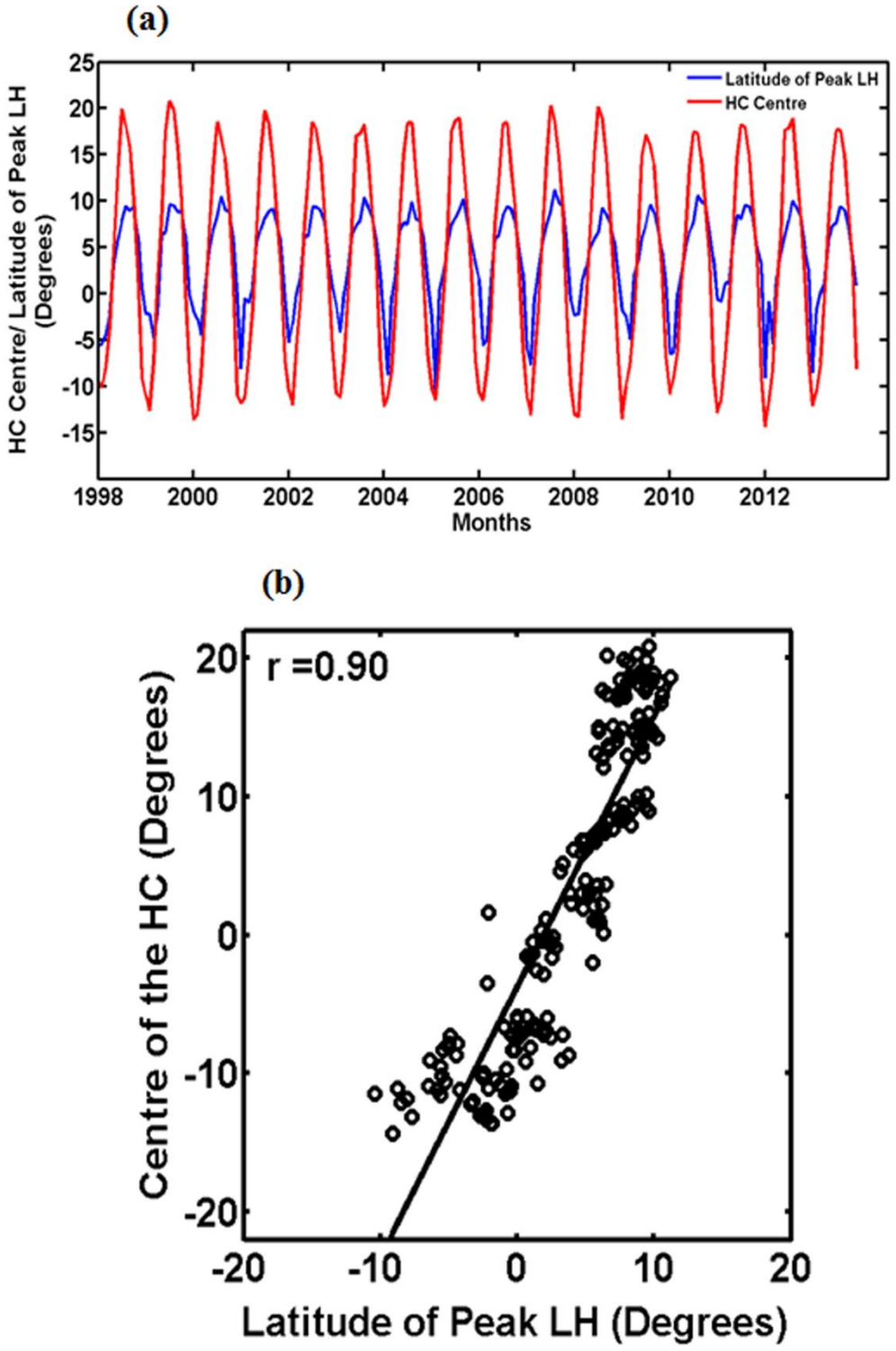

Figure 5.5: (a) Time series of the latitude of peak LH obtained from TRMM PR measurements and HC centre obtained from ERA-I reanalysis data, both for the period 1998-2013. (b) Regression analysis of the latitude of peak LH distribution and the centre of the HC.

To investigate the extent to which the latitude of peak LH influence the location of the HC centre, a time series (from 1998 to 2013) of the location of HC centre and the latitude of peak LH is constructed as shown in figure 5.5(a). From this figure, it is evident that the HC centre is always farther than the latitude of peak LH in both the hemispheres. The figure shows that the two parameters vary hand in hand, suggesting a good co-variability between the HC centre and the latitude of peak LH. The maximum poleward location of the HC centre is at $\sim 20^0$N in NH and at $\sim 10^0$S in the SH. The latitude of peak LH rarely crosses 10^0N in the NH and it lies between 3^0S and 10^0S in the SH. A correlation analysis between the two parameters is carried out as shown in figure 5.5(b), which indicates a very good linear correlation (correlation coefficient = 0.9) between HC centre and the latitude of peak LH that is significant at the 95% level. Even though the seasonal transitions are co-varying in both the parameters, the degree of variability in one parameter does not seem to be proportional to the other. This aspect will be further discussed in section 5.3.3.5. However, the annual cycle of the HC centre closely varies with that of the latitude of peak LH as shown in figure 5.5(a).

Further, the co-variability of the HC centre with the width of the LH distribution is investigated to examine their interdependency. The correlation analysis between these two parameters is depicted in figure 5.6. The analysis is carried out separately for the HC centres located in SH (red colour circles) and NH (blue colour circles). As the width of LH distribution exhibits different shapes in NH and SH, the correlation analysis is carried out separately. From this figure it is evident that the width of LH and the HC centre are positively correlated. The correlation coefficient is 0.51 when HC centre is in NH, and is -0.38 (negative sign does not indicate anti-correlation, it is because of negative SH latitudes) when HC centre is in the SH. Both the correlation coefficients are significant at the 95% level. Correlations are found to be better when the heating is more concentrated, as in the case of the NH HC centre. Figure 5.6 shows that as the width of LH distribution is more concentrated, the NH HC centre moves as far as 20^0 away from the equator. To be precise, the off-equatorial position of the NH HC centre shifts by 20^0 when the heating is concentrated within a width span of two degrees, ranging from $\sim 18^0$ to 20^0. On the other hand, LH released during austral summer season is widely distributed. The location of the SH HC centre moves

from 5^0S to 14^0S with the width of LH changing from 16^0 to 22^0. The slope of the regression line is relatively high in NH as compared to SH indicating that HC centre response to changes in the width of LH distribution is relatively high in NH. Even though the degree of variability of width of LH and HC centre differs from one hemisphere to another, it can be generalized from figure 5.6 that the off-equatorial position of the HC centre is directly proportional to the width of LH.

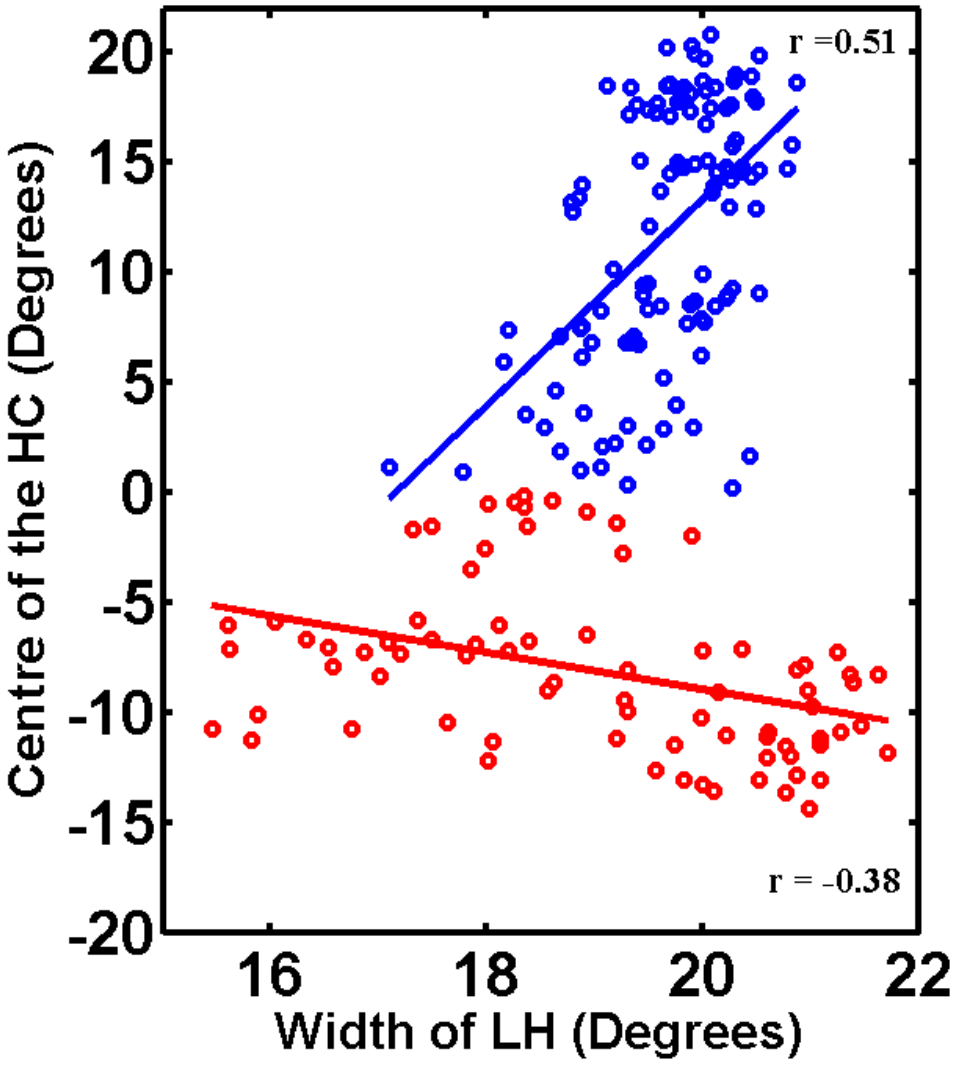

Figure 5.6: Regression analysis of the width of LH distribution and the centre of the HC. The analysis is carried out separately for the HC centre in NH (blue circles) and the SH (red circles).

The co-variability of the HC centre with the total LH released in ascending limb of HC is also investigated. The correlation between these two parameters shows a correlation coefficient of 0.58, which is significant at 95% level (figure not shown). The co-variability of the HC centre with the total LH release within the ascending limb of the HC is less than that between the HC centre and the latitude of peak LH, and comparable with that of the width of LH. However, the analysis emphasize that the LH released in the ascending region of HC is also an important factor which influence the position of HC centre. Thus it is envisaged that a combination of all the three LH parameters discussed above might be deciding the degree of variability of HC centre with respect to the LH-based parameters.

5.3.3.2 HC intensity and the LH parameters

As discussed in section 5.1, the modelling simulations show that the off-equatorial position as well as the distribution of heating significantly influences the HC strength and width (Hack *et al.*, 1989). The present section discusses this aspect using LH observations. Figure 5.7(a) shows the time series of normalized latitude of peak LH along with normalized NH and SH HC peak intensities. As mentioned earlier, the peak intensities are estimated from the MSF at 500hPa level for each month. The pattern of peak intensities are observed to be similar to that noted by Oort and Yienger (1996). It is clear from figure 5.7(a) that the annual cycle of HC intensity in both NH and SH is anti-correlated with the latitude of peak LH. To further investigate this aspect the correlation analysis is carried out. Figure 5.7(b-c) shows the correlation of latitude of peak LH with the peak northward and southward intensities of the HC, respectively, during the period of study. The northward intensities are represented by positive sign and southward intensities by negative sign. An anti-correlation between the two parameters can be observed in both the figures with correlation coefficients of -0.85 and -0.78, respectively, for the northward and southward intensities. This implies that the maximum northward intensity is observed when the latitude of peak heating is in the SH, and the maximum southward intensity is observed when the latitude of peak heating is in the NH. Further, these results indicate that farther the latitude of peak LH from the equator in the summer hemisphere, stronger is the HC intensity in the winter hemisphere. The figure also shows that the latitude of

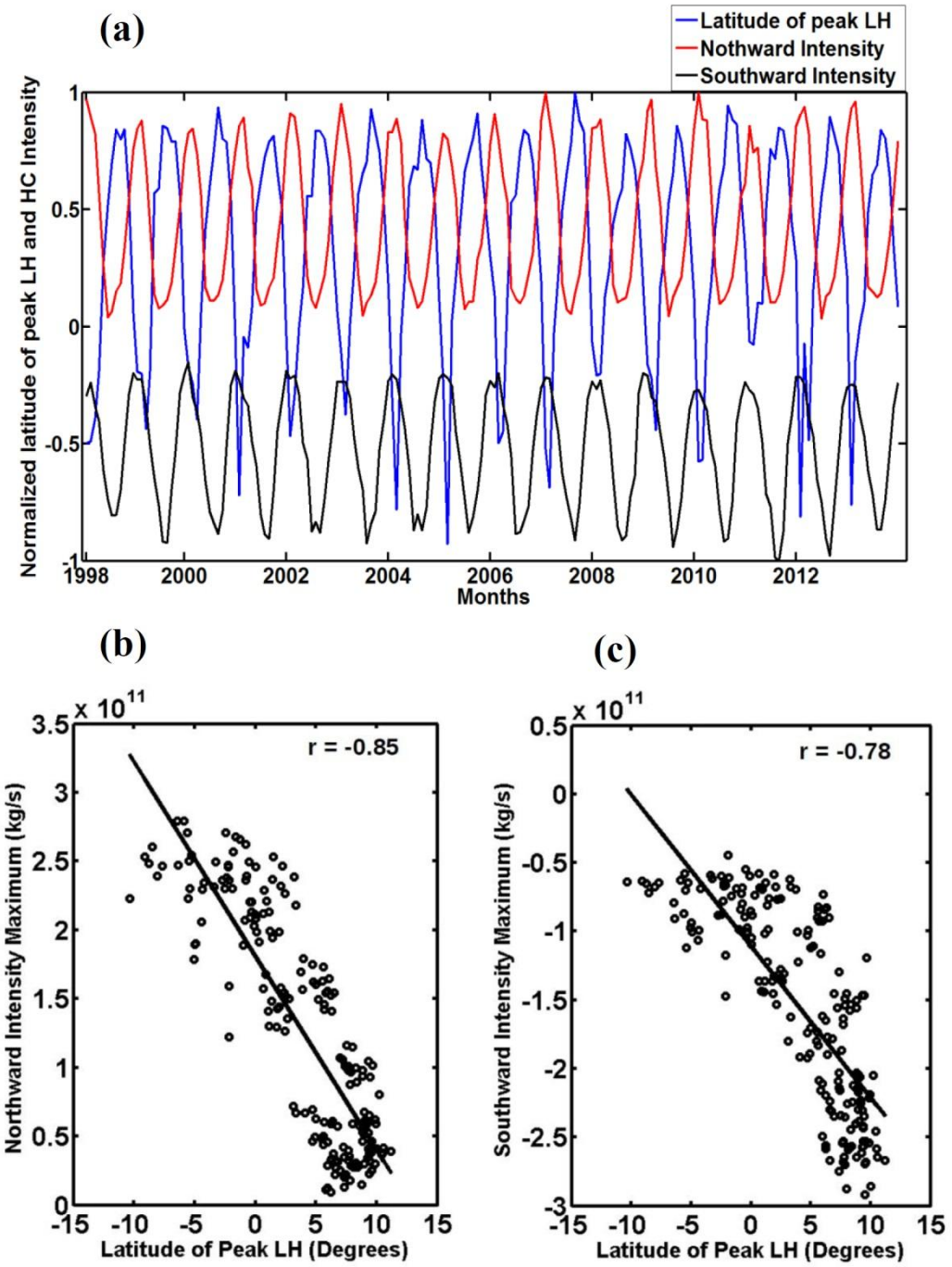

Figure 5.7: (a) Time series of the monthly mean latitude of peak LH, Northward intensity and Southward intensity of the HC. All the three quantities are normalized to their peak values to bring out their co-variability. The regression analysis of the latitude of peak LH with (b) Northward Intensity of the HC, and (c) Southward Intensity of the HC.

peak LH moves from 10^0S to 10^0N from the boreal winter to summer. This annual cycle is evident in figure 5.5(a) too. During boreal summer, the maximum off-equatorial position of the latitude of peak LH is at ~10^0N; the northward intensity during this time is ~0.2x10^{11}kg/s, and the southward intensity is ~ -2.5x10^{11}kg/s. On the other hand, the latitude of peak LH is at ~10^0S during boreal winter; the northward intensity is ~3x10^{11}kg/s, and the southward intensity is ~-0.5x10^{11}kg/s. This confirms the fact that the strength of the winter hemispheric cell is more when the latitude of peak LH lies far off from the equator in the summer hemisphere. This observation is in support of the modelling simulation of Lindzen and Hou, (1988), which showed that the intensity of the HC is enhanced when the heating latitude is displaced off the equator. Analysis of the correlation between the HC intensities and width of LH distribution showed low correlation and unexpected results (refer to Table 5.1 towards end of section 5.3.3). The width of LH distribution negatively correlated with the Northward intensity whereas it positively correlated with the Southward intensity with correlation coefficients of -0.24 and 0.24, respectively (figure not shown). This is rather unexpected. As discussed earlier, the LH distribution is narrow in NH and relatively wider in SH, these differences in the LH distribution may partly explain the observed features. A narrow and well-defined distribution of LH in the NH, which is responsible for the observed large Southward intensity of the HC, shows positive correlation. On the other hand, a wider distribution of LH in the SH, which is responsible for the observed large Northward intensity, shows negative correlation. The influence of LH released in ascending region of HC on the HC intensity is also examined, which shows similar correlation as that of the width of the LH distribution, i.e., negative correlation (-0.20) with Northward intensity and positive correlation (0.29) with Southward intensity. However, the degree of co-variability is poor as compared to that of latitude of peak LH. These observations thus show that latitude of peak LH has a say in determining the HC intensity as compared to the other two LH parameters. As mentioned earlier, correlation analysis of deseasonalized time series of these parameters will be further discussed.

5.3.3.3 Total width of HC and the LH parameters

The previous sections have discussed the role of various LH parameters in determining the strength and location of the HC centre. However, it is also necessary to look into influence of the LH parameters on the total width of HC. The correlation analysis of the three LH parameters with the total width of HC is carried out. The analysis has shown that the amount of LH released within the ascending region of the HC play a major role in determining the total width of the HC with a correlation coefficient of 0.52 as compared to the other two LH parameters discussed above (refer table 5.1). The latitude of peak LH shows a correlation of 0.41 and the width of LH distribution shows a correlation of 0.35 with the total width of HC. This section thus focuses on the influence of total LH released in ascent region of the HC on the total width of HC as these two parameters show good degree of variability. Figure 5.8(a) shows an inter-comparison of the mean annual cycle of total LH within the ascent area to that of the HC total width. It can be observed in figure 5.8(a) that the total width of the HC follows a pattern that closely follows the annual cycle of the sum of LH within the ascent region. The minimum in HC total width occurs during May, and is delayed by one month as compared to the time of occurrence of the minima in total LH within the ascent area. However, the time of occurrence of maximum of the two parameters falls in September. The inter-annual variability of the annual cycle, shown by the vertical bars in the figure, shows the largest value during August for the total LH release within the ascent area; while it is in June for the HC total width. The amplitude of annual cycle is more pronounced for the HC total width than for the cycle of the total LH within the ascent region. This implies that even a small change in the LH magnitude can lead to large changes in the total width of the HC. In order to clearly bring in the inter-annual variability among the two parameters, a time series of their anomalies from January 1998-December 2013 is constructed, and is shown in figure 5.8(b). The figure shows similar pattern of variations in the two parameters, especially after the year 2003. However, the LH anomaly magnitudes are smaller than that of the anomaly magnitudes for total width as mentioned earlier. This suggests that the total LH released within the ascent region play a significant role in determining the total width of the HC. Again, this is in support of the modelling simulation which shows

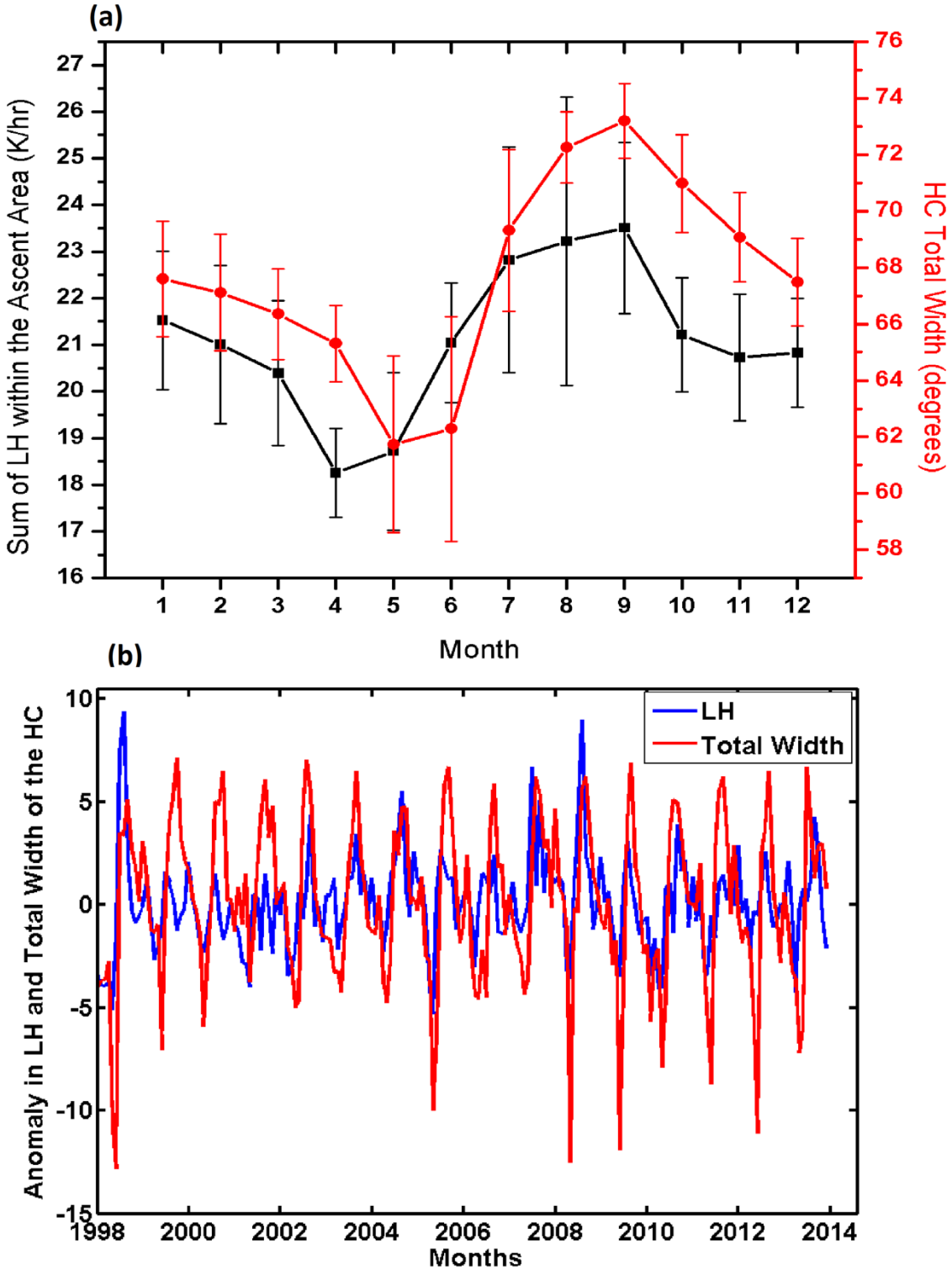

Figure 5.8: (a) The mean annual cycle of total width of the HC (*red line*) and LH released within the ascending limb of the HC (*black line*) for the period of 1998-2013. (b) Time series of anomalies (annual mean removed) of total width of the HC and LH released within the ascending limb of the HC (*blue line*).

that as the moist convections intensify, the amount of mid-tropospheric heating and the vertical extent of HC increase, leading to an increase in total width of the HC. The present results thus provide the observational evidence for previous modelling studies as well as quantify the degree of co-variability of LH and HC parameters using observational data of LH for the first time. The co-variability of HC centre, strength and width with the latitude of peak LH, width of LH distribution and total LH released within the ascending limb of the HC has been quantified and their degree of correlation along with 95% confidence intervals are summarized in table 5.1.

Table 5.1: Coefficient of correlation (along with the 95% confidence intervals in the brackets) between time series of different LH and HC parameters

Quantity	**Latitude of peak LH**	**Width of LH**	**Total LH in Ascending limb of HC**
Centre of HC	**0.90 (0.87, 0.92)**	**0.51 (0.37, 0.64)* (NH) -0.38 (-0.55, -0.17)*(SH)**	**0.58 (0.48, 0.66)**
Northward Intensity	**-0.85 (-0.88, -0.80)**	**-0.24 (-0.37, -0.1)**	**-0.20 (-0.34, -0.07)**
Southward Intensity	**-0.78 (-0.83, -0.72)**	**0.24 (0.1, 0.37)**	**0.29 (0.15, 0.41)**
Total Width	**0.41 (0.28, 0.52)**	**0.35 (0.22,0.46)**	**0.52(0.40 ,0.61)**

* Separately estimated for Southern and Northern Hemispheric Centres

However, as discussed earlier, though the correlation among HC and LH parameters shows reasonable degree of co-variability, it may be entirely due to the seasonal variations in the insolation. To further investigate this aspect, the deseasonalized time series of LH and HC parameters are constructed and discussed in the following section.

5.3.4 Correlation analyses of deseasonalized time series of LH and HC parameters

The seasonal changes in solar radiation received at the surface can affect the correlation between the LH and the HC parameters. Hence it is important to

account for this factor too while evaluating the co-variability of the two parameters. The seasonal variations can be removed by way of deseasonalization. For example, deseasonalized value of an HC parameter during January equals the value obtained by subtracting the 16 years' mean of this parameter for the month of January from that of each year's January. The deseasonalized time series' of the various LH and HC parameters are then correlated to investigate the influence of the former on the latter. To illustrate this aspect, the deseasonalized time series of all HC and LH parameters are constructed. The time series of the deseasonalized anomalies of the HC centre as well as the latitude of peak LH is shown in figure 5.9(a). A 5-point smoothing has been applied in these time series to reduce the noise and bring out a meaningful relationship between the two parameters. The two time series do not show high degree of co-variability as shown in figure 5.5(a) and significant deviations can be noticed. The deseasonalized time series of HC centre and latitude of peak LH have been found to correlate with correlation coefficient of 0.08, which is not significant. This analysis thus shows that the co-variations of HC centre and the latitude of peak LH are due to the apparent motion of the Sun across the tropical latitudes as their deseasonalized anomalies do not co-vary. It is an important observation as it shows for the first time that even though the mean positions of latitude of peak LH and HC centre co-vary but do not show same degree of co-variability at interannual time scales. The time series of deseasonalized HC centre and width of LH is shown in figure 5.9(b). The figure shows that both the parameters exhibit very good agreement, and has a reasonable degree of co-variability as compared to that in figure 5.9(a). In fact, the correlation analysis between the deseasonalized time series depicted in figure 5.9(b) shows that the width of LH distribution and the HC centre are correlated with regression coefficient of 0.53, which is significant at 95% level. Further, it is interesting to note the very good correlation between these two parameters, which were derived from two independent datasets. From the figures 5.9(a) and 5.9(b), it can be inferred that the deseasonalized HC centre is least correlated with the latitude of peak LH and well correlated with the width of LH distribution. An important result emerging from these observations is that the width of LH distribution plays a major role in the interannual variability of the HC centre as compared to latitude of peak LH. The results of correlation analysis among various HC and LH parameters after the

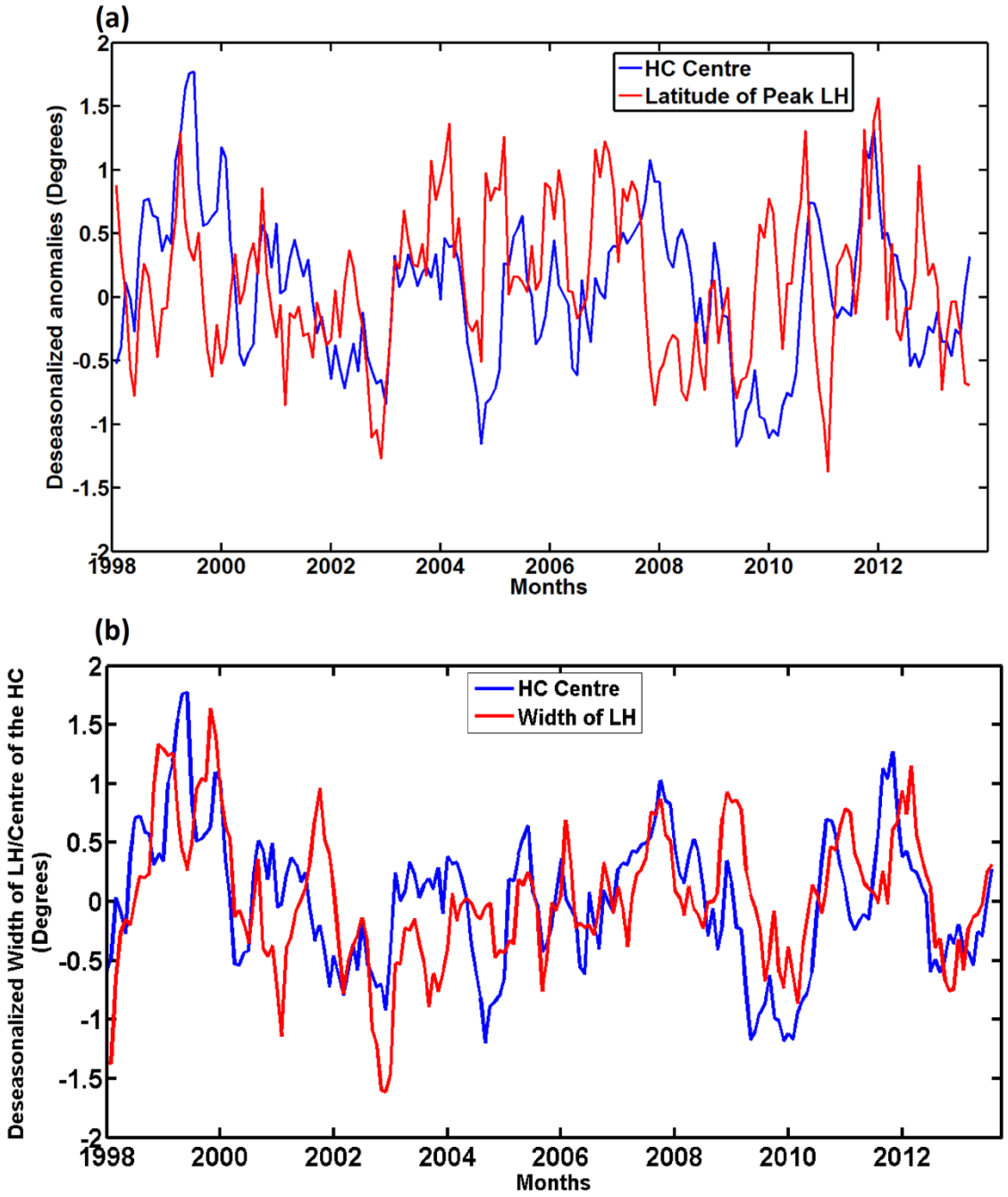

Figure 5.9: (a) Deseasonalized time series of the latitude of peak LH and the centre of the HC and (b) Deseasonalized time series of the HC centre and width of the LH.

deseasonalization are summarized in table 5.2. Significant differences have been observed for the correlation between the LH and the HC parameters with and without deseasonalization. Table 5.2 brings out that the deseasonalized HC centre is least correlated with the latitude of peak LH and well correlated with the width

of LH distribution, which brings out that the breadth of heating plays a significant role in determining the location of the HC centre and its inter-annual variability as discussed earlier. Also, the NH HC intensity is significantly correlated to the

Table 5.2: Coefficient of correlation between time series of different LH and HC parameters after deseasonalization of the series

Quantity	Latitude of peak LH	Width of LH	Total LH in Ascending limb of HC
Centre of HC	**0.08 (-0.06, 0.22)**	**0.53 (0.41, 0.62)**	**0.30 (0.17, 0.43)**
Northward Intensity	**-0.40 (-0.51, -0.27)**	**-0.36 (-0.47, -0.22)**	**-0.26 (-0.39, -0.12)**
Southward Intensity	**-0.03 (-0.17, -0.11)**	**-0.04 (-0.1, 0.18)**	**0.22 (0.08, 0.35)**
Total Width	**0.40 (0.26, 0.50)**	**0.46 (0.34, 0.57)**	**0.60 (0.47, 0.70)#**

#LH Data during 2003 to 2013 are used

latitude of peak LH (r= -0.40) upon deseasonalization, whereas the SH HC intensity does not show any significant correlation with the latitude of peak LH after deseasonalization. It is also evident from table 5.2 that NH HC intensities have reasonable co-variability with all the LH parameters. Thus it can be inferred that the latitude of peak heating as well as width of the LH distribution affects the intensity of the NH HC more strongly than the intensity of the SH HC on inter-annual time scales. Further investigations based on model simulations may be required to explain why the NH HC intensity alone shows the reasonable co-variability with LH parameters after deseasonalization. It can also be noted from table 5.2 that the total width of the HC has the highest correlation with total LH in the ascending region (r = 0.60), even after deseasonalization. This is again consistent with the modelling simulations that an increase in moist convection increases the LH release within the ascending limb of the HC, which in turn influences the vertical extent and total width of the HC. Thus it is inferred that upon deseasonalization, the HC centre co-varies with the width of the LH distribution, NH HC intensity co-varies with the latitude of peak LH, and the total

width of the HC co-varies with the total LH release within the ascending limb of the HC.

5.4 Summary

The present study quantified the influence of LH release on the spatial extent and intensity of the HC using the vertical profiles of LH derived from 16 years of space based observations of TRMM PR and MSF derived from the ERA-I reanalysis data. Observational data have seldom been used in establishing the influence of LH release on the strength and width of the HC, as most of the previous studies have relied upon modelling simulations for the same. The current study thus provided evidence for the results of these modelling simulations on how the HC is influenced by the LH release. The spatial distribution of the LH derived from the TRMM observations showed features of tropical convective activity consistent with the present knowledge, thus providing the credence for the TRMM LH measurements. While an analysis of the longitudinal distribution of LH brought out the zonal asymmetries associated with tropical atmospheric LH, vertical profiles of the zonally averaged LH revealed the thermodynamics involved in the process of cloud vertical development and sustenance. The vertical structure of zonal mean LH distribution also brought out the features of the HC, which are consistent with the present understanding on the tropical circulation. The LH profiles showed that peak latent heating occurs in the summer hemisphere, and there is marked seasonality above the ~4km level. Latitudinal distribution of the zonal mean LH during the solstice periods showed that the LH magnitudes are confined to a narrow latitudinal band in the NH during boreal summer, whereas it is broadly distributed in the SH during austral summer. This inter-hemispheric asymmetry seems to be an important character of the tropical LH distribution. The current study characterised the latitudinal distribution of column averaged (4-17km) and zonally averaged LH by means of three parameters, viz., the latitude of peak LH, width of LH distribution, and the LH released in ascent region of HC. The MSF estimated using ERA-I reanalysis data was used to characterise the HC parameters in terms of its centre, intensity and total width. The co-variability of LH and HC parameters were investigated using correlation analysis

to quantify the extent of former's influence on the latter. The significant outcomes from the correlation analysis are summarised as follows:

1. The HC centre and the latitude of peak LH shows a very good correlation with correlation coefficient of 0.9 significant at 95% level. However the correlation was observed to be insignificant after deseasonalization of the two time series. Thus the seasonal migration of the Sun cross the latitudes is found to affect the degree of co-variability between the two factors. Investigation of correlation of the HC centre with the other two LH parameters shows that the width of the LH distribution has better co-variability with the HC centre (r = 0.53) even after deseasonalization. The present analysis thus brings out the important result that the width of LH distribution plays a key role in modulating the location of the HC centre rather than the latitude of peak LH.
2. The latitude of peak LH and the HC intensities show very good degree of co-variability and are negatively correlated. The analysis shows that farther the latitude of peak LH from the equator in the summer hemisphere, stronger is the HC intensity in the winter hemisphere. This observation is consistent with the modelling simulation of Lindzen and Hou, (1988). Also the correlation analysis of HC intensities and the width of LH distribution show negative correlation with Northward intensity and positive correlation with Southward intensity. The correlation analyses of deseasonalized time series indicate that the latitude of peak heating as well as width of the LH distribution affects the intensity of the NH HC more strongly than the intensity of the SH HC on inter-annual time scales.
3. It is observed that the co-variability of the total width of the HC with the total LH released within the ascent region of the HC is relatively more than that with the other two LH parameters. The time series of these parameters as well as their annual cycle show significant degree of co-variability. This is in support of the modelling studies, which report that the intense moist convections increase the vertical extent of the HC, and thereby increase the total width of the HC. The correlation between these two parameters was high even after the deseasonalization process.

In a nutshell, the present study suggests that the LH distribution play a vital role in determining the strength and width of the HC. The position of the HC centre is

found to be influenced by the 'latitude of peak LH' before deseasonalization, and by the 'width of the LH distribution' after deseasonalization. In case of total width of the HC, the LH released in ascent region of the HC seems to play a major role as compared to the other two LH parameters. Most of the present results are consistent with that of the model simulations reported earlier. However, further studies are required to explore the discrepancies between modelled and observed influence of the different LH parameters on the HC strength and width, especially after the deseasonalization.

As discussed in section 5.1, even though the expansion of the HC in recent decades has been reported by several researchers, there is no general agreement on the processes through which the HC dynamics is affected by the various climate change signals. Using observations of LH, the present study shows that how the LH distribution which is directly related to tropical convection influences the HC dynamics. Any changes in the tropical convection due to natural or anthropogenic processes will be reflected in the LH distribution and thus in the HC dynamics. In this context, the current investigation on the co-variability of the LH distribution and the HC dynamics assumes its importance. Determining the percentage contribution of different sources (natural/anthropogenic) in modulating the LH parameters by means of observations can be a next step in identifying the key factor behind the HC expansion phenomena.

CHAPTER 6

LONG-TERM CHANGES IN HYDROLOGICAL PARAMETERS WITHIN THE ASCENDING AND DESCENDING BRANCHES OF THE HADLEY CIRCULATION

6.1 Introduction

As described in Chapter 1, the Hadley Circulation (HC) plays a key role in controlling the climate of tropics and sub-tropics. The tropical regions which fall under the ascending branches of HC are characterized by a wet climate, whereas the subtropical regions under the descending branches of the HC are either arid or semi-arid. Any change in the intensity or width of the HC will thus have paramount effects on the climate of the regions under the ascending and descending branches of the HC. Studies in the recent past have identified a poleward expansion of the HC (Fu *et al.*, 2006; Hu and Fu, 2007; Lu *et al.*, 2007; Seidel *et al.*, 2008;Stachnik and Schumacher, 2011; Nguyen *et al.*, 2013; Lucas *et al.*, 2014; Levine and Schneider, 2015; Mathew *et al.*, 2016). A major implication of the HC expansion is that it leads to an increase in the arid and semi-arid zones near the subtropics (Shin et al. 2012). As the aridity index in these regions change in response to the changing circulation patterns, the life-forms adapted to the established rainfall patterns are put under threat. Consequences of the poleward expansion has been addressed by several studies (Allan and Soden 2007; Zahn and Allan 2011; Zhou et al. 2011; Cai et al. 2012). However, studies have brought out that there is considerable longitudinal variability in the poleward shift of the dry zones in response to the changes in the HC (Chen et al. 2002; Cai et al. 2012; Post et al. 2014). Changes in strength of the HC has also been identified in the recent studies (Mitas and Clement 2005; Liu et al. 2012), which is again closely related to the changes in the extreme precipitation related events, such as floods and droughts, within the ascending and descending branches of the HC. In fact,

Chou *et al.*, (2013) has reported an increase in the severity of such events associated with the intensification of the HC. Thus the changes in the strength and width of the HC are signalled in the parameters of the hydrological cycle too.

Changes in the HC as well as hydrological cycle in a warming climate have been reported by observational as well as modelling studies. Though a consensus on the projected (Held and Soden, 2006; Lu *et al.*, 2007) and observed changes (Mitas and Clement, 2005) in the tropical circulation in a warming climate is yet to emerge, the signature of strengthening of hydrological cycle in a warming scenario is robust in both climate model simulations as well as in observations. Strengthening of the hydrological cycle is generally indicated in observational datasets by means of an increasing trend in precipitation over the HC ascending regions and a decreasing trend in precipitation within the HC descending regions. Zhou *et al.*, (2011) reported the trends in precipitation associated with the HC and showed that the subtropical dry zones have shifted $\sim 2^0$ per decade towards poles in the Northern Hemisphere (NH) during boreal summer and 0.3^0-0.7^0 per decade during Austral winter and autumnal equinox in the Southern Hemisphere (SH). In addition to this, the authors reported a poleward shift in the cloud boundaries as well as a narrowing of the high cloudiness region in the Inter-Tropical Convergence Zone (ITCZ) as well. These results emphatically provide evidence for strengthening of the hydrological cycle with the wet regions becoming wetter and dry regions turning drier, as also reported by Chou et al., (2009). However, Allan and Soden (2007) reported large discrepancy between the model-simulated and observed precipitation trends in the ascending and descending branches of the HC. Strengthening of hydrological cycle associated with the HC in a warming climate has been given by several other studies too (Held and Soden 2006; Wang and Lau 2006; Wentz et al. 2007; Allan et al. 2010; Bony et al. 2013). Efforts are now being put to identify the relation between seasonal and inter-annual variability of regional precipitation and the poleward expansion of the regional HC (Zhou et al. 2011; Cai et al. 2012). Thus, although the climate models and observations show consistent features in long-term changes of the hydrological cycle, the physical processes and regional signatures show some discrepancies among model projections.

As pointed out before, observational data show a strengthening of the HC whereas the model projections in a warming climate show a weakening of the circulation. Held and Soden, (2006) put forward that the weakening of tropical circulation given by the model simulations is due to the different responses of precipitation and water vapour in a warming climate. Fasullo and Trenberth, (2012) showed by means of observations and model simulations that the tropics and subtropics are teleconnected through the seasonal variation of relative humidity (RH), which in turn affects the cloud formation and precipitation. Modelling simulations by Wright *et al.*, (2010) and Sherwood *et al.*, (2010) reported that the poleward expansion of HC can partly explain the changes in RH in a warmer climate. Hence it is presumed that the RH is closely related with the changes in the HC. Sherwood *et al.*, (2010) emphasized that the role of the HC characteristics in controlling the subtropical moisture budget should be investigated, which they thought can explain the precipitation and cloud formation in association with the shifting of climate zones. Zahn and Allan, (2011) reported the long-term changes in water vapour transport associated with the HC using ERA-I reanalysis data. These authors showed a strengthening of the inward (at low levels) and outward (at mid- level) transport of water vapour in the ascending branch of the HC. Su *et al.*, (2014) reported that both vertical and meridional structure of RH and clouds are closely associated with the large-scale circulations. Lau and Kim, (2015) studied the HC changes and their role in increasing global dryness in a warming scenario by means of 33 climate model simulations. The results showed a reduction in RH in the upper troposphere over the deep tropics and in the lower troposphere over the extra-tropics. Thus there are strong evidences for the changes in RH associated with the poleward expansion of the HC in warmer climate, both in climate model simulations and in observations inclusive of reanalysis datasets.

Climate models use the information on RH to parameterize the clouds and hence calculate their radiative effects, which in turn determines the atmospheric energy budget. Hence the changes in RH have an influence on the fraction of cloud cover in the atmosphere. The changes in cloud cover as well as their vertical structure over a given location play an important role in determining the surface temperature, the meridional gradient of which determines the generation of

atmospheric circulations. Many studies in the past have reported the interactions between large-scale circulations and clouds, especially between the HC and clouds. Studies by Tselioudis *et al.*, (2016) inferred that high cloud cover of the mid-latitudes has significant correlation with the width of the HC in almost all regions and across all seasons. Eastman and Warren, (2012) identified a decline in the fraction of high and middle-level clouds at the mid-latitudes, as well as a poleward shift in the total cloud cover associated with the storm tracks of both the hemispheres. Decrease in mid-latitude cloud cover increases the outgoing long-wave radiation (OLR) amount, as discussed by Chen *et al.*, (2002), and is hence related to the phenomena of expansion of the subtropical dry zones. Norris *et al.*, (2016), using the observations on cloud cover from the International Satellite Cloud Climatology Project (ISCCP) and Extended Pathfinder Atmospheres (PATMOS-x) datasets, brought out that the high cloud top height has also increased at all latitudes, leading to a surface warming. Changes in the cloud fraction were observed not only in the subtropical regions, but in the tropical regions as well. For instance, Eastman and Warren, (2012) showed by means of surface observations that there is a strong northward shift of the cloud cover over the tropics, in addition to a decline in the amount of low cloud cover. Zhou *et al.*, (2011) using ISCCP dataset reported a decreasing trend in the total cloud fraction over tropics. Recent modelling studies by Su *et al.*, (2017) reported a decrease in high cloud fraction averaged over the tropics, in response to the increased surface warming due to CO_2. The authors attributed this decrease in tropical high cloud cover to the decrease in the area of ascent of the tropics and consequent strengthening of the ascent in response to the surface warming. Greater loss of long wave radiation over the tropics and cooling is thus expected to accompany this high cloud shrinkage. Su *et al.*, (2014) using 15 climate model simulations showed that the meridional structure of the HC will have weakening and strengthening regions within the tropics. These authors projected that there will be alternating ascending (5^0N-5^0S) and descending (5^0N-15^0N and 5^0N -15^0S) regions within the ascending limb of the HC. The changes in cloud fractions were observed to be consistent with this complex meridional structure of the HC. The vertical velocity projections showed weakening trend in the descending zones of the HC (15°N–30°N and 20°S–30°S) and strengthening trend at the flanks of the

descending zones (30°N to ~40°N and 30°S to ~40°S), which is consistent with the poleward expansion of the dry zones. However, it has to be remembered that these changes have been projected for the 2074-2098 period, and hence it is difficult to see its signature in the present day climate. Thus there exists ample evidence for changes in cloud fraction in association with the HC, and *vice versa,* in a warmer climate.

From the above discussion, it is clear that the components of hydrological cycle are modulated by the HC dynamics, especially in a warmer climate. Researchers have mostly relied on climate model simulations to establish a clear signal of global warming on the HC dynamics as well as its role in modulating the components of the hydrological cycle. In fact, the studies on HC and its link to hydrological cycle using climate model simulations are outpacing those using observations and reanalysis datasets. It is thus necessary to reduce this gap. Moreover, simultaneous investigations on long-term changes in all the three components of hydrological cycle viz., moisture, clouds and precipitation, with respect to the ascending and descending branches of the HC are seldom available. In this regard, the present study focuses on analysing the long-term changes in relative humidity, cloud fraction (resolved into low, mid and high level clouds) and precipitation within the ascending and descending limbs of HC using observational (GPCP) and reanalysis (ERA-I) data. The ascending and descending limbs of the HC are identified using the meridional Mass Stream Function (MSF) metric, a metric that can easily track the mass motion in the atmosphere in the meridional direction. The study thus attempts to discuss the influence of HC on the patterns and trends in the three main components of the hydrological cycle. The simultaneous investigation of long-term changes in relative humidity (RH), cloud fraction (CF) and rainfall (RF) within the ascending and descending regions of HC (identified using the MSF metrics) by means of observational and reanalysis datasets is a relatively new component of the present study as compared to the earlier studies. The datasets used and methods followed are discussed in section 6.2, results are discussed in section 6.3, and summary is provided in section 6.4.

6.2 Data and Methodology

The present study employs three components of hydrological cycle viz., RH, CF and RF, along with the HC parameters derived from MSF metric. The data on RH and CF is obtained from the ECMWF-Interim (ERA-I) reanalysis, and that on RF is obtained from the Global Precipitation Climatology Project (GPCP). A detailed description of GPCP and ERA-I datasets is given in Chapter 2. The GPCP rainfall dataset is constructed by combining various ground and satellite based observations of precipitation and gridding them onto 2.5°x2.5° grids (Adler et al. 2003). The monthly mean precipitation rates obtained from GPCP (version 2) for the period 1979-2016 are used in the present study. A zonal average of this monthly mean rainfall data from GPCP is used to construct the annual cycle of the magnitude as well as trend in RF.

The moisture and cloud cover data is obtained from ERA-I reanalysis (Dee et al. 2011). The zonal mean vertical profiles of RH obtained from the ERA-I reanalysis are used in the present study to investigate the RH trends in the ascending and descending branches of HC. The CF data from ERA-I is classified into low-, middle- and high- level clouds depending on the ratio of cloud top pressure to the surface pressure (defined as sigma). Sigma<0.45 represents high cloud cover, 0.45<sigma<0.8 represents middle cloud cover, and 0.8<sigma<1 represents low cloud cover fraction. The current study utilizes the zonal mean of these individual CF for the present study.

As mentioned in section 6.1, the ascending and descending branches of the HC are identified using the MSF metric. This metric is calculated from the meridional wind data obtained from the ERA-I reanalysis using the method described in Chapter 2. As previously done, MSF at 500hPa is chosen as the reference level to identify the HC parameters. The locations on either side of the equator where MSF becomes zero are marked as the HC edges; the location near to the equator where it has zero value is the HC centre; and the location on either side of the equator where MSF at 500hPa maximize(minimize) are defined as the centre of the hemispheric HC. The region between NH cell centre and the SH cell centre (which is inclusive of the HC centre) is the region where ascending motions

prevail. The region between cell centres and the HC edge for the respective hemispheres is identified as the region of descent.

6.3 Results and Discussion

6.3.1 Hadley Circulation: Ascending and Descending regions

The zonal mean meridional MSF is estimated from the ERA-I reanalysis meridional winds using method outlined in Chapter 2 for the period 1979-2016 for four seasons and are shown in figures 6.1(a-d) for boreal winter, vernal equinox, boreal summer and autumnal equinox, respectively. Positive values of MSF are indicative of a northward flow, whereas negative values indicate that the mass flow is southward. The MSF pattern shows strong winter cells and weak summer cells during solstices, which is consistent with the known features of the HC. The figure also shows that the SH cell is wider and stronger during autumnal equinox as compared to that during vernal equinox. This is one of the notable differences in the HC during the equinoxes. Ascending motions prevail within the latitude of maximum (positive) MSF and the latitude of minimum (negative) MSF, for example - between 20^0S and 15^0N during boreal winter. The region of descent in the NH extends from the latitude of maximum positive MSF (say, 15^0N during boreal winter) up to the latitude where MSF changes its sign (at $\sim 30^0$N during boreal winter). Similarly, the region of descent in the SH extends from latitude of minimum MSF (say, 10^0S during boreal summer) up to the latitude where MSF changes its sign (at 25^0S during boreal summer).

Further, as mentioned in section 6.2, the boundaries of HC ascending and descending regions are estimated from MSF at 500hPa. Figure 6.2 gives a holistic view of the annual cycle of the various boundaries of the HC obtained from the zonal mean MSF metric. Vertical bars show their inter-annual variability. The blue line shows the annual cycle of the centre of the HC, which is more or less consistent with the annual cycle of migration of the ITCZ. The magenta and green lines show the southward and northward boundaries of the ascending branch of the HC respectively. The area enclosed between these boundaries is the ascending region of the HC. The variation of the hydrological parameters in these regions will be discussed in the succeeding sections. The black and red lines

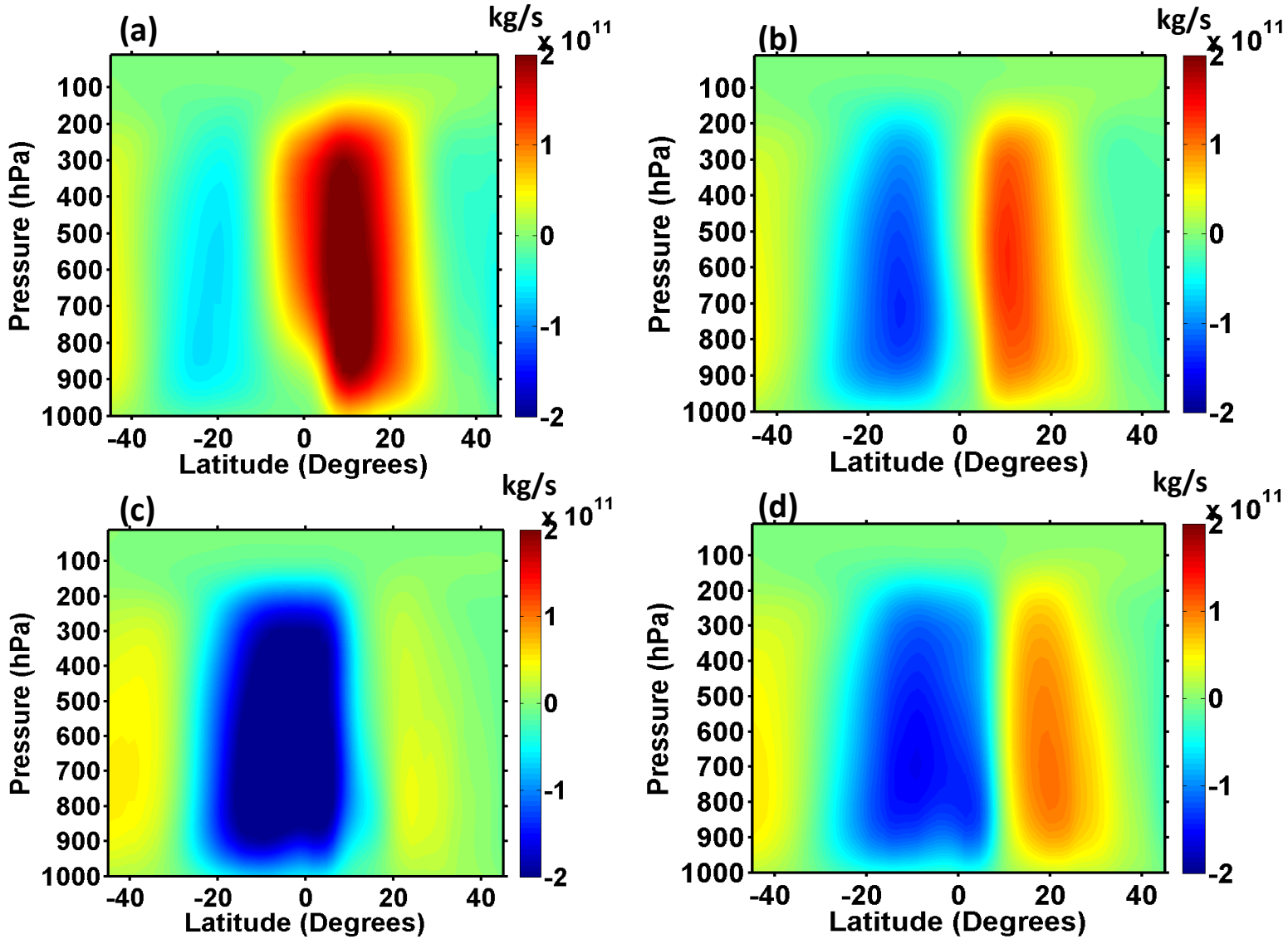

Figure 6.1: Latitude- pressure level cross sections of the zonal mean meridional stream function for (a) boreal winter (b) vernal equinox (c) boreal summer and (d) autumnal equinox seasons estimated from ERA-I reanalysis for the period 1979-2016.

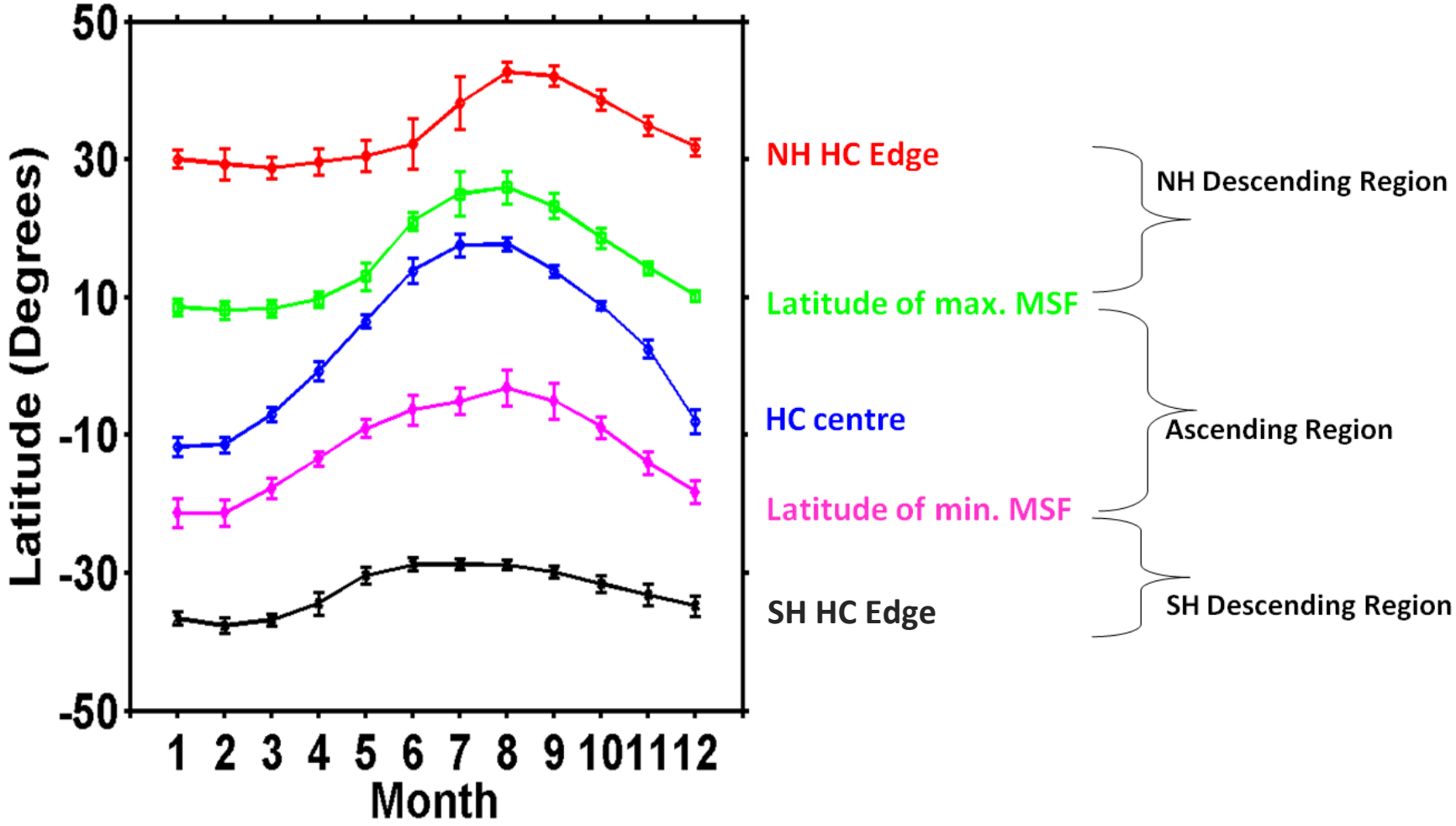

Figure 6.2: Annual cycle of the HC centre, HC edges and the NH (SH) cell centres. Vertical bars indicate the standard deviation corresponding to their inter-annual variability. HC ascending regions are defined as the region between the latitude of maximum MSF and the latitude of minimum MSF. HC descending regions are defined as the regions between the latitude of maximum (minimum) MSF and the NH (SH) HC edge.

represent the southward and northward edges of the HC respectively. The region between the boundaries of the ascending region and the edge of the HC represents the regions of descent associated with the HC in both the hemispheres. The distance between the southward and northward edges gives the total width of the HC. Figure 6.2 shows that the descent regions are wider during winter than summer, which is in conjunction with the stronger winter cell that can be seen in figure 6.1. The descending region is narrowest during boreal summer in the northern hemisphere. The ascending region is wider during boreal winter as well as summer seasons. All the features observed in the annual cycle of HC parameters are consistent with the present understanding thus validating the procedure adopted to identify them.

6.3.2 Zonal mean distribution of Relative Humidity, Cloud Fraction and Precipitation

As discussed in section 6.1, the atmospheric relative humidity, cloud fraction and rainfall are important components of the hydrological cycle, and are modulated by the HC. Figures 6.3(a) and (b) show the zonal mean latitudinal distribution of relative humidity (RH), total cloud fraction (CF) and rainfall (RF), which are normalized to their peak values, for the month of January and July, respectively. The RH corresponds to that at the 500hPa pressure level. The datasets have been averaged for the study period. The vertical lines are indicative of the mean value of the HC boundaries derived from figure 6.2 for a given month. From this figure it is evident that the RH, CF and RF show their maximum values within the ascending regions of the HC and minimum values in the descending region. This is a general feature of the hydrological cycle. The normalized peaks of RF show its maximum within the ascending regions of the HC during both January and July months whereas the CF shows a maximum of ~0.77 in January and ~0.8 in July. The peak value of CF occurs over high latitudes during both January (at ~61^0S) and July (at ~88^0N) (the latitude axis in figures 3(a) and 3(b) have been limited to 50^0 to highlight the HC region). Thus the peaks observed in CF over the ascending regions of the HC are secondary peaks, and the latitude of their occurrence coincides with the peaks observed in the RF. In the case of RH also the primary peaks are observed over high

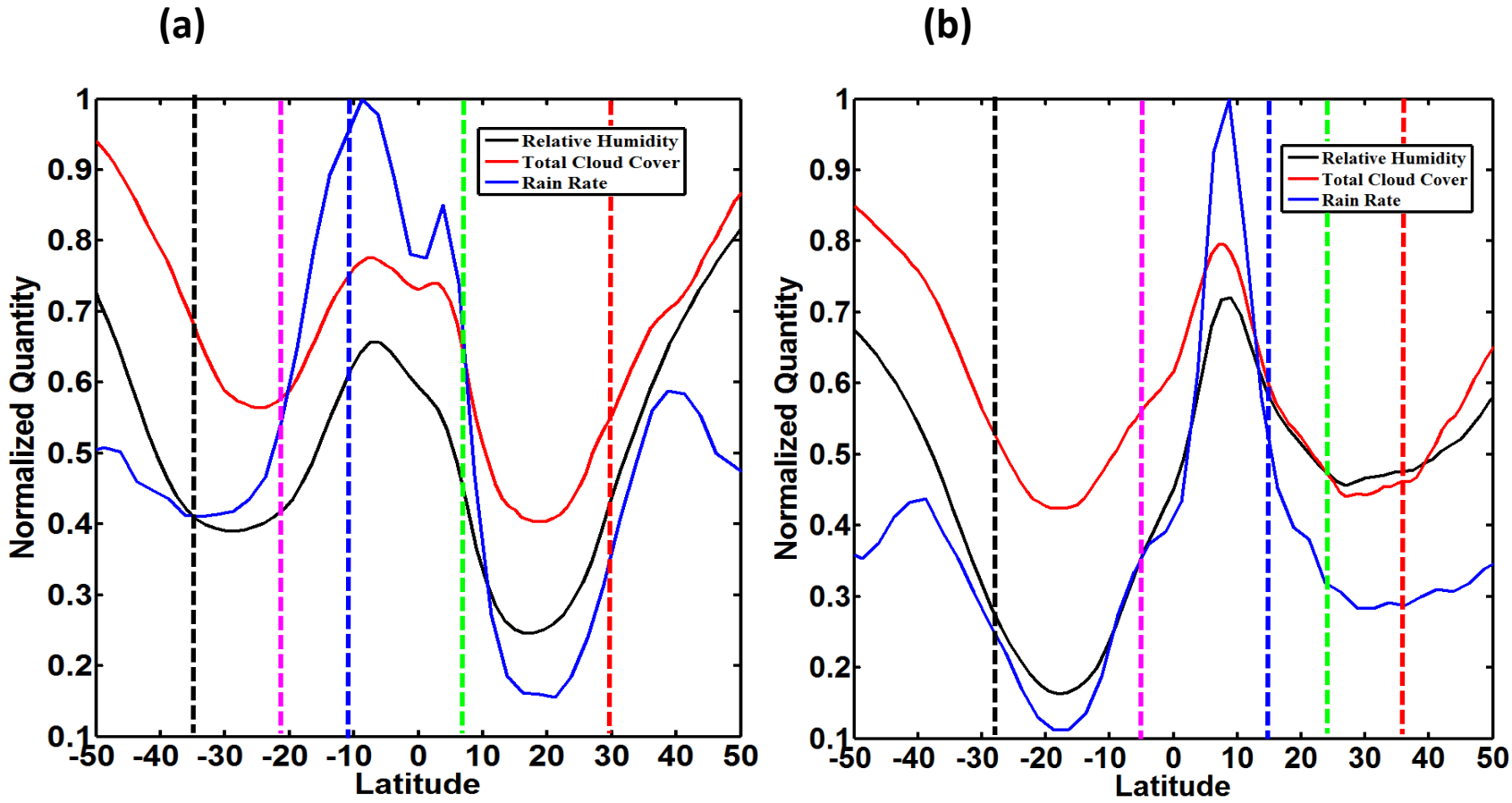

Figure 6.3: Latitudinal distribution of zonal mean relative humidity (RH), total cloud cover (CF) and rain rate (RF), which are normalized to their peak values for the months of (a) January (b) July during the study period. Vertical dashed lines correspond to the average location of the HC edges, HC centre and the NH/SH cell centres. *Colour codes same as for Figure 6.2*.

latitudes. The RH also shows its secondary peak in the ascending region of the HC, with magnitudes 0.66 in January and 0.71 in July as shown in figure 6.3. The observed pattern of peaks over the tropics in all the three parameters show a narrower distribution in the month of July as compared to the broader distribution of these parameters in the month of January. This aspect can be attributed to relatively large land region to the north of the equator; the atmospheric convection is concentrated in narrow regions over land as compared to that over the oceanic regions in the south. The minimum values of RH, CF and RF are found in the descending regions of the HC with notable differences in January and July. Thus figure 6.3 depicts the distribution of RH, CF and RF in the ascending and descending branches of the HC. The long term changes in RH, CF and RF parameters with respect to the HC are discussed in the following sections.

6.3.3 Long term changes in RH, CF and RF over the ascending and descending branches of the HC

6.3.3.1 Relative Humidity

Seasonal and regional changes in RH influence the cloud type and its distribution, which in turn can bring about changes in the radiative balance of the atmosphere. Since the HC largely depends on the amount of radiative imbalance between the tropics and the poleward latitudes, it is important to investigate the vertical structure as well as annual cycle of RH as a function of latitude. Figure 6.4(a) shows the annual cycle of zonal mean latitudinal distribution of RH at 500hPa averaged during the years 1979-2016, along with the various HC parameters. The black lines correspond to boundaries of ascending regions (dashed lines) and the edges (solid lines) of the HC. The magenta line corresponds to the annual cycle of the latitude of maximum (dashed line) and minimum (solid line) magnitudes of RH at 500hPa. The minimum in RH is estimated separately for Northern and Southern hemispheres. The standard deviations correspond to the inter-annual variations of respective parameters. As mentioned earlier, the region between the boundaries of ascending regions and the HC edges correspond to descending regions of the HC in either hemisphere. The RH at mid-troposphere is important, since the moisture at these

levels determine the ability of a parcel to remain saturated during the ascent. Theoretically, a RH of ~50-60% at middle troposphere is adequate to promote deep convection (Marks, 2015). It is clear from figure 6.4(a) that the deep tropics (between 10^0N and 10^0S) have RH ~53-65% at 500hPa, which is conducive for the formation of deep convection. The moisture content decreases on either side of the deep tropics, reaching the minimum value in the subtropical regions. The climatological RH of the subtropical dry zones is never >35%, as given by figure 6.4(a). The inter-annual variability of the latitude of minimum (maximum) RH is well within the region of descent (ascent) given by the MSF metric. The latitude of minimum (maximum) RH resides approximately at the middle of the descent (ascent) region of HC. Also, the latitude of maximum and minimum RH exhibits a poleward migration from winter to summer in the respective hemisphere. The 500hPa levels within the subtropical descent regions are drier during the winter season of the respective hemisphere. On the other hand, the 500hPa levels within the tropical ascent regions are moist during NH summer season (as compared to SH summer), wherein the low level inflow is primarily from the oceanic regions of the SH. From figure 6.4(a) it can be noted that the ascending region of HC derived from MSF metric clearly separates moist region from dry region and, thus, is very useful to investigate the long term changes in parameters associated with hydrological cycle with respect to the HC changes.

Figure 6.4(b) shows the annual cycle of the trends in zonal mean RH at 500hPa as a function of latitude. The purple contours represent the trends which are significant at the 95% level. The white patches correspond to the regions which show no trends. The figure shows a general moistening pattern in the ascending limb of the HC, especially at the edges of the ascending regions in either hemisphere. The largest trends (~1 to 1.5% per decade) are found to be on either side of latitude of maximum RH in both the hemispheres, which indicates a strengthening of the HC. Regions between the latitude of minimum RH and the SH edge (the descending region of HC) show significant negative trends ~ -0.5% to -1% per decade throughout the year, except during austral summer. On the other hand, regions

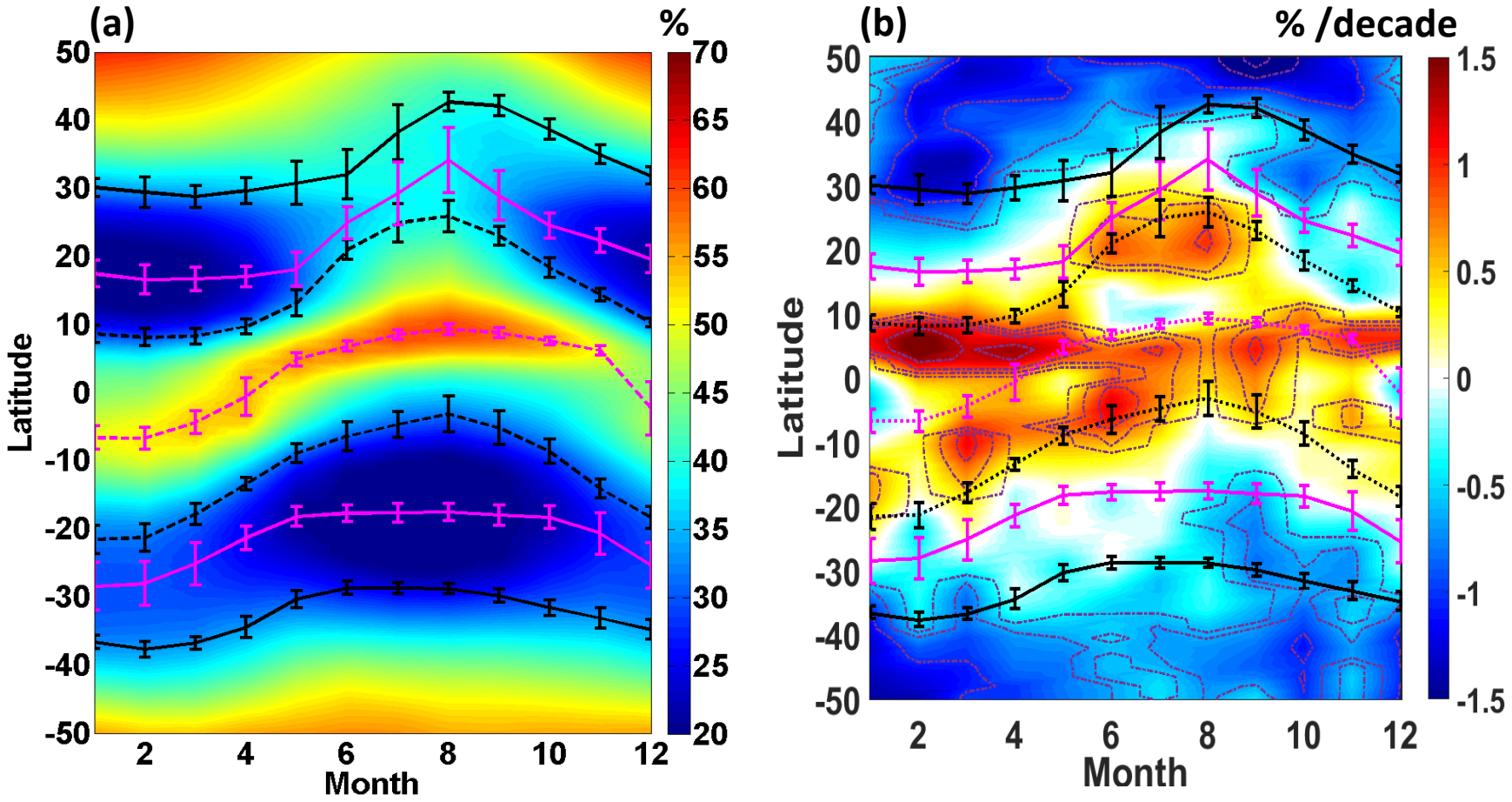

Figure 6.4: (a) Climatology of the annual cycle of zonal mean RH at 500hPa as a function of latitude for the period 1979-2016 obtained from the ERA-I dataset (b) Annual cycle of the trends in zonal mean RH at 500hPa as a function of latitude. *Black solid lines show the HC edges, black dashed lines show the individual cell centres. Region confined between the black dashed lines is the HC ascending region. The region between the black dashed line and the black solid line, in both hemispheres, is the HC descending region. Dashed magenta lines is the latitude of maximum 500hPa RH, whereas the solid magenta lines represent the latitude of minimum 500hPa RH. Purple contours in (b) show the trends significant at 95% level*.

between the latitude of minimum RH and the NH edge show negative trends during this time of the year. At the poleward edges of the HC in both the hemispheres, the RH shows decreasing trends (~ -0.5% to -1% per decade). Thus, a general positive trend in RH in the HC ascending regions and negative trend in the regions poleward of the HC edges point towards a mid-tropospheric moistening and drying process, respectively; this is presumed to be associated with the strengthening of the HC. Signature of poleward expansion of the HC can also be observed in the moistening (drying) of the equatorward (poleward) side of the latitude of minimum RH. Thus the long-term changes in the RH at 500hPa level are consistent with the strengthening as well as expansion of the HC.

In order to investigate whether this moistening/drying trend is consistent at all levels, climatology and trends in RH for different pressure levels are delineated in figures 6.5 and 6.6, respectively. The climatology of vertical variation in RH is analysed separately for the January and July months so as to explore the seasonal variations. Figure 6.5(a) and 6.5(b) shows the zonal mean climatology of RH in terms of latitude-pressure level sections for the months of January and July, respectively. In the lower troposphere, the RH is relatively high (~85% or more) during both months over the ascending regions of the HC. In the month of January, the RH at the 800-300hPa altitudes is ~30- 40% over the descending regions in the SH whereas it is below 30% in the NH. Thus NH descent regions are drier than that of SH in January. During the month of July also a similar pattern is observed; however, the descending branch of the SH is relatively drier (RH<20%) than its NH counterpart (RH is between 35% - 45%). The SH descending branch during July is in fact drier (RH <20%) than the NH descending branch (RH ~20% - 30%) during January. The mid-troposphere over the ascending region is relatively wetter during July (RH ~ 65% - 80%) than in the month of January (RH ~ 60%). Thus figure 6.5 depicts the mean climatology of RH, in terms of latitude-pressure level sections, within the ascending and descending branches of the HC, and is found to be consistent with the present understanding. Further, vertical structure of the trends in RH is estimated and is depicted in figures 6.6(a) and 6.6(b) for the months of January and July, respectively. Trends significant at the 95% level are represented by means of purple

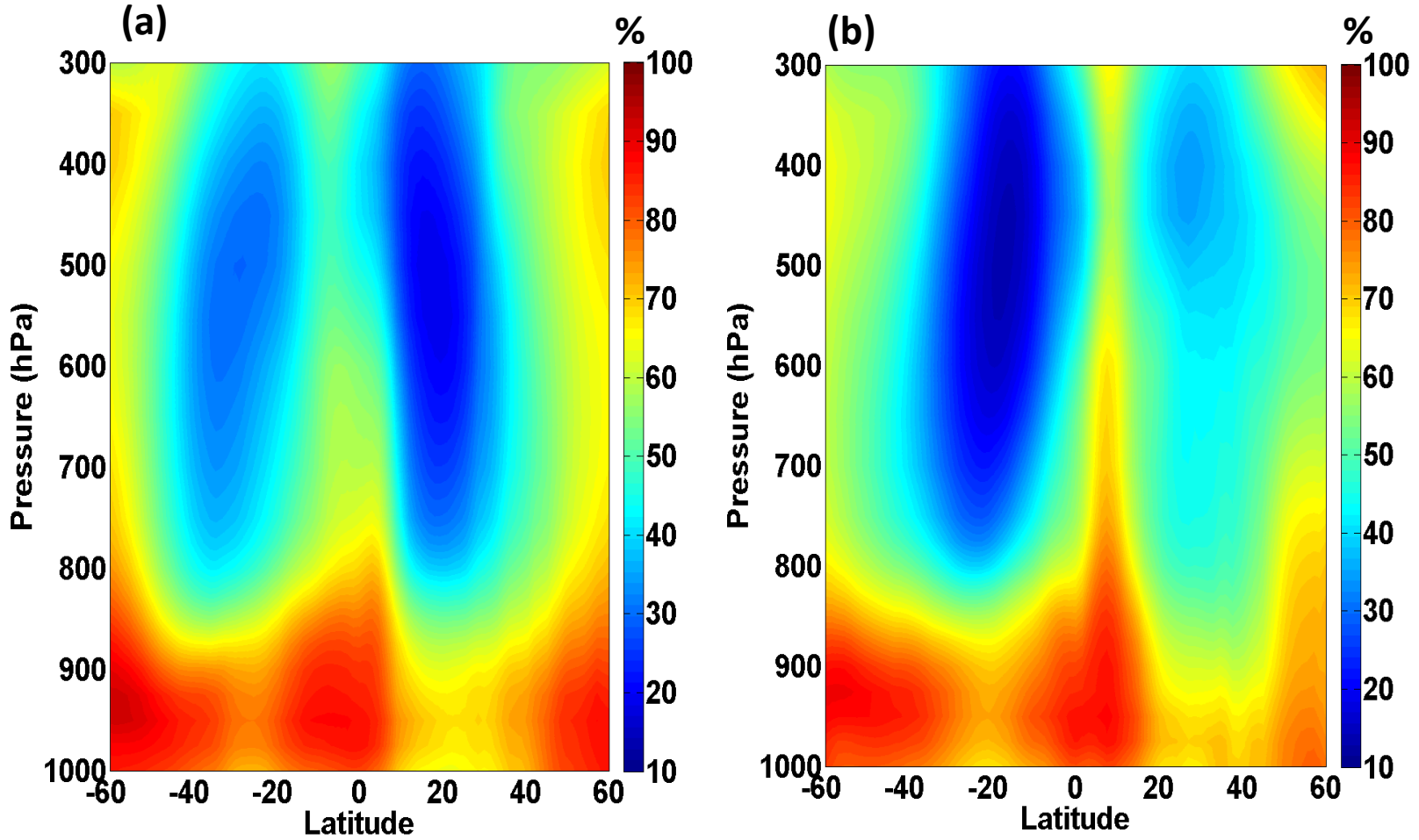

Figure 6.5: Climatology of the vertical distribution of RH as a function of latitude for (a) January (b) July during the period 1979-2016.

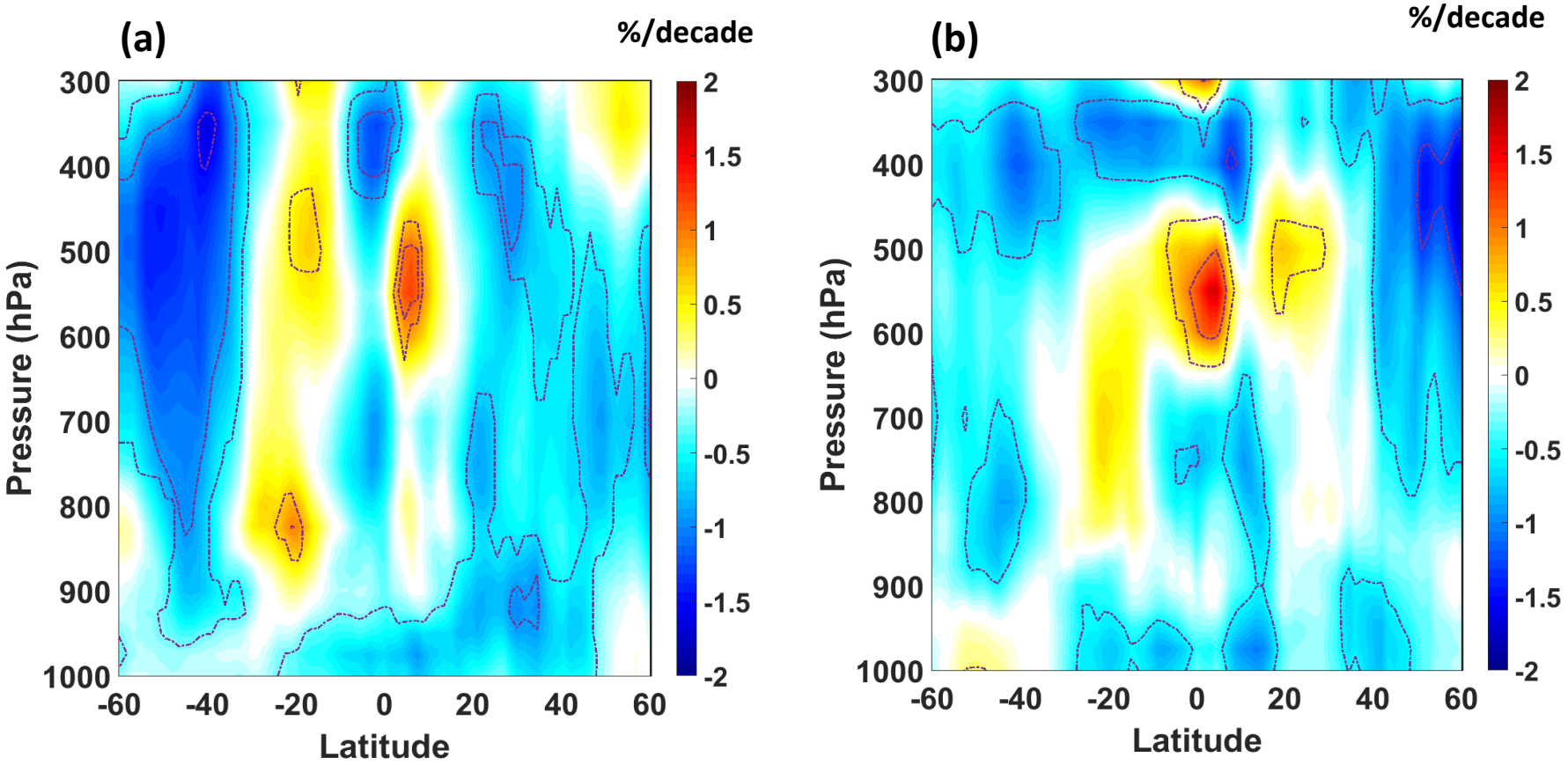

Figure 6.6: Vertical distribution of the trends in RH as a function of latitude for (a) January (b) July during the period 1979-2016. *Purple contours show the trends significant at the 95% level*.

contours. During the month of January, deep tropics show negative trends in RH throughout the troposphere and are significantly negative in the 400-300hPa altitudinal region (~ -1.5% per decade). Trends are significantly positive between 600-400hPa levels at the edges of ascending region (~0.5% – 1.5% per decade) and are the strongest in NH as shown in figure 6.6(a). However, the trends are positive throughout the troposphere at the edges of the SH ascending region. As mentioned earlier, a positive trend in RH in the mid troposphere at the edges of ascending region indicates the strengthening of the HC. Increased ascent due to strengthening of the HC is followed by a strengthening of the compensating return flow of the HC in the lower troposphere, which brings relatively more moisture to these levels. This feature can be noted from the significant positive trend ~0.75% per decade exhibited between 900hPa and 800hPa levels in SH (see figure 6.6(a)). However such a feature is not noticed at these levels in the NH. Stronger positive trend in lower tropospheric RH in SH is due to the dominance of oceanic region in the hemisphere. This aspect can be further confirmed from figure 6.5(a). This figure shows a relatively wetter lower troposphere in the SH subtropical region, from where the HC return flow begins, as compared to that in the NH. Figure 6.6(a) also brings out that the strongest drying is observed at the SH edge of the HC during the month of January (~ -1.5% per decade). A relatively weak drying trend (~ -0.5 to 1% per decade) is observed at the NH edges of the HC. During July, as shown by figure 6.6(b), there is strong moistening trend (0.5% – 1.5% per decade) between 600hPa and 500hPa levels at the edges of ascending region, and drying trend both above and below these levels. In the lower troposphere, again, a positive trend can be noted at the edges of the HC ascending region in the SH corresponding to the strengthening of the HC return flow. This feature is absent in the NH due to obvious reasons discussed earlier. During this month, the strongest drying trend is observed at the poleward edges of the HC in the NH (~ -1% to 1.5% per decade). Figure 6.6(b) also brings out that the deep tropics also show significant drying trend throughout the troposphere, expect at the mid-troposphere (600-500hPa). During both the months, the RH trends are negative below 900hPa, which is consistent with the increasing trends in surface temperature. Thus the vertical structure of RH and their long-term variability across

the latitudes show that there is mid-tropospheric moistening at the edges of ascending regions of HC and drying at their poleward edges. Earlier studies, which employed vertical velocity for separating the ascending and descending branches of the HC, reported a moistening of the ascending region and drying of the descending region. However, these studies did not show where exactly within the ascending region does the moistening takes place, as the trends have been derived for the entire ascending and descending region. The present results show that the moistening takes place at the edges of the ascending region rather than in the entire region; same is the case in drying trends in the descending regions.

6.3.3.2 Cloud Fraction

Figure 6.7(a) shows the annual cycle of the total CF as a function of latitude in conjunction with the annual cycle of the HC parameters. The CF has been derived from ERA-I reanalysis and averaged for the period 1979-2016. Limiting the current analysis to the regions within the HC boundaries, the latitude of maximum cloud fraction is observed to be well within the region of ascent, and is generally confined between 10^0N and 10^0S latitudes (In fact, the maximum cloud fraction occurs over the Southern Ocean in the ~60^0S -65^0S latitudinal belt during all the seasons. However, as the present analysis is limited to the HC latitudes, the maximum cloud fraction is located in deep tropics). The figure shows that the cloud fractions are between 50% and 75% within the region of ascent. Within the deep tropics, the cloud cover is observed to be more during boreal summer (~75%) than winter (~68%). The total cloud cover fraction falls off on either side of the observed deep tropical maxima. Subtropical dry zones are defined as the regions between the latitude of maximum (minimum) MSF and the poleward edge of the HC in the NH (SH). These dry zones are characterized by the low amounts of cloud fraction ~<40% since these are the regions under the descending limb of the HC. The cloud cover fraction is more or less uniform throughout the NH subtropical dry zone for all seasons except for boreal winter, wherein the cloud fraction is well below 30%. One more striking feature in figure 6.7(a) is that the cloud fraction over the descending region of the HC in SH is relatively more than that in NH, at least by 10%. This can be

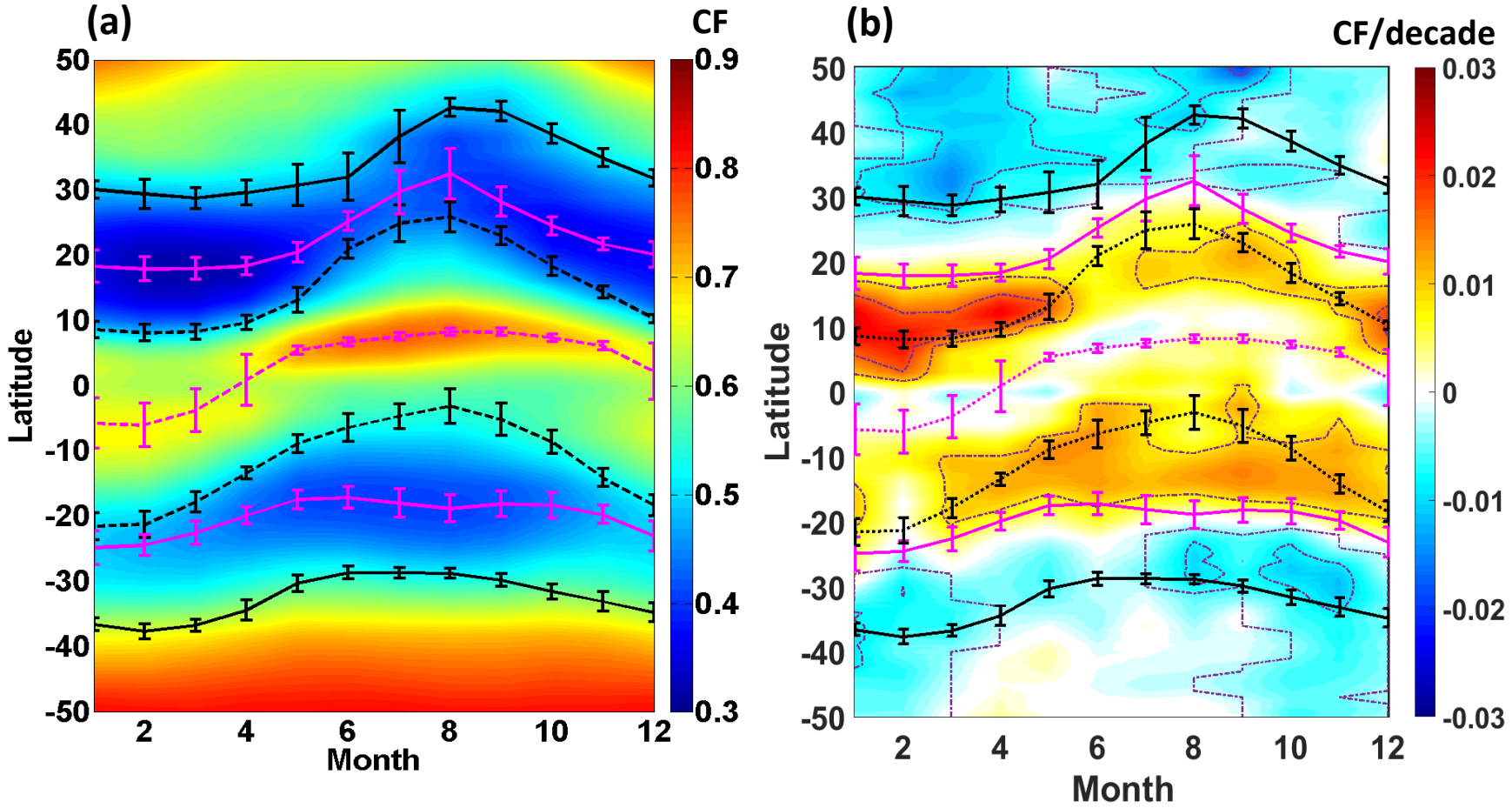

Figure 6.7: (a) Climatology of the annual cycle of zonal mean total CF expressed as a function of latitude for the period 1979-2016. (b) Annual cycle of the trends in zonal mean total CF expressed as a function of latitude. *Colour codes same as that of figure 6.4, but for HC parameters and total CF. Purple contours in (b) show the trends significant at the 95% level*.

explained by the relatively more oceanic region in SH subtropics as compared to NH. Under the descending branches of HC, especially over the oceanic regions, the stratocumulus clouds form persistently (Subrahmanyam and Kumar 2017). This aspect can be substantiated from figure 6.5, where the RH in the lower levels is comparatively more over the SH subtropical region than that in the NH during both January and July months. Further, the annual cycle of CF shown in figure 6.7(a) is consistent with that of RH depicted in figure 6.4(a). Thus it can be inferred from figure 6.7(a) that the annual cycle of latitudinal distribution of the CF is consistent with the present understanding, and also provides insights into its variability with respect to the HC boundaries. The annual cycle of trends in zonal mean total CF as a function of latitude is shown in figure 6.7(b). The trends significant at the 95% confidence level are represented here by means of purple contours. The most significant feature of this figure is the null/insignificant trend in total cloud cover in the regions close to the latitude of maximum cloud cover (indicated by dashed magenta line). Similar to the trends in RH, the trends in cloud cover also show significant increasing trends at the edges of the ascending region in SH as well as in NH, with stronger trends in the latter. Thus the region of ascent contain both increasing and decreasing cloud cover regions, with positive trends being shown by the regions on either side of the deep tropics. Average trend in these regions is ~1% per decade. It can also be noted from figure 6.7(b) that within the HC descending regions identified by the MSF metric, there are regions of positive as well as negative trends, separated by the latitude of minimum cloud cover. This feature can be noted in both the hemispheres. Regions equatorward of the latitude of minimum cloud cover show significant increasing trend in total cloud cover fraction (~1% - 2% per decade), and those poleward of the latitude of minimum cloud cover shows either null or negative trend. Positive trends in the NH subtropical zones equatorward of the latitude of minimum cloud cover are stronger during boreal winter (~2.5% per decade) than summer (~1% per decade). A decreasing trend ~0.5% - 1% per decade is observed at the poleward edges of HC in both the hemispheres as shown in

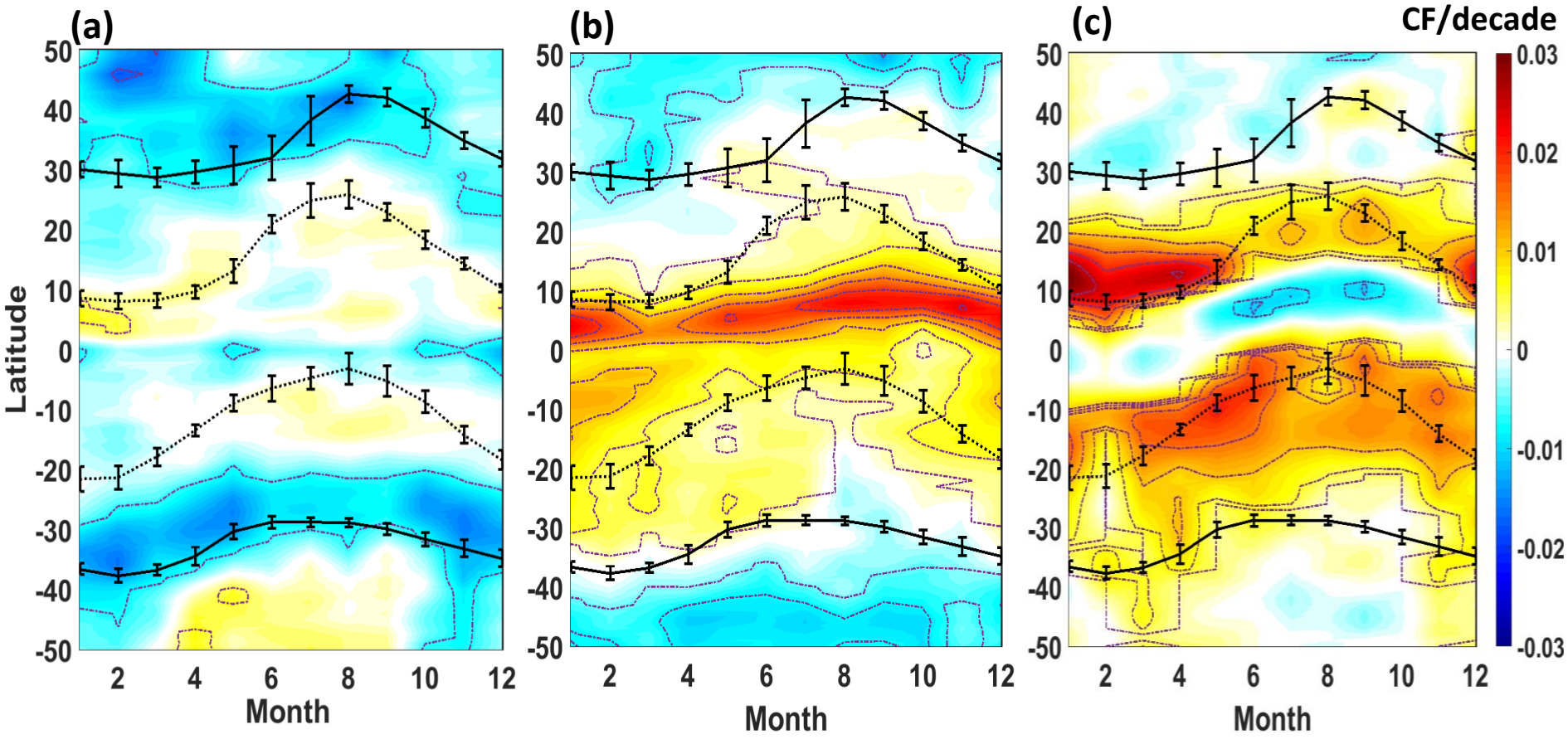

Figure 6.8: Annual cycle of the trends in (a) low (b) middle and (c) high level cloud fractions, expressed as a function of latitude, within the HC ascending and descending regions. *Outermost solid black lines in both hemispheres show the HC edges, inner dashed black lines show the boundaries of the HC ascending region. Purple contours show the trends significant at 95% level.*

figure 6.7(b), which is consistent with the trends observed in RH. The decreasing trends in total cloud cover in the extra-tropical regions which lie close to the poleward edge of the HC is suggestive of the expansion of the HC and the subtropical dry zones. As discussed in section 6.1, the 'type of cloud' also plays a role in the radiative balance of the atmosphere. Hence the trends in low level, middle level and high level cloud fractions are estimated to examine their contributions to the trends in total cloud fraction, and is shown in figure 6.8(a-c), respectively. The latitude of maximum and minimum cloud fraction is not indicated in these figures. However, the HC boundaries corresponding to the ascending and descending regions are provided. From these figures, it can be noted that the long-term changes in low level clouds with respect to the HC boundaries do not show any significant trend. An exception to this is at the poleward edges of HC in both hemispheres, wherein the trends are negative. In the deep tropics, the middle level cloud fractions depicted in figure 6.8(b) show strong positive trends (~2% per decade) in contrast to the strong negative trend in high cloud cover fraction (~-1% per decade) depicted in figure 6.8 (c). Such a decrease in deep tropical high cloud cover is in conjunction with the modelling studies, and is attributed to the increase in mean surface temperature over the tropics (Su et al. 2017). The striking feature of figure 6.8, however, is the similar pattern of trends in the high level cloud fraction shown in figure 6.8(c) and the total CF shown in figure 6.7(b), especially in the ascending region of the HC. The decreasing trend in total cloud cover in the near-equatorial regions is found to be consistent with the strong negative trend in high cloud cover in these regions. Again as in the case of RH and total cloud fraction, the increasing trends in the high cloud cover are found to be at the edges of the ascending branches in both the hemispheres and is ~1.5% per decade. The descending region of the HC in the SH shows slight increasing trend in the high cloud fraction; however this feature is not prominently seen in the total cloud fraction. This is because the significant decreasing trend in low cloud fraction in the descending region of the HC compensates the increasing trend in the high cloud fraction in the same region. Only low level clouds are expected on the poleward side of the subtropical dry zones because of the strong descent in these regions. Decreasing trend in low cloud fractions and hence, total cloud amount in these regions can reduce the amount of short-wave reflection to

space, increasing the surface temperature to higher values than before. This is consistent with the observed decreasing trends in RH at the poleward edges of the HC. From figures 6.7 and 6.8, it can thus be reiterated that the trends in total CF are contributed by high clouds in the ascending region (increasing trend) and by low clouds in the descending region (decreasing trend).

6.3.3.3 Precipitation

Many studies in the recent past have employed the precipitation metric to study the consequences of HC expansion on the tropical and sub-tropical climate. Figure 6.9(a) depicts the annual cycle of zonal mean RF derived from GPCP observational dataset (1979-2016) along with the HC boundaries. The figure shows that the latitude of minimum (maximum) RF lies well within the region of descent (ascent). This observation again justifies our choice of the MSF metric to distinguish the ascending and descending branches of the HC. RF falls below ~2.5mm/day in the descending regions for most time of the year, whereas it exceeds this value within the ascending regions. Subtropical regions are the driest during winter months, in both hemispheres. The annual cycle of precipitation maxima is consistent with the movement of ITCZ. The precipitation rate peaks in the NH during boreal summer. The zonal mean RF climatology depicted in figure 6.9(a) is thus consistent with the HC dynamics, especially within its ascending and descending branches.

In order to bring out the long term changes in precipitation rate with respect to the HC, monthly trends in the zonal mean RF is estimated as a function of latitude and is shown in figure 6.9(b) along with the HC boundaries. Purple contours show the trends significant at the 80% level (The 95% significant contours were also computed for RF trends, however the regions covered by these contours are relatively less as compared to RH and CF. In this regard, 80% significant level contours are shown instead of 95% in the figure 6.9(b)). This figure shows that as in the case of high cloud fraction, there is a general negative/null trend in RF within the deep tropics. Also, strong positive trends are observed in the regions to the north of the latitude of maximum RF. These observations indicate a northward migration of

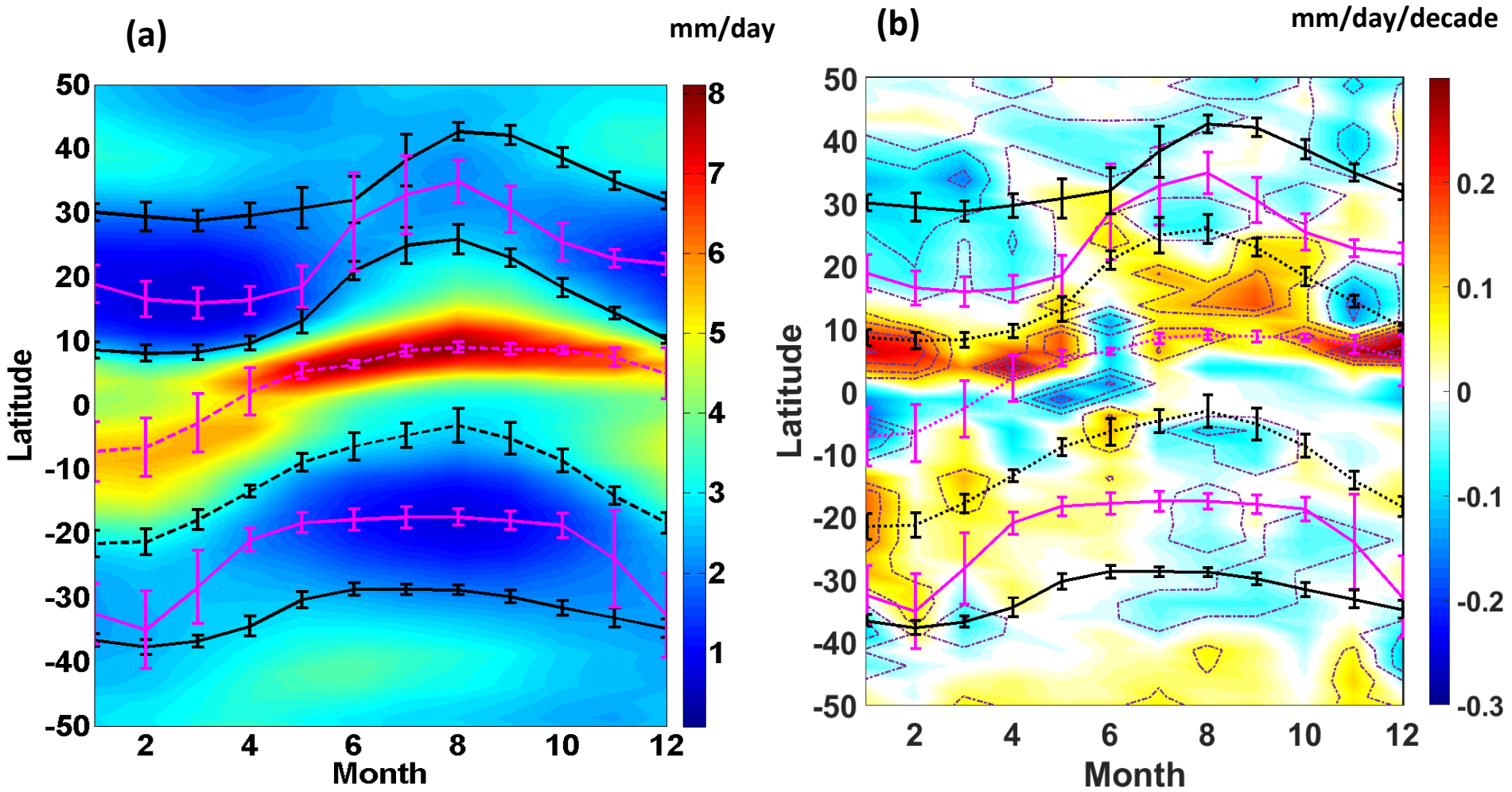

Figure 6.9: (a) Climatology of the annual cycle of zonal mean RF expressed as a function of latitude for the period 1979-2016 (b) Annual cycle of the trends in zonal mean RF expressed as a function of latitude. *Colour codes same as that of figure 6.4, but for HC parameters and RF. Purple contours in (b) show the trends significant at the 80% level.*

the precipitation maxima. One more striking feature of figure 6.9(b) is the location of maximum trend in precipitation at ~8^0 N -10^0N during most time of the year, except in June. The trend in RF recorded for these regions are ~0.2mm/day/decade. Note that these regions lie along the northward limit of the HC ascending region. This particular feature is also observed in RH and as well as in total CF trends shown in figures 6.4(b) and 6.7(b) respectively. In SH, positive trends ~0.05mm/day/decade are observed at the edges of ascending regions, especially during austral summer. It is interesting to note that strong positive trends are observed at the northern limit of HC ascending region during boreal winter, whereas slight decreasing trends are observed at the southern limit of the HC ascending region during austral winter. Most of the earlier studies have reported an overall increasing trend in precipitation within the ascending region of the HC; the present study clearly shows that the observed precipitation trend within the ascending region is not uniform. Positive trends are dominant in the northward part of the ascending region than in the southward part. Interestingly, increasing trends in precipitation ~ 0.06mm/day/decade is seen in the SH descent regions during austral summer and fall seasons. Drying trends (~ -0.4mm/day/decade) in the SH descent regions is seen during the hemisphere's winter and spring seasons. The descent regions poleward of the latitude of minimum RF in the NH show negative precipitation trends (~ -0.1mm/day/decade) for most time of the year, except during May-June, and in Nov-Dec. Precipitation trends within the NH descent regions is positive, but weak, in the regions equatorward of the latitude of minimum precipitation. The very same regions, however, show significant negative trends (~ -0.1mm/day/decade) in RF during October-November-December period. The significant negative trend observed at the NH edges of the HC are consistent with the HC expansion, similar to that observed for the case of RH and CF trends. However, in the SH, a consistent pattern in trends is not seen at the edges of the HC, except for a weak decreasing trend shown during austral winter and autumnal equinox seasons. Thus there is an indication of expansion of dry zones towards poles in both the hemispheres, especially during their respective winters. Overall, from figure 6.9(b) it can be inferred that ascending region of the HC as a whole has moved northward and also,

has intensified. However, it should be remembered that there are factors other than the HC changes which can influence the precipitation patterns, especially the regional factors. The long-term trends in the parameters associated with hydrological cycle, thus show consistent trends in the ascending and descending regions of HC as evident from figure 6.4(b), 6.7(b) and 6.9(b).

6.4 Summary

The present study investigates the influence of HC dynamics on the hydrological cycle parameters by estimating the long term changes in RH, CF and RF within the ascending and descending branches of the HC using reanalysis and observational data. The study has employed MSF metric calculated using the meridional wind component of the ERA-I reanalysis data so as to identify the HC boundaries. Preliminary analysis showed that the seasonal pattern as well annual cycle of the HC parameters is consistent with the present knowledge, thus substantiating the use of the MSF metric for identifying the HC parameters. Region between the latitude of maximum MSF (centre of the NH HC) and the latitude of minimum MSF (centre of the SH HC) was identified to be the HC ascending region. Regions between the latitude of maximum (minimum) MSF and the NH (SH) edge of the HC were identified as the regions of descent. An analysis of the zonal mean distribution of RH, CF and RF reveals that each of these parameters have a maximum in the HC ascending region, and minima in the HC descending region. The climatology and trend of each of the hydrological parameters, viz. RH, CF, and RF, within the ascending and descending regions of the HC are analysed in order to bring out the changes in these parameters occurring as a result of the changes in the strength and width of the HC. The study delineated the spatial distribution of the trends in RH, CF, and RF within the HC ascending/ descending regions. The following are the important observations drawn from the present study.

1. In the HC descending regions:
    i) There is a mid-tropospheric drying trend in the regions poleward of the latitude of minimum RH as well as at the HC edges. The mid-tropospheric RH

trend is positive in the regions equatorward of the latitude of the minimum RH.

ii) Regions equatorward of the latitude of minimum CF exhibit positive trends, whereas those poleward of it show either negative or null trends. The increasing total CF trends are stronger during boreal winter than during summer. The decreasing trend in total CF at the HC edges is attributed to a decrease in the fraction of low level clouds in these regions.

iii) Regions poleward of the latitude of minimum precipitation shows negative trends, whereas those equatorward of the latitude of minimum precipitation shows increasing trends in precipitation.

2. In the HC ascending regions:

i) The observed trends in mid-tropospheric RH indicate the moistening within the region of ascent, especially at the edges of the ascent region.

ii) Region of ascent contain both increasing and decreasing CF regions, with positive trends being shown by the regions on either side of the deep tropics. The decrease in CF over the deep tropical regions is attributed to the decreasing trend in the high cloud cover in these regions.

iii) Precipitation trends are positive at the edges of the ascent region, except in SH during austral winter and spring. In and near the latitude of maximum precipitation, there is a decreasing/null trend in RF.

iv) An analysis of the annual cycle of trend in RF indicates that the ascending region of the HC as a whole has moved northwards.

Thus RH, CF and RF parameters showed positive trend in and near the edges of the HC ascending regions. On the other hand, within the HC descending regions, these parameters showed both positive and negative trends. In fact, the trends are mostly negative near the poleward edges of the descending regions, and positive in the regions equatorward of it. Again, all the three parameters of hydrological cycle considered in the present study showed consistent trends in both ascending and descending regions of the HC. These results are in accordance with the observed phenomena of poleward expansion of the HC and the strengthening of the hydrological cycle associated with it. However, it is possible that the hydrological

cycle can be influenced by factors other than the HC. Hence the present study brought out the long term changes in all three parameters of the hydrological cycle, *simultaneously*, using reanalysis and observational data. It is for the first time that concurrent investigation of long term changes in all three parameters of the hydrological cycle has been reported with an emphasis to establish the link between the HC changes and their influence on the hydrological cycle in the present day climate. It is envisaged that the results discussed in the present study may be helpful in interpreting and evaluating model simulations of HC as well as hydrological cycle in warmer climate.

CHAPTER 7

SUMMARY AND FUTURE SCOPE

7.1 Summary

Hadley Circulation (HC) is a planetary scale circulation characterized by ascending motion in the tropics and descending motion in the subtropics. This tropical atmospheric circulation is responsible for the wet and dry climate of the tropical and the subtropical latitudes, respectively. HC is characterized using different parameters such as the meridional mass stream function (MSF), tropopause height, total column ozone, outgoing long-wave radiation, position of subtropical jet stream, cloud amount, and precipitation. Using these metrics, recent observational studies have shown that the HC has undergone a poleward expansion as well as strengthening over the past few decades. As observed by the climate scientists, such an expansion will have serious consequences due to the associated shift in precipitation patterns, poleward movement of jet streams and storm tracks, changes in distribution of climatically important trace gases in the stratosphere as well as changes in the ocean circulation. Owing to its direct impact on subtropical climate, many researchers across the globe are focusing on quantifying the variability in the width and strength of the HC. The present thesis discuss various facets of the phenomena of poleward expansion of the HC using four major atmospheric reanalysis datasets (NCEP, ERA-I, JRA55, and MERRA), network of global radiosonde observations (IGRA), satellite-based observations (COSMIC GPS-RO, TRMM SLH), as well as a combination of ground-based and space-based observations of precipitation (GPCP).

Although reanalysis provide spatially homogenous and long term data that can detect the trends in HC, these datasets combine model fields with sparsely distributed observations to form a spatially complete gridded meteorological dataset. Thus it has become the need of the hour that these datasets are validated using observations for global circulation studies. It is also important to evaluate

the newer reanalysis datasets for investigating HC dynamics. In this regard the current thesis characterized the HC using MSF metrics obtained from relatively new JRA55 reanalysis dataset and three widely used reanalysis datasets, *viz.*, NCEP, MERRA and ECMWF. The four reanalysis datasets have been compared with radiosonde observations from IGRA using the subsampling technique. Large scale features in the subsampled datasets show high resemblance with the IGRA dataset, reinforcing the fact that reanalysis datasets can be used for the studies on the global circulation, and HC in particular. It is for the first time that MSF from four major reanalysis datasets are validated against global network of radiosonde measurements for use in atmospheric general circulation studies. A qualitative comparison of MSF among all the reanalysis datasets for winter and summer solstices reproduced the well-known features of the HC. Annual cycle of the northern and southern hemispheric edges, centre and total width of the HC has been analyzed, and considerable consistency with present knowledge on the same has been found. This confirmed the correctness of the algorithm that has been developed to calculate the MSF as well as edges of the HC. It has also been found that the annual cycle of HC edges in both hemispheres, HC centre, as well as its total width is consistent amongst the datasets, with comparable interannual variability also. Interannual variability in the total width of the HC has been charted out for each month in order to bring out annual cycle of the HC expansion rates. It was found that the trends obtained at the 95% confidence interval derived from all the four reanalysis datasets are significant during the month of July, and that the expansion trend ($\sim 1.5^0$ latitude per decade) is consistent among these datasets.

The tropical heating is closely tied to the land-sea distribution and hence, the expansion rate also varies from region to region. Hence it is necessary to delineate the regional features of the HC. The thesis brought out the regional features of the zonally averaged circulation using a measurable metric- the tropopause. Atmospheric temperature measurements obtained from highly resolved COSMIC GPS-RO observations were used for the same. Zonal mean HC edges defined by the meridional gradient in tropopause height (*TpGr*) and the meridional gradient in tropospheric dry bulk static stability (*BSS*) were extended to zonally resolve the features of the tropical belt. In addition, a third metric was

proposed to delineate the regional features of the HC- the amplitude of the annual oscillation of the tropopause height over the subtropical region (*TpAO*). The *TpAO* metric has potential use in climate models with a poor tropopause structure since it does not rely on any gradient/threshold calculation. Width of the tropical belt derived from the *TpGr, BSS,* and *TpAO* metrics were evaluated against the width estimated using the well-known MSF metric derived from ERA-I reanalysis data, and were found to be consistent. Analysis of interannual variability in the seasonal mean of the regional tropical belt edges brought out that the tropical belt widths are consistent in the Middle East and South Asian regions during boreal summer, in the Australian region during austral winter, and in the South American and African continents during austral summer; hence favoring to identify the expansion rate of the tropics. The thesis also quantified the contribution of every 10° longitudinal zone to the zonal mean tropical width. The analysis brought out that Indian and West Pacific sectors play a significant role in increasing the zonal mean tropical belt width during boreal summer, whereas the West Pacific and South American sectors increases zonal mean tropical belt width during boreal winter. The Atlantic and East Pacific sectors were found to decrease the zonal mean tropical belt width in boreal summer as well as winter seasons. It is envisaged that the present results will have potential applications in investigating the zonally resolved trends in the tropical expansion.

Climate model simulations have identified that tropospheric warming due to greenhouse gas forcing, stratospheric cooling due to ozone depletion, SST variability within the tropics, inter-hemispheric asymmetry of absorbing aerosols such as black carbon etc. can lead to expansion of the HC. However, the atmospheric processes through which these factors influence the HC is not very clear. But these factors can influence the thermal structure of the troposphere, which in turn can affect the cloud formation and latent heating distribution within the HC ascending branches. The thesis thus investigated the role of mid-tropospheric latent heat (LH) release in modulating the strength and width of the HC. The space-based observations of LH from TRMM were used for the same. Spatial distribution of LH derived from TRMM observations showed features of the tropical convective activity and its zonal asymmetries, consistent with the present knowledge. It was also found that the zonal mean LH during the solstices

is confined to a narrow latitudinal band in NH during boreal summer, whereas it is broadly distributed in SH during boreal winter. This inter-hemispheric asymmetry is an important character of the tropical LH distribution. The zonal mean latitudinal distribution of column averaged LH was characterized by means of three parameters, viz., the latitude of peak LH, width of LH distribution and the LH released in ascent region of HC. The MSF estimated using ERA-I reanalysis data was used to characterize the HC parameters in terms of its centre, intensity and total width. Co-variability of the LH and HC parameters were investigated to quantify the influence of LH release on the spatial extent and intensity of the HC. The results showed that the latitude of peak LH significantly influences the position of the HC centre as well as strength. The present analysis also revealed that the total LH within the ascending limb of the HC substantially influences the total width of the HC. Marked changes were observed in the covariability of the time series of the LH and the HC parameters after deseasonalization, and the same were quantified in the thesis. The current thesis, for the first time, provides observational evidence on the role of latent heating in modulating the width and intensity of the HC.

Proper adaptation strategies can be formulated to deal with the consequences of the HC if only the pattern of changes in the hydrological cycle associated with the expansion and intensification of the HC in the present warming climate is correctly identified. However a clear signature of the HC changes in moisture, cloud and precipitation is far from understating in the present day climate. This is partly because most of the research focusing on the role of HC dynamics in modulating the components of hydrological cycle relied on climate model simulations for a future state of the climate. The present thesis thus evaluated the long term changes in relative humidity (RH), cloud fraction (CF) and precipitation parameters of the hydrological cycle, simultaneously, using reanalysis and observational data. RH and CF data were obtained from the ERA-I reanalysis and precipitation measurements from GPCP. The study analysed the long term trends in the hydrological cycle parameters within the ascending and descending branches of the HC, which were identified using the MSF metric calculated from ERA-I reanalysis. The study brought out that all the three parameters of the hydrological cycle show positive trend in and near the poleward edges of the HC

ascending regions and negative trends near the poleward edges of the descending regions. Unlike earlier studies which reported the trends in precipitation within the ascending/descending regions of HC as a whole (assuming that the trends are uniform in these regions), the present study delineate the trends within the ascending and descending regions of HC. The results were observed to be in accordance with the observed phenomena of the poleward expansion of the HC and the strengthening of the hydrological cycle associated with it. It is for the first time that concurrent investigation of long term changes in all three parameters of the hydrological cycle has been reported with an emphasis to establish the link between the HC changes and their influence on the hydrological cycle in the present day climate.

7.2 Future Scope

The current thesis depicted that the zonal mean HC exhibits significant poleward expansion even on a seasonal basis, which is presumed to have significant influence of the climate of the tropics/subtropics and the biodiversity which depends on it. The thesis brought out that the zonal mean width of the HC is contributed by different longitudinal regimes in a specific manner. This suggests that regional variability in the *rate* of expansion should be addressed using observational data. Such a quantification of the regional HC expansion rates and concurrent analysis of the factors contributing to the HC expansion in these regions shall pave way to bring out the core reason behind the HC expansion phenomena. Having identified in the thesis that the tropical latent heating and its distribution plays a significant role in controlling the HC dynamics, determining the percentage contribution of different sources (natural/anthropogenic) in modulating the latent heating distribution by means of observations can be a next step in identifying the key factor behind the HC expansion phenomena. Once the right forcing factors are available, a future projection of the HC expansion using climate models or an ensemble of these models (such as CMIP5) will produce results that are consistent with observations. This shall once again confirm the "driver(s)" of HC expansion, and shall also help us to formulate the right kind of adaptation strategies. The strengthening of the hydrological cycle in line with the HC expansion phenomena observed by the analysis in the present thesis is

suggestive of an intensification of the HC itself. It is envisaged that changes in the strength of the HC can have significant influence on the stratospheric BD circulation. It is also quite possible that the intensification of the HC is related to the changes in the width of the Inter Tropical Convergence Zone (ITCZ) since the ascending limb of the HC has been theoretically found to be related to the breadth of ITCZ. Exploring the relationship between HC intensification and the changes in ITCZ as well as BD circulation can thus be a topic for future research, in addition to the investigation on the drivers and future projection of the HC expansion phenomena.

BIBLIOGRAPHY

Adam O, Schneider T, Harnik N (2014) Role of changes in mean temperatures vs. temperature gradients in the recent widening of the Hadley circulation. J Clim 1:7450–7461. doi: 10.1175/JCLI-D-14-00140.1

Adler RF, Huffman GJ, Chang A, et al (2003) The Version-2 Global Precipitation Climatology Project (GPCP) Monthly Precipitation Analysis (1979 – Present). J Hydrometeorol 4:1147–1167. doi: 10.1175/1525-7541(2003)004<1147:TVGPCP>2.0.CO;2

Ahrens DC (2009) Meteorology Today, 9th edn. Brooks/Cole, Cengage Learning, Belmont, CA

Allan RP, Soden BJ (2007) Large discrepancy between observed and simulated precipitation trends in the ascending and descending branches of the tropical circulation. Geophys Res Lett 34:1–6. doi: 10.1029/2007GL031460

Allan RP, Soden BJ, John VO, et al (2010) Current changes in tropical precipitation. Environ Res Lett 5:025205. doi: 10.1088/1748-9326/5/2/025205

Allen RJ, Norris JR, Kovilakam M (2014) Influence of anthropogenic aerosols and the Pacific Decadal Oscillation on tropical belt width. Nat Geosci 7:270–274. doi: 10.1038/ngeo2091

Allen RJ, Sherwood SC, Norris JR, Zender CS (2012) Recent Northern Hemisphere tropical expansion primarily driven by black carbon and tropospheric ozone. Nature 485:350–354. doi: 10.1038/nature11097

Allen RJ, Sherwood SC (2011) The impact of natural versus anthropogenic aerosols on atmospheric circulation in the Community Atmosphere Model. Clim Dyn 36:1959–1978. doi: 10.1007/s00382-010-0898-8

Ao CO, Hajj AJ (2013) Monitoring the width of the tropical belt with GPS radio occultation measurements. Geophys Res Lett 40:6236–6241. doi: 10.1002/2013GL058203

Baines PG (2006) The Zonal Structure of the Hadley Circulation. Adv Atmos Sci 23:1–15. doi: 10.1007/s00376-006-0869-5

Barry RG, Chorley RJ (2003) Atmosphere, Weather, and Climate, 8th edn. Routledge, USA

Bates JR (1972) Tropical disturbances and the general circulation. Q J R Meteorol Soc 98:1–16. doi: 10.1002/qj.49709841502

Bender FA-M, Ramanathan V, Tselioudis G (2012) Changes in extratropical storm track cloudiness 1983 – 2008 : observational support for a poleward shift. Clim Dyn 38:2037–2053. doi: 10.1007/s00382-011-1065-6

Bengtsson L, Arkin P, Berrisford P, et al (2007) The need for a dynamical climate reanalysis. Bull Am Meteorol Soc 88:495–501. doi: 10.1175/BAMS-88-4-495

Birner T (2010) Recent widening of the tropical belt from global tropopause statistics : Sensitivities. J Geophys Res 115:1–13. doi: 10.1029/2010JD014664

Bony S, Bellon G, Klocke D, et al (2013) Robust direct effect of carbon dioxide on tropical circulation and regional precipitation. Nat Geosci 6:1–5. doi: 10.1038/ngeo1799

Breed GA, Stichter S, Crone EE (2013) Climate-driven changes in northeastern US butterfly communities. Nat Clim Chang 3:142–145. doi: 10.1038/nclimate1663

Cai W, Cowan T, Thatcher M (2012) Rainfall reductions over Southern Hemisphere semi-arid regions: the role of subtropical dry zone expansion. Sci Rep 2:1–5. doi: 10.1038/srep00702

Chen J, Carlson BE, Genio AD Del (2002) Evidence for Strengthening of the Tropical General Circulation in the 1990s. Science (80-) 295:838–841.

Chen S, Wei K, Chen W, Song L (2014) Regional changes in the annual mean Hadley circulation in recent decades. J Geophys Res Atmos 119:7815–7832. doi: 10.1002/2014JD021540

Chou C, Neelin JD, Chen CA, Tu JY (2009) Evaluating the "rich-get-richer" mechanism in tropical precipitation change under global warming. J Clim 22:1982–2005. doi: 10.1175/2008JCLI2471.1

Chou C, Chiang JCH, Lan C, et al (2013) Increase in the range between wet and dry season precipitation. Nat Geosci 6:263–267. doi: 10.1038/ngeo1744

Clement AC (2006) The Role of the Ocean in the Seasonal Cycle of the Hadley Circulation. J Atmos Sci 63:3351–3365. doi: 10.1175/JAS3811.1

Cook KH (2003) Role of Continents in Driving the Hadley Cells. J Atmos Sci 60:957–976. doi: 10.1175/1520-0469(2003)060<0957:ROCIDT>2.0.CO;2

Danard MB (1966) On the Contribution of Released Latent Heat to Changes in Available Potential Energy. J Appl Meteorol 5:81–84. doi: 10.1175/1520-0450(1966)005<0081:OTCORL>2.0.CO;2

Davis NA, Birner T (2013) Seasonal to multidecadal variability of the width of the tropical belt. J Geophys Res Atmos 118:7773–7787. doi: 10.1002/jgrd.50610

Davis N, Birner T (2016) Climate Model Biases in the Width of the Tropical Belt. J Clim 29:1935–1954. doi: 10.1175/JCLI-D-15-0336.1

Davis SM, Rosenlof KH (2012) A multidiagnostic intercomparison of tropical-width time series using reanalyses and satellite observations. J Clim 25:1061–1078. doi: 10.1175/JCLI-D-11-00127.1

Davis N, Birner T (2017) On the Discrepancies in Tropical Belt Expansion between Reanalyses and Climate Models and among Tropical Belt Width Metrics. J Clim 30:1211–1231. doi: 10.1175/JCLI-D-16-0371.1

Dee DP, Uppala SM, Simmons AJ, et al (2011) The ERA-Interim reanalysis: Configuration and performance of the data assimilation system. Q J R Meteorol Soc 137:553–597. doi: 10.1002/qj.828

Diaz HF, Bradley RS (2004) The Hadley Circulation: Present, Past and Future, 1st edn. Kluwer Academic Publishers, The Netherlands

Durre I, Vose RS, Wuertz DB (2006) Overview of the integrated global radiosonde archive. J Clim 19:53–68. doi: 10.1175/JCLI3594.1

Eastman R, Warren SG (2012) A 39-Yr Survey of Cloud Changes from Land Stations Worldwide 1971 – 2009 : Long-Term Trends , Relation to Aerosols , and Expansion of the Tropical Belt. J Clim 26:1286–1303. doi: 10.1175/JCLI-D-12-00280.1

Fasullo JT, Trenberth KE (2012) A Less Cloudy Future : The Role in Climate Sensitivity. Science (80-) 338:792–794. doi: 10.1126/science.1227465

Feldel N, Bordoni S (2016) Characterizing the Hadley Circulation Response through Regional Climate Feedbacks. J Clim 29:613–622. doi: 10.1175/JCLI-D-15-0424.1

Frierson DMW, Lu J, Chen G (2007) Width of the Hadley cell in simple and comprehensive general circulation models. Geophys Res Lett 34:1–5. doi: 10.1029/2007GL031115

Fu Q, Johanson CM, Wallace JM, Reichler T (2006) Enhanced Mid-Latitude Tropospheric Warming in Satellite measurements. Science (80-) 312:1179. doi: 10.1126/science.1125566

Fueglistaler S, Dessler AE, Dunkerton TJ, et al (2009) Tropical tropopause layer. Rev Geophys. doi: 10.1029/2008RG000267

Garcia RR, Randel WJ (2008) Acceleration of the Brewer–Dobson Circulation due to Increases in Greenhouse Gases. J Atmos Sci 65:2731–2739. doi: 10.1175/2008JAS2712.1

Gastineau G, Li L, Le Treut H (2009) The Hadley and Walker circulation changes in global warming conditions described by idealized atmospheric simulations. J Clim 22:3993–4013. doi: 10.1175/2009JCLI2794.1

Grise KM, Davis SM, Staten PW, Adam O (2018) Regional and Seasonal Characteristics of the Recent Expansion of the Tropics. J Clim. doi: 10.1175/JCLI-D-18-0060.1

Goody RM, Walker JCG (1972) The Atmospheres. Prentice-Hall, Englewood Cliffs, New Jersey

Hack JJ, Schubert WH, Stevens DE, Kuo H-C (1989) Response of the Hadley Circulation to Convective Forcing in the ITCZ. J Atmos Sci 46:2957–2973. doi: 10.1175/1520-0469(1989)046<2957:ROTHCT>2.0.CO;2

Harada Y, Kamahori H, Kobayashi C, et al (2016) The JRA-55 Reanalysis: Representation of Atmospheric Circulation and Climate Variability. J Meteorol Soc Japan Ser II 94:269–302. doi: 10.2151/jmsj.2016-015

Held IM, Hou AY (1980) Nonlinear Axially Symmetric Circulaton in a Nearly Inviscid Atmoshere. J Atmos Sci 37:515–533. doi: 10.1175/1520-0469(1980)037<0515:NASCIA>2.0.CO;2

Held IM, Soden BJ (2006) Robust Responses of the Hydrological Cycle to Global Warming. J Clim 19:5686–5699. doi: 10.1175/JCLI3990.1

Ho S, Goldberg M, Kuo Y-H, et al (2009) Calibration of Temperature in the Lower Stratosphere from Microwave Measurements Using COSMIC Radio Occultation Data: Preliminary Results. Terr Atmos Ocean Sci 20:87–100. doi: 10.3319/TAO.2007.12.06.01(F3C)

Holm E V. (2003) Revision of the ECMWF humidity analysis: Construction of a Gaussian control variable. In: Proceedings of the ECMWF/GEWEX Workshop on Humidity Analysis, 8-11 July 2002. ECMWF: Reading, UK,

Holton JR (2004) An Introduction to Dynamic Meteorology, 4th edn. Elsevier Academic Press, USA

Holton JR, Haynes PH, McIntyre ME, et al (1995) Stratosphere-Troposphere Exchange. Rev Geophys 33:403–439.

Hou AY, Lindzen RS (1992) Influence of concentrated heating on the Hadley Circulation. J Atmos Sci 49:1233–1241. doi: 10.1175/1520-0469(1992)049<1233:TIOCHO>2.0.CO;2

Houze RAJ (1997) Stratiform precipitation in the tropics: A meteorological paradox? Bull Am Meteorol Soc 78:2179–2196. doi: 10.1175/1520-0477(1997)078<2179:SPIROC>2.0.CO;2

Hu Y, Fu Q (2007) Observed poleward expansion of the Hadley circulation since 1979. Atmos Chem Phys Discuss 7:9367–9384. doi: 10.5194/acpd-7-9367-2007

Hu Y, Tao L, Liu J (2013) Poleward expansion of the hadley circulation in CMIP5 simulations. Adv Atmos Sci 30:790–795. doi: 10.1007/s00376-012-2187-4

Hudson R, Andrade M, Follette M, Frolov A (2006) The total ozone field separated into meteorological regimes—Part II: Northern hemisphere mid-latitude total ozone trends. Atmos Chem Phys 6:5183–5191. doi: 10.5194/acp-6-5183-2006

Huffman GJ, Adler RF, Arkin P, et al (1997) The global precipitation climatology project (GPCP) combined precipitation dataset. Bull Am Meteorol Soc 78:5–20. doi: 10.1175/1520-0477(1997)078<0005:TGPCPG>2.0.CO;2

Hurrell J, Visbeck M, Anna P (2011) WCRP Coupled Model Intercomparison Project- Phase 5.

Issac J, Turton S (2014) Expansion of the Tropics – Evidence and implications. James Cook University, Cairnes, Australia

James IN (2003) Hadley circulation. Encycl. Atmos. Sci. 919–993.

Johanson CM, Fu Q (2009) Hadley cell widening: Model simulations versus observations. J Clim 22:2713–2725. doi: 10.1175/2008JCLI2620.1

John SR, Kumar KK (2011) TIMED/SABER observations of global cold point mesopause variability at diurnal and planetary wave scales. J Geophys Res Sp Phys. doi: 10.1029/2010JA015945

Kang SM, Deser C, Polvani LM (2013) Uncertainty in climate change projections of the hadley circulation: The role of internal variability. J Clim 26:7541–7554. doi: 10.1175/JCLI-D-12-00788.1

Karnauskas KB, Ummenhofer CC (2014) On the dynamics of the Hadley circulation and subtropical drying. Clim Dyn 42:2259–2269. doi: 10.1007/s00382-014-2129-1

Kjellsson J (2015) Weakening of the global atmospheric circulation with global warming. Clim Dyn 45:975–988. doi: 10.1007/s00382-014-2337-8

Kalnay E (2002) Atmospheric modeling, data assimilation and predictability, 1st edn. Cambridge University Press, NewYork

Kalnay E, Kanamitsu M, Kistler R, et al (1996) The NCEP/NCAR 40-Year Reanalysis Project. Bull Am Meteorol Soc 77:437–471. doi: 10.1175/1520-0477(1996)077<0437:TNYRP>2.0.CO;2

Kanamitsu M, Ebisuzaki W, Woollen J, et al (2002) NCEP-DOE AMIP-II Reanalysis (R-2). Bull Am Meteorol Soc 83:1631–1643. doi: 10.1175/BAMS-83-11-1631

Kobayashi S, Ota Y, Harada Y, et al (2014) The JRA-55 Reanalysis: General Specifications and Basic Characteristics. J Meteorol Soc Japan 93:5–48. doi: 10.2151/jmsj.2015-001

Kumar KK (2004) Studies on Tropical Mesoscale Convective Systems and associated atmospheric dynamics using VHF and UHF Radars. Sri Venkateswara University, Tirupati,India

Kummerow C, Simpson J, Thiele O, et al (2000) The Status of the Tropical Rainfall Measuring Mission (TRMM) after Two Years in Orbit. J Appl Meteorol 39:1965–1982. doi: 10.1175/1520-0450(2001)040<1965:TSOTTR>2.0.CO;2

Kuo YH, Sokolovskiy S V., Anthes RA, Vandenberghe F (2000) Assimilation of GPS radio occultation data for numerical weather prediction. Terr Atmos Ocean Sci 11:157–186. doi: 10.3319/TAO.2000.11.1.157(COSMIC)

Kurisinski ER, Hajj GA, Schofield JT, et al (1997) Observing the Earth's atmosphere with radio occultation measurements using the Global Positioning System. J Geophys Res 102:23,429–23,465. doi: 10.1029/97JD01569

Läderach A, Raible CC (2013) Lower-tropospheric humidity: Climatology, trends and the relation to the ITCZ. Tellus, Ser A Dyn Meteorol Oceanogr 65:1–13. doi: 10.3402/tellusa.v65i0.20413

Lau K-M, Yang S (2002) Walker Circulation. Encycl. Atmos. Sci. 1:1-6

Lau WKM, Kim K (2015) Robust Hadley Circulation changes and increasing global dryness due to CO2 warming from CMIP5 model projections. Proc Natl Acad Sci 112:3630–3635. doi: 10.1073/pnas.1418682112

Leroux M (2014) Dynamic Analysis of Weather and Climate: Atmospheric circulation, Perturbations, Climatic evolution. Springer Berlin Heidelberg

Levine XJ, Schneider T (2015) Baroclinic Eddies and the Extent of the Hadley Circulation : An Idealized GCM Study. J Atmos Sci 72:2744–2761. doi: 10.1175/JAS-D-14-0152.1

Lindzen RS, Hou AY (1988) Hadley Circulations for Zonally Averaged Heating Centred off the Equator. J Atmos Sci 45:2416–2427. doi: 10.1175/1520-0469(1988)045<2416:HCFZAH>2.0.CO;2

Liou K. (2002) An Introduction to Atmospheric Radiation, 2nd edn. Academic Press Inc., UK

Liu Z, Ostrenga D, Teng W, Kempler S (2012a) Tropical rainfall measuring mission (TRMM) precipitation data and services for research and applications. Bull Am Meteorol Soc 93:1317–1325. doi: 10.1175/BAMS-D-11-00152.1

Liu J, Song M, Hu Y, Ren X (2012b) Changes in the strength and width of the Hadley Circulation since 1871. Clim Past 8:1169–1175. doi: 10.5194/cp-8-1169-2012

Liu Y, Xu T, Liu J (2014) Characteristics of the seasonal variation of the global tropopause revealed by COSMIC/GPS data. Adv Sp Res 54:2274–2285. doi: 10.1016/j.asr.2014.08.020

Lockwood JG (1979) Causes of Climate. Edward Arnold, London

Loeb NG, Rutan DaA, Kato S, Wang W (2014) Observing Interannual Variations in Hadley Circulation Atmospheric Diabatic Heating and Circulation Strength. J Clim 27:4139–4158. doi: 10.1175/JCLI-D-13-00656.1

Lu J, Vecchi GA, Reichler T (2007) Expansion of the Headley cell under global warming. Geophys Res Lett 34:1–5. doi: 10.1029/2006GL028443

Lucas C, Nguyen H, Timbal B (2012) An observational analysis of Southern Hemisphere tropical expansion. J Geophys Res Atmos 117:1–18. doi: 10.1029/2011JD017033

Lucas C, Nguyen H (2015) Regional characteristics of tropical expansion and the role of climate variability. J Geophys Res Atmos. doi: 10.1002/2015JD023130

Lucas C, Timbal B, Nguyen H (2014) The expanding tropics: A critical assessment of the observational and modeling studies. Wiley Interdiscip Rev Clim Chang 5:89–112. doi: 10.1002/wcc.251

Marshall J, Plumb AR (2008) Atmosphere, Ocean and Climate Dynamics: An Introductory Text. Elsevier Academic Press, USA

Marks FD (2015) Hurricanes: Observation. Encycl. Atmos. Sci. Vol6 35–56.

Mathew SS, Kumar KK (2018a) Estimation of Zonally Resolved Edges of the Tropical Belt Using GPS-RO Measurements. IEEE J Sel Top Appl Earth Obs Remote Sens 1–7. doi: 10.1109/JSTARS.2018.2828342

Mathew SS, Kumar KK, Subrahmanyam K V. (2016) Hadley cell dynamics in Japanese Reanalysis - 55 dataset : evaluation using other reanalysis datasets and global radiosonde network observations. Clim Dyn. doi: 10.1007/s00382-016-3051-5

Mathew SS, Kumar KK (2018b) On the role of precipitation latent heating in modulating the strength and width of the Hadley circulation. Theor Appl Climatol 1–13. doi: 10.1007/s00704-018-2515-4

McIlveen R (1992) Fundamentals of weather and climate, 2nd edn. Spinger-Science&Business Media, Berlin

Mitas CM, Clement A (2006) Recent behavior of the Hadley cell and tropical thermodynamics in climate models and reanalyses. Geophys Res Lett 33:1–4. doi: 10.1029/2005GL024406

Mitas CM, Clement A (2005) Has the Hadley cell been strengthening in recent decades? Geophys Res Lett 32:1–5. doi: 10.1029/2004GL021765

Mohankumar K (2008) Stratosphere-Troposphere Exchange: An Introduction, 1st edn. Spinger Netherlands

Murakami M (1995) Managing Water for Peace in the Middle East; Alternative Strategies 1st edn. United Nations University Press, Tokyo

Nguyen H, Evans A, Lucas C, et al (2013) The Hadley Circulation in Reanalyses: Climatology, variability, and Change. J Clim 26:3357–3376. doi: 10.1175/JCLI-D-12-00224.1

Nguyen H, Hendon HH, Lim EP, et al (2018) Variability of the extent of the Hadley circulation in the southern hemisphere: a regional perspective. Clim Dyn 50:129–142. doi: 10.1007/s00382-017-3592-2

Norris JR, Allen RJ, Evan AT, et al (2016) Evidence for climate change in the satellite cloud record. Nature 536:72–75. doi: 10.1038/nature18273

Oort AH, Yienger JJ (1996) Observed interannual variability in the Hadley circulation and its connection to ENSO. J Clim 9:2751–2767. doi: 10.1175/1520- 0442(1996)009<2751:OIVITH>2.0.CO;2.

Polvani LM, Waugh DW, Correa GJP, Son S-W (2011) Stratospheric Ozone Depletion : The Main Driver of Twentieth-Century Atmospheric Circulation Changes in the Southern Hemisphere. J Clim 24:795–813. doi: 10.1175/2010JCLI3772.1

Post DA, Timbal B, Chiew FHS, et al (2014) Decrease in southeastern Australian water availability linked to ongoing Hadley cell expansion. Earth's Futur 2:231–238. doi: 10.1002/2013EF000194

Quan X, Diaz HF, Hoerling MP (2004) Change of the Tropical Hadley Cell Since 1950. In: Diaz HF, Bradley RS (eds) The Hadley Circulation: Present, Past, and Future: An Introduction. Kluwer Academic Publishers, pp 85–120

Quan X-W, Hoerling MP, Perlwitz J, et al (2014) How fast are the tropics expanding? J Clim 27:1999–2013. doi: 10.1175/JCLI-D-13-00287.1

Randall D (2008) Reanalysis of Historical Climate for Key Atmospheric Features: Implications for Attribution of Causes of Observed Change.Ratnam MV, Patra AK, Murthy BVK (2010) Tropical mesopause: Is it always close to 100 km? J Geophys Res Atmos 115:1–8. doi: 10.1029/2009JD012531

Ratnam MV, Patra AK, Murthy BVK (2010) Tropical mesopause: Is it always close to 100 km? J Geophys Res Atmos 115:1–8. doi: 10.1029/2009JD012531

Reichler T (2009) Changes in the atmospheric circulation as indicator of climate change. In: Letcher TM (ed) Climate Change: Observed Impacts on Planet Earth, 1st edn. Elsevier B.V., pp 145–164

Reid GC, Gage KS (1996) The tropical tropopause over the western Pacific: wave driving, convection, and the annual cycle. J Geophys Res 101:21233–21241. doi: 10.1029/96JD01622

Remsberg EE (2015) Methane as a diagnostic tracer of changes in the Brewer-Dobson circulation of the stratosphere. Atmos Chem Phys 15:3739–3754. doi: 10.5194/acp-15-3739-2015

Reynolds RW, Rayner NA, Smith TM, et al (2002) An improved in situ and satellite SST analysis for climate. J Clim 15:1609–1625. doi: 10.1175/1520-0442(2002)015<1609:AIISAS>2.0.CO;2

Rieckh T, Scherllin-Pirscher B, Ladstädter F, Foelsche U (2014) Characteristics of tropopause parameters as observed with GPS radio occultation. Atmos Meas Tech 7:3947–3958. doi: 10.5194/amt-7-3947-2014

Riehl H, Malkus JS (1958) On the heat balance in the Equatorial trough zone. Geophysica 6:503–538.

Rienecker MM, Suarez MJ, Gelaro R, et al (2011) MERRA: NASA's modern-era retrospective analysis for research and applications. J Clim 24:3624–3648. doi: 10.1175/JCLI-D-11-00015.1

Rind D, Rossow WB (1984) The effects of physical processes on Hadley circulation. J Atmos Sci 41:479–507. doi: 10.1175/1520-0469(1984)041<0479:TEOPPO>2.0.CO;2

Salby ML, Callaghan PF (2005) Interaction between the Brewer – Dobson Circulation and the Hadley Circulation. J Clim 18:4303–4316. doi: 10.1175/JCLI3509.1

Santer BD, Wigley TML, Boyle JS, et al (2000) Statistical significance of trends and trend differences in layer-average atmospheric temperature time series. J Geophys Res 105:7337–7356. doi: 10.1029/1999JD901105

Schneider T, O'Gorman PA, Levine XJ (2010) Water vapor and the dynamics of climate changes. Rev Geophys 48:1–22. doi: 10.1029/2009RG000302

Schmidt T, Heise S, Wickert J, et al (2005) GPS radio occultation with CHAMP and SAC-C : global monitoring of thermal tropopause parameters. Atmos Chem Phys 5:1473–1488. doi: 10.5194/acp-5-1473-2005

Schumacher C, Houze RAJ, Kraucunas I (2004) The Tropical Dynamical Response to Latent Heating Estimates Derived from the TRMM Precipitation Radar. J Atmos Sci 61:1341–1358. doi: 10.1175/1520-0469(2004)061<1341:TTDRTL>2.0.CO;2

Seidel D, Fu Q, Randel W, Reichler T (2008) Widening of the tropical belt in a changing climate. Nat Geosci 1:21–24. doi: 10.1038/ngeo.2007.38

Seidel DJ, Randel WJ (2007) Recent widening of the tropical belt: Evidence from tropopause observations. J Geophys Res Atmos 112:1–6. doi: 10.1029/2007JD008861

Seidel DJ, Randel WJ (2006) Variability and Trends in the Global Tropopause Estimated from Radiosonde Data. J Geophys Res Atmos 111:1–17. doi: 10.1029/2006JD007363

Seidel DJ, Ross RJ, Angell JK, Reid GC (2001) Climatological characteristics of the tropical tropopause as revealed by radiosondes. J Geophys Res 106:7857–7878. doi: 10.1029/2000JD900837

Seo K, Frierson DMW, Son J, et al (2014) A mechanism for future changes in Hadley circulation strength in CMIP5 climate change simulations. Geophys Res Lett 40:5251–5258. doi: 10.1002/2014GL060868

Sherwood SC, Ingram W, Tsushima Y, et al (2010) Relative humidity changes in a warmer climate. J Geophys Res 115:1–11. doi: 10.1029/2009JD012585

Shin S, Chung I-U, Kim H-J (2012) Relationship between the expansion of drylands and the intensification of Hadley circulation during the late twentieth century. Meteorol Atmos Phys 118:117–128. doi: 10.1007/s00703-012-0220-x

Shige S, Takayabu YN, Tao W-K, Johnson DE (2004) Spectral Retrieval of Latent Heating Profiles from TRMM PR Data . Part I : Development of a Model-Based Algorithm. J Appl Meteorol 43:1095–1113. doi: 10.1175/1520-0450(2004)043<1095:SROLHP>2.0.CO;2

Shige S, Takayabu YN, Tao W-K, Shie C-L (2007) Spectral Retrieval of Latent Heating Profiles from TRMM PR Data . Part II :Algorithm Improvement and Heating Estimates over Tropical Ocean Regions. J Appl Meteorol Climatol 46:1098–1124. doi: 10.1175/JAM2510.1

Simpson J, Adler RF, North GR (1988) A proposed TRMM satellite. Bull Am Meteorol Soc 69:278–295. doi: 10.1175/1520-0477(1988)069<0278:APTRMM>2.0.CO;2

Son S, Tandon NF, Polvani LM, Waugh DW (2009) Ozone hole and Southern Hemisphere climate change. Geophys Res Lett 36:1–5. doi: 10.1029/2009GL038671

Son SW, Gerber EP, Perlwitz J, et al (2010) Impact of stratospheric ozone on Southern Hemisphere circulation change : A multimodel assessment. J Geophys Res 115:1–18. doi: 10.1029/2010JD014271

Stachnik JP, Schumacher C (2011) A comparison of the Hadley circulation in modern reanalyses. J Geophys Res 116:1–14. doi: 10.1029/2011JD016677

Staten PW, Rutz JJ, Reichler T, Lu J (2012) Breaking down the tropospheric circulation response by forcing. Clim Dyn 39:2361–2375. doi: 10.1007/s00382-011-1267-y

Sturaro G (2003) Patterns of Variability in the Satellite Microwave Sounding Unit Temperature Record : Comparison With Surface and Reanalysis Data. Int J Climatol 23:1799–1820. doi: 10.1002/joc.975

Solomon A, Polvani LM, Waugh DW, Davis SM (2016) Contrasting upper and lower atmospheric metrics of tropical expansion in the Southern Hemisphere. Geophys Res Lett 43:10496–10503. doi: 10.1002/2016GL070917

Son SW, Tandon NF, Polvani LM (2011) The fine-scale structure of the global tropopause derived from COSMIC GPS radio occultation measurements. J Geophys Res 116:1–17. doi: 10.1029/2011JD016030

Subrahmanyam KV, Kumar KK (2017) CloudSat observations of multi layered clouds across the globe. Clim Dyn 49:327–341. doi: 10.1007/s00382-016-3345-7

Su H, Jiang JH, Neelin JD, et al (2017) Tightening of tropical ascent and high clouds key to precipitation change in a warmer climate. Nat Commun 8:1–9. doi: 10.1038/ncomms15771

Su H, Jiang JH, Zhai C, et al (2014) Weakening and strengthening sructures in the HC under global warming and implications for cloud response and climate sensitivity. J Geophys Res Atmos 119:5787–5805. doi: 10.1002/2014JD021642

Tao L, Hu Y, Liu J (2015) Anthropogenic forcing on the Hadley circulation in CMIP5 simulations. Clim Dyn. doi: 10.1007/s00382-015-2772-1

Tao W-K, Smith EA, Adler RF, et al (2006) Retrieval of Latent Heating from TRMM measurements. Bull Am Meteorol Soc 87:1555–1572. doi: 10.1175/BAMS-87-11-1555

Taylor KE, Stouffer RJ, Meehl GA (2012) An overview of CMIP5 and the experiment design. Bull Am Meteorol Soc 93:485–498. doi: 10.1175/BAMS-D-11-00094.1

Telegadas K (1971) The upper portion of the Hadley cell circulation as deduced from the 1968 French and Chinese nuclear tests. J Geophys Res 76:5018–5024. doi: 10.1029/JC076i021p05018

Trenberth KE, Stepaniak DP (2004) The flow of energy through the earth's climate system. Q J R Meteorol Soc 130:2677–2701. doi: 10.1256/qj.04.83

Tselioudis G, Lipat BR, Konsta D, et al (2016) Midlatitude cloud shifts, their primary link to the Hadley cell, and their diverse radiative effects. Geophys Res Lett 43:4594–4601. doi: 10.1002/2016GL068242

Vecchi GA, Soden BJ (2006) Global Warming and the Weakening of the Tropical Circulation. J Clim 20:4316–4340. doi: 10.1175/JCLI4258.1

Waliser DE, Shi Z, Lanzante JR, Oort AH (1999) The Hadley circulation: assessing NCEP/NCAR reanalysis and sparse in-situ estimates. Clim Dyn 15:719–735. doi: 10.1007/s003820050312

Wallace JM, Hobbs P V. (2006) Atmospheric Science: An Introductory Survey, 2nd edn. Elsevier Academic Press, USA

Wang H, Lau KM (2006) Atmospheric hydrological cycle in the tropics in twentieth century coupled climate simulations. Int J Climatol 26:655–678. doi: 10.1002/joc.1279

Waugh DW, Garfinkel CI, Polvani LM (2015) Drivers of the Recent Tropical Expansion in the Southern Hemisphere : Changing SSTs or Ozone Depletion ? J Clim 28:6581–6586. doi: 10.1175/JCLI-D-15-0138.1

Webster P. (1994) The Role of Hydrological Processes in Ocean-Atmosphere Interractions. Rev Geophys 32:427–476. doi: 10.1029/94RG01873

Wentz FJ, Wentz FJ, Ricciardulli L, et al (2007) How Much More Rain Will Global Warming Bring. Science (80-) 317:233–235. doi: 10.1126/science.1140746

Wilcox LJ, Hoskins BJ, Shine KP, et al (2012) A global blended tropopause based on ERA data . Part II : Trends and tropical broadening thermal tropopause with one based on potential vorticity has been developed. Q J R Meteorol Soc 138:576–584. doi: 10.1002/qj.910

WMO M (1957) A three-dimensional science: Second session of the commission for aerology. WMO Bull IV 4:134–138.

Wright JS, Sobel A, Galewsky J (2010) Diagnosis of Zonal Mean Relative Humidity Changes in a Warmer Climate. J Clim 23:4556–4569. doi: 10.1175/2010JCLI3488.1

Zahn M, Allan RP (2011) Changes in water vapor transports of the ascending branch of the tropical circulation. J Geophys Res 116:1–12. doi: 10.1029/2011JD016206

Zhou YP, Xu KM, Sud YC, Betts AK (2011) Recent trends of the tropical hydrological cycle inferred from Global Precipitation Climatology Project and International Satellite Cloud Climatology Project data. J Geophys Res 116:1–16. doi: 10.1029/2010JD015197